LOUGHBOROUGH UNIVERSITY

Free Surface Films of Binary Liquid Mixtures

by

Fathi Ali M. Bribesh

A DOCTORAL THESIS
Submitted in partial fulfillment of the requirements
for the award of
Doctor of Philosophy of Loughborough University

in the

Faculty of Science
Department of Mathematical Sciences

May 2012

"The significant problems we face cannot be solved at the same level of thinking we were at when we created them."

Albert Einstein (1879-1955).

LOUGHBOROUGH UNIVERSITY

Abstract

Faculty of Science
Department of Mathematical Sciences

Doctor of Philosophy

by Fathi Ali M. Bribesh

Model-H is used to describe structures found in the phase separation in films of binary liquid mixture that have a surface that is free to deform and also may energetically prefer one of the components. The film rests on a solid smooth substrate that has no preference for any component. On the one hand the study focuses on static aspects by investigating steady states that are characterised by their concentration and film height profiles. A large variety of such states are systematically analysed by numerically constructing bifurcation diagrams in dependence of a number of control parameters. The numerical method used is based on minimising the free energy functional at given constraints within a finite element method for a variable domain shape. The structure of the bifurcation diagrams is related to the symmetry properties of the individual solutions on the various branches. On the other hand the full time dependent model-H is linearised about selected steady states, in particular, the laterally invariant, i.e. layered states. The resulting dispersion relations are discussed and related to the corresponding bifurcation points of the steady states. In general, the results do well agree and confirm each other.

The described analysis is performed for a number of important cases whose comparison allows us to gain an advanced understanding of the system behaviour: We distinguish the critical and off-critical case that correspond to zero and non-zero mean concentration, respectively. In the critical case the investigation focuses on (i) flat films without surface bias, (ii) flat films with surface bias, (iii) height-modulated films without surface bias, and (iv) height-modulated films with surface bias. Each case is analysed for several mean film heights and (if applicable) energetic bias at the free surface using the lateral domain size as main control parameter. Linear stability analyses of layered films and symmetry considerations are used to understand the structures of the determined bifurcation diagrams. For off-critical mixtures our study is more restricted. There we consider height-modulated films without and with surface bias for several mean film heights and (if applicable) energetic bias employing the mean concentration as main control parameter.

Keywords:

Binary mixture, Phase separation, Thin liquid films, Free surface, Model-H, Linear stability analysis, Bifurcations of steady state, Critical and off-critical mixture, Marangoni forces at free surface, Finite element method.

In this thesis:

Chapter 5 is based on the publication:

- F. A. M. Bribesh, L. Fraštia and U. Thiele. Decomposition driven interface evolution for layers of binary mixtures: III. Two-dimensional steady film states. Phys. Fluids, submitted (2012).

Chapter 6 of this thesis is based on a manuscript intended to be submitted in summer 2012.

Acknowledgements

I am heartily thankful to my supervisor, **Uwe Thiele**, whose encouragement, guidance and support from the initial to the final level enabled me to develop an understanding of the subject and the guidance to avoid getting lost in my exploration. Uwe was a fabulous advisor: sharp, cheery, perceptive, and mindful of the things that truly matter.

My deep grateful thanks to **Ľubor Fraštia**, for offering me the "*MSS*" software that he had created and I have modified to serve my problem.

Lastly, I offer my regards and blessings to **Santiago Madruga**, my colleague and all of those who supported me in any respect during the completion of the project.

Fathi Bribesh.

Contents

List of Figures

List of Tables

This thesis is dedicated to my parents.
For their endless love, support and encouragement

Chapter 1

Introduction

In fluid dynamics lubrication theory describes the flow of fluids in geometries in which one of the spatial dimensions is significantly smaller than the others. One example is thin liquid layers with a free surface that flow or rest on a solid substrate. They are often referred to as thin liquid films [20, 67]. Such films are widely used in many industrial technologies. For instance, they are part of major processing techniques related to protective and adhesive coatings, painting, dyeing, spraying, and cleaning. They are also involved in microfluidic processes employed in the fabrication of electronics, fuel and solar cells [43]. They also occur in a number of natural processes, e.g., they are present as tear films in the eye [82]. The study of thin liquid films may be considered to be a field where physics, chemistry, and sometimes biology meet to understand a variety of everyday live applications. The understanding in depth of these processes requires as well a knowledge of the micro- and nano-structuring of thin films of mixtures as some of the emerging technological applications are related to structured polymer coatings on solid substrates.

Several ways exist to create liquid films. Very common is to drive a coating layer of liquid onto a solid surface by an external force, such as gravity or centrifugal forces [54, 71, 76, 98]. The latter process is called “spin coating” and allows for a good control of the film thickness, for instance, via an adjustment of the spin speed [81]. Occasionally, the film can be as thin as a few nanometrs. Ideally, the films have a perfectly uniform height (thickness). However, in reality the height is normally not perfectly regular. The free surface of the film may be affected by capillary waves or by inhomogeneities of the substrate. This may produce irregularities in the film thickness over the horizontal

direction. Furthermore, advancing interfaces as e.g., liquid fronts during the spin coating process can be particularly affected by the driving forces, resulting e.g. in fingering instabilities that are observed, for instance, when paint drips [17, 27, 29]. These effects occur for liquid films that consist of a single liquid but may become more complex if the film consists of a mixture of liquids.

In general, one may say that dealing with films of mixtures is more complicated than with films of a simple liquid. Already a film of simple liquid may dewet a solid substrate [23, 77], i.e., the film ruptures under the influence of effective intermolecular forces between solid (or liquid) substrate, film and ambient gas phase. As a result the system forms random arrangements of droplets or holes [83]. The process is called "dewetting". In contrast, "wetting" denotes the opposite process when a liquid spreads over a substrate [12, 23]. A bulk mixture may decompose when the components of the mixture are more attracted to themselves than to the other components [16, 66]. The resulting phase separation (decomposition, demixing) process results in drop or labyrinthine structures that coarsen over time. The two processes of dewetting and decomposition are already intricate and the subject of many studies. However, a thin layer of a liquid mixture may undergo both processes – demixing and dewetting – at the same time [38].

Both, demixing and dewetting phenomena have been theoretically studied on many occasions. However, most studies focus on decomposition in bulk systems, i.e., without solid substrates or free surfaces. Many of the studies of decomposition are based on the so called Cahn-Hilliard theory [16] using a Landau-Cahn free energy functional. The Cahn-Hilliard equation is considered a good tool to model and study such processes. Many authors have studied and mathematically modelled the physics of phase separation. Among those investigations are Refs. [15, 28, 63, 100]. However, most of the studies neglect the contribution of the confining boundary. As an exception, a relatively small number of theoretical studies describes the phase separation phenomenon in a gap between solid walls [11, 33, 50]; others consider a single wall [32] either on a horizontal [41] or on an inclined substrate [59]. The above studies focus on transport by simple diffusion of the components alone, without taking hydrodynamic transport into account. Other authors have coupled the transport equations for the concentration, the Cahn-Hilliard equation [39, 40], and of momentum, the Navier-Stokes equation, to describe phase separation of a binary liquid mixture or a liquid-gas mixture. The resulting model is known as model-H [45], and has mainly been employed to study the coupling of fluid dynamics and diffusion in the bulk [4, 6, 49, 55, 69, 92, 94]. The model has been

re-derived and supplemented with boundary conditions for velocity and concentration fields at the free surface and the substrate in Ref. [87]. The resulting completed model has been used to determine special steady states, namely, in the form of homogeneous and stratified films.

The theoretical description of the structuring processes involves complicated partial differential equations (PDE) that take the form of evolution equations. Often, the resulting evolution is simulated in time to model the system behaviour. This, however, does not allow us to construct a complete picture of the system as unstable solutions of the governing equations are excluded right from the beginning. In general, for many physical systems the mathematical analysis corresponds to the solution of a parameter-dependent systems of *nonlinear* equations that typically have more than one solution. Therefore it is desirable to compute a set of solutions that is as complete as possible. This allows for a search for solutions with certain desirable properties. The resulting solution sets presented with dependence on some control parameter are called bifurcation diagrams. For simple problems they can often be calculated analytically. If this is not possible the bifurcation diagrams and their singularities as, for instance, folds and branching points may be determined employing numerical parameter continuation algorithms. Often, the symmetries of the underlying equations and of the individual solutions play an important role in the understanding of the bifurcation behaviour.

In the present work, we focus on the thickness profiles of liquid films and at the same time on the phase separation inside the film. The film is situated on a horizontal solid, perfectly smooth and energetically neutral substrate and consists of a binary mixture of demixing liquids. The surface is open to the ambient gas, (i.e., the surface is free to deform). The modulated free surface and concentration fields are described through a pair of non-linear evolution equations: model-H as re-derived in Ref. [87]. It couples the convective Cahn-Hilliard equation and the Navier-Stokes equations amended by a concentration dependent stress tensor. The model is simplified assuming an isothermal setting. In our study we follow and extend Ref. [87]. In particular, we consider a two-dimensional system (see Fig. 1.1) that corresponds to a domain whose length corresponds to the lateral domain size and whose height corresponds to the mean film thickness. If the film surface is kept flat the domain is rectangular. This is not the case if the surface is free to deform. Depending on system size and control parameters, our system may undergo a phase separation which is strongly influenced by the interfacial conditions. Here, we investigate non-linear laterally periodic steady state solutions and their bifurcation as functions of various control parameters such as the film thickness,

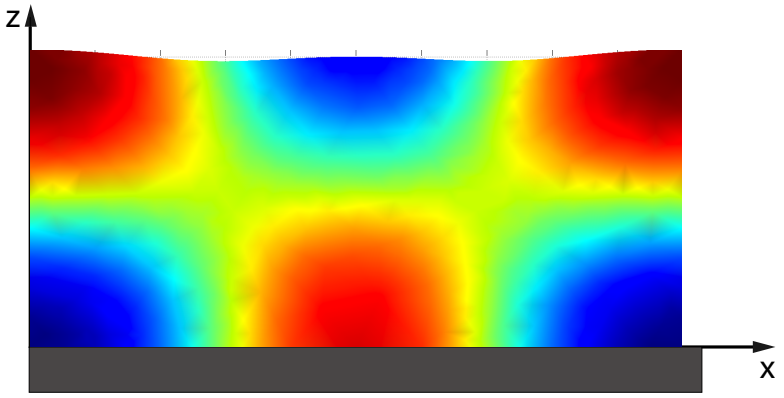

Figure 1.1: Shown is a 2-dimensional concentration profile of the system

energetic bias at the free surface and the lateral domain size. In our study, we distinguish between critical mixtures and off-critical mixtures. In critical mixture, the mean concentration of the two liquids is equal. However, in the off-critical mixture the mean concentration of the two liquids is different.

Beside the distinction with regard to mean concentration we make a further distinction related to the free surface. We introduce two types of films: (i) films with an imposed flat free surface and (ii) films with a modulated free surface. For the flat surface films we monitor the changes in the bifurcation diagrams for the free energy of the system and the L_2-norm of the concentration field. For films with surface modulations we also monitor the L_2-norm of the film thickness. In addition to the study of the bifurcation diagrams we look at the linear stability (in time) with respect to lateral structuring modes for all layered solutions. Note that these transversally invariant solutions correspond to one-dimensional solutions studied in [87]. The structure of the bifurcation diagrams is related to the symmetry properties of the individual solutions on the various branches. For the critical case we employ the lateral domain size as our main control parameter and fix the film thickness and the energetic bias at several selected values. However, in the off-critical case we use the mean concentration as the main control parameter and fix the lateral domain size, film thickness and the energetic bias at selected values.

Systems that are related to our study have been investigated extensively in experimental work that form a primary motivation for our work. In the following discussion we introduce several experimental set-ups and material combinations in more detail than in the sketch provided above. First, we discuss the production of thin films in general and then continue with systems that investigate the relation of phase separation and film thickness modulations for layers of binary liquid mixtures that correspond either to the critical or the off-critical case.

Fluid properties such as density and viscosity and experimental conditions as temperature and pressure are sensitive parameters and important when selecting fluids for particular experimental settings. Thin film experiments are commonly performed with oils or polymers Ref. [38] on silicon substrates. Oils are used because they are chemically inert, i.e., they do not react with most other materials including soft solid substrates made of rubber and plastic. They are also thermally stable even when they are heated or cooled for a long time. Silicon substrates are widely used as a solid substrates as they are very smooth and readily available.

Spin coating [52] is a widely known method for producing uniform thin films on flat substrates. In industry this method is normally used if one aims at creating uniform films. At the start an excess amount of a pure liquid, solution or mixture is placed on the substrate that is then rotated at a sufficiently high speed in order to spread the fluid by centrifugal forces. The higher the rotating speed is chosen, the thinner is the produced film. During the spinning process first the centrally placed drop spreads, when the advancing contact line of the drop reaches the edge of the substrate, part of the fluid is spun off over the edge. As a result the substrate is completely covered by the fluid (see Fig. 1.2). If the pure liquid or the solvent of the solution is volatile, the volatile liquid evaporates in parallel with the spinning process. Depending on spinning speed and evaporation rate the processes of evaporation and spin off dominate the overall thinning behaviour during different stages of the process [61]. When the spin coating method is applied to a solution of a single component the usual result is an unstructured smooth thin film of that component. In contrast, if a solution of a mixture of polymers is used, then the polymer mixture may undergo a phase separation and develop structures on the micro- or nano-scale. This might either already happen during the spin coating process or during a subsequent annealing step, e.g., via heating above the glass transition temperature where the polymer becomes a liquid.

Such structuring of films by the decomposition of a liquid mixture may also trigger an additional dewetting phenomenon. It is usually said that fluctuations in the concentration field may result in the roughening of the surface profile [48], by producing droplets of one liquid inside the other liquid [38] and phase separation [51]. There are many possible morphologies that result from phase separation. It is a complex non-equilibrium process and its outcome are profiles that depend sensitively on the details of the creation process of the thin film and on the properties of the used mixture. Phase separation may take place in the direction parallel to the substrate resulting in a purely lateral structure, i.e., films that consist of vertically homogeneous regions of phase 1 and vertically

homogeneous regions of phase 2. Alternatively, the decomposition can take place perpendicularly to the substrate resulting in stratified layers [2, 24, 60, 75, 88]. The control of the process of phase separation through a better understanding of the phenomenon is highly desirable in the application of thin liquid films. Many studies on phase separation particularly for spin coated films are restricted to the analysis of the structure of the final films. Others have developed techniques to study the process of phase separation in spin coated films in situ. They establish the sequence of the processes which lead to the final phase separated structure in the film. This gives the basis to understand the development of the morphology in the mixed polymer thin films (see Fig. 1.2). Experimental investi-

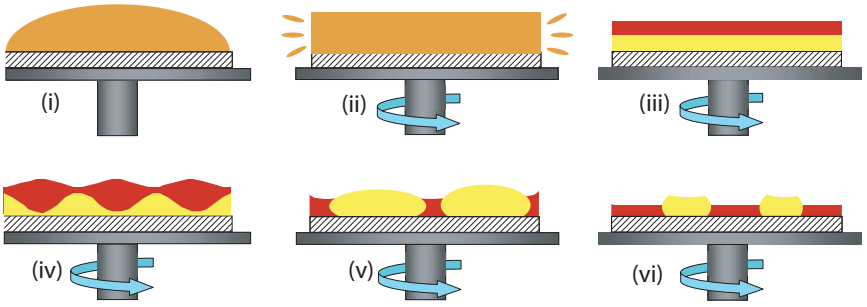

(A)

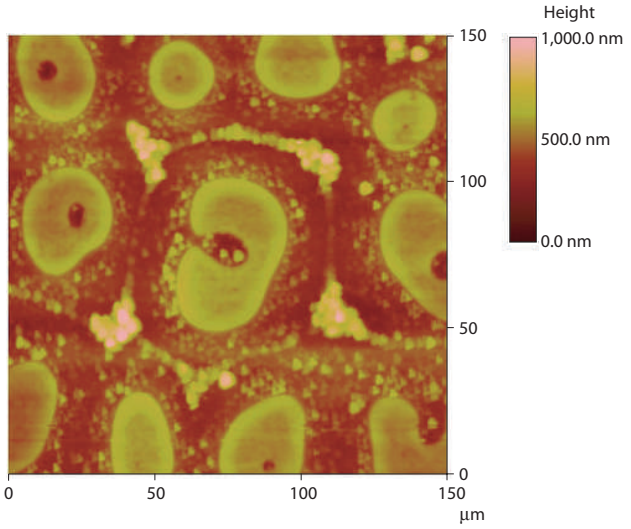

(B)

Figure 1.2: Schematic model shows the deformation of films of binary mixture during the process of spin coating until the final stage of morphology (reproduced from [44]).

gations introduced in Ref. [44] found that phase separation initially takes place through the formation of wetting layers at the surface and the substrate (see stages (i)-(iii) in Fig. 1.2(A)), and when the film thickness decreases below the critical one, the interface becomes unstable, "thermally excited capillary waves are amplified with a mechanism to select a length scale, resulting in the observed off-specular scattering" (see stage (iv)

in Fig. 1.2(A)). As the film becomes thinner the instability grows which leads to an increase in the off-specular scattered intensity and an increase in the roughness of the free surface of the film. To some extent, the amplitude of the instability becomes such that the free surface and the inner liquid-liquid interface meet. At this point a rapid movement of the three-phase (liquid-liquid-gas) contact lines takes place yielding a laterally phase-separated structure as shown in stage (v) in Fig. 1.2(A). Simultaneously, as the total polymer concentration is increased through the ongoing evaporation of the solvent and the boundaries in the equilibrium phase diagram change, phase separation may be initiated in one or both phases, leading to a hierarchical, secondary phase-separation see stage (vi) of Fig. 1.2(A). In thin films of immiscible binary mixture, experiments demonstrate that phase separation can proceed [44] in a multistage process as indicated in Fig. 1.2(A). The further thinning of the film consequent to a characteristic modulation in the visibility of interference fringes measured during the scattering process. Second, the interface between these two layers develops an instability with a well defined wave vector. In other words, this is made manifest both through a continuous decrease in fringe visibility and in the onset of off-specular scattering. When the instabilities grow to such an extent that the highest interfacial protrusions touch the top surface of the film, the film breaks up rapidly into lateral domains. At some point during this process a secondary phase separation takes place within the primary domains. This is obvious from the morphology of the final stage shown in Fig. 1.2(B).

Other observations show that the film thickness can be a control parameter of phase separation, i.e., the lateral phase separation in thicker films is considerably stronger than that in thinner ones [38, 95]. In the experiment in Ref. [95] a blend of polystyrene (PS) and polymethylmethacrylate (PMMA) is used. In Fig. 1.3 it is shown that the film thickness is decreased by altering the speed of spin coating from 140 nm in panel (A) to 80 nm in panel (D). In such films, phase separation starts during solvent evaporation and continues until the film reaches equilibrium. However, during solvent evaporation the film thins and geometrical constraints also become important. The characteristic size of the phase-separated domains decreases with decreasing film thickness and the images from (A) to (D) in Fig. 1.3 exhibited a self-similar domain structure. As confirmed by a qualitative observation of the spin-coating process, films of a larger film thickness take longer to dry, allowing for longer diffusion times and a higher degree of domain-coarsening during the spin-coating procedure. The resulting increase in lateral domain size is compatible with the assumption of a spinodal decomposition process of a binary mixture with subsequent domain growth, constrained to a quasi-two dimensional

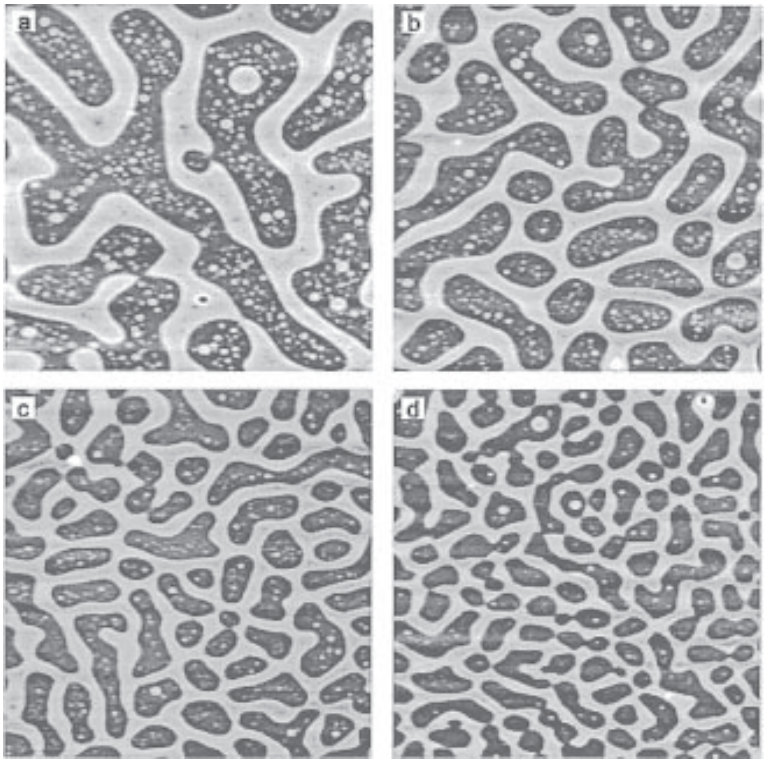

Figure 1.3: A series of final structures as obtained for different mean film thickness of a PS/PMMA mixture produced by spin-coating. The average film thickness is varied by adjusting the rotation speed of the spin coater from 2000 rpm to 1000 rpm. The film thickness in panel (A) is 140 nm, in panel (B) is 105 nm, in panel (C) is 95 nm, and in panel (D) is 80 nm. The PMMA phase is the bright domain and the dark is the PS phase. Reproduced from [38].

configuration by the thickness of the film. Fig. 1.3 indicates that the growth of domain size proceeds significantly faster than a linear relation.

The formation of other patterns is observed in films of off-critical blends that are relatively rich in one component. The effect of off-critical composition has been the focus of experimental investigation aiming at determining phase diagrams for decomposition in thin films [68]. In confined flows of polymer blends of polybutadiene/polydimethylsiloxane one has observed that the droplet size depends on composition [90]. In the presence of an external temperature gradients, micro-convective patterns have been studied in polystyrene/polybutdadien blends and it has been shown that off-critical compositions give rise to irregular droplets in the early stages of the phase separation process as compared to more spherical droplets observed for critical mixtures [62]. On the theoretical side, the influence of the average composition has been discussed by means of phase diagrams derived from Hamiltonian approaches [84], whereas lower solution temperature phenomena are described by state equations arising from the Sanchez and Lacombe theory [97]. Particularly interesting for applications such as the oil recovery from porous media is the effect that a confinement at the microscale has on the

behaviour of blends. For polymer blends confined in cylindric geometries it has been shown, that the phase separation in the spinodal region driven by infinitesimal perturbations is independent of the confinement, whereas phase separation via nucleation and growth is strongly affected by confinement [86].

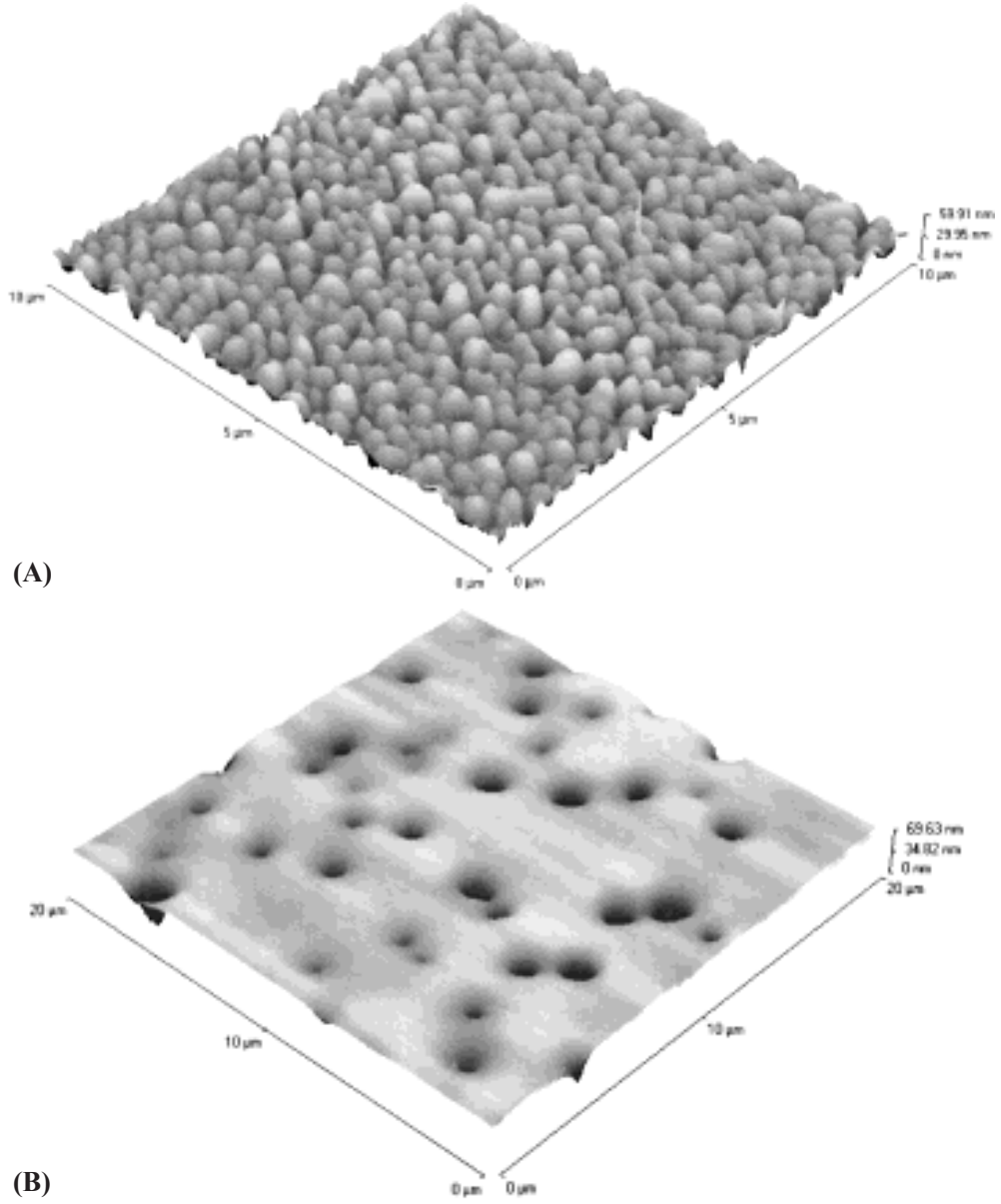

Figure 1.4: Atomic force microscopy (AFM) image of an ultra-thin film of a blend of deuterated poly(styrene) (dPS)/poly-(vinylmethylether) (PVME) at off-critical composition with film thickness $L \approx 1000$Å. The concentration of dPS is in (A) $\phi_{dPS} = 0.10$, and in (B) $\phi_{dPS} = 0.35$. The films were annealed for 17min at $160°C$. Apparently, the elevations in (A) correspond to dPS-rich minority droplets, while the depressions in (B) correspond to regions of PVME-rich minority droplets. Reproduced from [30].

Further experiments in Ref. [30] show that droplets of the minority phase tend to form at off-critical polymer compositions and the presence of these droplets within the film

layer leads to a distortion of the free surface. Often the droplets form by nucleation or via a breakup of an early-stage bicontinuous spinodal decomposition pattern. In general, the observations show that droplets have higher surface tension than the surrounding medium cause a local elevation of the liquid-gas boundary, while droplets of lower surface tension result in a depression in the film surface. The surface topography contains elevations or bumps rather than the bicontinuous structure seen for critical mixtures. Direct observations of surface perturbations created by the droplets within the film also makes it possible to follow the droplet kinetics. The presence of such droplets within these ultra-thin polymer layers should have a disruptive influence on the film. In Fig. 1.4(B) it is found that the initially smooth film surface evolves to form holes. The kinetics of the formation of the holes in the dPS-rich films is much slower than the growth of the elevations (mound structures) seen in Fig. 1.4(A). This is likely a consequence of the higher viscosity of the dPS-rich phase. There are other situations where holes and mounds occur in thin polymer films. For example, some of the features appear to be similar to defect structures found in block copolymer (a polymer formed of two or more sub-chains that consist of different molecules) films Ref. [30].

The surface patterns in copolymer films arise from a reorganisation of incomplete block copolymer layers. Depending on the film thickness, either islands or holes can be formed. For dense systems the formation of islands appears to be very different from the formation of holes [19]. Smooth films form for quantised values of film thickness, that are controlled by the domain spacing. In the early stage, thin, elongated elevations are created. This, more or less, connected network splits progressively into shorter and shorter segments and leads, finally, to rounded islands [19]. Clearly, this is a different type of surface pattern formation than found in thin blend films. Hole formation also occurs in polymer dewetting [77].

Another experimental study of off-critical films is presented in Ref. [42] where the film thickness is controlled in the range of between 1 nm and 100 nm. The sample is annealed to allow for phase separation. Panels (A,B,C) of Fig. 1.5 show the topography of films of thickness $(40, 15, 7)\ \mathrm{nm}$, respectively. Panels (D,E,F) give a measurement of the frictional force for the samples corresponding to (A,B,C). The results show that the thinner film develops smaller and more bumps. The number of bumps of the minority phase (PS) is inversely proportional to the film thickness. The bumps correspond to the dPS-rich phase and the PMMA-rich area forms the background.

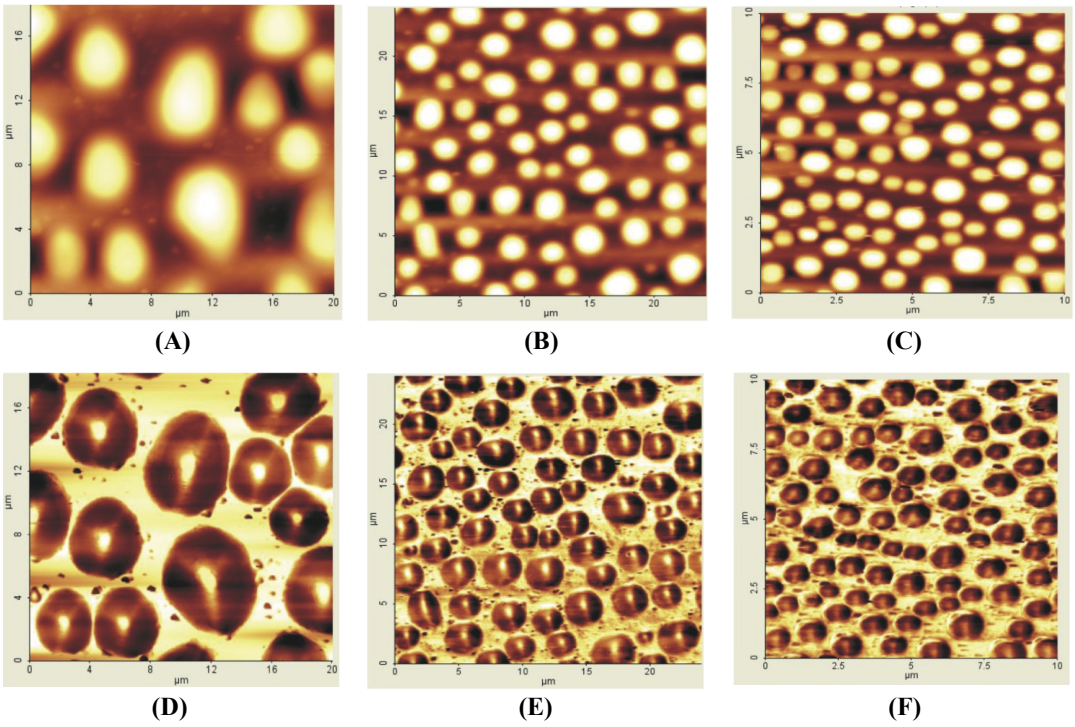

Figure 1.5: Representative images of the topography (panels A,B,C) and of the fractional force (panels D,E,F) of SP/PMMA blend films with a 5 wt% diblock copolymer. The thickness of the films are $40\mathrm{nm}(\mathrm{A},\mathrm{D})$, $15\mathrm{nm}(\mathrm{B},\mathrm{E})$, $7\mathrm{nm}(\mathrm{C},\mathrm{F})$. On the frictional force images, the bright spots at the centre of islands are clear. Reproduced from [42].

The presented experimental studies indicate that in general a purely lateral structure can be produced in very thin films, while, stratified structures are not present in very thin films. For thicker films the film becomes able to produce stratified layer or purely vertical structuring. Also the phase separation for both, the critical and off-critical cases, crucially depend on the film thickness. In the off-critical films it is expected to see droplets of the minority phase embedded in a background of the majority phase. Other situations show that holes and mounds occur in off-critical films.

Our main aim in the present thesis is to systematically analyse the structures that may emerge in films of binary mixtures of immiscible liquids. The underlying mathematical model is model-H that we review in Chapter 3 after briefly discussing in Chapter 2 basic physical, mathematical and computational concepts that are used in the subsequent chapters either explicitly or implicitly. In particular, our interest focus on the determination of film thickness and concentration profiles for a two-dimensional system in the two-phase region as literature studies of such free surface films are limited to fully non-linear results for the one-dimensional case [87] and its two-dimensional linear instability modes [57]. On the one hand our study focus on static aspects by investigating two-dimensional steady states that are characterised by their concentration

and film height profiles. A large variety of such states are systematically analysed by numerically constructing bifurcation diagrams as a function of a number of control parameters. The numerical method used is based on minimising the free energy functional at given constraints within a finite element method for a variable domain shape. It is also presented in Chapter 3. The structure of the bifurcation diagrams is related to the symmetry properties of the individual solutions on the various branches. On the other hand the full time dependent model-H is linearised about selected steady states as introduced in Chapter 4. The chapter continues with a presentation of selected linear results for vertical, horizontal and checkerboard instability modes for homogeneous films. Stability results for laterally invariant, i.e. layered states are discussed alongside the bifurcation diagrams in the subsequent chapters that present the various steady states.

The previously introduced analysis is performed for a number of important cases whose comparison allows us to gain an advanced understanding of the system behaviour: We focus on the critical and off-critical case in Chapters 5 and 6, respectively. In particular, in Chapter 5 the investigation focuses on (i) flat films without surface bias, (ii) flat films with surface bias, (iii) height-modulated films without surface bias, and (iv) height-modulated films with surface bias. Each case is analysed for several mean film heights and (if applicable) energetic bias at the free surface using the lateral domain size as main control parameter. Linear stability analyses of layered films in the form of dispersion relations allow for an independent second determination of the bifurcation points of the various steady state solution branches that bifurcate from the homogeneous (weakly stratified) and the stratified solutions for different energetic biases. The study of the bifurcation diagrams is furthermore supplemented by an investigation of the symmetry groups of the concentration profiles on the various. As a result we are able to completely understand the structure of the determined bifurcation diagrams in cases (i) to (iv).

The results presented in Chapter 6 for off-critical mixtures focus on the role of the additional major control parameter, the mean concentration. In particular, we only consider height-modulated films without and with surface bias for several mean film heights and (if applicable) energetic bias employing the mean concentration as main control parameter. The bifurcation diagrams of the films are supplemented by concentration profiles at particular mean concentrations selected in such a way that they well illustrate the behaviour of the films as one follows the individual steady solution branches.

Finally, Chapter 7 concludes and discusses possible future work.

Chapter 2

Theoretical and Numerical Background

2.1 Introduction

The observation of phenomena associated with fluids has probably started many centuries ago. In fact, almost any action a person does involves some kind of fluid mechanics problem. Recently, the rise of the empirical sciences, mathematics, and computing has pushed the general scientific study of fluid mechanics. It continues to receive increasing attention as technical requirements of modern applications request a better control of the dynamics of a wide variety of simple and complex fluids [31, 35, 65, 78].

The models for the flow of thin films are mostly based on the continuity and Navier-Stokes equations which present a system of partial differential equations to describe the fluid flow, e.g. of air or liquids. The equations express the conservation of mass and momentum, respectively.

A wide range of problems are investigated in fluid dynamics. Many of them involve the movement of a fluid on/in/around solids (that may be rigid or elastic). In particular, the boundary between a solid and a fluid is a widely discussed part of modern fluid mechanics and has to be carefully considered especially for small scale applications. The study of thin layers of fluid attracts a large attention within fluid mechanics as thin films play a very important role in modern technology. The mathematical treatment of thin liquid films combines the Navier-Stokes equations with new ideas. Numerous papers were published that combine critical ideas: (i) the lubrication approximation

which takes advantage of the thinness of the layer (film) through the small quantity

$$\epsilon = H/L \tag{2.1}$$

where L is a characteristic film length and H is the characteristic film height. This is equivalent to the assumption that the thickness of the thin film is small as compared to the horizontal extent of the fluid. Employing the lubrication theory, the Navier-Stokes equations are simplified and the system may be studied in a more systematic way [67].

In any physical problem one has to translate the problem into a mathematical expression which reflects an accurate understanding of all the basic physics involved. In this chapter we introduce fundamental concepts which will be employed in the model we study later on.

2.2 Fluid Properties

There exist many properties of fluids that distinguish the various gases and liquids. Among fluids there can be wide differences in their behaviour and their deformation such as how fluids are affected by solid walls, how fluid phases interact and how material properties affect the flow itself. The analysis of the behaviour of fluids is based on both the familiar material properties and laws of non-equilibrium thermodynamics that relate continuity of mass, momentum, and energy. Sometimes one describes the properties of fluids in asymptotic ways as, for instance, in the case of the assumption of an ideal fluid that is assumed to be inviscid. This assumption is a useful concept when mathematical solutions are being considered which simplifies the model and helps to achieve some practically useful solutions. It is very important to understand the various properties to be introduced in the mathematical models.

2.2.1 Density and (in)Compressibility

The fluid density is defined as its mass per unit volume and it can be considered as a measure of how tightly the molecules of fluid are packed. It is usually denoted by the symbol ρ and is calculated by dividing the mass m by the volume V

$$\rho = \frac{m}{V}. \tag{2.2}$$

One of the most common uses of density is in how different fluids interact when mixed together. It is well known that a fluid with lower density rises within one of higher density. In fluid mechanics, density can be a key concept to analyse how fluids interact with each other.

The property of compressibility refers to changes in the density that result from changes in the pressure. In reality, all fluids are compressible to some extend. Often, however, the changes in the pressure result in a negligible change in density. In this case the flow is called "incompressible". Mathematically, incompressibility means

$$\frac{\mathrm{D}\rho}{\mathrm{D}t} = 0 \tag{2.3}$$

where $\frac{\mathrm{D}}{\mathrm{D}t} = \frac{\partial}{\partial t} + \mathbf{v} \cdot \nabla$ is the substantial derivative, i.e., the derivative in the frame moving with the fluid element. The validity of the incompressibility assumption depends on the fluid properties. Practically, Eq. (2.3) reveals that the study of incompressible fluids is much easier than the one of compressible fluids.

2.2.2 Viscosity and (non)Newtonian Behaviour

The term "viscosity" refers to the effect internal friction has on the fluid motion. The ratio between inertial and viscous forces (Reynolds number) is used to evaluate whether viscous or inviscid equations are appropriate to the problem. Close to solid boundaries the viscosity always plays an important role and cannot be neglected. The no-slip condition at the solid-liquid interface for instance (see section 2.4), can generate a thin region of large strain rate, a so called boundary layer, which enhances the effect of even a small amount of viscosity, and thus generates vorticity.

A Newtonian fluid is a fluid whose stress at each point is linearly proportional to the strain rate at that point [8]. All gases and most liquids such as water and oils for instance are considered to be Newtonian fluids. Mathematically, the simplest equation that describes the behaviour of a Newtonian fluid is

$$\tau = \mu \frac{dv}{dy} \tag{2.4}$$

where τ is the shear stress, μ is the dynamic viscosity of the fluid, and the derivative of v with respect to y is the velocity gradient perpendicular to the direction of shear stress. The viscosity in a pure Newtonian fluid only depends on pressure and temperature,

but not on the forces acting on it. For incompressible fluids of constant viscosity the components of the shear stress tensor are given by

$$\tau_{ij} = \mu \left(\frac{\partial v_i}{\partial x_j} + \frac{\partial v_j}{\partial x_i} \right). \tag{2.5}$$

As a result, the complete stress tensor is

$$\mathbb{T}_{ij} = -p\delta_{ij} + \mu \left(\frac{\partial v_i}{\partial x_j} + \frac{\partial v_j}{\partial x_i} \right) \tag{2.6}$$

where p is the pressure and δ_{ij} is the Kronecker delta. If a fluid does not satisfy this relation, it is termed a non-Newtonian fluid. Many particle suspensions and most highly viscous fluids are examples of non-Newtonion fluids. An extensive literature is available regarding analytic and numerical studies in both Newtonian and non-Newtonian fluids, see for instance [18, 37, 80].

2.2.3 Interfacial Tensions, Capillarity and Wettability

The surface tension of a liquid manifests itself by a depression or rise of the free surface of a liquid. It is responsible for creating drops and bubbles of liquid as well as for the breakage of a liquid jet inside another phase into many drops. The surface tension unit corresponds to a force per length and is measured in [N/m]. Surface tension results from the sharp changes in the density between two adjoined materials or phases. The

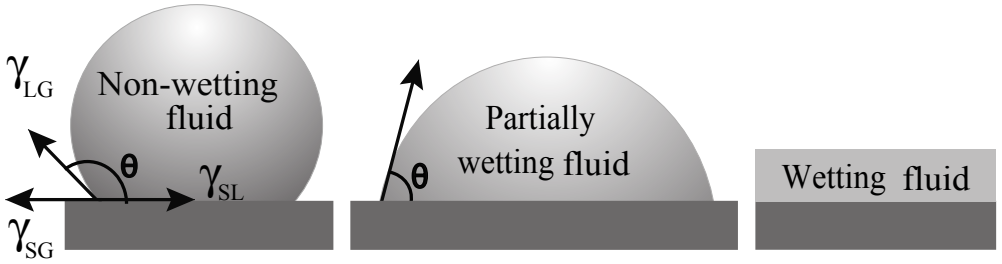

Figure 2.1: Schematic diagram for wetting, partially wetting, and non-wetting fluids of solid substrate

relation between surface tension and the pressure difference between the two opposite sides of the surface is based on geometry. Suppose that a small element of a curved surface is taken into consideration. If the surface tension is constant, then the tangential component of the forces cancel because of symmetry. This is not the case in the normal direction. There the surface tension forces pull the surface into one direction. There

needs to exist a pressure difference to balance the surface tension. Otherwise bubbles would always collapse.

The process of the spreading of liquids on solid substrates is called wetting and is related to wettability properties. It can be related to the contact angle θ (see Fig. 2.1) and to the spreading coefficient. The behaviour depends on the properties of the solid surface, the liquid and the ambient gas (or second liquid). Wettability is a major factor that controls the distribution of fluids on the walls of a reservoir.

There exists a surface tension between a solid and a fluid, and also between two immiscible fluids. The equilibrium configuration at a three-phase contact depends on the relative values of the surface tensions between each pair of the three phases and satisfies the Young's law

$$\gamma_{SG} = \gamma_{SL} + \gamma_{LG} \cos\theta \tag{2.7}$$

where γ_{SG}, γ_{SL} and γ_{LG} are the surface tensions of the solid-gas, solid-liquid and liquid-gas interfaces, respectively (see Fig. 2.1). If $\theta < 90\,^\circ$ then the liquid is said to partially wet the substrate, if $\theta > 90\,^\circ$ then the liquid is said to not wet the substrate. When the liquid covers the whole solid surface, i.e., $\theta = 0\,^\circ$, then one says the liquid completely wets the solid. I.e., the surface is coated by a liquid film. [23, 53]

2.3 Transport Equations

When a fluid fills a region of space say Ω then we can write the representation of the flow of this fluid considering the position $\mathbf{r} = (x, y, z)$ in Ω, the velocity of fluid particle $\mathbf{v} = \mathbf{v}(\mathbf{r}, t)$, the density $\rho = \rho(\mathbf{r}, t)$, the pressure $p = p(\mathbf{r}, t)$ of the fluid at position $\mathbf{r}$ and time t. If the fluid is Newtonian then the density, pressure and the velocity are governed by the Navier-Stokes equation which represents momentum transport, the continuity equation that represents mass conservation and by some constitutive relation connecting the density ρ and pressure p.

2.3.1 Navier-Stokes Equations of Momentum Transport

The Navier-Stokes equations are a system of non-linear partial differential equations which govern the motion of a Newtonian fluid. The fluid can be a liquid or a gas. In essence, they represent the balance between the rate of change of momentum of

an element of fluid and the forces that act on it. The equations were first introduced by Claude-Louis Navier and George Gabriel Stokes to describe the motion of simple fluids. They result from applying Newton's second law to fluid motion, together with the assumption that the fluid stress is the sum of viscous stress and pressure term. The equations are used to describe a large number of physical, biological and engineering applications [26, 34, 89].

The equations establish relations between the rates of change of pressure, velocity, and acceleration. The derivation of the Navier-Stokes equations is based on applications of momentum and mass conservation in an arbitrary control volume. The resulting equations have the form

$$\rho\left(\frac{\partial \mathbf{v}}{\partial t} + \mathbf{v}\cdot\nabla\mathbf{v}\right) = \nabla\cdot\mathbb{T} + \mathbf{f} \tag{2.8}$$

where ρ is the fluid density, $\mathbf{v}$ is the velocity of the liquid, ∇ is the Nabla operator, $\mathbb{T}$ is the stress tensor given by Eq. (2.6), and $\mathbf{f}$ presents the body forces that act on the fluid, $\nabla\mathbf{v}$ is the tensor derivative of the velocity vector. The nonlinear term $\mathbf{v}\cdot\nabla\mathbf{v}$ corresponds to convective momentum transport. The term $\nabla\cdot\mathbb{T} = \nabla p + \nabla\cdot\underline{\tau}$ represents gradients of stresses in the fluid and is responsible for diffusive momentum transport [1, 8]. Individually, ∇p is the pressure gradient, and $\nabla\cdot\underline{\tau}$ represents viscous forces. The body forces may include, e.g., gravity, centrifugal force, electromagnetic forces that depend on the nature of the particular problem.

On many occasions the material derivative

$$\frac{D}{Dt} = \frac{\partial}{\partial t} + \mathbf{v}\cdot\nabla \tag{2.9}$$

is used, and Eqs. (2.8) are rewritten as

$$\rho\frac{D\mathbf{v}}{Dt} = -\nabla p + \nabla\cdot\underline{\tau} + \mathbf{f}. \tag{2.10}$$

An important body of work focuses on incompressible flow for Newtonian fluids. In that case $\nabla\cdot\mathbf{v} = 0$ and the viscosity is constant. In consequence the Navier-Stokes equations can be rewritten in classical form

$$\rho\left(\frac{\partial \mathbf{v}}{\partial t} + \mathbf{v}\cdot\nabla\mathbf{v}\right) = -\nabla p + \mu\nabla^2\mathbf{v} + \mathbf{f}. \tag{2.11}$$

The first term $\frac{\partial \mathbf{v}}{\partial t}$ represents the unsteady acceleration. The LHS of Eq. (2.11) represents inertia (per unit volume), whereas the sum of the first two terms on the RHS of the equation represents the divergence of stress. Overall, the LHS describes acceleration of a fluid element in its moving frame, and RHS is the sum of divergence of stress and body forces.

2.3.2 Non-dimensionlisation

In many situations, not all of the terms in Eq. (2.11) are equally important. In fact, the static situation is the most trivial situation. In this case all of the terms involving the velocity are zero, the pressure gradient and the external forces are the only contributions. There are many other possibilities that can be considered. The difficult task in any particular situation is to determine which of the terms are small, and which are large.

The Reynolds number is the most important parameter which indicates the relative importance of viscous and inertial forces in a given situation. Assume the characteristic velocity scale is V_0 and the characteristic length scale for the variation of the velocity is L. Then the orders of magnitude of the terms in the equation are

$$\frac{\partial \mathbf{v}}{\partial t} \approx \frac{V_0}{\tau} = \frac{V_0^2}{L} \approx \mathbf{v} \cdot \nabla \mathbf{v}, \quad \mu \nabla^2 \mathbf{v} \approx \frac{\mu V_0}{L^2}, \tag{2.12}$$

where we introduce the time scale $\tau = L/V_0$. The ratio of the inertial terms to the viscous term is a characteristic dimensionless number called the Reynolds number.

$$\mathrm{Re} = \frac{\rho V_0 L}{\mu}. \tag{2.13}$$

Non-dimensionalising Eqs. (2.8) using non-dimensional variables $\tilde{t} = (V_0/L)t$, $\tilde{\mathbf{v}} = \mathbf{v}/V_0$ and $\tilde{\mathbf{r}} = \mathbf{r}/L$ one obtains after dropping the tildes:

$$\frac{\partial \mathbf{v}}{\partial t} + \mathbf{v} \cdot \nabla \mathbf{v} = -\nabla p + \frac{1}{\mathrm{Re}} \nabla^2 \mathbf{v} + \mathbf{f}. \tag{2.14}$$

Note that, $\tilde{p} = (1/(\rho V_0^2))p$ is the pressure scale and $\tilde{\mathbf{f}} = (L/(\rho V_0^2))\mathbf{f}$ is the scale of body forces. This scaling explains why all flows with the same Reynolds number are related by similarity relations. When the Reynolds number is very large the flow is rather inviscid, and can be described away from solid walls by Euler's equation. Under these conditions turbulence can occur. However for small Reynolds number the flow is

very viscous and no turbulence is found. Then, one may neglect the inertial terms in the Navier-Stokes equations and obtain creeping flow or Stokes equations (see section 2.3.3).

To non-dimensionalise a system of equations, the following steps need to be taken:

- Identify all the independent and dependent variables
- Replace each of them with a quantity scaled relative to a characteristic unit to be determined
- Divide through by the coefficient of the highest order polynomial or derivative term
- Choose judiciously the definition of the characteristic unit for each variable so that the coefficients of as many terms as possible become 1
- Rewrite the system of equations in terms of their new dimensionless quantities.

The last three steps are usually specific to the problem where non-dimensionalisation is applied. However, almost all systems require the first two steps to be performed.

2.3.3 Turbulent vs Laminar Flow and the Stokes Limit

At large Re number the flow is often characterised by a chaotic and stochastic behaviour showing random eddies or/and recirculation. The flow is called turbulent and is characterised by rapid variations in velocity, pressure, high momentum convection and/or low momentum diffusion. If the flow is not turbulent then it is called laminar. In fact, the presence of eddies and recirculation does not necessarily indicate turbulent flow. Such phenomena may be present also in laminar flow. Mathematically, turbulent flow is often described by Reynolds decomposition, in which the flow is broken down into the sum of an average component and a perturbation component. Turbulent flows can be described well through the Navier-Stokes equations where Reynolds number is high. Steady flow occurs when all time derivatives introduced in the flow field vanish, i.e., in steady states the properties of the flow do not change over time at a given point in the system. Otherwise, flow is unsteady. Turbulent flows are highly unsteady. A turbulent flow can, however, be statistically stationary [70]. The random field $U(x,t)$ is statistically stationary if all statistic measures are invariant in time. This means that the flow

has constant statistical properties. Often, the mean field is the object of interest, and this is steady too in a statistically stationary flow. Steady flows are often more tractable than otherwise similar unsteady flows. The governing equations of a steady problem have one dimension fewer (time) than the governing equations of the same problem without taking advantage of the steadiness of the flow field.

For Stokes flow convective momentum transport is negligible as inertial forces are relatively small compared with viscous forces, i.e. the Reynolds number is small. This is a typical situation in flows where the fluid velocity is very small, the viscosities are very large, or the length-scales of the flow are very small. Under this conditions the Navier-Stokes equations are reduced to Stokes equations.

In the unsteady case (if the time scale $\neq L/V_0$ where V_0 and L as defined in section 2.3.2) one has

$$\rho\frac{\partial \mathbf{v}}{\partial t} = \nabla \cdot \mathbb{T} + \mathbf{f}, \tag{2.15}$$

while in the steady case the equation reduced to

$$\nabla p = \mu\nabla^2\mathbf{v} + \mathbf{f}. \tag{2.16}$$

2.3.4 Mass Transport and Continuity Equation

The continuity equation is an expression of the mass conservation. Consider the differential volume element $\Delta V = \Delta x\Delta y\Delta z$ shown in Fig. 2.2(A). The conservation of mass for the volume ΔV is written in the expression (rate of change of mass in ΔV = rate of mass convected into ΔV-rate of mass convected out of ΔV) which can be formulated mathematically in the equation

$$\begin{aligned}\Delta x\Delta y\Delta z\frac{\partial \rho}{\partial t} = \Delta y\Delta z\Big[(\rho v_x)|_x - (\rho v_x)|_{x+\Delta x}\Big] + \Delta x\Delta z\Big[(\rho v_y)|_y - (\rho v_y)|_{y+\Delta y}\Big] \\ + \Delta x\Delta y\Big[(\rho v_z)|_z - (\rho v_z)|_{z+\Delta z}\Big]\end{aligned} \tag{2.17}$$

where ρ is the density of the fluid in ΔV. By dividing each side of Eq. (2.17) by ΔV, and taking the limit as $\Delta V \to 0$ and after invoking the definition of the partial derivative we obtain the equation

$$\frac{\partial \rho}{\partial t} = -\Big[\frac{\partial}{\partial x}(\rho v_x) + \frac{\partial}{\partial y}(\rho v_y) + \frac{\partial}{\partial z}(\rho v_z)\Big], \tag{2.18}$$

which can be expressed as

$$\frac{\partial \rho}{\partial t} = -\nabla \cdot (\rho \mathbf{v}). \tag{2.19}$$

Eq. (2.19) is the differential expression of the continuity equation and it can be rearranged as

$$\frac{D\rho}{Dt} = -\rho(\nabla \cdot \mathbf{v}) \tag{2.20}$$

where $\frac{D}{Dt}$ is the material derivative given by Eq. (2.9).

If the fluid is assumed to be incompressible, i.e., the (local) fluid density ρ is constant. This means that ρ of a fluid element does not change along a trajectory, implying $\frac{D\rho}{Dt} = 0$. This reduces the continuity equation to

$$\nabla \cdot \mathbf{v} = 0. \tag{2.21}$$

The continuity equation can be derived in a similar way using an arbitrary fixed closed infinitesimal region (see Fig. 2.2(B)). Conservation of mass to such volume is expressed by the following integral

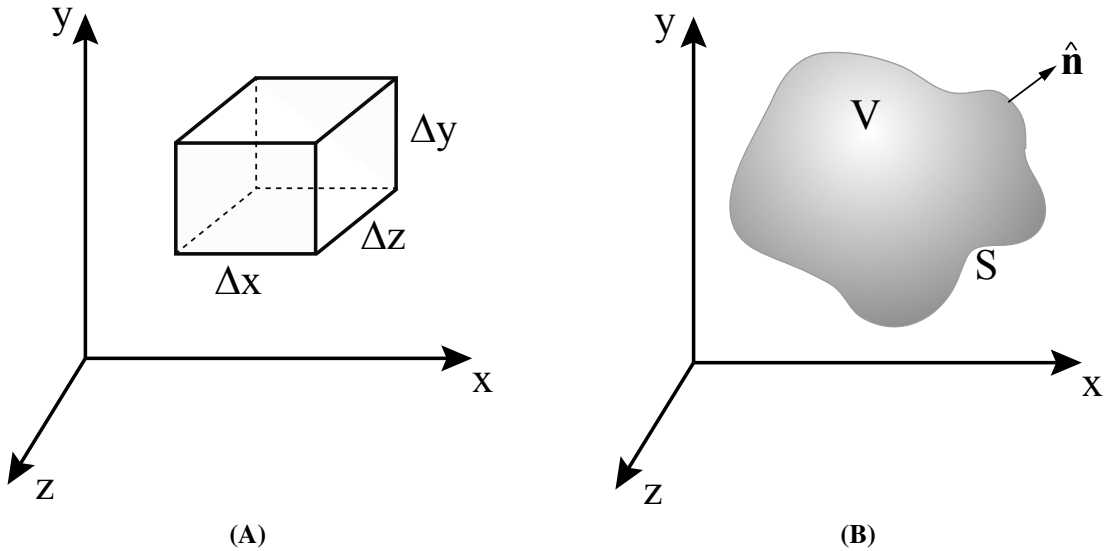

Figure 2.2: Shown are, (A) an arbitrary closed infinitesimal control volume element, (B) an arbitrary fixed closed infinitesimal region

$$\frac{d}{dt}\int_V \rho dV = -\oint_S (\mathbf{n} \cdot \rho \mathbf{v}) dS. \tag{2.22}$$

Eqs. (2.19) and (2.22) are equivalent. This is shown using the divergence theorem which states that, if V is a volume bounded by a closed surface S and $\mathbf{A}$ is a continuous vector field then one can write

$$\int_V (\nabla \cdot A) dV = \oint_S (\mathbf{n} \cdot \mathbf{A}) dS. \tag{2.23}$$

I.e., the surface integral in Eq. (2.22) can be converted to the volume integral

$$\frac{d}{dt} \int_V \rho dV = - \int_V (\nabla \cdot \rho \mathbf{v}) dV. \tag{2.24}$$

As we fix the control volume in space, the ordinary derivative can be moved inside the integral by changing it into a partial derivative, and we can write both sides of the equation to be consolidated within the integration

$$\int_V \left[\frac{\partial \rho}{\partial t} + (\nabla \cdot \rho \mathbf{v}) \right] dV = 0. \tag{2.25}$$

Since this equation is satisfied for an arbitrary volume V, the integrand must vanish which gives Eq. (2.19).

2.3.5 Mass Diffusion and the Cahn-Hilliard Equations for Mixtures

The Cahn-Hilliard equation describes the decomposition of a binary mixture [16]. It is based on a free energy functional that takes into account contributions at the diffuse interface between the two components which come from composition gradients. It is used to study the dynamics of phase separation. The Cahn-Hilliard equation is formulated as

$$\frac{\partial c}{\partial t} = m \Delta \left[f'(c) - \kappa \Delta c \right] \tag{2.26}$$

where m is the mobility and c is the concentration difference. The equation characterises important features of two-phase systems. It corresponds to a gradient dynamics for the free energy functional

$$\psi[c, \nabla c] = \int \left[f(c) + \frac{1}{2} \kappa |\nabla c|^2 \right] d\mathbf{r}. \tag{2.27}$$

The local energy $f(c)$ is often approximated by a double well potential (see the upper part of Fig. 2.3). The gradient term with the positive constant κ represents the interfacial energy of the diffuse interface between the phases. The system consists of component 1 characterised by the local concentration c_1 and component 2 characterised by the local concentration c_2. The local concentrations are scaled such that $c_1+c_2 = 1$. Furthermore, we use $c = c_1 - c_2$ as concentration variable.

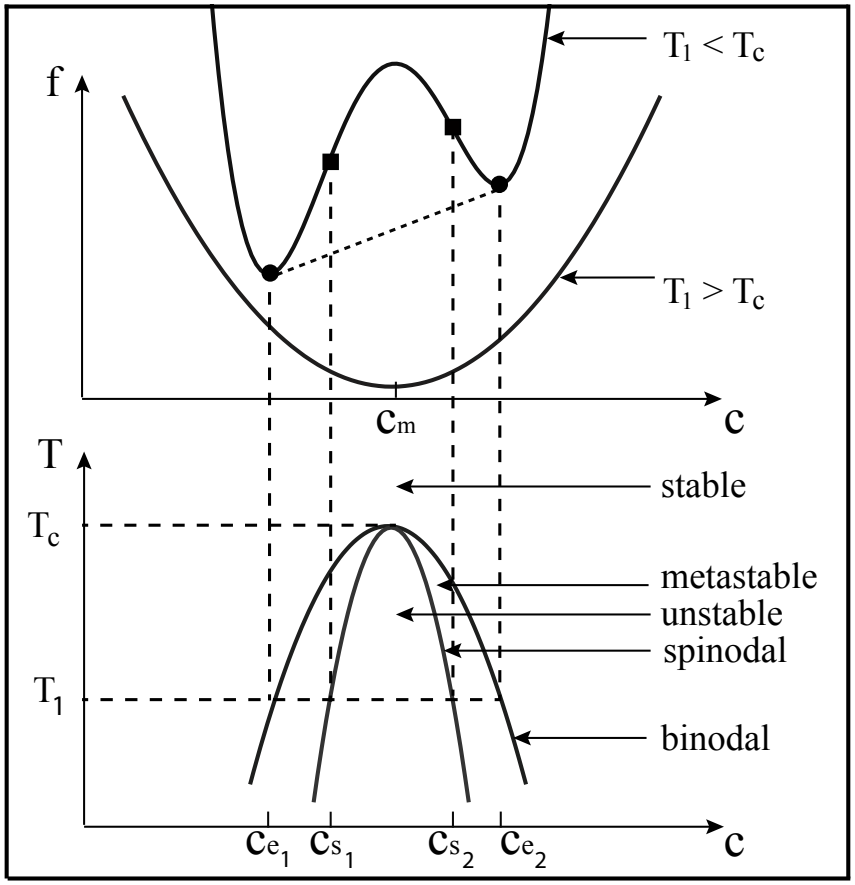

Figure 2.3: Free energy f as a function of c at temperatures $T > T_c$, and $T_1 < T_c$ with spinodal points marked by squares and binodal points marked by dots. Underneath is the phase diagram of f as a function of c and T. Recreated after Fig. 1 of [3].

The free energy function f may change between qualitatively different forms depending on temperature T. If T is high, then f is convex in c (see Fig. 2.3). In our case, when the temperature of the mixture is lower than the critical one, the free energy density diagram changes from a single well to a double well, and mixtures which have a concentration between the two binodal points c_{e_1} and c_{e_2} of the diagram become unstable. When $f''(c) < 0$, any perturbation that causes the mixture phases to separate tends to reduce the total bulk free energy. However, for mixtures which are partially separated and satisfy the condition of concentrations $c_1 < c_2$ for which $f'(c_1) > f'(c_2)$, the concentration moves from the c_1 into the c_2 phase. This tends to decrease the total bulk free

energy. If we consider a mixture comprised of a finite number of volumes say v_i, each with distinct concentration corresponding to c_i then it is possible to determine the binodal points i.e., the equilibrium concentration values by minimising the total bulk free energy. This indicates that for an asymmetric double-well function f, the binodal points do not lie at the minima of each well, but on a double tangent line shown in Fig. 2.3.

A miscibility gap (where the system can not take any arbitrary concentration) is observed when f takes a double-well form. The phase diagram shown in Fig. 2.3 corresponds to the latter form of f. The particular positions of concentration values c_{e_1}, and c_{e_2}, defined by the common tangent to f, determine the coexistence curve in the Tc-plane, indicated as the binodal. These concentrations are characterised by an identical chemical potential (slope of the tangent) and may coexist. Above the binodal is the region that represents stable single phase states, the complement of this region refers to states that are thermodynamically unstable. The inflection points c_{s_1}, c_{s_2} of f determine a curve indicated by the spinodal. That curve separates the metastable and unstable subregions with $f'' > 0$ and $f'' < 0$, respectively. In the homogeneous state, the system quenched below a critical temperature undergoes separation into two phases. For inner states of the spinodal, the path to phase separation is traditionally classified as spinodal decomposition, whereas in the metastable region as nucleation. See, however, Ref. [64] for a subtle correction of this picture.

When the system is inside the spinodal line it is linearly unstable and the order parameter fluctuations grow. The gradient term in Eq. (2.27) has a smoothing effect on interfaces between the two phases. In consequence, jumps of c are not allowed, instead different phases are separated by diffuse interfaces, that is, small subregions with rapid changes of c. The thickness of these interfaces is related to the value of κ. In the limit $\kappa \to 0$ the surface area of the interface is minimised locally in Ω [85].

2.4 Boundary Conditions

Beside using the governing bulk equations to solve a flow problem, one has to specify boundary conditions that model the behaviour of the fluid at solid boundaries of various types and at liquid gas interfaces.

At a Solid Substrate Nearly all flow observations on the meso and macro scale indicate that a fluid does not move relative to a solid surface, neither in the tangential

direction nor in the perpendicular one. These conditions are called the no-slip and no-penetration condition. For instance, if a considered solid surface does not move, the no-slip condition is $\mathbf{v} \cdot \mathbf{t} = 0$ where $\mathbf{t}$ is the unit vector in the tangential direction. The no-slip condition is normally invoked for every solid-fluid interface. Furthermore, if the substrate is not porous, the normal component of the fluid velocity, $\mathbf{v} \cdot \mathbf{n}$, is zero. This is the so-called no-penetration boundary condition.

At a Free Surface Two boundary conditions are required at the free surface: (i) Kinematic boundary condition which relates fluid motion to the change of position of the free surface. (ii) The dynamic boundary condition that is concerned with the force balance at the free surface. It requires continuity of tangential and normal forces across the free surface. The traction exerted by the liquid onto the gas is equal and opposite to the traction exerted by the gas on the liquid. Here we give them in the form of Eq. 3.13 below where the first term of the RHS of the equation corresponds to the Laplace or curvature pressure that acts normal to the free surface and the second term corresponds to Marangoni force which act tangentially to the interface and results from the variation of the surface tension along the surface caused normally by a solutal or thermal Marangoni effect.

2.4.1 Periodic Lateral Boundary Conditions

There is a difference between finite and infinite systems. As all simulations take place in a finite domain, periodic boundary conditions is an option used in dynamics simulations to avoid problems with boundary effects caused by finite size and make the system more like an infinite one, at the cost of possible periodicity effects. When a system is bounded but free of physical walls it becomes important to use periodic boundary conditions. This is equivalent to considering an infinite array of identical copies of the system region filling a space. The consequences of this periodicity in general are: (i) Any flux that leaves the simulation region of the system through a particular bounding face immediately enters the system region through the opposite face, i.e., when a flux leaves the right-hand face, it enters the simulation box through the left-hand face. (ii) Fluxes lying within a distance of a boundary interact with those in an adjacent copy of the system. In fact, using periodic boundary conditions is topologically equivalent to mapping the region onto a torus. As our system is a rectangular system, periodic boundary conditions are used on the lateral edges of the system.

2.5 Finite Element Method

Because of the difficulty of solving most fluid dynamics problems analytically, often numerical methods are employed to tackle them. They play a very important role in solving such problems, in particular, methods that have more flexibility when dealing with problems involving various materials, distinct boundary conditions or irregular domains. Because of their importance, a variety of numerical methods have been developed. Some of them are quite simple but others are quite advanced. Examples for the latter methods are, for instance, Finite Difference Methods, Finite Volume Methods, and Finite Element Methods. The Finite Element Method (FEM) was mentioned first by the mathematician Richard Courant, who utilised Ritz method of numerical analysis and variational calculus to obtain approximate solutions to vibration systems. Since the rapid decline in the cost of computers and the increase in computing power, nowadays supercomputers and even personal computers are able to produce accurate results for many kinds of problems.

FEM uses a system of points called nodes which make a grid called a mesh. This mesh is programmed to contain the structural properties which define how the structure will react to certain loading conditions. Nodes are assigned at a certain density throughout the material depending on the anticipated stress levels of particular areas. Regions which will receive large amounts of stress usually have a higher node density than those which experience little or no stress. Regions of interest may consist of high concentration areas, high stress areas, high energy areas or regions that show other complex details [9, 47, 101].

The mesh is similar to a spider web: Each node, is connected by a mesh element to each of the adjacent nodes. This web of vectors is what carries the material properties to the object. Actually finite element methods provide a greater flexibility to model complex geometries than other methods such as finite differences and finite volume methods. It has been widely used in solving structural, mechanical, and fluid dynamics problems as well as problems of other disciplines. The code we employ called "mss" implements a finite element method to solve a variation problem [36].

2.5.1 Finite Element Displacement

Usually when FEM are applied to physical or engineering problems described by differential equations or by variational approaches then continuous expressions need to be converted to discrete finite element expressions. The procedure is called finite element discretization and depends on the type of elements that are implemented and also on the approximation accuracy. This process incorporates boundary conditions and produces a discrete system of equations that needs to be solved. For our case finite element discretization can be summarised in the following points.

- The continuum problem is divided by notional lines or surfaces (depending on the problems dimension) into a number of non-overlapping finite elements, see Fig. 3.2 for our case.
- The lines form a mesh and meet at a number of nodal points.
- The displacements of nodal points are the unknown parameters of the problem.
- A set of functions is established to uniquely define the state of displacement within each finite element and on its boundaries in terms of its nodal displacements.
- The displacement functions will define the physical properties within an element and on its boundaries in a unique manner, in terms of the nodal displacements.
- A system of forces concentrated at the nodes and equilibrating the boundary stresses and any distributed loads generates so-called stiffness matrix.

2.5.2 Two Dimensional Strain Triangular Elements

Finite element approximations are usually developed with shape functions expressed in terms of parent element coordinates. In our 2D-problem, linear triangular elements have been used employing a so-called area coordinate system. The area coordinate system divides the area of a triangular element into three proportional areas. Isoparametric coordinates are considered i.e. shape functions are fixed for all the unknown values. Using matrix expressions unknowns can be rewritten with respect to shape functions [9]. The three linear shape functions N_i, with $i = 1, 2, 3$ are constructed in such a way that

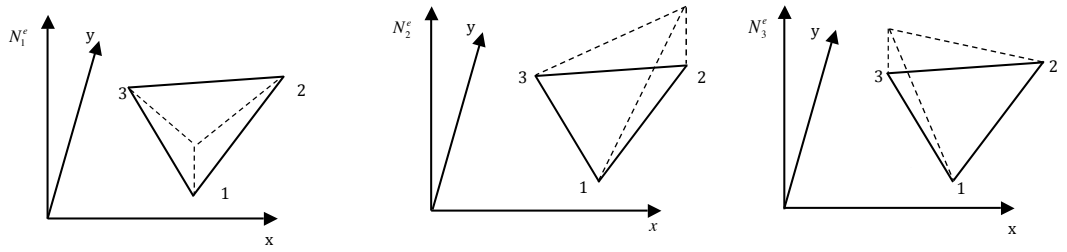

Figure 2.4: Three-node triangular element shape functions

they are equal to one at the node i and are linearly reduced to zero at the other two nodes (see Fig. 2.4). The summation of $N_i, i = 1, 2, 3$ will represent the plane at the height of one over the three nodes and thus it will be parallel to the triangle 123, consequently for every $N_i, i = 1, 2, 3$ we have $\sum_{i=1}^{3} N_i = 1$. The shape functions are determined as,

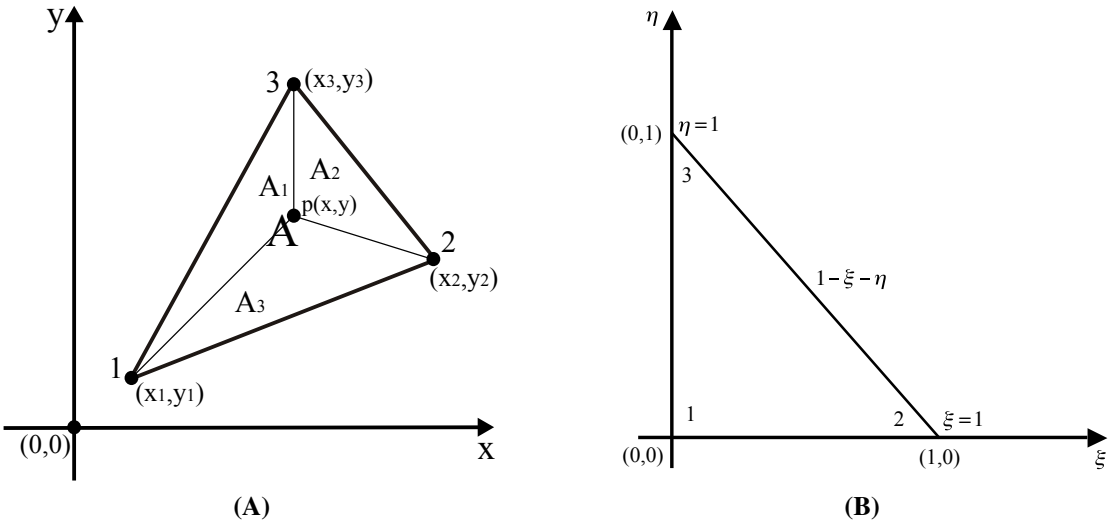

Figure 2.5: (A) Area coordinate system, (B) Isoparametric natural coordinate system

$N_1 = \xi$, $N_2 = \eta$, and $N_3 = 1 - \xi - \eta$, where ξ, η are natural coordinates, i.e. area coordinates (see Fig. 2.5). One notices that only two N_i are linearly independent. As mentioned above, any point on the triangle divides its area into three areas $A_i, i = 1, 2, 3$ with summation equal the whole area of that element, and at every point inside the triangle one can write

$$N_1 = \frac{A_1}{A}, \quad N_2 = \frac{A_2}{A}, \quad \text{and} \quad N_3 = \frac{A_3}{A}. \tag{2.28}$$

From now onwards we rename the vector $\mathbf{N} = (N_1, N_2, N_3)$ as $\mathbf{H}$ for later compatibility.

2.5.3 Mesh Adaption

Frequently, finite element results can be made more accurate by utilising procedures for error estimation and subsequent generation of a more precise mesh. One of these procedures is known as adaptive mesh. The process depends on previous results at all stages [101]. In particular, it is possible to adaptively refine the mesh so that the accuracy of a certain quantity of interest satisfies some specified criteria. One way is to reduce the Root Mean Square error represented by the difference between the original control points and the new control point locations calculated in the transformation process. Various refinement procedures can be applied, that fall mainly into two categories:

1- The p-refinement in which one uses the same element size but increases, generally hierarchically, the order of the polynomial used in their definition. p-refinement is divided into subclasses: One, in which the polynomial order is increased uniformly throughout the whole domain. In another one the polynomial order is increased locally using hierarchical refinement. In neither of these, a direct procedure has been developed which allows the prediction of the best refinement to be used to obtain a given error. Much work has been reported in the literature, one can refer to [9, 101].

2- The h-refinement in which the same class of elements is used but they are changed in size, in some locations made larger and in others made smaller, to provide maximal economy in reaching the desired accuracy. h-refinement is divided into subclasses as it can be applied and thought of in different ways. The first of these h-refinement methods is element subdivision (enrichment). Here refinement can be conveniently implemented and existing elements, if they show too much error, are simply divided into smaller ones keeping the original element boundaries intact. The second method is known as r-refinement, which keeps the total number of nodes constant and adjusts their position to obtain an optimal approximation. The last method, is that of a complete mesh regeneration or re-meshing. Here, on the basis of a given solution, a new element size is predicted in all the domain and a totally new mesh is generated. This refinement method is used in our system where the refinement predominantly takes place in the diffuse interface regions, and in zones along the free surface, where high concentration gradients and/or surface curvature are detected. The refinement could be repeated once more before the final solution is obtained.

2.6 Symmetry

A set S is said to be symmetric under a transformation g if g maps the set onto itself $gS = S$. Here the set S refers to a solution (bifurcation branches) [79]. Symmetry operations are used to analyse and classify our solutions by symmetry groups. This requires examination of the symmetries present in their structures.

A solution has reflectional symmetry if it can be bisected by one or more 'mirror' axes. In this example the portion on the left hand side of such an axis relates to the portion on the right hand side by being its mirror image. All the points on the mirror (reflection) axis remain fixed. However, it has translational symmetry if its profiles can be moved to congruent profiles by a glide in any direction, while it is still keeping the same orientation. All points of the solution must move the same distance in the same direction. The symmetry of glide-reflection is a motion combining a reflection and translation, along the direction of the reflection axis, consecutively. Two successive glide-reflection operations along an axis are equivalent to one unit of translation in the same direction. In addition to these four symmetry operations, there are two other symmetries which are in fact characteristics of every solution profile, the identity and inverse symmetry. The identity is equivalent to no movement at all. Here the profile is effectively left in exactly the same position, i.e., each point is mapped onto itself. For every symmetry of a solution there is another symmetry which will take the solution back to its original position. This is called the inverse symmetry.

A symmetry group is a set of symmetry operations satisfying the following conditions:

- The identity symmetry is included in the set
- For every symmetry operation moving a solution from position A to position B, there exists a unique inverse operation which is able to move the solution back from position B to its original position.
- Each symmetry operation in the group can be followed by another operation resulting in a new operation that is also a member of the symmetry group.

In symmetric bifurcation theory, one studies how the trajectories of symmetric vector fields behave when parameters are varied [56]. In general the theory makes it possible to analyse symmetric dynamical systems in a systematic manner. The results are able to explain several phenomena that can be observed in simulations of specific equations.

Elements of symmetry based analysis which is known as equivariant bifurcation theory are employed in the study to sort and relate the various obtained solutions, e.g. by understanding the involved symmetry breaking bifurcations, see Chapter 5. Thereby the explanation of the behaviour of our system becomes more visible and understandable.

Our results contain many types of symmetries as the symmetry of the individual solution, the symmetry of the solutions branches and the symmetry of the bifurcation diagrams.

2.7 Summary

We have introduced basic concepts that are used either explicitly or implicitly in this thesis. As the properties of the fluid are very important in mathematical modelling, the concepts of density and compressibility of fluid have been introduced. As we work with Newtonian fluids, we introduced the concepts of viscosity and Newtonian behaviour of fluid. The interfacial tension, wettability and the capillarity where the fluid can produce significant changes in the concentration fields, surface topographies, and surface morphologies. Consequently, the transport equations represented by Cahn-Hilliard equation and Navier-Stokes equations have been introduced as well as the continuity equation which presents the mass conservation. As we will use non-dimensional form of model-H, we have given an idea about this subject. Since the equations are supplemented by boundary conditions we have introduced general concepts related to the boundary conditions at the free surface and the substrate. However, at the lateral edges of the container of our system we will consider periodic boundary conditions. In terms of the finite element method, we have explained the finite element displacement using triangular elements and we have given an idea about the mesh adaption. Finally, we have given some basic concepts about symmetry.

Chapter 3

The Model and Numerical Procedures

3.1 Introduction

Phase-field models are able to deal with multiphase systems including various boundary conditions at the free interfaces by a continuous description of the entire domain, including the interfacial regions. This continuous variation is realised with the assistance of one or several order parameter(s), called phase-field functions that distinguish the thermodynamic phases. In a sharp interface model, the basic equations are written for each phase separately and the boundary conditions are specified explicitly at the interface. However, in a diffuse interface theory the basic equations with supplementary terms depending on variations of the phase field are written only once for the entire system without interface conditions. Then the physics of the interface becomes part of the bulk description and two transport processes can be observed when the system evolves towards a minimum of the free energy. The first one is the diffusion of the individual components within the binary mixture that may lead to phase separation, while the second corresponds to the convective motion of the binary fluid. By neglecting the convective flow, the process of phase-separation can be described by the theory of Cahn and Hilliard [16] which is based on minimisation mentioned above of the free energy functional that includes the square of the density gradient which is introduced by Van der Waals [91]. Simulations of the phase separation in thin films have been able to reproduce the experimental coarsening phenomena [99], the interplay of phase separation and the wetting behaviour of the components for an unstable binary mixture with off-critical composition [73], the surface interaction with molecules of the binary mixture via long-ranged Van der Waals interaction [74], and the dynamics of phase separation in

binary mixtures near a surface with a preferential attraction for one of the components of the mixture [72].

An important model used to describes the phase separation in liquid systems is model-H [45, 94]. The model consists of a modified Cahn-Hilliard equation which includes advection of the order parameter that represents the mixture composition, amended Navier-Stokes equations, and the continuity equation. The equations of conservation of mass and momentum are coupled through the convective term of the convection-diffusion equation, which is driven by a composition-dependent body force. As noted in [49], when the system is composed of single-phase domains separated by sharp interfaces, this force incorporates capillary effects and plays the role of the Marangoni force. Model- H shows that during the early stages of the phase-separation process (i.e., spinodal decomposition), initial instabilities grow exponentially, forming at the end single-phase micro domains whose size corresponds to the fastest growing mode of the linear regime [94].

Various problems have been treated with phase field models. Examples are the motion of phase separating liquid drops in two dimensions where convection and diffusion are coupled via the body force [93], and the phase separation taking place when an initially homogeneous liquid binary mixture is moved deeply into its two-phase region Ref. [94]. A phase-field model for Marangoni convection in a liquid-gas system with a deformable interface, heated from below was developed in Ref. [13], and a phase field model for analysing the influence of evaporation on Marangoni convection in liquid-vapour system was proposed in Ref. [14]. The behaviour of miscible liquids was theoretically studied by means of a diffuse interface approach in order to show the existence of an effective interfacial tension between them [10]. Interfacial phenomena in miscible liquids are transient since the system is driven to a homogeneous equilibrium by diffusion. However, if the diffusion coefficient is sufficiently small, capillary forces can lead to a significant fluid motion. This situation was investigated by numerical simulations of miscible drops, jets, and plane interfaces in Ref. [10]. A mathematical model of non-isothermal phase separation was suggested in Ref. [3], but the hydrodynamic phenomena have not been included there. An attempt to construct a phase-field model for non-isothermal immiscible incompressible liquids has been undertaken by [5]. Ref. [87] proposed a dynamic model for describing the coupled decomposition and profile evolution of a free-surface film of a binary mixture and analysed steady base states. The phase separation in a binary mixture subjected to a temperature gradient was investigated in experimental work in Ref. [7].

3.2 Model-H

For our purpose to study binary mixtures problems, the isothermal model-H is an adequate description as it couples the transport equations for momentum, and the mass density of one of the components, i.e., the Navier-Stokes equations and the convective Cahn-Hilliard equation. The model has been formulated in various ways according to the particular definition of pressure used. As the present study extends on results of reference Ref. [87], we describe model-H following their notation.

We will consider a binary fluid with constant density ρ which implies $\nabla.\mathbf{v} = 0$. This is possible if an identical mass density of the two pure components is assumed. Furthermore, an isothermal setting is considered, i.e., a constant temperature T. The local densities of the two components ρ_1 and ρ_2 are expressed in terms of concentrations $c_1 = \rho_1/\rho$ and $c_2 = \rho_2/\rho$ where $\rho = \rho_1 + \rho_2$. Model-H in terms of the concentration c defined by

$$c = c_1 - c_2 = 2c_1 - 1 \tag{3.1}$$

is written in the form of two coupled equations. The first one describes the transport of concentration:

$$\frac{\partial c}{\partial t} + \mathbf{v} \cdot \nabla c = -\nabla \cdot \Big\{ M \nabla \Big[\sigma_c \Delta c - \partial_c f(c) \Big] \Big\} \tag{3.2}$$

where $\sigma_c = \rho^2 \xi / 4$, and $M = 4k_3/\rho^2$. where ξ is the dimensional stiffness of the diffuse interface, and k_3 is the kinetic coefficient of the dimensional Cahn Hilliard equation. The chemical potential is given by $\tilde{\mu}_d = \rho \mu_d = 2\partial_c f(c)$, where μ_d is the difference in the chemical potential of component 1 and component 2 and $f(c)$ is the concentration dependent part of the local free energy which is assumed to be a symmetric double-well potential.

The second equation describes the transport of momentum:

$$\begin{aligned} \rho \frac{\partial \mathbf{v}}{\partial t} + \rho \mathbf{v} \cdot \nabla \mathbf{v} = & -\nabla \cdot \Big\{ \sigma_c (\nabla c)(\nabla c) \\ & + \Big[p - \sigma_c (c+1) \Delta c - \frac{\sigma_c}{2} (\nabla c)^2 \Big] \mathbb{I} \Big\} + \eta \Delta \mathbf{v} \end{aligned} \tag{3.3}$$

where p is the mechanical pressure for homogeneous material in the thermodynamic equilibrium which is not dependent on gradients or derivatives. The term $(p - \sigma_c(c+1)\Delta c - \frac{\sigma_c}{2}(\nabla c)^2)$ is introduced as an effective pressure and denoted by p_{eff} [87] and $\eta \Delta \mathbf{v}$ is the viscosity term. If a finite domain is considered (see Fig. 3.1), then Eqs. (3.2) and (3.3) must be supplemented with boundary conditions. We first introduce boundary

conditions for the concentration and the velocity at the surfaces. The boundary condi-

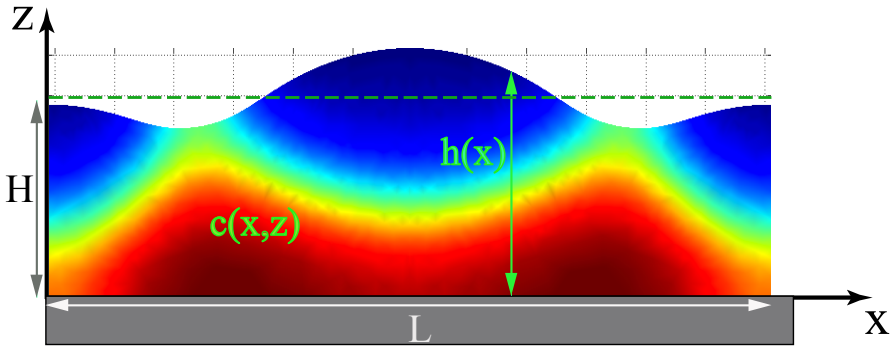

Figure 3.1: Sketch of the two-dimensional (2d) geometry: An infinitely extended free-surface film of a liquid binary mixture on a horizontal smooth solid substrate.

tions for the concentration field at the substrate where $z = 0$ are as follows:
Zero diffusive flux through the rigid substrate

$$\partial_z \Big[\sigma_c \Delta c - \partial_c f(c)\Big] = 0, \tag{3.4}$$

an energetic condition related to a possible preferred adsorption of one component at the substrate

$$\Big[-\sigma_c \partial_z c - \sigma^- \Delta_{||} c + \partial_c f^-(c)\Big] = 0 \tag{3.5}$$

where $\Delta_{||} = \nabla_{||} \cdot \nabla_{||}$, $\nabla_{||} = (\partial_x, \partial_y)$, and $f^-(c)$ is the excess free energy at the substrate. Focusing on surface energies that do not depend on concentration gradients ($\sigma^- = 0$) we have

$$\Big[-\sigma_c \partial_z c + \partial_c f^-(c)\Big] = 0. \tag{3.6}$$

At the free surface $h(x, z, t)$, the boundary conditions are (i) zero diffusive flux through the moving surface

$$\mathbf{n} \cdot \nabla \Big[\sigma_c \Delta c - \partial_c f(c)\Big] = 0 \tag{3.7}$$

where $\mathbf{n}$ is the outwards normal vector at the free surface given by

$$\mathbf{n} = \frac{(-\partial_x h, 1)}{\sqrt{1 + (\partial_x h)^2}}, \tag{3.8}$$

and (ii) an energetic condition

$$\Big[\sigma_c (\mathbf{n} \cdot \nabla) c - \sigma^+ \Delta_s c + \partial_c f^+(c)\Big] = 0 \tag{3.9}$$

where $\Delta_s = \nabla_s \cdot \nabla_s$ the surface Laplace operator, i.e., ∇_s is the surface gradient operator $\nabla_s = \mathbf{t} \cdot \nabla$ and the tangent vector $\mathbf{t}$ is given by

$$\mathbf{t} = \frac{(1, \partial_x h)}{\sqrt{1 + (\partial_x h)^2}}. \tag{3.10}$$

Assuming as before $\sigma^+ = 0$ results in

$$\Big[\sigma_c(\mathbf{n} \cdot \nabla)c + \partial_c f^+(c)\Big] = 0. \tag{3.11}$$

The boundary conditions for the velocity field are the no-slip and no-penetration conditions at the solid substrate ($z = 0$), i.e.,

$$\mathbf{v} = 0, \tag{3.12}$$

and the force equilibrium at free surface

$$(\underline{\tau} - \underline{\tau}_{air}) \cdot \mathbf{n} = -\gamma(c)\mathbf{n}\nabla \cdot \mathbf{n} + \nabla_s \gamma(c) \tag{3.13}$$

where $\underline{\tau} = -\sigma_c(\nabla c)(\nabla c) - \Big[p - \sigma_c(c+1)\Delta c - \frac{\sigma_c}{2}(\nabla c)^2\Big]\mathbb{I} + \eta[\nabla \mathbf{v} + (\nabla \mathbf{v})^T]$ is the stress tensor and the ambient air is assumed to not transmit any forces ($\underline{\tau}_{air} = 0$). The function $\gamma(c)$ is the concentration dependent surface tension. Note that $\nabla \cdot \mathbf{n}$ corresponds to the curvature of the free surface. A kinematic condition at the free surface indicates that the surface follows the flow field.

$$(\partial_t \mathbf{h}) \cdot \mathbf{n} = \mathbf{v} \cdot \mathbf{n} \tag{3.14}$$

where $\mathbf{h}$ is defined as $\mathbf{h} = h(x, y, t)\mathbf{e}_z$.

3.3 Dimensionless Form of Model-H

In Chapter 4 below, we discuss the linear stability of layered steady states employing the fully time-dependent model-H. Preparing for that analysis, we rewrite the governing equations and the boundary conditions of model-H in dimensionless form using the scales introduced in Ref. [57, 87]. We use $l = C\sqrt{\sigma_c/E}$ as length scale which corresponds to the thickness of the diffuse interface between the two phases, $U = ME/lC^2$ as velocity scale, $\tau = l/U = l^2C^2/(ME)$ as time scale. The energy scale is E. Choosing the pressure scale based on the energy $P = E$ and C is the concentration at the

binodal given by $C = \sqrt{a/b}$. The parameter M is the diffusive mobility in the Cahn-Hilliard equation. With these scales, two dimensionless numbers appear in the governing equations, the pressure number $\mathrm{Ps} = \rho M^2 E^2 / C^6 \sigma_c$ and the Reynolds number $\mathrm{Re} = ME\rho/\eta C^2$.
Eqs. (3.2) and (3.3) in the dimensionless form are

$$\partial_t c + \mathbf{v} \cdot \nabla c = -\nabla \cdot \big\{ \nabla [\Delta c - \partial_c f(c)] \big\}, \tag{3.15}$$

$$\mathrm{Ps}\Big[\frac{\partial \mathbf{v}}{\partial t} + \mathbf{v} \cdot \nabla \mathbf{v}\Big] = -\nabla \cdot \big\{ (\nabla c)(\nabla c) + p_{\mathrm{eff}} \underline{\mathbf{I}} \big\} + \frac{\mathrm{Ps}}{\mathrm{Re}} \boldsymbol{\Delta} \mathbf{v}, \tag{3.16}$$

respectively, and the continuity equation is given by

$$\nabla \cdot \mathbf{v} = 0. \tag{3.17}$$

The diagonal of the stress tensor contains the effective pressure given as

$$p_{\mathbf{eff}} = p - (c+1)(\nabla c) - \frac{(\nabla c)^2}{2}. \tag{3.18}$$

where p represents the normal pressure and $f(c)$ is the bulk free energy. Eqs. (3.15) and (3.16) are supplemented by the non-dimensional boundary conditions. For the concentration field the boundary conditions at the substrate (Eq. 3.4) become

$$\partial_z \Big[(\partial_{xx} + \partial_{zz}) c - \partial_c f(c) \Big] = 0 \tag{3.19}$$

This condition prevents the diffusive mass flux through the substrate, whereas the following condition

$$-\partial_z c + \mathrm{S} \partial_c f^-(c) = 0 \tag{3.20}$$

allows for energetic bias at the substrate, where f^- is the non-dimensional free energy at the substrate defined by the relation

$$f^-(c) = \gamma_s + a^- c + \frac{1}{2} b^- c^2. \tag{3.21}$$

The parameter S indicates the dimensionless surface tension of the liquid-gas interface at $c = 0$ and the dimensionless solid liquid interface tension at $c = 0$ is represented by $\mathrm{S}\gamma_s$. The parameters a^- and b^- refer to adsorption preference of one of the components at the substrate and changes in the mixing behaviour of the components at the substrate, respectively. Similar conditions are applied at the curved free surface $z = h(x, y, t)$,

i.e.,

$$\Big[\partial_z - (\partial_x h)\partial_x\Big]\Big[(\partial_{xx} + \partial_{zz})c - \partial_c f(c)\Big] = 0, \tag{3.22}$$

$$\Big[\partial_z - (\partial_x h)\partial_x\Big]c + \mathrm{S}\partial_c f^+(c)\sqrt{1 + (\partial_x h)^2} = 0 \tag{3.23}$$

where

$$f^+(c) = \alpha + a^+ c + \frac{1}{2}b^+ c^2. \tag{3.24}$$

is the free energy at the free surface. The boundary conditions for the velocity field at the substrate are the no-slip and no-penetration conditions

$$u = w = 0 \quad \text{at} \quad z = 0 \tag{3.25}$$

At the free surface the conditions result from the balance of tangential forces

$$\begin{aligned} -[\partial_x c + (\partial_x h)\partial_z c][\partial_z c - (\partial_x h)(\partial_x c)] + \frac{\mathrm{Ps}}{\mathrm{Re}}[(u_z + w_x)(1 - h_x^2) \\ + 2(w_z - u_x)h_x] = \mathrm{S}\sqrt{1 + h_x^2}[\partial_x + (\partial_x h)\partial_z]f^+(c) \end{aligned} \tag{3.26}$$

and normal force

$$\begin{aligned} -\frac{1}{1 + {h_x}^2}[\partial_z c - (\partial_x h)(\partial_x c)]^2 - p_{\mathbf{eff}} + \frac{\mathrm{Ps}}{\mathrm{Re}}\frac{2}{1 + h_x^2}[u_x h_x^2 + w_z \\ - h_x(u_z + w_x)] = \mathrm{S}f^+(c)\partial_x\Big[\frac{\partial_x h}{\sqrt{1 + h_x^2}}\Big]. \end{aligned} \tag{3.27}$$

The kinematic boundary condition becomes

$$\partial_t h = w - u\partial_x h. \tag{3.28}$$

Now if we consider a flat film ($h = h_0$) of quiescent mixture ($\mathbf{v}_0 = 0$) with stratified layers ($c(x, z) = c_0(z)$), then it is a steady solution of the following one-dimensional non-convective Cahn-Hilliard equation

$$\partial_{zz}\Big[\partial_{zz}c_0 - \partial_c f(c)|_{c_0}\Big] = 0 \tag{3.29}$$

and the boundary conditions

$$\partial_z \Big[\partial_{zz} c_0 - \partial_c f(c)|_{c_0} \Big] = 0 \quad \text{at} \quad z = 0, h_0 \tag{3.30}$$

$$\pm \partial_z c_0 + \mathrm{S} \partial_c f^{\pm}(c)|_{c_0} = 0 \quad \text{at} \quad z = 0, h_0. \tag{3.31}$$

where the "-" sign is at the substrate ($z = 0$), and the "+" sign is at the free surface ($z = h_0$).

3.4 Variational Approach to Steady States

The static limit of the bulk equations and boundary conditions constituting model-H can be alternatively derived minimising the free energy functional (appendix of Ref. [87]). For a two dimensional free surface film of binary mixture this free energy functional can be split into two terms

$$F[c(x,z), h(x)] = F_b[c(x,z), h(x)] + F_s[c(x, h(x)), h(x)] \tag{3.32}$$

where $c(x,z)$ is the concentration field and $h(x)$ is the film height depending on x. The first term on the right hand side is the film bulk energy and the second term represents the interface energies at the upper and lower film surfaces. The two terms F_b and F_s are defined respectively as

$$F_b = \int_{-\infty}^{\infty} \int_0^{h(x)} \Big[\frac{\sigma_c}{2} (\nabla c)^2 + f(c) \Big] dz dx - \lambda_d \Big[\int_\Omega c_1 dA - C_1 A \Big] - \lambda \Big[\int_\Omega dA - A \Big] \tag{3.33}$$

and

$$F_s = \oint_{\partial\Omega} f_s(c) ds. \tag{3.34}$$

The concentration field is defined in all the bulk and depends on position, i.e., $c = c(\mathbf{x}) = c(x,z)$. The film thickness only depends on position along the substrate, i.e., $h = h(x)$. The film domain is restricted to $\Omega = (-\infty, \infty) \times [0, h(x)]$, and $\partial\Omega$ indicates the boundary of Ω. The surface energy is assumed not to depend on the gradient of c. Lagrange multipliers λ_d, λ ensure that both the concentration of component 1, $c_1 = \frac{1}{2}(c+1)$ and the total area of the domain have the prescribed values C_1 and A,

respectively. F has to be varied with respect to all possible degrees of freedom [87]. In our case these are small changes of the concentration field and of the film thickness defined as $c(\mathbf{x};\epsilon) = c(\mathbf{x}) + \epsilon\eta(\mathbf{x})$ and $h(x;\epsilon) = h(x) + \epsilon\zeta(x)$, respectively, where symbols ζ and η denote arbitrary variations. Using the definitions of c and h, the variations can be computed by the limits

$$\delta h(x) = \lim_{\epsilon\to 0} \frac{h(x;\epsilon) - h(x)}{\epsilon} = \zeta(x) \tag{3.35}$$

and

$$\delta c(\mathbf{x}) = \lim_{\epsilon\to 0} \frac{c(\mathbf{x};\epsilon) - c(\mathbf{x})}{\epsilon} = \eta(\mathbf{x}), \tag{3.36}$$

respectively. The variation of the bulk energy is given by

$$\delta F_b = \lim_{\epsilon\to 0} \frac{F_b\Big[c(\mathbf{x};\epsilon), h(x;\epsilon)\Big] - F_b\Big[c(\mathbf{x}), h(x)\Big]}{\epsilon} \tag{3.37}$$

This results in the following form (for details see [87]),

$$\begin{aligned}
\delta F_b = &\int_{-\infty}^{\infty}\int_{0}^{h(x)} \Big[-\sigma_c[\nabla c(\mathbf{x})] + \Big(\partial_c f - \frac{\lambda_d}{2}\Big)\Big]\eta dz dx \\
&- \Big[\int_\Omega c_1 dA - C_1 A\Big]\delta\lambda_d - \Big[\int_\Omega dA - A\Big]\delta\lambda \\
&+ \oint_{\partial\Omega} \sigma_c\big(\nabla c\big).\mathbf{n}\eta ds \\
&+ \int_{-\infty}^{\infty} \Big[\frac{\sigma_c}{2}(\nabla c)^2 + f(c) - \lambda_d c_1 - \lambda\Big]\zeta(x)dx.
\end{aligned} \tag{3.38}$$

The surface energy F_s is represented as a summation of two terms, the free surface term F_s^{top} and the term of liquid solid interface F_s^{bot}

$$F_s^{top} = \int_{-\infty}^{\infty} f_s[c(\mathbf{x}_s)]\frac{ds}{dx}dx = \int_{-\infty}^{\infty} f_s[c(\mathbf{x}_s)]\sqrt{1 + [\partial_x h(x)]^2}dx \tag{3.39}$$

where $\mathbf{x}_s = [x, h(x)]$. To evaluate $\delta\mathbf{x}_s$ we write

$$\begin{aligned}
\delta\mathbf{x}_s &= \lim_{\epsilon\to 0} \frac{(\mathbf{x}_s;\epsilon) - \mathbf{x}_s}{\epsilon} \\
&= \lim_{\epsilon\to 0} \frac{[x, h(x) + \epsilon\zeta(x)] - [x, h(x)]}{\epsilon} = [0, \zeta(x)].
\end{aligned} \tag{3.40}$$

Consequently,

$$\delta c\big[\mathbf{x}_s(x)\big] = \nabla c(\mathbf{x}_s(x)).\delta\mathbf{x}_s(x) + \eta(\mathbf{x}_s(x)). \tag{3.41}$$

As a result when varying F_s^{top} one obtains

$$\delta F_s^{top} = \int_{-\infty}^{\infty} \Big[\big[(\mathbf{n}.\nabla c)\partial_c f_s + f_s\kappa\big]\frac{dx}{ds}\zeta + (\partial_c f_s)\eta\Big]ds \tag{3.42}$$

δF_s^{bot} has a similar form as the second term of δF_s^{top}. i.e.,

$$\delta F_s^{bot} = \int_{-\infty}^{\infty} \partial_c f_s \eta dx \tag{3.43}$$

For the local bulk energy $f(c)$ a simple double well quartic potential is employed and defined in dimensionless form as

$$f(c) = \frac{1}{4}(c^2-1)^2. \tag{3.44}$$

The surface energies of the liquid-gas and liquid-solid interfaces that are considered here are given by Eq. (3.24) and Eq. (3.21), respectively, where $b^{\pm} = 0$ and $a^- = \gamma_s = 0$, i.e., we assume a linear Marangoni effect at the free surface and no effect at the substrate (asymmetric case). In terms of the energetic bias we focus on the case where $a^+ > 0$. To characterise steady states for the two dimensional system, we determine the L_2-norms of surface deflection $||\delta h||$ and concentration field $||\delta c||$ as

$$||\delta c|| = \sqrt{\frac{1}{L\bar{h}}\int_0^L \int_0^{h(x)} \big(c(\mathbf{x}) - \bar{c}\big)^2 dz dx}, \tag{3.45}$$

the normalised L_2-norm of the film thickness profile

$$||\delta h|| = \sqrt{\frac{1}{L}\int_0^L \big(h(x) - \bar{h}\big)^2 dx}, \tag{3.46}$$

and the normalised energy

$$E = \frac{1}{L}\int_0^L \left\{ a^+ c\sqrt{1+(\partial_x h)^2} + \int_0^{h(x)} \left[\frac{1}{2}(\nabla c)^2 + f(c)\right] dz \right\} dx - \bar{h} f(1). \tag{3.47}$$

In the next section we will describe how to discretise Eqs. (3.33), (3.42), (3.43) in terms of finite elements.

3.5 Energy Functional in Terms of Finite Elements

In this section we show how the minimisation of the energy functional is formulated in terms of finite elements. The domain has to be discretised into a number of finite elements. We use linear triangular elements described in section 2.5.2. A partition (mesh or triangulation) is established over the entire system domain in which one must ensure, that the finite element approximations converge to the exact solution of the model.

First, we rewrite the energy functional given by Eq. (3.32) to obtain

$$F[c(\mathbf{x}), h(x), \lambda_d, \lambda] = \int_0^L \int_0^{h(x)} \Big[\frac{1}{2}(\nabla c)^2 + f(c) - \lambda_d c - \lambda\Big] d\mathbf{x} + \int_0^L \gamma(c)\sqrt{1 + [h'(x)]^2} dx + \lambda_d \bar{c} A + \lambda A \tag{3.48}$$

where $\mathbf{x} = (x, z)$, $d\mathbf{x} = (dx, dz)$, and the bulk energy $f(c)$ is given by (Eq. 3.44).

The surface energy f_s is defined as

$$f_s(c) = \begin{cases} \alpha + a^+ c, & \text{at free surface} \\ \\ 0, & \text{at the substrate} \end{cases}$$

where α and $a^+ > 0$ are constants. For films with an imposed flat surface we chose $\alpha = 1000$ while for films with height modulations $\alpha = 1$ is used. From now onwards we indicate $f_s(c)$ at the free surface by f^+, and at the substrate by f^-, i.e.,

$$f^+(c) = \alpha + a^+ c, \tag{3.49}$$

$$f^-(c) = 0. \tag{3.50}$$

We convert from the cartesian coordinate system to a natural isoparametric coordinate system for easy usage of the finite element method. We write

$$x = \begin{bmatrix} \xi & \eta & 1 - \xi - \eta \end{bmatrix} \begin{Bmatrix} x_1 \\ x_2 \\ x_3 \end{Bmatrix} = \mathbf{H}(\boldsymbol{\xi})\hat{\mathbf{x}}_x, \tag{3.51}$$

$$z = \begin{bmatrix} \xi & \eta & 1-\xi-\eta \end{bmatrix} \begin{Bmatrix} z_1 \\ z_2 \\ z_3 \end{Bmatrix} = \mathbf{H}(\boldsymbol{\xi})\hat{\mathbf{z}}_x, \tag{3.52}$$

$$h = \begin{bmatrix} \xi_s & \eta_s & 1-\xi_s-\eta_s \end{bmatrix} \begin{Bmatrix} h_1 \\ h_2 \\ h_3 \end{Bmatrix} = \mathbf{H}_s(\xi_s)\hat{\mathbf{h}}, \tag{3.53}$$

$$c = \begin{bmatrix} \xi & \eta & 1-\xi-\eta \end{bmatrix} \begin{Bmatrix} c_1 \\ c_2 \\ c_3 \end{Bmatrix} = \mathbf{H}(\boldsymbol{\xi})\hat{\mathbf{c}} \tag{3.54}$$

where $\boldsymbol{\xi}$ denotes the pair of the area coordinates (ξ, η), and ξ_s, η_s are the values of ξ, η at the surface, and $\hat{\mathbf{x}}_x, \hat{\mathbf{x}}_z, \hat{\mathbf{h}}, \hat{\mathbf{x}}$ are unknown nodal values. In terms of Eqs. (3.51)-(3.54), the functional given by Eq. (3.48) becomes

$$F[c(\boldsymbol{\xi}), h(\xi_s), \lambda_d, \lambda] = \int_{\Omega(\boldsymbol{\xi})} \left[\frac{1}{2}[(\nabla c(\boldsymbol{\xi})]^2 + f(c(\boldsymbol{\xi}), x(\boldsymbol{\xi})) - \lambda_d c(\boldsymbol{\xi}) - \lambda\right] J_A(\boldsymbol{\xi}) d^2(\boldsymbol{\xi}) \tag{3.55}$$

$$+ \int_{\partial\Omega^t(\xi_s)} J_s(\xi_s) d\xi_s + \lambda_d C_1 A_0 + \lambda A_0$$

where ∇ is the gradient in x-space, $J_A = \partial(x, z)/\partial(\xi, \eta)$, and $J_s = ds/d\xi_s$.

To determine the stationary condition for the functional (3.55) we need to evaluate δF. Using Eqs. (3.51)- (3.54) one writes $\delta x, \delta z, \delta h, \delta c$ as follows

$$\delta x(\boldsymbol{\xi}) = \mathbf{H}(\boldsymbol{\xi})\delta\hat{\mathbf{x}}_x, \tag{3.56}$$

$$\delta z(\boldsymbol{\xi}) = \mathbf{H}(\boldsymbol{\xi})\delta\hat{\mathbf{x}}_z, \tag{3.57}$$

$$\delta h(\xi_s) = \mathbf{H}_s(\xi_s)\delta\hat{\mathbf{h}}, \tag{3.58}$$

$$\delta c(\boldsymbol{\xi}) = \mathbf{H}(\boldsymbol{\xi})\delta\hat{\mathbf{c}}. \tag{3.59}$$

Next we write the energy functional (3.48) in terms of finite elements following the steps of Ref. [36]. We write for component i of $\hat{\mathbf{x}}_\mathbf{x}$

$$\hat{x}_{x_i} = \text{const.}, \tag{3.60}$$

$$\hat{x}_{z_i} = \frac{\hat{x}_{z_0 i}}{\boldsymbol{H}_s(\xi_s(\hat{x}_{x_i}))\hat{\boldsymbol{h}}_0}\boldsymbol{H}_s(\xi_s(\hat{x}_{x_i}))\hat{\boldsymbol{h}}, \tag{3.61}$$

$$\hat{x}_z = \boldsymbol{Q}\hat{\boldsymbol{h}} \tag{3.62}$$

using Eqs. (3.60), (3.61) one obtains

$$\delta x = 0, \qquad \delta z = \boldsymbol{H}(\boldsymbol{\xi})\delta\hat{\boldsymbol{x}}_z = \boldsymbol{H}(\boldsymbol{\xi})\boldsymbol{Q}\delta\hat{\boldsymbol{h}}, \tag{3.63}$$

$$(\nabla c)(\boldsymbol{\xi}) = \boldsymbol{T}^T(\boldsymbol{\xi})\left[\partial_{\boldsymbol{\xi}}\boldsymbol{H}^T(\boldsymbol{\xi})\right]^T\hat{\boldsymbol{c}} \tag{3.64}$$

where $T(\boldsymbol{\xi}) = (\partial_{\boldsymbol{\xi}}\boldsymbol{x})^{-1}$ is the inverted transformation matrix $\partial_{\boldsymbol{\xi}}\boldsymbol{x}$ defined as

$$dx = (\partial_{\boldsymbol{\xi}}\boldsymbol{x})d\boldsymbol{\xi}. \tag{3.65}$$

In the following derivation, we use index notation with Einstein's convention of summation. Eq. (3.64) reads

$$(\nabla_i c)(\boldsymbol{\xi}) = T_{ji}(\boldsymbol{\xi})\left[\partial_{\xi_j}H_l(\boldsymbol{\xi})\right]\hat{c}_l. \tag{3.66}$$

The resulting variation of ∇c is

$$\begin{aligned}\delta(\nabla_i c) &= T_{ji}(\boldsymbol{\xi})\left[\partial_{\xi_j}H_l(\boldsymbol{\xi})\right]\delta\hat{c}_l - T_{j2}(\boldsymbol{\xi})(\partial_{\xi_n}H_m)Q_{ml}\delta\hat{h}_l T_{ni}(\boldsymbol{\xi})\left[\partial_{\xi_j}H_k(\boldsymbol{\xi})\right]\hat{c}_k \\ &= (\nabla_i H_l)\delta\hat{c}_l - (\nabla_2 H_k)\hat{c}_k(\nabla_i H_m)Q_{ml}\delta\hat{h}_l\end{aligned} \tag{3.67}$$

where $\nabla_2 \equiv \partial_z$ in matrix notation we have

$$\begin{aligned}\delta(\nabla c) &= (\nabla\boldsymbol{H})\delta\hat{\boldsymbol{c}} - (\partial_z\boldsymbol{H})\hat{\boldsymbol{c}}(\nabla\boldsymbol{H})\boldsymbol{Q}\delta\hat{h} \\ &= (\nabla\boldsymbol{H})\delta\hat{\boldsymbol{c}} - (\partial_z c)(\nabla\boldsymbol{H})\boldsymbol{Q}\delta\hat{\boldsymbol{h}}.\end{aligned} \tag{3.68}$$

The variations of the Jacobian are

$$\begin{aligned}\delta J_A &= \partial_\xi x\partial_\eta\delta z - \partial_\eta x\partial_\xi\delta z \\ &= (\partial_\xi x\partial_\eta H_i - \partial_\eta x\partial_\xi H_i)Q_{ij}\delta\hat{h}_j \\ &= J_A(\partial_z H_i)Q_{ij}\delta\hat{h}_j \\ &= J_A(\partial_z\boldsymbol{H})\boldsymbol{Q}\delta\hat{\boldsymbol{h}},\end{aligned} \tag{3.69}$$

and

$$\begin{aligned}\delta J_s &= J_s^{-1}\partial_{\xi_s} h(\xi_s)\partial_{\xi_s}\delta h(\xi_s)\\ &= J_s^{-1}\partial_{\xi_s}\boldsymbol{H}_s\hat{\boldsymbol{h}}\partial_{\xi_s}\boldsymbol{H}_s\delta\hat{\boldsymbol{h}}.\end{aligned} \tag{3.70}$$

Now, we are ready to rewrite the energy functional using finite elements. First we write the energy functional (3.55) in the form

$$\begin{aligned}\mathbf{F} &= \mathbf{F}[c(\boldsymbol{\xi}), h(\xi_s), \lambda_d, \lambda]\\ &= \int_{\Omega(\boldsymbol{\xi})}\left\{\frac{1}{2}(\nabla c(\boldsymbol{\xi}))^2 + f\big(c(\boldsymbol{\xi})\big) + \lambda_d c(\boldsymbol{\xi}) - \lambda\right\}J_A(\boldsymbol{\xi})d^2\boldsymbol{\xi}\\ &\qquad + \int_{\Omega(\boldsymbol{\xi_s})}\gamma(\xi_s)J_s(\xi_s)d\xi_s + \lambda_d C_1 A_0 + \lambda A_0\end{aligned} \tag{3.71}$$

then, the variational formula can be written as

$$\begin{aligned}\delta\mathbf{F} &= \delta\mathbf{F}[\hat{\mathbf{c}}, \hat{\mathbf{h}}, \lambda_d, \lambda]\\ &= \delta\hat{\mathbf{c}}^T\mathbf{F}_{\hat{\mathbf{c}}} + \delta\hat{\mathbf{h}}^T\mathbf{F}_{\hat{\mathbf{h}}} + \delta\lambda_d\mathbf{F}_{\lambda_d} + \delta\lambda\mathbf{F}_{\lambda}.\end{aligned} \tag{3.72}$$

The four terms on the right hand side of Eq. (3.72) can be formulated individually in the following expressions,

$$\begin{aligned}\delta\hat{\mathbf{c}}^T\mathbf{F}_{\hat{\mathbf{c}}} = \delta\hat{\mathbf{c}}^T\ &\left\{\int_\Omega\left\{\frac{1}{2}(\nabla\mathbf{H})^T(\nabla c) + \mathbf{H}^T\partial_c f(c,\mathbf{x}) - \frac{\lambda_d}{2}\right\}d^2\xi\right.\\ &\left.+\int_{\partial\Omega^t(\xi_s)}\mathbf{H}_s^T(\xi_s)\frac{d\gamma}{dc}J_s{}^{-1}d\xi_s + \int_{\partial\Omega^b(\xi_s)}\mathbf{H}_s^T(\xi_s)\frac{d\gamma}{dc}J_s{}^{-1}d\xi_s\right\},\end{aligned} \tag{3.73}$$

$$\begin{aligned}\delta\hat{\mathbf{h}}^T\mathbf{F}_{\hat{\mathbf{h}}} = \delta\hat{\mathbf{h}}^T\Bigg\{&Q^T\int_\Omega\left\{\frac{-1}{2}(\nabla\mathbf{H})^T(\nabla c)\partial_z c + \mathbf{H}^T\partial_z f(c,\mathbf{x})\right\}d^2\xi\\ &+Q^T\int_\Omega(\partial_z\mathbf{H})^T J_A\left\{\frac{(\nabla c)^2}{8} + f(c,\mathbf{x}) - \lambda_d c_1 - \lambda\right\}d^2\xi\\ &+\int_{\partial\Omega^t(\xi_s)}(\partial_\xi\mathbf{H}_s^T(\xi_s))\gamma(c(\xi))(\partial_\xi\mathbf{H}_s)\hat{\mathbf{h}}J_s^{-1}d\xi_s\Bigg\},\end{aligned} \tag{3.74}$$

$$\delta\lambda_d\mathbf{F}_{\lambda_d} = \delta\lambda_d\left\{-\int_\Omega c_1 d\xi + C_1 A\right\}, \tag{3.75}$$

$$\delta\lambda \mathbf{F}_\lambda = \delta\lambda \left\{ -\int_0^L h(x)dx + A \right\}. \tag{3.76}$$

where $d^2\xi = dzdx$, the Jacobian is $J_A = \partial(x,z)/\partial(\xi,\eta)$ and $J_s = ds/d\xi_s$.

At this point the system of equations is written in terms of the finite element method. Initially, a coarse 11×6 nodes domain is used which was automatically created using matlab's pdetool (see Fig. 3.2). The basic mesh is created with a maximum element edge size to allow us to produce 10 elements along the horizontal edge of the original rectangular domain and 5 elements along the vertical edge. To start the calculations we produce a solution built on an initial approximation on the coarse mesh as a starting solution. The coarse mesh is used to effectively obtain the indicative numerical solution for given values of the parameters which are the mean height H, the energetic bias a^+, and for the continuation parameters (the lateral domain size L or the mean concentration c). Once the calculations start, the dimensions of the starting rectangle are rescaled according to the surface profile of the film. Many functions are introduced into the code

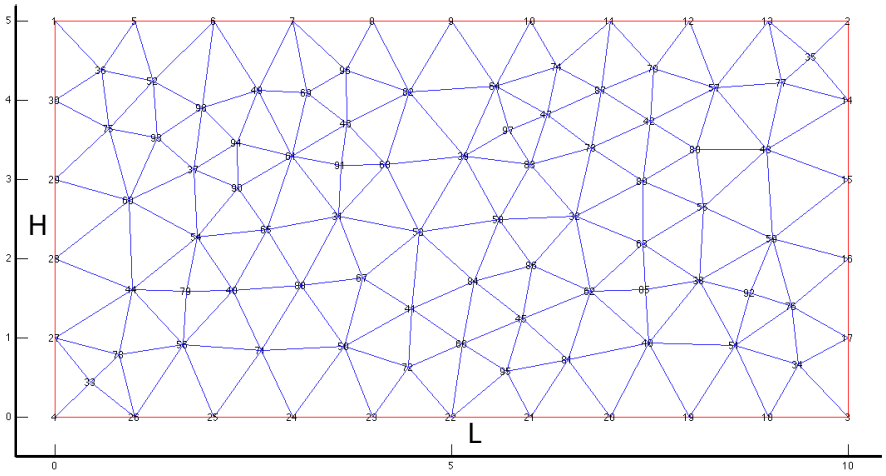

Figure 3.2: Finite element discretisation of the domain in the xz-plane using a linear triangular elements.

to produce various starting solutions over the original rectangular domain. Integrals are calculated numerically using Gaussian quadrature while Newton's iteration method is used to refine the starting solution. We use different ways to adjust the concentration of the components to produce the coarse starting solutions, which is one of the most difficult parts. One needs a good guess to find the wanted solution, in particular, in regions where several solutions exist. Once the coarse solution is obtained the code saves it to be used as an initial approximation for the adaptive mesh refinement and further computation of the refined solution. The refinement is then repeated once more and the

final solution is obtained. The refinement predominantly takes place in the diffuse interface region, and in zones along the free surface, where high concentration gradients and/or surface curvature occur. The considered continuation parameter is advanced and the previous solution on the basic coarse mesh can be used as an initial approximation for the next run.

3.6 Summary

The bulk equations and the boundary conditions of Model-H have been introduced following the steps of Ref. [87]. Then the variational approach to the steady states derived alternatively by minimising the free energy functional. The energy functional is written in terms of finite element discretisation. The domain has been discretised into linear triangular elements using a natural isoparametric coordinate system. The resulting variational problem is numerically solved employing finite element method on an adaptive grid. The developed numerical scheme allows us to obtain the coupled steady-state film thickness profile and the concentration profile inside the film. In the following chapters, we introduce the linear stability of the full time dependent model-H as well as bifurcation diagrams for various film thicknesses and energetic biases at the free surface. The bifurcations of the critical case are compared with the symmetry groups. For the off-critical case we only introduced the bifurcation diagrams.

As the study of the linear stability is a part of the results presented in this dissertation, in the following chapter we introduce the linear stability analysis for the full time dependent model-H in non-dimensionlised form.

Chapter 4

Linear Stability Analysis

4.1 Introduction

The dispersion relation $\beta = \beta(k)$ relates the growth rate ω of an harmonic mode to its wave number k and is obtained from the linearised evolution equation, i.e., it is the function for which the plane waves $e^{ikx+\beta t}$ (real $\beta > 0$ $[\beta < 0]$ that correspond to growth [decay]) solve the equation of first order in time.

As a consequence of the previous chapter, we study the linear stability of laterally homogeneous steady states of thin films of binary liquid that are bounded by a rigid solid substrate and an upper free surface. The full time dependent model-H is used to describe the dynamics within the film. The bulk equations are supplied by boundary conditions at the substrate and the free surface as explained in section 3.3.

To develop a good understanding of linear stability for several cases of steady state solutions we first introduce the concept of the linear stability analysis. The parameter limits within which instabilities of steady state solutions are found can be determined by employing infinitesimal perturbations about these states into the full time dependent model-H. Within a certain range of parameters, the solution may be stable or unstable to infinitesimal perturbations. Furthermore, it may change between the stable and unstable state when changing a parameter or the wave number of the perturbation. The latter case is shown in Fig. 4.1, where the solution is unstable for the wave number $0 < k < k_c$ and stable for $k > k_c$. The calculations are done numerically for steady stratified flat

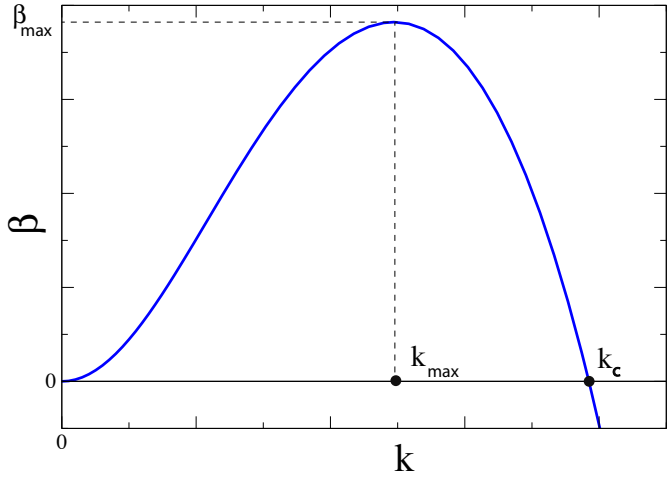

Figure 4.1: The dimensionless growth rate of perturbations with dimensionless wave number k. The positive growth rate corresponds to the growth of a perturbation, while a negative growth rate indicates decay. Therefore the unstable domain is $k \in (0, k_c)$.

films, i.e., for concentration profiles $c_0(z)$, velocity $\mathbf{v}_0 = 0$, pressure $p_0(z) = -(\partial_z c_0)^2$, and film thickness $h_0 = H$.

In this chapter we investigate their linear stability with respect to lateral perturbations of the wavenumber k and growth rate β. Analytical results for homogeneous films are also studied in section 4.5.

4.2 Linearised Model-H

We want to study the linear stability of the homogeneous and nearly homogeneous films without and with energetic bias, respectively, and also of vertically stratified two-layer films. First, we linearise the full time-dependent model-H, i.e., the dimensionless governing equations (mass balance, momentum, and continuity equations) and the boundary conditions introduced in Chapter 3, i.e., Eqs. (3.16) - (3.28). To analyse the stability of the quiescent base states with respect to infinitesimal perturbation the solution of the problem has to be written in the following form:

The velocity field $\mathbf{v}$ is

$$\mathbf{v} = \mathbf{v_0} + \epsilon \mathbf{v_1}(z) e^{\beta t + ikx} \tag{4.1}$$

where $\mathbf{v} = (u, w)$, $\mathbf{v_0} = (u_0, w_0)$, and $\mathbf{v_1} = (u_1, w_1)$. The small parameter $\epsilon \ll 1$ will be used in the linearization. The pressure p is

$$p = p_0(z) + \epsilon p_1(z) e^{\beta t + ikx} \tag{4.2}$$

where $p_0 = -(\partial_z c_0)^2$. The concentration field c

$$c = c_0(z) + \epsilon c_1(z) e^{\beta t + ikx}, \tag{4.3}$$

and the film height h

$$h = h_0 + \epsilon h_1 e^{\beta t + ikx}. \tag{4.4}$$

The fields $\epsilon \mathbf{v}_1$, ϵp_1, ϵc_1, and ϵh_1 are infinitesimally small perturbations of the fields $\mathbf{v_0}$, p_0, c_0, and h_0 respectively. β is the growth rate, and k is the wave number. The perturbations u_1, w_1, p_1, c_1 are functions of z, whereas h_1 is a scalar. We have decomposed the lateral perturbations of all fields into normal modes e^{ikx}

To start, we consider the steady state $(u_0, w_0) = (0, 0)$ and introduce expressions (4.1) - (4.4) into Eqs. (3.16) - (3.28), and linearise in ϵ. The time derivative of $\mathbf{v}$ becomes

$$\frac{\partial \mathbf{v}}{\partial t} = \epsilon \beta \mathbf{v_1} e^{\beta t + ikx}, \tag{4.5}$$

whereas $\Delta \mathbf{v}$ is

$$\Delta \mathbf{v} = \left[(-k^2 + \partial_{zz}) \mathbf{v}_1 \right] \epsilon e^{\beta t + ikx}. \tag{4.6}$$

One may neglect

$$\begin{aligned} \mathbf{v} \cdot \nabla \mathbf{v} &= \left[(u, w) \cdot (\partial_x, \partial_z) \right] (u, w) \\ &= (iku_1{}^2 + w_1(\partial_z u_1), iku_1 w_1 + w_1(\partial_z w_1)) \epsilon^2 e^{2(\beta t + ikx)}, \end{aligned} \tag{4.7}$$

as it is $O(\epsilon^2)$.
Since $p_0 = -(\partial_z c_0)^2$, one uses Eqs. (4.2) and (3.18) to write

$$p_{\text{eff}} \mathbf{I} = (-(\partial_z c_0)^2 + p_1 \epsilon e^{\beta t + ikx}) \mathbf{I}, \tag{4.8}$$

with

$$\nabla c = (ikc_1, \partial_z c_0 + \partial_z c_1)\epsilon e^{\beta t + ikx}. \tag{4.9}$$

Also one finds $(\nabla c)(\nabla c)$ as

$$\begin{aligned}(\nabla c)(\nabla c) &= \begin{bmatrix} (\partial_x c)(\partial_x c) & (\partial_x c)(\partial_z c) \\ (\partial_z c)(\partial_x c) & (\partial_z c)(\partial_z c) \end{bmatrix} \\ &= \begin{bmatrix} 0 & 0 \\ 0 & (\partial_z c_0)^2 \end{bmatrix} + \begin{bmatrix} 0 & ikc_1(\partial_z c_0) \\ ikc_1(\partial_z c_0) & 2(\partial_z c_0)(\partial_z c_1) \end{bmatrix} \epsilon e^{\beta t + ikx} + O(\epsilon^2).\end{aligned} \tag{4.10}$$

Substituting (4.5), (4.6), (4.7), (4.8), and (4.10) into Eq. (3.16) yields

$$\begin{aligned}\epsilon\beta \,\mathrm{Ps}\, \mathbf{v_1} = \Bigg\{ &\begin{bmatrix} -ikp_1 - ik\partial_z(c_1(\partial_z c_0)) & -2\partial_z((\partial_z c_0)(\partial_z c_1)) + \partial_z p_1 \end{bmatrix} \\ &+ \frac{\mathrm{Ps}}{\mathrm{Re}}(\partial_{zz} - k^2)\mathbf{v}_1 \Bigg\}\epsilon + O(\epsilon^2).\end{aligned} \tag{4.11}$$

Taking the linear terms in ϵ and writing $\mathbf{v}_1$ component-wise we obtain the linearised equations of (3.16)

$$\beta \,\mathrm{Ps}\, u_1 = -ik\partial_z(c_1(\partial_z c_0)) - ikp_1 + \frac{\mathrm{Ps}}{\mathrm{Re}}(\partial_{zz} - k^2)u_1, \tag{4.12}$$

and,

$$\beta \,\mathrm{Ps}\, w_1 = k^2 c_1(\partial_z c_0) - 2\partial_z[(\partial_z c_0)(\partial_z c_1)] - \partial_z p_1 + \frac{\mathrm{Ps}}{\mathrm{Re}}(\partial_{zz} - k^2)w_1. \tag{4.13}$$

Next, we linearize the Cahn-Hilliard equation (3.15) using Eqs. (4.1) - (4.4). With

$$\partial_c f(c) = \partial_c f|_{c_0} + \epsilon \partial_{cc} f|_{c_0} c_1 e^{\beta t + ikx}, \tag{4.14}$$

to order $O(\epsilon)$ one finds

$$\beta c_1 + w_1 \partial_z c_0 = -\big(\partial_{zz} - k^2\big)\Big[\big(\partial_{zz} - k^2\big)c_1 - c_1 \partial_{cc} f|_{c_0}\Big]. \tag{4.15}$$

Since $u_0 = w_0 = 0$, the incompressibility condition $\nabla \cdot \mathbf{v} = 0$, takes the form

$$0 = \nabla \cdot \mathbf{v} = iku_1 + \partial_z w_1. \tag{4.16}$$

Now we linearise the boundary conditions. For the kinematic condition at the free surface (3.28), we get

$$\beta h_1 = w_1. \tag{4.17}$$

The linearised forms of the condition of zero diffusional flux (Eq. (3.19)) on substrate (at $z = 0$), and on the free surface (at $z = h_0$), are

$$\partial_z \Big[\big(\partial_{zz} - k^2\big) c_1 - c_1 \partial_{cc} f|_{c_0} \Big] = 0, \tag{4.18}$$

The energy bias conditions at the free surface and the substrate become

$$-\partial_z c_0 + \mathrm{S}\partial_{cc} f^-|_{c_0} = 0, \quad z = 0 \tag{4.19}$$

and

$$-\partial_z c_0 + \mathrm{S}\partial_{cc} f^+|_{c_0} = 0, \quad z = h_0, \tag{4.20}$$

respectively, whereas the no-slip and no-penetration conditions at the substrate become

$$u_1 = w_1 = 0. \tag{4.21}$$

The tangential force balance at $z = h_0$ becomes

$$-ik(\partial_z c_0)[c_1 + h_1(\partial_z c_0)] + \frac{\mathrm{Ps}}{\mathrm{Re}}(\partial_z u_1 + ikw_1) = ikS[c_1 + h_1(\partial_z c_0)]\partial_c f^+|_{c_0}. \tag{4.22}$$

This equation is reordered to obtain

$$\begin{aligned} \frac{\mathrm{Ps}}{\mathrm{Re}}(\partial_z u_1 + ikw_1) &= ikc_1 \Big[\partial_z c_0 + \mathrm{S}\partial_c f^+|_{c_0}\Big] + ikh_1(\partial_z c_0)\Big[\partial_z c_0 + \mathrm{S}\partial_c f^+|_{c_0}\Big] \\ &= ik\Big[\partial_z c_0 + \mathrm{S}\partial_c f^+|_{c_0}\Big]\Big[c_1 + h_1(\partial_z c_0))\Big] \\ &= 0. \end{aligned} \tag{4.23}$$

Which means that there are no Marangoni forces in $O(\epsilon)$. Finally, we linearise the normal force boundary condition (3.27) and obtain

$$2(\partial_z c_0)(\partial_z c_1) + p_1 - 2\frac{\mathrm{Ps}}{\mathrm{Re}}(\partial_z w_1) = -k^2 h_1 \mathrm{S} f^+(c). \tag{4.24}$$

In the following two sections we investigate the eigenvalue problem for the stratified and homogeneous films.

4.3 Eigenvalue Problem for the Stratified Film

To solve the eigenvalue problem for the stratified film we need to eliminate the pressure from the equations and boundary conditions. First of all we eliminate the pressure term from the linearised Navier-Stokes equations. To do so we take a z-derivative of Eq. (4.12) and get

$$\beta \mathrm{Ps}(\partial_z u_1) = -ik\partial_{zz}(c_1(\partial_z c_0)) - ik(\partial_z p_1) + \frac{\mathrm{Ps}}{\mathrm{Re}}(\partial_{zz} - k^2)(\partial_z u_1). \tag{4.25}$$

Then, we multiply Eq. (4.13) by (ik)

$$ik\beta(\mathrm{Ps})w_1 = ik\Big[k^2 c_1(\partial_z c_0) - 2\partial_z[(\partial_z c_0)(\partial_z c_1)]\Big] - ik(\partial_z p_1) + ik\frac{\mathrm{Ps}}{\mathrm{Re}}(\partial_{zz} - k^2)w_1. \tag{4.26}$$

Subtracting Eq. (4.26) from Eq. (4.25) one obtains

$$\begin{aligned}\beta(\mathrm{Ps})(\partial_z u_1) - ik\beta(\mathrm{Ps})w_1 = &-ik\partial_{zz}(c_1(\partial_z c_0)) + \frac{\mathrm{Ps}}{\mathrm{Re}}(\partial_{zz} - k^2)(\partial_z u_1) \\ &+ ik[-k^2 c_1(\partial_z c_0) + 2\partial_z(\partial_z c_0)(\partial_z c_1)] - ik\frac{\mathrm{Ps}}{\mathrm{Re}}(\partial_{zz} - k^2)w_1.\end{aligned} \tag{4.27}$$

Differentiating the incompressibility condition Eq. (4.16) three times w.r.t. z one has

$$ik\partial_{zzz}u_1 = -\partial_{zzzz}w_1 \tag{4.28}$$

Next, one introduces (4.28), in Eq. (4.27) and gets after rearranging a linear equation for the vertical component of velocity w_1 and concentration c_1

$$\begin{aligned}\partial_{zzzz}w_1 =&\beta(\mathrm{Re})(\partial_{zz} - k^2)w_1 + k^2\frac{\mathrm{Re}}{\mathrm{Ps}}\partial_{zz}(c_1(\partial_z c_0)) + 2k^2\partial_{zz}w_1 \\ &+ k^4\frac{\mathrm{Re}}{\mathrm{Ps}}c_1(\partial_z c_0) - 2k^2\frac{\mathrm{Re}}{\mathrm{Ps}}\partial_z\Big((\partial_z c_0)(\partial_z c_1)\Big) - k^4 w_1.\end{aligned} \tag{4.29}$$

Since the linearised Cahn-Hilliard equation (4.15) does not contain any pressure terms, we may rearrange it as

$$\partial_{zzzz}c_1 = -(\beta c_1 + w_1\partial_z c_0) - \big[(k^4 - 2k^2\partial_{zz})c_1 - (\partial_{zz} - k^2)(c_1\partial_{cc}f|_{c_0})\big]. \tag{4.30}$$

As a result we have bulk equations for c_1 and w_1. The fields u_1 and p_1 may be obtained via Eqs. (4.16) and (4.12), respectively. Next we list the boundary conditions:

$$w_1 = \partial_z w_1 = 0 \quad \text{at} \quad z = 0, \tag{4.31}$$

$$\frac{\mathrm{Ps}}{\mathrm{Re}}(\partial_{zz} w_1 + k^2 w_1) = 0, \quad \text{at} \quad z = h_0. \tag{4.32}$$

and rewrite Eq. (4.12) in the form

$$ikp_1 = \frac{\mathrm{Ps}}{\mathrm{Re}}(\partial_{zz} - k^2)u_1 - \beta(\mathrm{Ps})u_1 - ik\partial_z(c_1(\partial_z c_0)), \tag{4.33}$$

and multiply Eq. (4.24) by (ik) to obtain

$$2ik(\partial_z c_0)(\partial_z c_1) + ikp_1 - 2ik\frac{\mathrm{Ps}}{\mathrm{Re}}(\partial_z w_1) = -2ik^3 h_1 \mathrm{S} f^+(c). \tag{4.34}$$

Substituting (4.33) in Eq. (4.34) and using Eq. (4.28) one obtains after rearranging

$$\begin{aligned} k^2\partial_z(\partial_z c_0)(\partial_z c_1) + \frac{\mathrm{Ps}}{\mathrm{Re}}(\partial_{zz} - 3k^2)\partial_z w_1 - \beta(\mathrm{Ps})\partial_z w_1 \\ - k^2 c_1(\partial_{zz} c_0) = k^4\Big(\frac{w_1}{\beta}\Big)\mathrm{S} f^+|_{c_0}, \quad \text{at} \quad z = h_0, \end{aligned} \tag{4.35}$$

where we used $h_1 = w_1/\beta$, i.e. Eq. (4.35) now only involves c_1 and w_1.

Furthermore we have

$$\partial_z[(\partial_{zz} - k^2)c_1 - c_1\partial_{cc} f|_{c_0})] = 0 \quad \text{at} \quad z = 0, h_0, \tag{4.36}$$

$$-\partial_z c_1 + c_1 \mathrm{S}\partial_{cc} f^-|_{c_0} = 0 \quad \text{at} \quad z = 0, \tag{4.37}$$

and

$$\partial_z c_1 + c_1 \mathrm{S}\partial_{cc} f^+|_{c_0} = 0 \quad \text{at} \quad z = h_0. \tag{4.38}$$

Now we have obtained the tools to study the linear stability of the stratified films. In the next section we will simplify the expressions for the special case of homogeneous films.

4.4 Eigenvalue Problem for the Homogeneous Film

If the concentration of the base state does not dependent on z then all the derivatives of c_0 are zero, and from Eq. (4.29) we obtain

$$\partial_{zzzz} w_1 = \beta(\mathrm{Re})(\partial_{zz} - k^2) w_1 + 2k^2(\partial_{zz} w_1) - k^4 w_1 \tag{4.39}$$

whereas Eq. (4.30) takes the form

$$\partial_{zzzz} c_1 = -\beta c_1 - (k^4 - 2k^2\partial_{zz}) c_1 - (\partial_{zz} - k^2)(c_1 \partial_{cc} f|_{c_0}) \tag{4.40}$$

while the boundary conditions are

$$w_1 = \partial_z w_1 = 0 \quad \text{at} \quad z = 0, \tag{4.41}$$

$$\frac{\mathrm{Ps}}{\mathrm{Re}}(\partial_{zz} w_1 + k^2 w_1) = 0, \quad \text{at} \quad z = h_0. \tag{4.42}$$

From Eq. (4.35) we obtain

$$\frac{\mathrm{Ps}}{\mathrm{Re}}(\partial_{zz} - 3k^2)(\partial_z w_1) - \beta(\mathrm{Ps})(\partial_z w_1) = k^4 \Big(\frac{w_1}{\beta}\Big) \mathrm{S} f^+|_{c_0} \quad \text{at} \quad z = h_0. \tag{4.43}$$

Furthermore,

$$\partial_z[(\partial_{zz} - k^2) c_1 - c_1 \partial_{cc} f|_{c_0})] = 0 \quad \text{at} \quad z = 0, h_0, \tag{4.44}$$

$$-\partial_z c_1 + c_1 \mathrm{S} \partial_{cc} f^-|_{c_0} = 0 \quad \text{at} \quad z = 0, \tag{4.45}$$

and, finally

$$\partial_z c_1 + c_1 \mathrm{S} \partial_{cc} f^+|_{c_0} = 0 \quad \text{at} \quad z = h_0. \tag{4.46}$$

Since we are using a constant free energy at the substrate and only linearly biased free energy at the free surface, the derivatives $\partial_{cc} f^{\pm}|_{c_0}$ are zero, and the boundary conditions (4.37), (4.45) and (4.38), (4.46) can be rewritten, respectively as

$$-\partial_z c_1 = 0 \quad \text{at} \quad z = 0, \tag{4.47}$$

and

$$\partial_z c_1 = 0 \quad \text{at} \quad z = h_0. \tag{4.48}$$

Note that in this case c_1 and w_1 are entirely decoupled.

The calculations of the layered base states and of their linear stability are performed using numerical continuation techniques (AUTO) [25]. This technique allows to follow known solutions when a given set of control parameters is changed. Together, the equations for the steady state (3.29) and for the real linear perturbations (4.29) and (4.30) can be rewritten as a ten-dimensional dynamical system

$$\mathbf{y}' = \mathbf{f}(\mathbf{y}(z), \lambda) \tag{4.49}$$

where

$$\mathbf{y} = (c_0, c_{0z}, c_1, c_{1z}, c_{1zz}, c_{1zzz}, w_1, w_{1z}, w_{1zz}, w_{1zzz}), \tag{4.50}$$

and λ represents the parameters β, k, Re, Ps/Re, S, and $\bar{c}$. This system of ordinary differential equations, together with the boundary conditions at the substrate $(z = 0)$ and at the free surface $(z = h)$ which are given by Eqs. (4.31, 4.32, (4.35 - 4.38), and one integral condition (mass conservation), is discretised in space. The resulting algebraic system of equations is solved using iterative technique method starting from known solutions. In particular, AUTO uses a combination of Newton and Chord iterative methods.

When the solution is reached, the code proceeds along the solution branch by a small step (determined by user) in the parameter space defined by the free continuation parameters and restarts the iteration. The boundary conditions and the integral conditions require another free parameters which are determined simultaneously and they are considered as a part of the solution of the differential equation.

4.5 Linear Stability Results for Homogeneous Films

The homogeneous films $(c_0 = 0)$ are steady solutions only in the neutral case $(a^+ = 0)$ where the dispersion relation can be determined analytically. Referring to the dispersion relation introduced in section 4.3 by the linearised Eqs. (4.29) and (4.30), we remember that the perturbations in the concentration and in the velocities decouple. This implies

that advection does not influence the evolution in the linear stage, all velocity modes are stable and no surface deflection develops. All unstable modes are purely diffusive and similar to the ones obtained in a Cahn-Hilliard model for the decomposition of a mixture in a finite gap [50, 57].

For $c_0 = constant$ one may use a harmonic ansatz not only for the lateral but also for the vertical spatial dependence, i.e., the ansatz becomes $c(x,z,t) = \epsilon\ \exp(ik_x x + ik_z z + \beta t)$ where k_x and k_z are lateral and vertical wavenumbers, respectively. After linearisation in ϵ one obtains the dispersion relation extracted from Eq. (4.40)

$$\beta = -(k_x^2 + k_z^2)\left[(k_x^2 + k_z^2) + \partial_{cc} f|_{c_0}\right]. \tag{4.51}$$

In the critical case, the film is unstable ($\beta > 0$) for modes with $(k_x)^2 + (k_z)^2 < 1$. For finite domains it is convenient to introduce vertical and lateral mode numbers $n = k_z H/2\pi$ and $m = k_x L/2\pi$, respectively. They count the number of periods of a mode of a certain wavenumber that fit into the domain. For the employed boundary conditions, n and m can take integer and half-integer values. First, we fix the mode number in the vertical direction, i.e., where $k_z = 0$ and consider purely lateral structuring with mode numbers $m = 1/2, 1, 3/2, 2, \ldots$ above critical domain sizes $L_c^m = 2\pi m$. Similarly, for $k_x = 0$ one obtains purely vertical structuring (layered films) with mode numbers $n = 1/2, 1, \ldots$ above critical film heights $H_c^n = 2\pi n$. Finally, the homogenous film is unstable w.r.t. checkerboard modes, i.e., $m \neq 0$ and $n \neq 0$, for

$$L_c^{\mathrm{cb}} = \frac{mH}{\sqrt{(H/2\pi)^2 - n^2}} \tag{4.52}$$

where we have used the mean film thickness as parameter. The number of unstable modes for certain film thicknesses H and domain sizes L can be obtained from Fig. 4.2 where the linear stability thresholds for the various modes are given. Note that the stability thresholds for vertical, lateral and checkerboard modes also correspond to loci of symmetry breaking bifurcations where branches of vertically structured (layered), laterally structured, and checkerboard structured steady solutions branch off the trivial homogeneous solution. In the following we denote both, the linear modes and the fully nonlinear solutions branching of the trivial solution, by their corresponding pair of mode numbers (m, n).

The eigenfunctions in the horizontal and vertical direction are given by $e^{ik_x x}$ and $e^{ik_z z}$, respectively. Depending on the mode number, lateral domain size, and the film thickness

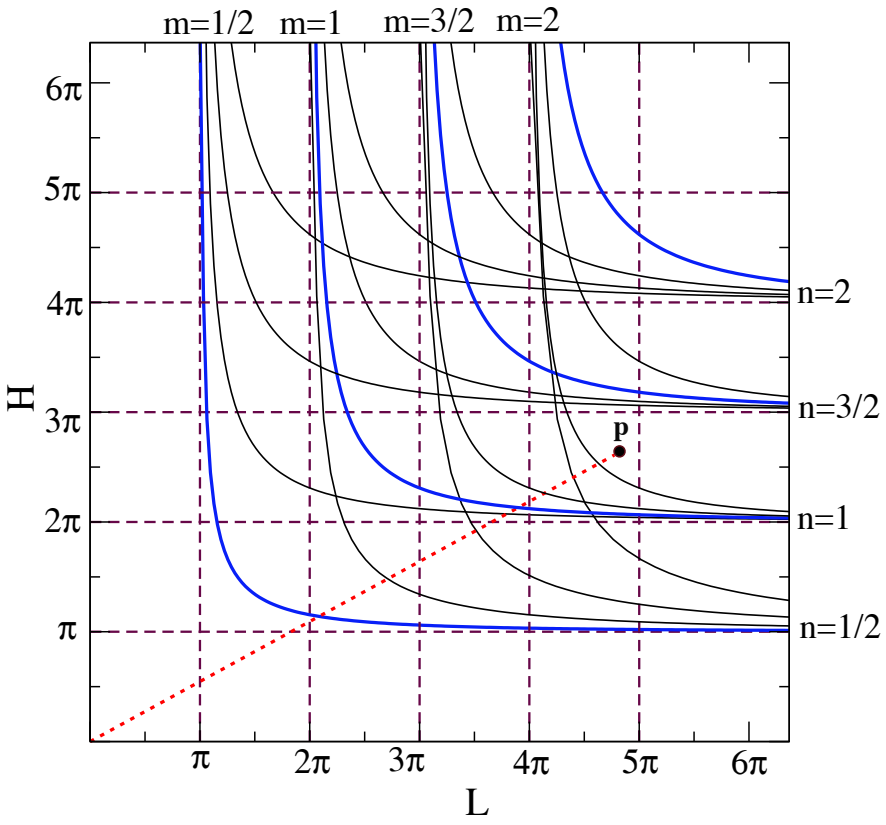

Figure 4.2: Linear stability thresholds for and loci of symmetry breaking bifurcations from the trivial homogeneous flat film state (without energetic bias, $a^+ = 0$) as a function of the domain size L and the film thickness H. The horizontal and vertical dashed lines represent thresholds for vertical structuring, i.e., $(0, n)$ modes, and lateral structuring, i.e., $(m, 0)$ modes, respectively. The solid lines correspond to checker-board modes (m, n) with $m, n = 1/2, 1, 3/2, 2$. The mean concentration is $\bar{c} = 0$. The number of unstable modes for a given pair L and H is obtained by counting the number of thresholds one crosses when moving on a straight line from the corresponding point P in the (L, H)-plane to the origin. The example for P in the figure corresponds to 14 unstable modes.

we write

$$k_x = 2\pi m/L, \qquad m = 0, 1/2, 1, 3/2, 2, ... \tag{4.53}$$

and

$$k_z = 2\pi n/H, \qquad n = 0, 1/2, 1, 3/2, 2, ... \tag{4.54}$$

Fixing the mode number in the vertical direction at $n = 0$ yields

$$k_z = 0 \tag{4.55}$$

and one obtains the dispersion relation

$$\beta = (k_x)^2 \left[(k_x)^2 + 3c_0^2 - 1 \right]. \tag{4.56}$$

For $\beta = 0$ we have

$$k_x = \sqrt{1 - 3c_0^2}. \tag{4.57}$$

In the critical mixture case we have $c_0 = 0$ and the critical wave number in the horizontal direction is given by

$$k_c^L = 2\pi m / L_c = 1 \tag{4.58}$$

i.e., the critical lateral domain size depending on the mode number is given by

$$L_c = \frac{2\pi m}{k_c^L} = 2\pi m, \quad m = 1/2, 1, 3/2, 2, ... \tag{4.59}$$

Similarly, for the vertical direction one obtains

$$H_c = \frac{2\pi n}{k_c^H} = 2\pi n, \quad n = 1/2, 1, 3/2, 2, ... \tag{4.60}$$

Note that, the critical film thicknesses of neutral film are depicted in Fig. 4.2 by the horizontal dashed lines, and the critical lateral domain sizes depicted by the vertical dashed lines.

4.6 Linear Stability for Off-critical Films

Here we calculate the linear stability for neutral films (without energetic bias) for the off-critical case ($\bar{c} \neq 0$). We know the film is stable if $\beta < 0$, and unstable otherwise. To find the critical mean concentration we assume $\beta = 0$ in Eq. (4.51) and write

$$0 = (k_x)^2 + (k_z)^2 + 3\bar{c}_c^2 - 1. \tag{4.61}$$

Now we replace the mode numbers for lateral domain size (k_x), and the film thickness (k_z) using Eqs. (4.53) and (4.54), respectively. One obtains

$$0 = \left(\frac{2\pi m}{L}\right)^2 + \left(\frac{2\pi n}{H}\right)^2 + 3\bar{c}_c^2 - 1. \tag{4.62}$$

Rewriting this equation explicitly in terms of the critical mean concentration $\bar{c}_c$,

$$\bar{c}_c = \sqrt{\frac{1 - \left(\frac{2\pi m}{L}\right)^2 - \left(\frac{2\pi n}{H}\right)^2}{3}}, \qquad \left(\frac{2\pi m}{L}\right)^2 + \left(\frac{2\pi n}{H}\right)^2 \leq 1. \tag{4.63}$$

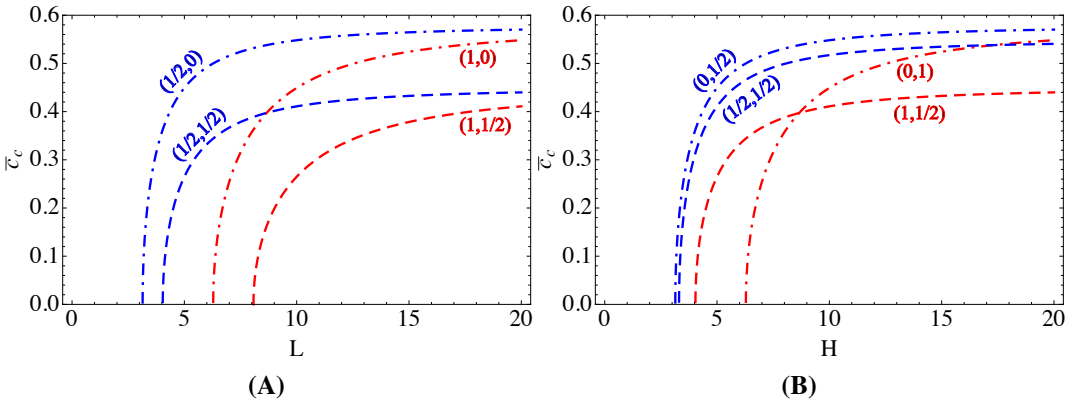

Figure 4.3: For the off-critical films without energetic bias, we show in (A) the critical mean concentration for the laterally structured and checkerboard films of thickness $H = 5$ versus the lateral domain size L. (B) gives the critical mean concentration for the stratified and checkerboard films at lateral domain size $L = 10$ versus the film thickness H. The branches of the films are indicated in the legends.

This equation can be used to indicate the bifurcation points for the off-critical films see Chapter 6. Fig. 4.3 indicates the critical mean concentration for the neutral laterally structured, stratified and checkerboard solutions depending on both the lateral domain size L and the film thickness H. Note that, the critical mean concentration for the films $(1/2, 0)$ and $(1, 0)$ does not depended on the film thickness H, and for the stratified films $(0, 1/2)$ and $(0, 1)$ does not depended on the lateral domain size L (compare these branches in Panels (A) and B of Fig. 4.3). This will be observed also in Chapter 6 as we consider two different film thicknesses for the neutral case.

4.7 Summary and Outlook

In Chapter 4, first we have introduced the tools to perform linear a stability analysis of homogeneous and vertically stratified steady films with respect to harmonic disturbances in the lateral direction. The eigenvalue problem for infinitesimal perturbations of the base state solution has been considered. The evolution of the corresponding normal modes determines the growth rate of the disturbances as a function of the lateral wave number k. The linear stability analysis of the system has been carried out in the general case and the long-wave limit of the general dispersion relation is derived. The stability of the system is investigated in the absence of flow, and in the presence of the Marangoni effect. Finally, the influence of Korteweg stresses on the stability is also introduced.

In the next chapter, we discuss results for 1d steady states that correspond to layered 2d states and 2d steady states together with the linear stability of the relevant layered states. We work with a small number of fixed mean film heights and use the energetic bias in 1d varying the domain size in 2d, at various fixed energetic bias as control parameters.

Chapter 5

Non-linear Analysis for Critical Mixture

5.1 Introduction

Many partial differential equations contain parameters in addition to their variables. If a set of linear differential equations is solved for different parameter values, it is often found that the qualitative changes are not large. However, in our strongly nonlinear model one may find sets of parameter values which are close to each other but result in model behaviour that is qualitatively different. For instance, a stable equilibrium point might become unstable and the system undergoes a bifurcation. Bifurcations often change the attractors of a dynamical system. Stable equilibrium points are attractors, but they are not the only possibility. We will present simple numerical results in which we will see important bifurcations and their consequences. These bifurcations are related to the symmetry groups of the solutions. Although in fact, we do not treat our system employing full scale equivariant bifurcation theory, we use consideration of the symmetries of our solutions to understand the structure of our bifurcation diagrams and to predict any missing branches.

In this chapter we study various fully two-dimensional steady film states that are characterised by non-uniform concentration profiles within the film and a free surface that can be flat or with modulations. The numerical tools employed are presented in [36]. The analysis is performed with and without energetic bias at the free surface.

Using the parameters for polymer blends as in Ref. [57], Sections 5.2 discusses the 1d (layered) film states. The following Section 5.3 analyses fully two-dimensional steady film states and relates their features to the results of the linear stability analysis. In particular, we present results for the cases of (i) a flat film without energetic bias at the free surface (Section 5.3.1), (ii) a flat film with energetic bias (Section 5.3.2, (iii) a height-modulated film without energetic bias (Section 5.3.3), and (iv) a height-modulated film with energetic bias (Section 5.3.4). Note that here the influence of the composition of the film is not discussed as we focus on the "critical case", i.e., a symmetric blend where the concentrations of the two components are equal. The "off-critical case", i.e., of a non-symmetric blend where the concentrations of the two components are not equal, is considered in Chapter 6.

5.2 One-dimensional Case – Stratified Films

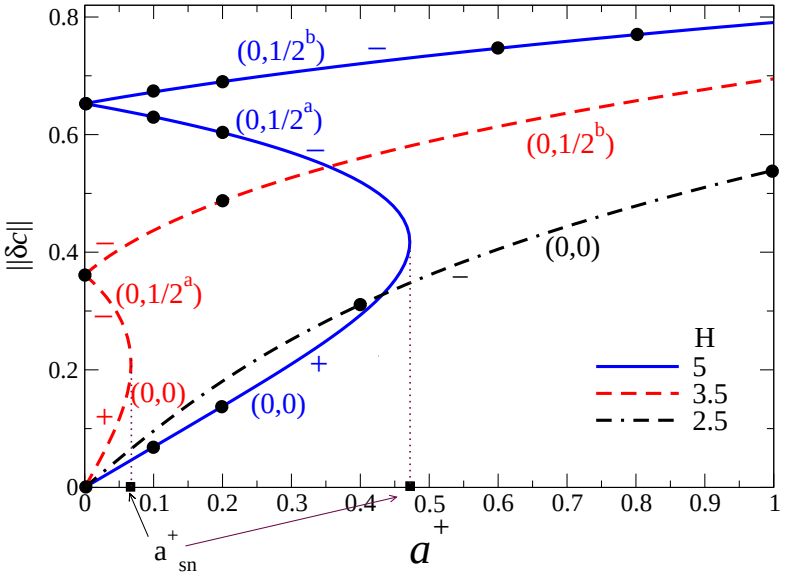

Figure 5.1: Branches of steady vertical concentration profiles for layered films with biased free surface ($a^+ \geq 0$) of a critical mixture $\bar{c} = 0$ in dependence of a^+. The thicknesses are $H = 2.5$ (black dot-dashed line), $H = 3.5$ (red dashed line), and $H = 5$ (blue solid line). The vertical dotted lines indicate the location of the saddle node bifurcation points. The black dots indicate solutions at particular values of a^+ that are further discussed later on. The symbols "+" and "-" indicate linear stability and instability w.r.t. one-dimensional perturbations, respectively.

Before we embark on the study of fully 2d solutions we discuss the possible stratified states, i.e., layered flat films without any lateral structure. They are studied in detail in Ref. [87]. We briefly review the cases of neutral and asymmetrically biased free surface that are relevant here.

Depending on the film thickness, homogeneous films may demix into a number of different stratified states that can be characterised by their energy and the 1d-norm of the concentration profile. Normally, the energy of the solutions is higher for a larger number of layers, i.e., multilayer film states occur in the time evolution as transients only. The thicker the films, the more layered states exist. In the neutral case subsequent layered states branch off the trivial state at $H = 2n\pi$ (cf. Section 4.5). For $\bar{c} = 0$ all bifurcations are supercritical. Note that $2n + 1$ corresponds to the number of layers: $n = 1/2$ is a two-layer state, $n = 1$ a three layer state, i.e., a sandwich structure.

Particularly interesting are the two-layer and the sandwich structure. For $H < 3\pi$ they are the only nontrivial solutions. In Fig. 5.1, the trivial ($n = 0$) and the two-layer ($n = 1/2$) state for a neutral surface are indicated by the black dots at $a^+ = 0$. The $n = 1/2$ solution is not present for $H = 2.5 < \pi$. For $H = 3.5$ and $H = 5.0$ it actually represents two solutions, called $n = 1/2^a$ and $n = 1/2^b$. They are related by the symmetries $z \to H - z$ and $c \to -c$ and can therefore not be distinguished by global measures like the energy or norm. In the context of two-dimensional states, we call the stratified, laterally homogeneous films $(0, n)$ branches, where the zero corresponds to the lateral mode number m.

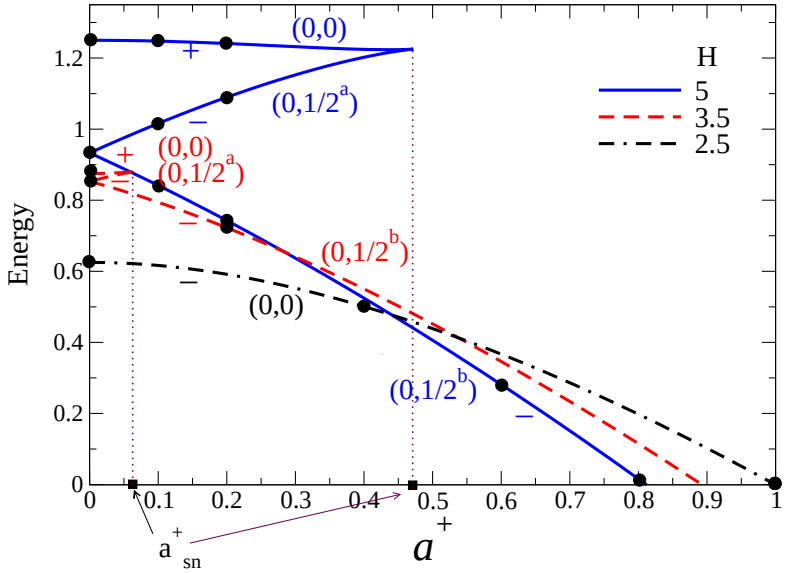

Figure 5.2: Branches of steady layered films of critical mixture $\bar{c} = 0$ are characterised by their energy in dependence of the bias $a^+ \geq 0$ at the free surface. Film heights, and symbols are as in Fig 5.1.

Introducing the energetic bias ($a^+ > 0$) breaks the symmetry between the two $n = 1/2$ solutions as now component two is preferred at the free surface. This implies that for $a^+ > 0$ two branches emerge from the single $n = 1/2$ dot at $a^+ = 0$. The $n =$

$1/2^b$ branch is the one of two that is more relevant. It has component two at the free surface and is therefore of lower energy (and larger norm) than the $n = 1/2^a$ branch that has component one at the free surface. Note, however, that both branches are linearly stable. The $n = 1/2^b$ branch has a norm [energy] that monotonically increases [decreases] with increasing bias. For $a^+ > 0$ the homogeneous $n = 0$ state does not exist anymore as such. Component one is enriched at the surface and the norm increases from zero. We call this a weakly stratified film. The enrichment layer becomes more pronounced with increasing bias. The state is, however, linearly unstable even in 1d and the corresponding branch annihilates with the $n = 1/2^a$ branch in a saddle-node bifurcation at $a^+_{\rm sn}$. For $H = 2.5$ the weakly stratified layer is stable (cf. also Fig.10 of Ref. [87]). The saddle-node itself emerges at $H_c = \pi$ from the dot at the origin (Fig. 5.1), then moves for increasing H towards larger norms and larger a^+. For $a^+ > a^+_{\rm sn}$ only the $n = 1/2^b$ branch exists.

5.3 Steady States in the Two-dimensional Case

All the 1d states obtained in the previous section (Fig. 5.1) correspond to laterally invariant 2d states, i.e., stratified layers $c_0(x, z) = c_0(z)$. They may be unstable with respect to lateral perturbations $c_1(z)\exp(\beta t + ikx)$ (cf. Chapter 4). Whenever a (real) eigenvalue β (growth rate) crosses zero we expect a branch of steady two-dimensional states to bifurcate from the stratified (or homogeneous) state. In the following, the results of the linear analysis are discussed alongside the bifurcation diagrams of the 2d states as obtained by the fully nonlinear analysis (cf. Section 3.4).

We distinguish four cases: flat and modulated films without and with energetic bias at the free surface. Each case is discussed for a number of film thicknesses $H < 2\pi$. Similar studies may be performed for larger thicknesses, however, then the bifurcation diagrams become rather crowded. In the cases with energetic bias we look at one to three different strengths a^+.

In each of the cases we will determine several branches of steady solutions. To order the various solutions and to discuss relations between the branches we employ some ideas from equivariant bifurcation theory [21, 22, 46]. This will allow us to infer the multiplicity of the various branches, the character of the symmetry breaking bifurcations and help to determine the stability of the solutions. Note, however, that we will sort our numerical results using a convenient selection of symmetries (reflections, inversions

and rotations in a space spanned by the spatial coordinates and the concentration). To keep the picture simple we exclude whenever possible translations. A proper group theoretical treatment is beyond the scope of the present work.

From the linear stability analysis of homogeneous films we deduce that the complexity of the bifurcation diagrams will increase with increasing film thickness and lateral domain size because an increasing number of modes becomes linearly unstable. Based on this we distinguish "thin films" ($0 < H < \pi$) where the homogeneous film is only unstable w.r.t. lateral modes, "medium films" ($\pi \leq H < 2\pi$) where additionally the first vertical structuring mode is unstable, and "thick films" ($H \geq 2\pi$) where more vertical modes are unstable. We will not analyse such thick films as we expect the picture to be too involved. Our study focuses on thin and medium films.

5.3.1 Flat Films Without Energetic Bias

In the first case we impose a flat free surface without energetic bias. This corresponds to the limit of large and concentration-independent surface tension. The symmetry group that leaves the system of equations, boundary and integral conditions invariant is $\mathbf{Z}_2^x \times \mathbf{Z}_2^z \times \mathbf{Z}_2^c$. The superscripts indicate which coordinate/field the symmetry refers to, i.e., $\mathbf{Z}_2^x \times \mathbf{Z}_2^z = \mathbf{D}_2^{xz}$ is the dihedral group of the rectangle that the domain forms in the (x, z)-plane and $\mathbf{Z}_2^c$ is a cyclic group of order 2 that corresponds to reflection in c, i.e., the transformation $c \to -c$. The corresponding group table is given as Table A.1 in Appendix A. The trivial homogeneous solution $c(x, z) = 0$ is invariant under the full group. All solutions that bifurcate from it must be invariant under one of its subgroups.

Thin film of thickness $H = 2.5$ For films of thickness $H = 2.5 < H_c = \pi$, layered or checker-board states do not exist (Sections 4.5 and 5.2). The trivial state is present for all domain sizes L and corresponds to the horizontal line at $||\delta c|| = 0$ ($E = 0.625$) in the bifurcation diagram in Fig. 5.3. For $L > L_c = \pi$, laterally structured films exist as expected from the linear analysis. The corresponding dispersion relation is given in Fig. 5.4 (case $a^+ = 0$). The growth rate β crosses zero at $k_c^{ls} = 1.0$, i.e., the critical domain size is $L_c^{ls} = 2\pi$.

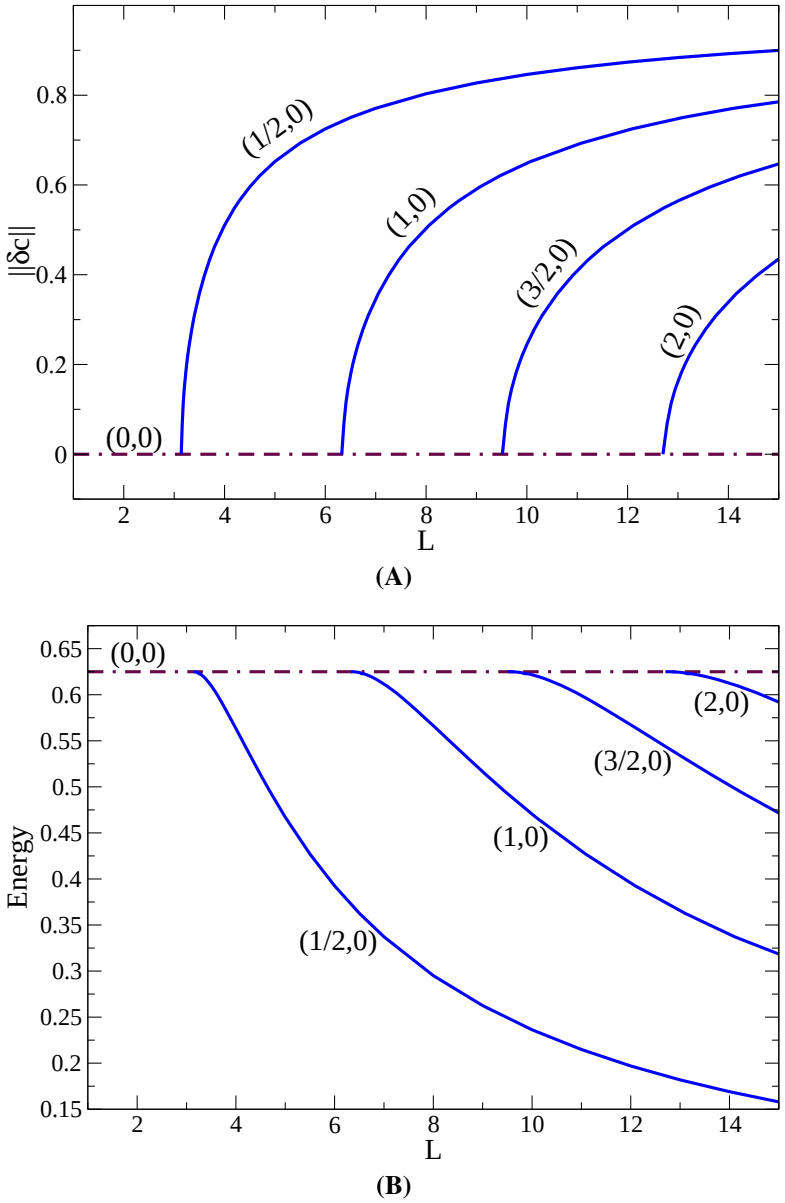

Figure 5.3: The bifurcation diagram for steady state solutions in dependence of the domain size L for flat films of thickness $H = 2.5$, and without energetic bias ($a^+ = 0$). Shown are (A) the L_2-norm for the concentration field (Eq. (3.45)), and (B) the energy E (Eq. (3.47)). The dot-dashed horizontal line corresponds to the homogenous (0,0) solution whereas the solid lines are the various laterally structured film states (m,0).

In Fig. 5.3 the first four branches of laterally structured patterns are shown; with lateral mode numbers $m = 1/2, 1, 3/2$ and 2. We call them $(m, 0)$ branches, where the zero corresponds to the vertical mode number n. The first one bifurcates at $L = L^{ls}_{1/2} = \pi$ and consists of films laterally demixed into two parts. A typical concentration profile is given on the left of the second row of Fig. 5.5. These profiles correspond to half a lateral period and are invariant under the subgroup $\{I, \sigma_{xc}, \pi_z, \rho_{xzc}\}$ and to translations $T^x_{L/m} = T^x_{2L}$, i.e., to translations in x by multiples of $2L$ in the embedded PBC system. The subgroup is the same for all branches where $2m$ is odd. The next branch bifurcates

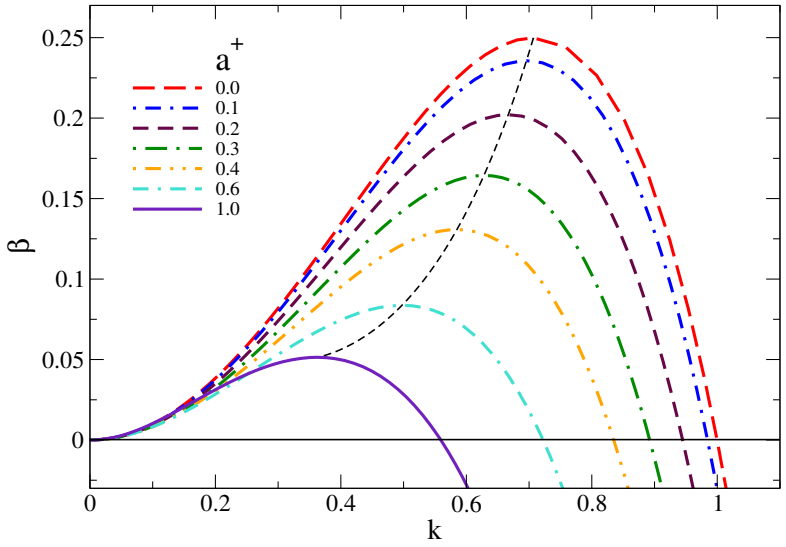

Figure 5.4: The linear stability of a thin flat homogeneous film ($(0,0)$ branch for $H = 2.5$) is characterised by the dispersion relation, i.e., by the dependence of the growth rate on the lateral wave number. Shown are cases without ($a^+ = 0$) and with ($a^+ > 0$) energetic bias at the free surface for a^+ as given in the legend. Transport may occur via diffusion and convection, but the interface is kept flat. The thin dashed line is parameterized by a^+ and follows the maximum $(k_{\max}, \beta_{\max})$ of the dispersion relation.

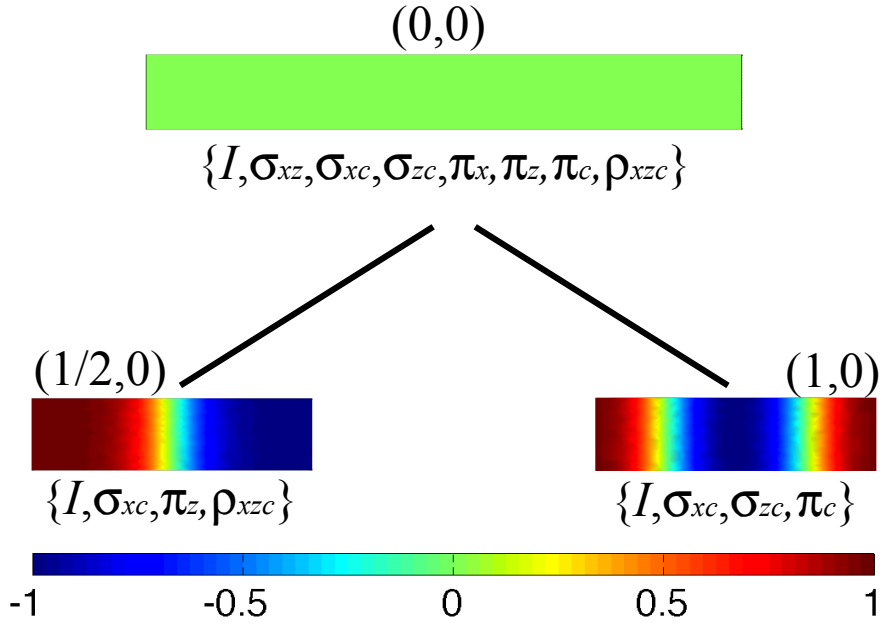

Figure 5.5: For the case of films of thickness $H = 2.5$ without energetic bias we show (i) typical steady concentration profiles on the $(0,0)$, $(1/2,0)$ and $(1,0)$ branches, (ii) the corresponding symmetry groups and (iii) the subgroup relation between them that correspond to the pitchfork bifurcations in the bifurcation diagram of Fig. 5.3. Translations are not included in the scheme, but are discussed in the main text. The concentration profiles for the $(1/2,0)$ and $(1,0)$ branch are at $L = 5$ and $L = 8$, respectively.

at $L = L_1^{ls} = 2\pi$. It is the first branch of periodic solutions and is therefore directly predicted by the linear stability theory. The solutions consists of three different regions (see right part of the second row of Fig. 5.5) and are invariant under the subgroup

$\{I, \sigma_{xc}, \sigma_{zc}, \pi_c\}$ and to translations $T^x_{L/m} = T^x_L$ by multiples of L in the PBC system. This applies to all branches with even $2m$. As the solutions have no vertical structure, all of them inherit the symmetry w.r.t. vertical reflection (σ_{xc}) from the trivial state. The corresponding relation of the subgroups together with example profiles is given in Fig. 5.5.

Note that the bifurcations at the L^{ls}_m are actually pitchfork bifurcations. At each of them two branches emerge. Their solutions are related by the symmetry $\sigma_{xz} : c \to -c$.

The importance of the various solutions in a real physical system may be deduced from their energies (Fig. 5.3). For $L < \pi$ only the trivial state exists, and for $L > \pi$ the $(1/2, 0)$ branch is always the one of lowest energy, i.e., the system will always evolve towards it. The other solutions might still occur as transient states during a vertical coarsening process.

Film of medium thickness $H = 5$ In the previous section we have studied films with $H < H_c = \pi$. There, no laterally homogeneous solutions exist beside the trivial one. For $H > H_c$ layered structures are possible.

Here we consider $H = 5$, i.e., $H_c < H < 2H_c$, where the stratified bilayer $(0, 1/2)$ branch exists but not the trilayer $(0, 1)$ branch (cf. Fig. 5.1 at $a^+ = 0$). The corresponding bifurcation diagram is given in Fig. 5.6. For selected concentration profiles see Fig. 5.7. The horizontal lines in Fig. 5.6 represent the trivial $(0, 0)$ branch ($||\delta c|| = 0$, $E = 1.25$) and the $(0, 1/2)$ branch of two-layer stratified states ($||\delta c|| = 0.65$, $E = 0.94$ (see 3rd profile on middle row in Fig. 5.7(B)). Again there are two $(0, 1/2)$ branches with the same global measures whose solutions are related by the symmetry $\sigma_{xz} : c \to -c$.

They correspond to half a vertical period and are invariant under the subgroup $\{I, \sigma_{zc}, \pi_x, \rho_{xzc}\}$ and under translations $T^z_{H/n} = T^z_{2H}$ in z by multiples of $2H$ in the PBC system. The $(0, 1)$ branch exists only at larger $H > 2\pi$ and has solutions that correspond to trilayer or sandwich films. They are invariant under the subgroup $\{I, \sigma_{zc}, \sigma_{xc}, \pi_c\}$ and under translations $T^z_{H/n} = T^z_H$ in z by multiples of H in the PBC system. We will not discuss them further and do not include them or the related secondary branches in Fig. 5.7.

As for $H = 2.5$, the branches of laterally structured films bifurcate from the trivial one at $L^{ls}_m = 2m\pi$. Fig. 5.6 gives the branches with the lateral mode numbers $m =$

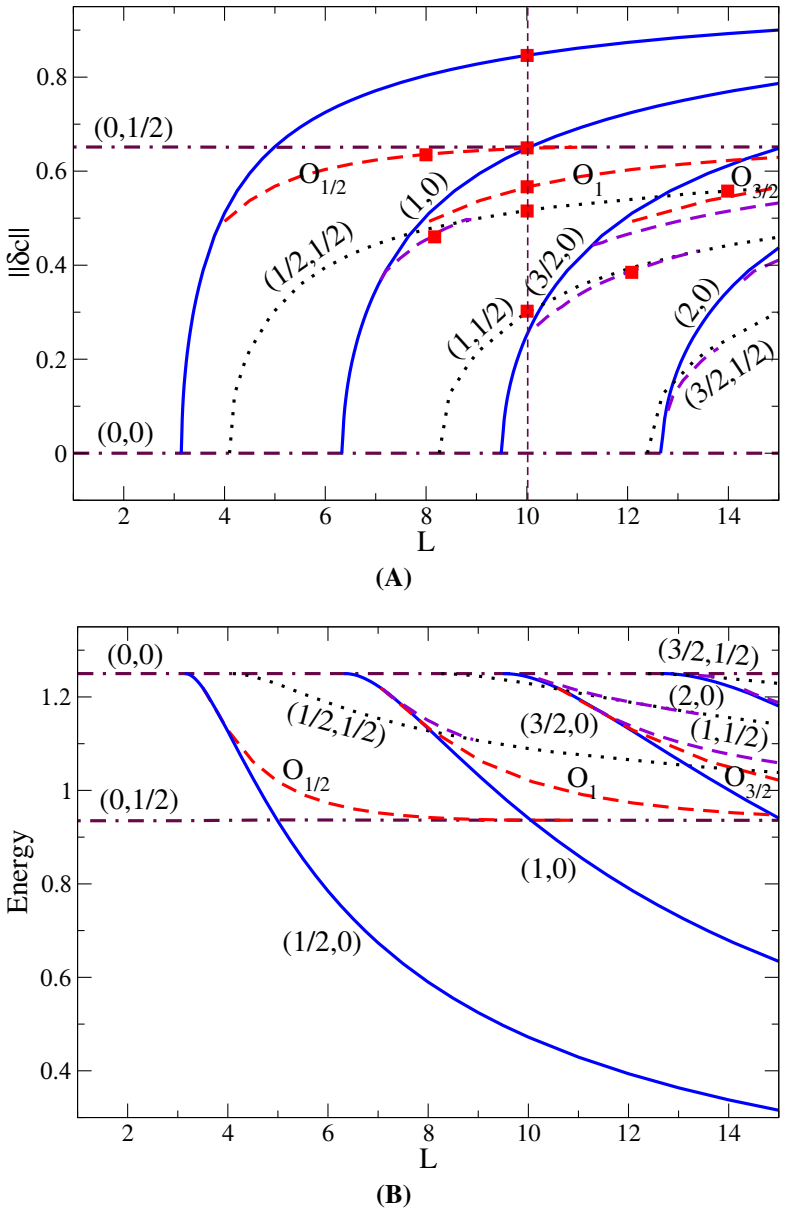

Figure 5.6: The bifurcation diagrams for steady film solutions in dependence of the domain size L for flat films of thickness $H = 5$ and without energetic bias ($a^+ = 0$). Shown are (A) the L_2-norm for the concentration field, and (B) the energy E. The dot-dashed lines correspond to the laterally homogenous $(0, n)$-solutions for $n = 0$ (dash-dash-dot) and $n = 1/2$ (dash-dot); the solid lines are laterally structured $(m, 0)$-states for $m = 1/2, 1, 3/2$ and 2; the dotted lines are checker-board $(m, 1/2)$-states for $m = 1/2, 1$ and $3/2$; the dashed lines corresponds to various types of oblique solutions that are further explained in the main text. The small red squares and green dots in panel (A) mark solutions that are given in Fig. 5.7.

$1/2, 1, 3/2$ and 2. Concentration profiles are shown for $m = 1/2$ and $m = 1$ on the second row of Fig. 5.7. Comparing Figs. 5.6 and 5.3 one notices that for all branches with $n = 0$, the energy in the $H = 5$ case is twice the one for $H = 2.5$. The norms for

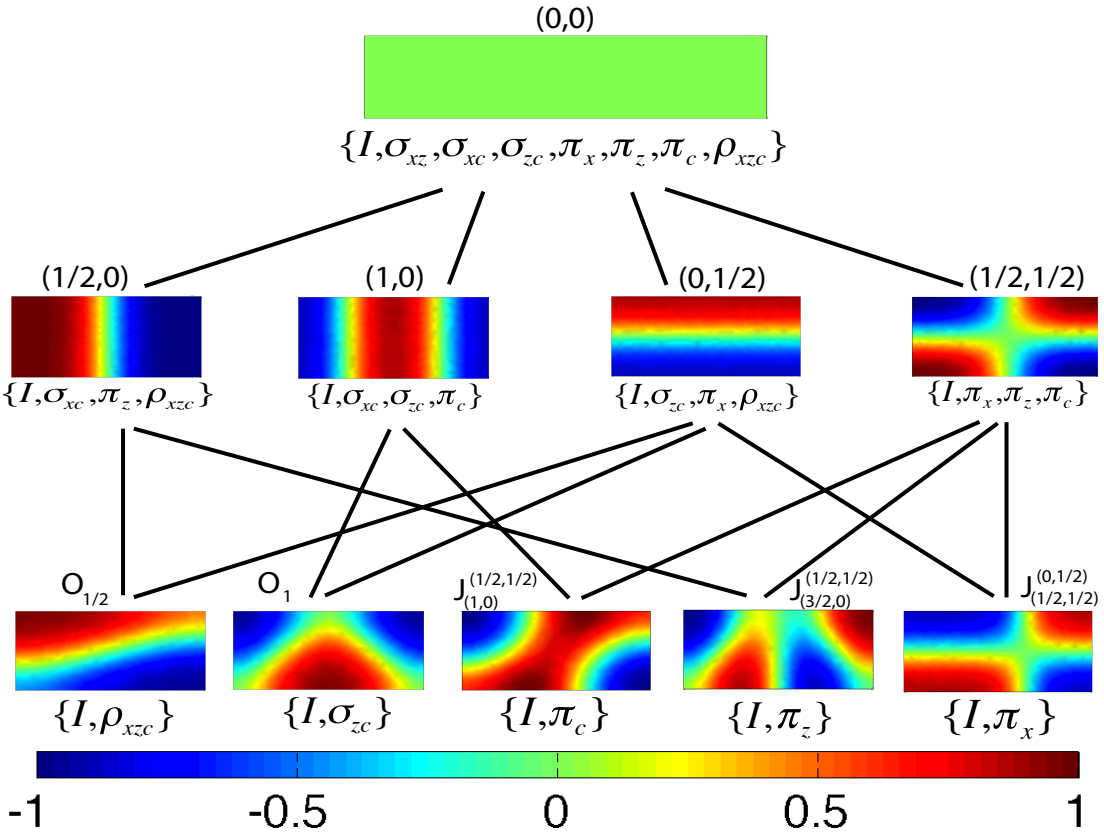

Figure 5.7: For the case of films of thickness $H = 5$ without energetic bias we show (i) typical steady concentration profiles on the various branches in the bifurcation diagram of Fig. 5.6, (ii) the corresponding symmetry groups and (iii) the subgroup relations between them that correspond to the various occurring pitchfork bifurcations. Translations are not included in the scheme, but are discussed in the main text. The concentration profiles on the second row are on branches (from the left): $(1/2, 0)$, $(1, 0)$, $(0, 1/2)$ and $(1/2, 1/2)$ all for $L = 10$, whereas the ones on the third row are on branches (from the left) $O_{1/2}$ at $L = 8$, O_1 at $L = 10$, $J^{(1/2,1/2)}_{(1,0)}$ that joins $(1, 0)$ and $(1/2, 1/2)$ at $L = 8.2$, $J^{(1,1/2)}_{(3/2,0)}$ joining $(3/2, 0)$ and $(1, 1/2)$ at $L = 12$, and $J^{(0,1/2)}_{(1/2,1/2)}$ that joins $(1/2, 1/2)$ and $(0, 1/2)$ at $L = 14$. They are marked by small red squares in Fig. 5.6(A).

the concentration fields are identical. This is as expected for the present case without energetic bias.

The two laterally structured $(1/2, 0)$ branches are linearly unstable when they emerge from the $(0, 0)$ branch at $L = \pi$, then they stabilise at symmetry-breaking pitchfork bifurcations at about $L = 3.9$ where four branches of oblique solutions ($O_{1/2}$) emerge (two from each $(1/2, 0)$ branch). A profile is given on the very left of the third row of Fig. 5.7. The four branches end at about $L = 11.0$ in two further pitchfork bifurcations on the $(0, 1/2)$ branches (Fig. 5.6). The schematic bifurcation diagram in Fig. 5.9 illustrates the multiple branches. For each branch it also indicates the stability and provides a pictogram of the corresponding decomposition pattern. Along the oblique branches the

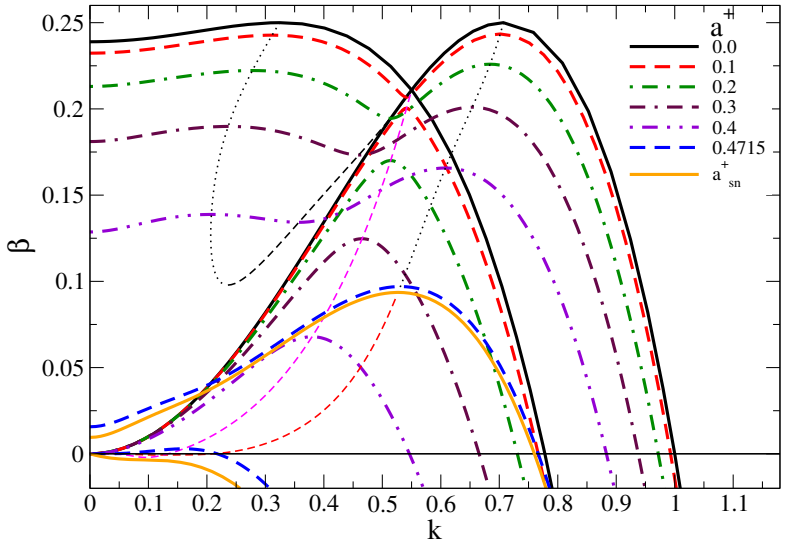

Figure 5.8: The linear stability of a flat homogeneous film of medium thickness [$(0,0)$ branch for $H = 5.0$] is characterised by the dispersion relation. Shown are the cases without ($a^+ = 0$) and with ($a^+ > 0$) energetic bias at the free surface for a^+ as given in the legend. Given are two sets of dispersion curves: for the lateral instability mode (larger $k_{\max}$ at $a^+ = 0$), and for the checker-board instability mode (smaller $k_{\max}$ at $a^+ = 0$). The thin dotted and dashed lines are parameterized by a^+ and follow the maxima ($k_{\max}, \beta_{\max}$) and minima of the dispersion relations.

originally [on $(1/2,0)$ branches] vertical liquid-liquid interface turns until it becomes horizontal [on $(0,1/2)$ branches]. Note that both – the $(1/2,0)$- and the $(0,1/2)$ branch are linearly stable for $3.9 < L < 11.0$, i.e., where the $O_{1/2}$ branches exists. All the solutions on all the $O_{1/2}$ branches are invariant under the subgroup $\{I, \rho_{xzc}\}$ and under translations T^x_{2L} by multiples of $2L$ in the PBC system. The corresponding relations between the mentioned subgroups are given in Fig. 5.7.

Similar sets of branches of oblique solutions connect all $(m,0)$ branches with the $(0,1/2)$ branch. We call them O_m branches. A profile on the O_1 branch that connects the $(1,0)$ and the $(0,1/2)$ branch is given in Fig. 5.7 (second on row three). Other branches of oblique solutions connect checker-board branches (discussed next) and various $(m,0)$ branches. Fig. 5.6 shows in total eight branches of oblique solutions.

Another type of solution that becomes possible for $H > H_c$ are checker-board states. They bifurcate from the homogeneous solution at $L^{\rm cb}_m = mL^{\rm cb}_c$ [cf. Fig. 4.2 and Eq. (4.52)]. For $H = 5$, we only have states with $n = 1/2$, giving $L^{\rm cb}_c = 10\pi/\sqrt{25-\pi^2} = 8.08$ (see also the leftmost dispersion curve in Fig. 5.8 that crosses zero at $k_c = 0.78$, i.e., results in a critical L of 8.06). The first checker-board branch is denoted by $(1/2,1/2)$ and emerges at $L^{\rm cb}_{1/2} = 4.04$ (see Fig. 5.6 and rightmost concentration profile on second row of Fig. 5.7). Note that the values obtained with the different methods do well

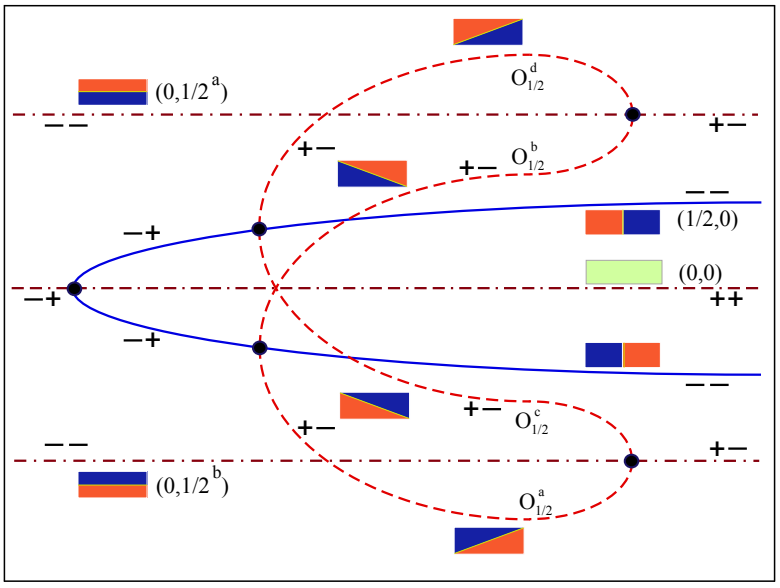

Figure 5.9: Schematic bifurcation diagram for the various pitchfork bifurcations (marked by black dots) involved in the transitions between the $(0,0)$ branch of homogeneous solutions, the $(1/2,0)$ branches of laterally structured states, the $O_{1/2}$ branches of oblique solutions, and the $(0,1/2)$ branches of stratified states. The line styles correspond to the ones in Fig. 5.6. The symbols "+" and "-" indicate the stability of the branches, and the small pictograms indicate the various decomposition patterns on the branches (red: liquid 1, blue: liquid 2)

agree. The $(1/2,1/2)$ states are invariant under the subgroup $\{I,\pi_x,\pi_z,\pi_c\}$ and under translations T^x_{2L} by multiples of $2L$ and T^z_{2L} by multiples of $2H$ in the PBC system. Their branch is connected to the $(m,0)$ branches (with $m > 1/2$) via branches of oblique solutions (two profiles are given on row three of Fig. 5.7) that are all invariant under $\{I,\pi_c\}$ (branches $J^{(1/2,1/2)}_{(1,0)}$ and $J^{(3/2,1/2)}_{(2,0)}$) or $\{I,\pi_z\}$ (branch $J^{(1/2,1/2)}_{(3/2,0)}$) or $\{I,\rho_{xzc}\}$ (branch $J^{(1,1/2)}_{(3/2,0)}$). The checker-board branch is also connected to the layered $(0,1/2)$ branch. The connecting $J^{(0,1/2)}_{(1/2,1/2)}$ branch is invariant under $\{I,\pi_x\}$ (see e.g., the rightmost profile on row three of Fig. 5.7). All the ones mentioned are invariant under translations T^x_{2L} and T^z_{2L} in the PBC system. The relations between subgroups corresponding to the various steady states for such films are given in Fig. 5.7. Note that all the discussed branches emerge via pitchfork bifurcations. At each such bifurcation there emerge two branches that are related by the symmetry that is broken. The schematic bifurcation diagram in Fig. 5.10 illustrates this for the secondary branches emerging from the $(1/2,1/2)$ and $(1,0)$ branches. For each branch it also indicates the stability and provides a pictogram of the corresponding decomposition pattern.

Due to the existence of vertical and horizontal liquid-liquid interfaces, the checker-board solutions have a rather large energy. Note that all liquid-liquid interfaces of the checker-board and laterally structured solutions meet the free surface at an angle of

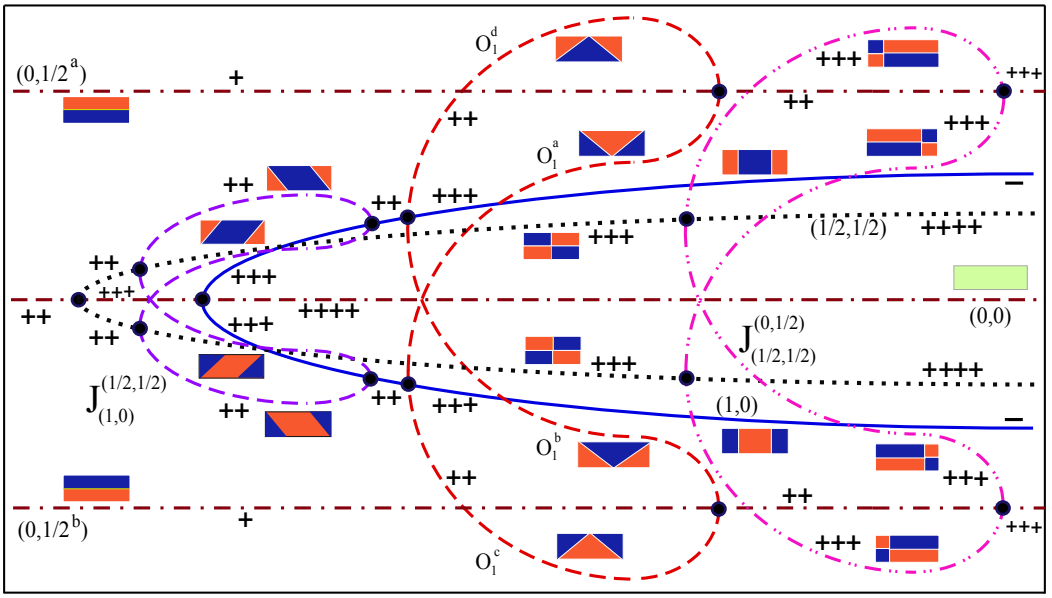

Figure 5.10: Schematic bifurcation diagram for the various pitchfork bifurcations (marked by black dots) involved in the transitions between the $(0,0)$ branch of homogeneous solutions, the $(1/2,0)$ branches of laterally structured states, the $(1/2,1/2)$ branches of checkerboard state, the O_1 branches of oblique solutions, and the $(0,1/2)$ branches of stratified states. The line styles correspond to the ones in Fig. 5.6. The symbols "+" and "-" indicate the stability of the branches, and the small pictograms indicate the various decomposition patterns on the branches (red: liquid 1, blue: liquid 2).

$\pi/2$ corresponding to the zero energetic bias ($a^+ = 0$). An exception are the oblique solutions where two liquid-liquid interfaces meet the free surface at the same point. This allows for an angle of $\pi/4$ (see Fig. 5.7, second profile on row three).

Finally, we discuss the importance of the various solutions in a real physical system based on their energies (Fig. 5.6(B)). In contrast to the case of $H = 2.5$, here the trivial state is always unstable: below $L_c = \pi$ w.r.t. the vertical $n = 1/2$ instability mode and above L_c additionally to the lateral $m = 1/2$ instability mode. Both, the stratified $(0,1/2)$ branch and the laterally structured $(1/2,0)$ branch are linearly stable between the pitchfork bifurcations that limit the range of existence of the $O_{1/2}$ branch. The latter consists of unstable threshold solutions that have to be overcome to switch between the two stable branches. Note that the Maxwell point L_{maxw} where the $(1/2,0)$ branch and the $(0,1/2)$ branch are of equal energy lies well inside the interval. An estimate determined in the limit of a sharp liquid-liquid interface gives $L_{\mathrm{maxw}} = H/(1-a^+) = 5$, actually, a trivial result for $a^+ = 0$. All other solutions are of higher energy and might only occur as transient states during a coarsening process. They might also gain importance for ratios S of interfacial tensions that are larger than one.

5.3.2 Flat Films With Energetic Bias

Next, we study films with a linear energetic bias ($a^+ > 0$) at the flat free surface. The homogeneous state $||\delta c|| = 0$ only exists in the neutral case ($a^+ = 0$). When increasing a^+, the film becomes weakly stratified. The norm $||\delta c||$ increases, whereas the energy slightly decreases (cf. Figs. 5.1 and 5.2 above). Note that the energetic bias breaks the $\sigma_{xz} : c \to -c$ symmetry. In consequence, the symmetry group under which the equations and boundary conditions are invariant is smaller than the one for the system without bias. It corresponds to $\mathbf{Z}_2^x$ (with elements $\{I, \sigma_{zc}\}$) and the translations T_∞^x. The bias also results in an increasing distinction between many of the profiles that had before emerged in a common pitchfork bifurcation. In the case of the two-layer stratified films this is well visible in Figs. 5.1 and 5.2. Now, the solution with component 2 at the free surface is energetically preferred. The second stratified solution (fluid 1 at the free surface) annihilates with the weakly stratified state in a saddle node bifurcation at a^+_{sn} (Fig. 5.1).

Thin film of thickness $H = 2.5$ As the bifurcation diagram for biased flat films with $H = 2.5$ looks rather similar to the one for the neutral case (Fig. 5.3) we only mention the important differences: (i) The weakly stratified branch takes the role of the trivial homogeneous branch in the neutral case. The corresponding profiles are invariant under $\{I, \sigma_{zc}\}$ and translations T_∞^x; (ii) The points L_c^m where the laterally structured branches bifurcate shift to larger L as a^+ is increased, corresponding to a decreasing critical wave number k_c (Fig. 5.13). Laterally structured solutions are only invariant under translations $T_{L/m}^x$ and the identity $\{I\}$ ($2m$ odd) or $\{I, \sigma_{zc}\}$ ($2m$ even); (iii) The angle between the diffuse liquid-liquid interface and the liquid-gas interface is not $\pi/2$ anymore as the preferred fluid 2 now occupies a larger part of the free surface than fluid 1. Therefore, the notion "laterally structured film" is not literally correct anymore. However, we continue to use it as it indicates to which solution at $a^+ = 0$ the solution at hand is related. (iv) For rather high $a^+ = 1$, the bifurcation from the trivial state is subcritical (see Fig. 5.11) and there exist (even for $H < \pi$) solutions with an oblique liquid-liquid interface that represent a transition state between the weakly stratified and laterally structured branches (see profiles of $O_{1/2}$ and O_1 in Fig. 5.12). The branch of oblique solutions joins the laterally structured film in a saddle node bifurcation when the diffuse interface passes the corners of the domain.

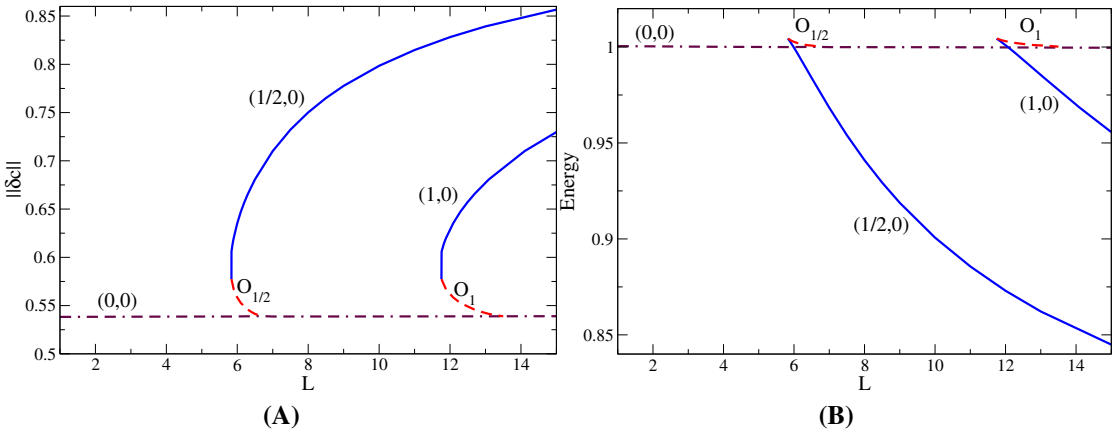

Figure 5.11: The bifurcation diagrams for steady film solutions as a function of the domain size L for flat films of thickness $H = 2.5$ and with energetic bias ($a^+ = 1$). Shown are (A) the L_2-norm for the concentration field, and (B) the energy E. The (dash-dash-dot) line corresponds to the weakly stratified $(0,0)$-solutions, the red dashed lines correspond to the oblique solutions $O_{1/2}$, O_1 and the solid blue lines are laterally structured $(m,0)$-states for $m = 1/2$, and 1.

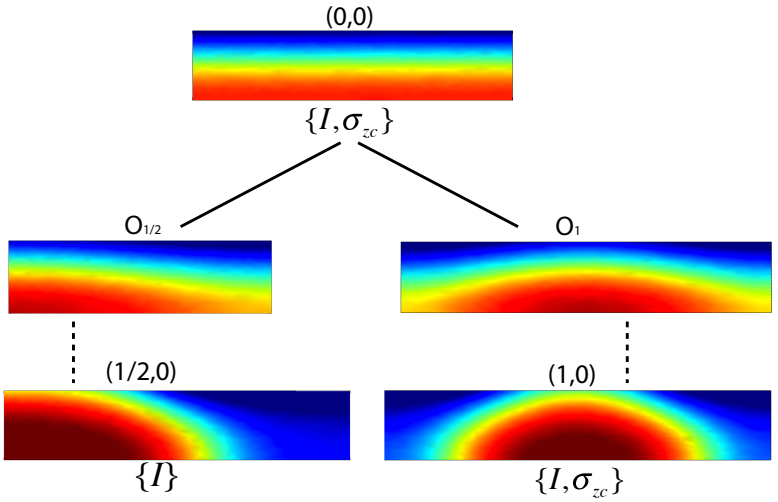

Figure 5.12: For the case of films of thickness $H = 2.5$ with energetic bias $a^+ = 1$ we show (i) typical steady concentration profiles on the various branches in the bifurcation diagram of Fig. 5.11, (ii) the corresponding symmetry groups and (iii) the subgroup relations between them that correspond to the various occurring pitchfork bifurcations. Translations are not included in the scheme. The concentration profiles of branch $(0,0)$ is for $L = 10$, $O_{1/2}$ for $L = 6.3$, O_1 for $L = 12.5$, (1/2,0) for $L = 10$ and $(1,0)$ is at $L = 13$.

The linear stability of the stratified states is analysed for several $a^+ > 0$ in Fig. 5.4 above. The maximal growth rate $\beta_{\max}$ and the critical wavenumber k_c are given as functions of a^+ in Fig. 5.13(A) and (B), respectively. At $a^+ = 0$ one has $k_c = 1$ and $\beta_{\max} = 2.5$. Both decrease as a^+ increases. Overall the bias makes the films less unstable, and correspondingly the bifurcation points $L_c^m = 2m\pi/k_c$ are shifted towards larger domain sizes. Next we consider thicker films with $H = 5 > \pi$.

Film of medium thickness $H = 5$ Increasing a^+ from zero for flat films of thickness $H = 5$, results in significant changes in the bifurcation diagrams. Consider, e.g., the points on the line $a^+ = 0.2$ in Fig. 5.1. The two stratified solution branches $(0, 1/2^a)$ and $(0, 1/2^b)$ now differ resulting from the broken symmetry $\sigma_{xz} : c \to -c$. In consequence, the related (four-fold) oblique branch O_m (cf. Fig. 5.6) splits into two two-fold branches. The solutions on the two that form each pair are related by $\sigma_{zc} : x \to -x$. For the resulting bifurcation diagram see Fig 5.14. The split oblique solutions branches are called O_m^a and O_m^b and are given as dashed red lines. One of them now ends in a (symmetry-conserving) saddle-node bifurcation together with the laterally structured branch. The other one continues towards the weakly stratified solution. Corresponding profiles, their symmetry groups and relations between them are given in Fig. 5.15. The checker-board solutions do not split with increasing a^+ because both branches behave identically (they are related by the translation $T^x_{L/2m}$). The oblique branches O_m^a approach the stratified $(0, 1/2^a)$ branch but do actually not bifurcate from it (see below). The oblique branches O_m^b bifurcate from the stratified (0,$1/2^b$) branch in good agreement with the linear results of Fig. 5.16.

A similar split occurs for all the J branches (that connect the various checkerboard branches to other branches). For $a^+ = 0$ they are four-fold (cf. Fig. 5.10), but for $a^+ > 0$ each splits into two two-fold branches. However, the resulting difference between the branches is very small and not well visible in Fig. 5.14. In consequence, the connection between the J branches and the checkerboard branches is not a pitchfork anymore: It is replaced by a saddle node between the left hand part of the checkerboard branches and one of the two-fold J branches and a continuous transition between the other two-fold J branch and the right hand part of the checkerboard branch. This agrees with the fact that the J branches and the checkerboard branches they connect to, have the same symmetry (see Fig. 5.15). In general, one may distinguish a high and a low

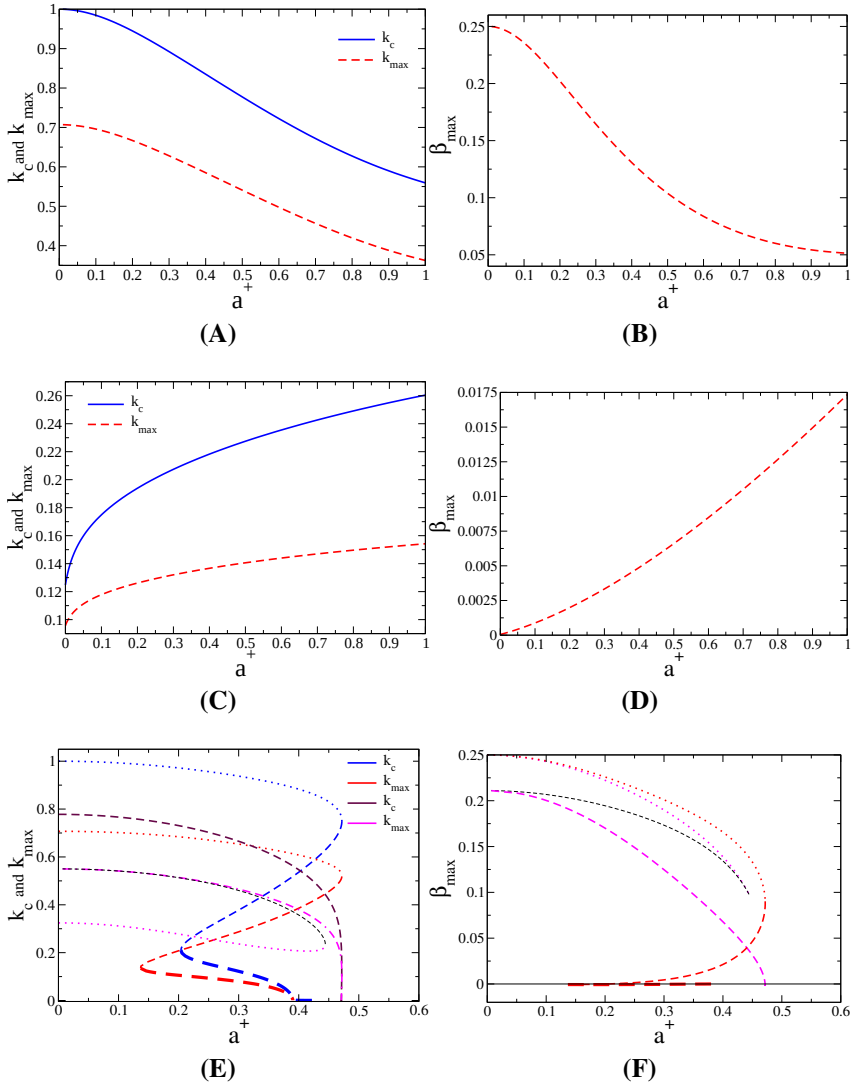

Figure 5.13: Characteristics of the dispersion relations are given as functions of the energetic bias a^+ at the flat free surface for (A,B) homogeneous films of $H = 2.5$, (C,D) the $(0, 1/2^b)$ branch for $H = 5$, and (E,F) the $(0, 0)$, $(0, 1/2^a)$ branches for $H = 5$ (cf. Figs. 5.1, 5.4, 5.8 and 5.16). The left column gives the critical wavenumber k_c (for line styles see legend) and the wave number of the fastest growing mode while the right column gives the corresponding maximal growth rate $\beta_{\max}$ (with the linestyles corresponding to the ones of $k_{\max}$). The situation in the last row is involved as (i) two branches join in the saddle node at $a^+_{\rm sn} \approx 0.47$ and (ii) there are two unstable modes that can have maxima and minima at $k \neq 0$ [cf. Figs. 5.8 and 5.16(B)]. The lines in (E,F) show the loci of maxima and minima employing the same linestyles as used to track them in Fig. 5.8. In particular, the additional dashed (brown) and dash-dash-dotted (magenta) line give k_c and $k_{\max}$ for the checkerboard mode. For further discussion see main text.

energy group of solution branches (Fig 5.14(B)). The high energy group consists of the weakly stratified $(0, 0)$, the stratified (0,$1/2^a$), all checker-board $(m, 1/2)$, and all oblique O^a_m and J branches (see profiles left of dotted line in Fig. 5.15). All of them are confined between the $(0, 0)$ and $(0, 1/2^a)$ branch. Fig 5.1 shows that an increase in the bias a^+ increases the difference between the stratified $(0, 1/2^a)$ and $(0, 1/2^b)$

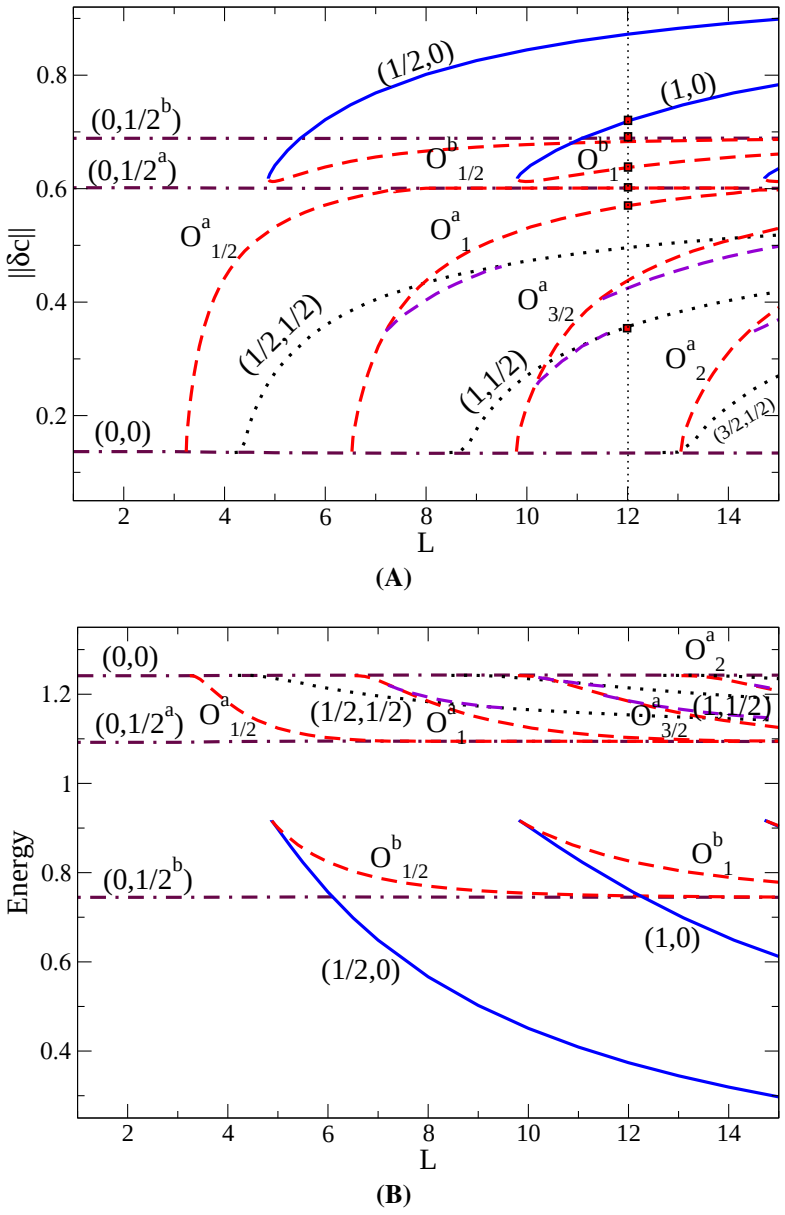

Figure 5.14: Bifurcation diagrams for steady state solutions in dependence of the lateral domain size L, for flat film of thickness $H = 5$ with a moderate energetic bias at the free surface ($a^+ = 0.2$). Panels (A) and (B) give the L_2-norm of the concentration field and the energy, respectively. The (maroon) dash-dash-dotted line represents the trivial (weakly stratified) solution, the (maroon) dash-dotted lines represent the stratified $(0, 1/2^a)$ and $(0, 1/2^b)$ branches, the (blue) solid curves represent the laterally structured $(m, 0)$ branches ($m = 1/2, 1$), the (red) dashed lines represent the oblique branches O^a_m ($m = 1/2, 1, 3/2, 2$) and $O^b_m, m = 1/2, 1$, and the (black) dotted curves represent the checker-board $(m, 1/2)$ branches ($m = 1/2, 1, 3/2$).

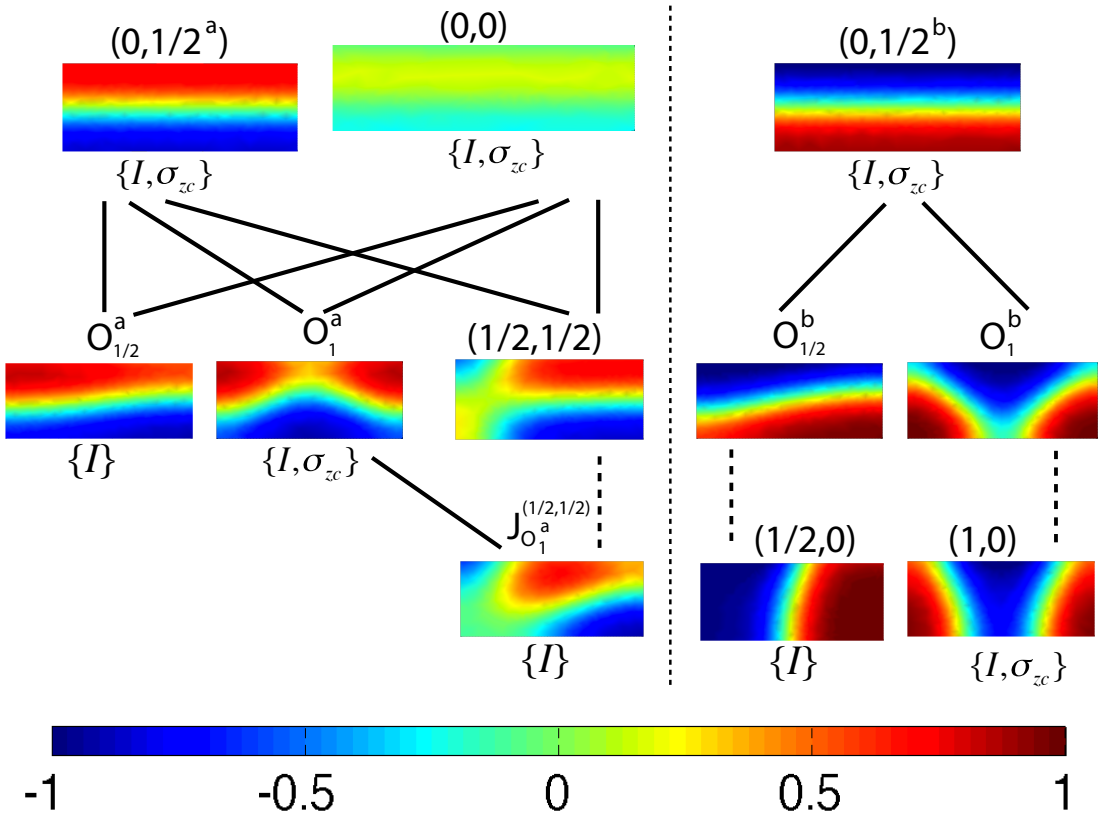

Figure 5.15: For the case of films of thickness $H = 5$ with energetic bias we show (i) typical steady concentration profiles on the various branches in the bifurcation diagram of Fig. 5.14, (ii) corresponding symmetries and (iii) the relations between the branches that correspond to the various symmetry-breaking pitchfork and not symmetry-breaking saddle-node bifurcations as solid and dashed straight lines, respectively. Symmetries w.r.t. translations are not included in this and similar scheme throughout the paper, but are discussed in the main text when relevant. Here, in two of the pitchfork bifurcation from the laterally invariant $(0, 0)$ and $(0, 1/2)$ solutions, the translational symmetry T^x_∞ is actually the only one that is broken. The concentration profiles on the first row are on branches (from the left): $(0, 1/2^a)$, $(0, 0)$, and $(0, 1/2^b)$ all for $L = 12$, whereas the ones on the second row are on branches (from the left) $O^a_{1/2}$ at $L = 7$, O^a_1 at $L = 12$, $(1/2, 1/2)$ at $L = 12$, $O^b_{1/2}$ at $L = 12$, O^b_1 at $L = 12$, the ones on the third row are on branches (from the left) $J^{(1/2,1/2)}_{O^a_1}$ that joins O^a_1 and $(1/2, 1/2)$ taken at $L = 9$, $(1/2, 0)$, and $(1, 0)$ both at $L = 12$. The vertical dotted line separates solutions on the high (left) and low (right) energy group of branches (see main text).

branches. However, the difference between the $(0,0)$ and $(0,1/2^a)$ branch decreases. They approach each other and annihilate at the saddle-node at $a^+_{\rm sn}$. In consequence, the entire group of high energy solutions vanishes at $a^+_{\rm sn}$. Only the low energy group remains for $a > a^+_{\rm sn}$. It consists of the stratified (0,$1/2^b$) branch, the laterally structured $(m,0)$ branches, and the oblique O^b_m branches that connect the other two (see profiles right of dotted line in Fig. 5.15).

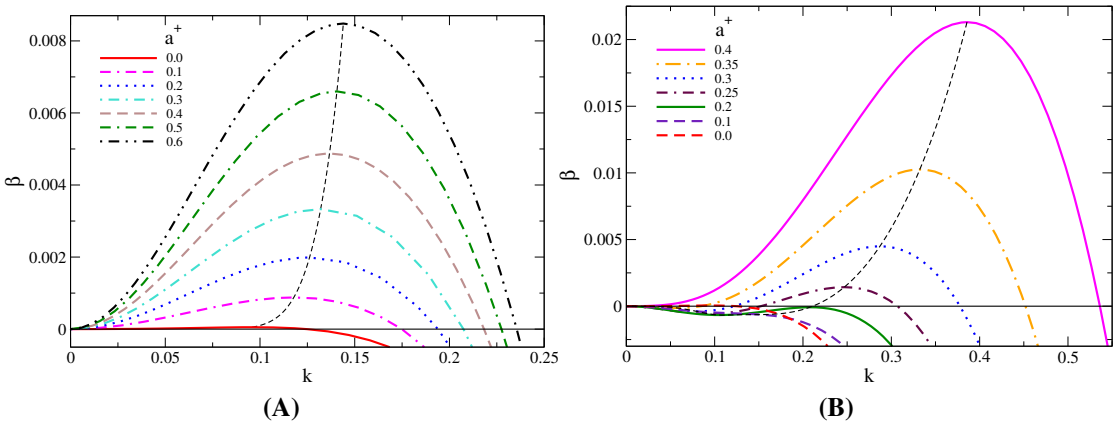

Figure 5.16: Linear stability w.r.t. lateral perturbations for the stratified (A) $(0,1/2^b)$ and (B) $(0,1/2^a)$ branch at $H = 5$ for various biases a^+ as given in the legend. The thin dashed lines are parameterized by a^+ and follow the maxima $(k_{\rm max}, \beta_{\rm max})$ of the dispersion relations.

Next we consider how well the primary bifurcations in Fig. 5.14 agree with the linear stability results. Nearly all stratified solutions become unstable to lateral perturbations above some critical L_c (as discussed for $a^+ = 0$). Fig. 5.8 above gives the dispersion relations for the weakly stratified film for various a^+. Figs. 5.13(C) and (D) show as dotted lines k_c, $k_{\rm max}$ and $\beta_{\rm max}$ as a function of a^+. The two respective dispersion relations for each a^+ correspond to checker-board and lateral mode, respectively. For $a^+ = 0.2$, the growth rates cross zero (Fig. 5.8) at about $k_c \approx 0.73$, i.e., $L_c = 8.6$ (checker-board mode), and at $k_c \approx 0.97$, i.e., $L_c = 6.5$ (lateral mode). This agrees well with the $L_c = \frac{2\pi}{k_c}$ values for the $m = 1$ branches in the bifurcation diagram Fig. 5.14.

Fig. 5.16 gives dispersion relations for the two stratified $(0,1/2)$ branches, whereas Figs. 5.13(C) to (F) give k_c, $k_{\rm max}$ and $\beta_{\rm max}$ for the two branches as thick solid and dashed lines, respectively. The behaviour of the energetically favourable $(0,1/2^b)$ branch is straightforward [Fig. 5.16(A) and Figs. 5.13(C) and (D)]: The larger the bias the more unstable w.r.t. lateral perturbations it becomes. Critical and fastest growing wavenumber and maximal growth rate all increase with a^+. At $a^+ = 0.2$, we find $k_c = 0.19$, i.e., $L_c = 33.1$. This agrees well with the point where the $O^b_{1/2}$ bifurcates from the stratified $(0,1/2^b)$ branch a bit above $L = 16$ (slightly beyond the right hand border of Fig. 5.14).

The situation is more intricate for the $(0, 1/2^a)$ branch [see Fig. 5.16(B) and Figs. 5.13(E) and (F)]. When increasing a^+, first the critical wavenumber and maximal growth rate decrease, the solution becomes stable against lateral perturbations at about $a^+ \approx 0.05$. Note, that this part is not visible in Figs. 5.13(E) and (F) as growth rate and wavenumber are very small. However, a further increase in a^+ leads to a finite wavelength instability slightly above $a^+ = 0.2$ with $k_c \approx 0.21$]see Fig. 5.16(B), curve for $a^+ = 0.2$ and folds in Figs. 5.13(e,f)]. Therefore, at $a^+ > 0.2$ there should be two more bifurcations of solutions of period one at about $L_c \approx 30$. In Fig. 5.14, it seems that the $O^a_{1/2}$ branch bifurcates from the $(0, 1/2^a)$ branch at about $L = 7.5$. This is, however, not the case. Upon inspection, the respective solutions on the two branches look still rather different implying that the $O^a_{1/2}$ branch continues to exist for larger L. Our linear stability results actually indicate that it exists for arbitrary large L as the $(0, 1/2^a)$ branch is linearly stable. However, as the bifurcations come into being at slightly larger a^+ our numerical procedure is not able to capture the $O^a_{1/2}$ branch at larger L. At larger a^+, the $(0, 1/2^a)$ solution is only unstable w.r.t. the related lateral mode in a range of wave numbers. For instance, at $a^+ = 0.3$ the $(0, 1/2^a)$ film is unstable between $k = 0.125$ and $k = 0.357$ (see Fig. 5.16(B)). The band of unstable wave numbers widens till the smaller one reaches zero (cf. curve for $a^+ = 0.4$ and k_c in Fig. 5.13(C)). Here, we will not discuss these effects further. Finally, we briefly discuss the behaviour for $a^+ > a^+_{\rm sn}$.

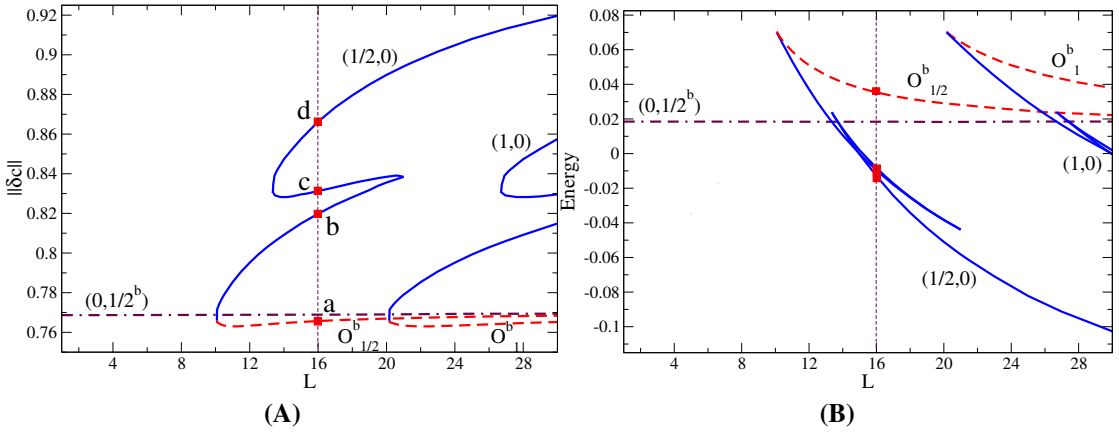

Figure 5.17: Bifurcation diagram for steady state solutions for flat films of thickness $H = 5$ with a free surface with a large energetic bias of $a^+ = 0.8$. Given (A) the L_2-norm of the concentration field and (B) the energy as functions of the lateral domain size L.

Slightly above $a^+_{\rm sn}$ the low energy group of branches does not change its appearance. At large a^+, however, additional structures appear, see the bifurcation diagram in Fig 5.17 for an example ($a^+ = 0.8$). Although the laterally structured $(1/2, 0)$ solutions ultimately still annihilate at low L with the oblique $O^b_{1/2}$ branch, the branch has acquired

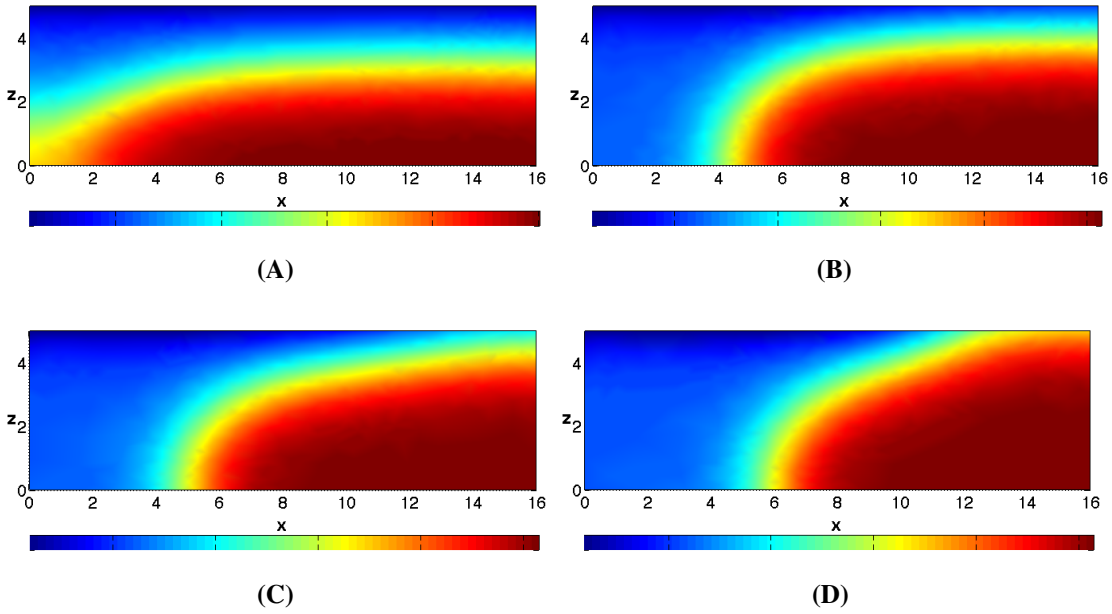

Figure 5.18: Shown are the film and concentration profiles for flat films of mean height $H = 5$ and $a^+ = 0.8$ that are marked by small squares in the bifurcation diagrams of Fig. 5.17 on the line $L = 16$ ordered from bottom to top. Panel (A) shows the oblique solution ${O_1}^b$ in its way to join to the stratified $(0,1/2^b)$ branch. Panel (B), (C), and (D) show how the stratified solution $(0,1/2^b)$ changes appearance in a complex way.

an additional pair of saddle node bifurcations, i.e., in a small range in L there exist now three stable and two unstable profiles.

The film profiles (A,B,C,D) shown in Fig. 5.18 correspond to the labels (a,b,c,d) shown in Fig. 5.17(A), respectively. The profiles elucidate that the transition between the oblique solutions O^b_m and the laterally structured solutions $(m, 0)$, $m = 1/2, 1, ...$ happens in a complex manner. The $(1/2, 0)$ and $O^b_{1/2}$ branch connected passing through four sub-branches with transitions occurring at the three saddle node bifurcations. In the following discussion we explain how the profiles change in these transition. Fig. 5.18(A) shows the concentration profile for the oblique film $O^b_{1/2}$ at the label (a). Note that, on this sub-branch the interface between liquid 1 and liquid 2 straightens as we follow the branch towards larger L and becomes straight horizontal line at the bifurcation point where this branch joins the stratified branch $(0, 1/2)$. At the saddle node bifurcation between labels (a) and (b) (see Fig. 5.17) the interface between the components passes through the lower left corner (lower right corner) of the domain to facilitate the transition between profiles (A) and (B) of Fig. 5.18. At the saddle node between labels (b) and (c) (see Fig. 5.17) the interface between the components reaches the upper right corner (upper left corner) of the domain (see transition between profiles (B) and (C)). Along this branch the interface remains in connection with the corner until we reach to

next saddle node bifurcation between labels (c) and (d) where the interface between the components becomes completely disconnected from the corner of the domain. We can then see the predominantly laterally structured film (see Fig. 5.18(D)).

5.3.3 Height-modulated Films Without Energetic Bias

Now we lift the restriction of an imposed flat free surface and study films with a surface that is free to move. Practically, this is done by reducing the value of α to 1 in Eq. (3.49). In consequence, solutions are then not only characterised by the energy E and norm $||\delta c||$ of the concentration field, but also by the norm $||\delta h||$ of the film thickness profile $h(x)$ [see Eq. (3.46)]. We start with an investigation of the behaviour without energetic bias at the free surface ($a^+ = 0$) for films with $H = 2.5$ and $H = 5$.

The case $a^+ > 0$ is briefly treated in Section 5.3.4. The main difference to the case of an imposed flat surface is that now the free surface reacts to non-homogeneous concentration profiles. In the contact region of a diffuse interface between the two components and the free surface the horizontal and vertical force components have to be balanced. On the one hand this leads to changes in all solutions discussed above in the case of a flat surface. On the other hand it allows for new solutions that only exist because of the new degree of freedom. To illustrate the changes in the known solutions we show

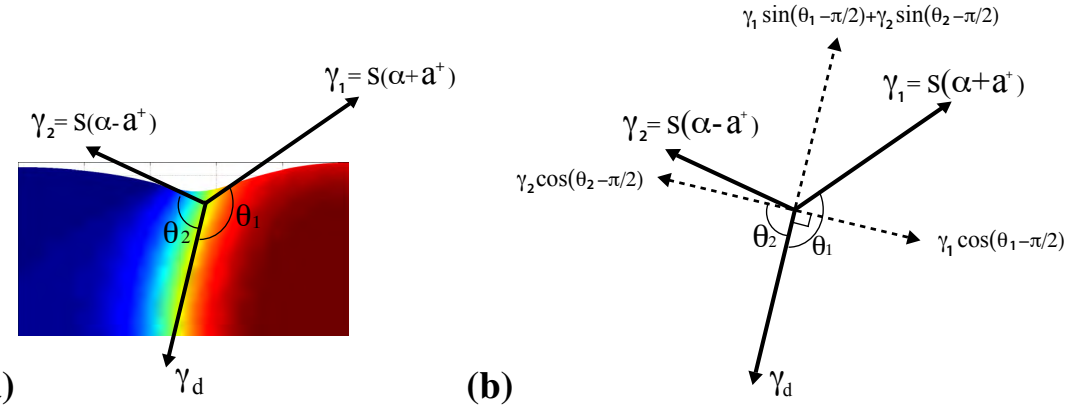

Figure 5.19: (colour online) Panel (a) shows the film and concentration profile of the surface modulated film $(1/2, 0)$ with energetic bias at the free surface with the forces acting at the contact point. It also indicates the definitions of the non-dimensional tensions γ_1, γ_2 and $\gamma_d = 1$. Panel (b) shows analysing the forces in a perpendicular directions at equilibrium.

in Fig. 5.19 a film from the $(1/2, 0)$ branch. The concentration profile shows lateral structuring where θ_i is the angle between the liquid-liquid interface and the free surface of liquid i [58]. In the sharp interface limit $\cos(\pi - \theta) = 1/(2S)$.

In the presence of the energetic bias, the equilibrium of interfacial forces gives the following two equations

$$\gamma_d = -\gamma_1 \cos\theta_1 - \gamma_2 \cos\theta_2, \tag{5.1}$$

$$\gamma_1 \sin\theta_1 = \gamma_2 \sin\theta_2. \tag{5.2}$$

Solving Eq. (5.1) and Eq. (5.2) for θ_1 and θ_2 one obtains the general relation

$$\cos\theta_1 = \frac{\gamma_2^2 - \gamma_1^2 - \gamma_d^2}{2\gamma_1\gamma_d} = \frac{-4S^2\alpha a^+ - \gamma_d^2}{2S\gamma_d(\alpha + a^+)}, \tag{5.3}$$

$$\cos\theta_2 = \frac{\gamma_1^2 - \gamma_2^2 - \gamma_d^2}{2\gamma_2\gamma_d} = \frac{4S^2\alpha a^+ - \gamma_d^2}{2S\gamma_d(\alpha - a^+)}. \tag{5.4}$$

For our case of a modulated free surface with $\alpha = 1$ and $\gamma_d = 1$ we have

$$\cos\theta_1 = -\frac{1 + 4S^2 a^+}{2S(1 + a^+)} \tag{5.5}$$

$$\cos\theta_2 = -\frac{1 - 4S^2 a^+}{2S(1 - a^+)}. \tag{5.6}$$

However, for an imposed flat surface ($\alpha \gg 1$) with $\gamma_d = 1$, the relations become $\cos\theta_1 = -2Sa^+$ and $\cos\theta_2 = 2Sa^+$. Below, these relations will be checked against our diffuse interface results. For the case without energetic bias ($a^+ = 0$) if we assume $S = \gamma_d = 1$ in Eqs. (5.3) and (5.4) then we obtain

$$\theta_1 = \theta_2 = \cos^{-1}(\frac{-1}{2}) = 2\pi/3. \tag{5.7}$$

Resulting from these relations the energetic bias must satisfy the inequality $|a^+| < 0.5$. Fig. 5.20 shows how the angles θ_1 and θ_2 vary for positive energetic bias for $\alpha = 1$ and large α ($\alpha \to \infty$).

Films of small thickness ($H = 2.5$) For $H = 2.5$, the bifurcation diagram in terms of $||\delta c||$ (see Fig. 5.21(A)) looks rather similar as the one for flat films (Fig. 5.3(A)). As expected, the points L_c^m where the laterally structured branches bifurcate are identical to the ones in the flat case, however, the $||\delta c||$ along the bifurcating branch is slightly larger than in the flat case (at max $\approx 5\%$ for the parameter values we study). The energy is lower than in the flat case (not shown) mainly resulting from the additional degree of freedom that can be appreciated in Fig. 5.3(B) where $||\delta h||$ is shown. On every

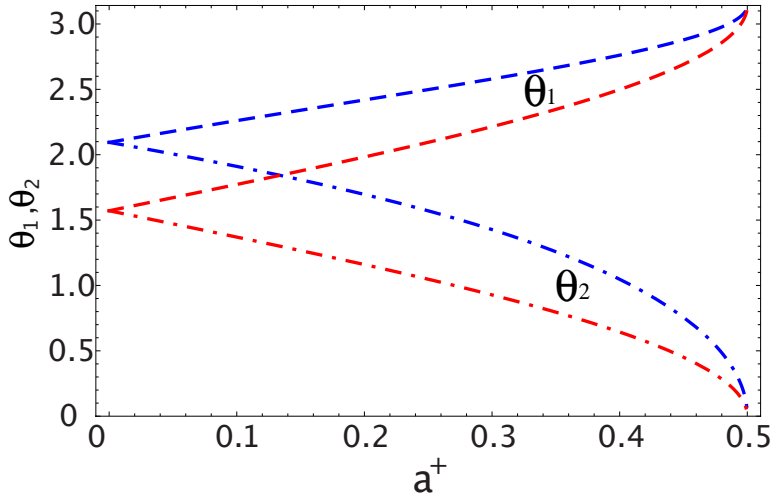

Figure 5.20: Shown are the equilibrium liquid-liquid contact angles in radian in dependence of the energetic bias. The dashed curves correspond to θ_1 and the dot-dashed curves correspond to θ_2. The blue curves are at $\alpha = 1$, and the red curves are at large α, i.e., $\alpha \to \infty$. Here we consider $S = 1$.

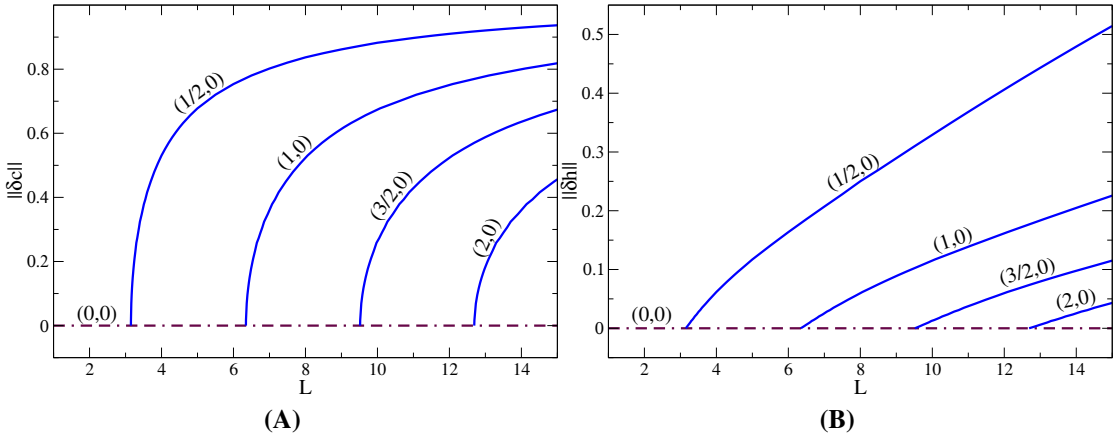

Figure 5.21: The bifurcation diagram for steady state solutions in dependence of the domain size L for films with surface modulations of thickness $H = 2.5$, and without energetic bias ($a^+ = 0$). Shown are (A) the L_2-norm for the concentration field Eq. (3.45), and (B) the L_2-norm for the surface modulations Eq. (3.46). The dot-dashed horizontal line corresponds to the homogenous solution $(0, 0)$ whereas the solid lines are the various laterally structured film states.

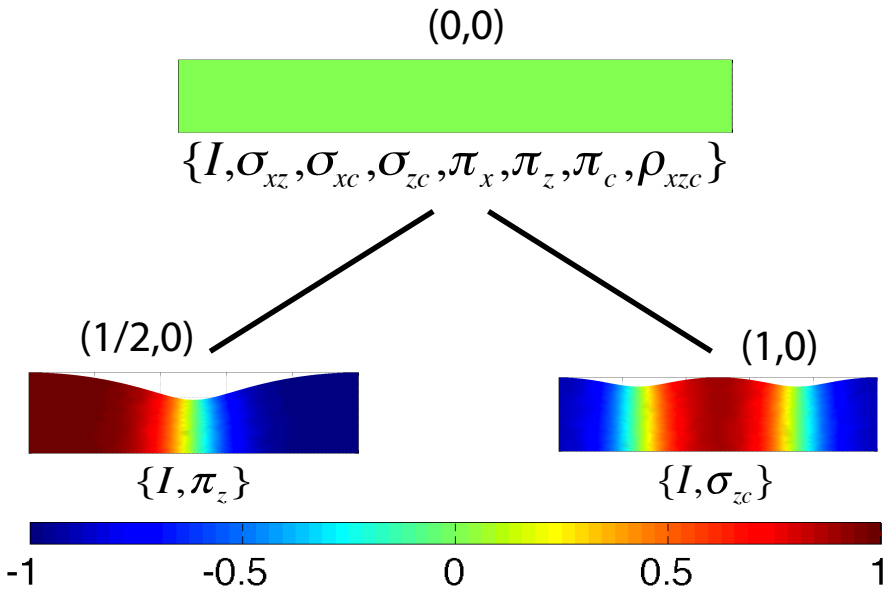

Figure 5.22: For the case of height modulated films of thickness $H = 2.5$ without energetic bias we show (i) typical steady concentration profiles on the $(0,0)$, $(1/2,0)$ and $(1,0)$ branches, (ii) the corresponding symmetries and (iii) the relations between the branches; cf. bifurcation diagram Fig. 5.21. The concentration profiles for the $(1/2,0)$ and $(1,0)$ branch are at $L = 10$. For remarks on symmetries and line styles see caption of Fig. 5.15.

laterally structured branch $(m,0)$, the surface modulation monotonically increases with the lateral domain size. Typical profiles, their symmetries and the relations between them are given in Fig. 5.22. The dispersion relation for the homogeneous solutions is given below in Fig. 5.28 (case $a^+ = 0$) and is identical to the one in the case of a flat surface (cf. Fig. 5.4).

Note that the symmetry group for the homogeneous solution is identical to the one in the flat non-biased case, whereas the ones of the laterally structured branches do not agree (cf. Fig. 5.5). This is due to the fact that any lateral structuring causes a surface modulation and therefore also breaks the $z \to -z$ symmetry. For fixed domain size, the branches of higher mode number have a smaller surface modulation as more diffuse interfaces 'pin' the free surface.

Films of medium thickness ($H = 5$) Increasing the film height to $H > \pi$, layered solutions become possible, a situation analysed for neutral and bias flat films in section 5.3.2. Allowing the free surface to change its profile, on the one hand modifies the already known solutions. On the other hand, we find that a modulated surface allows for additional large-amplitude solutions. The bifurcation diagram for $H = 5.0$ for

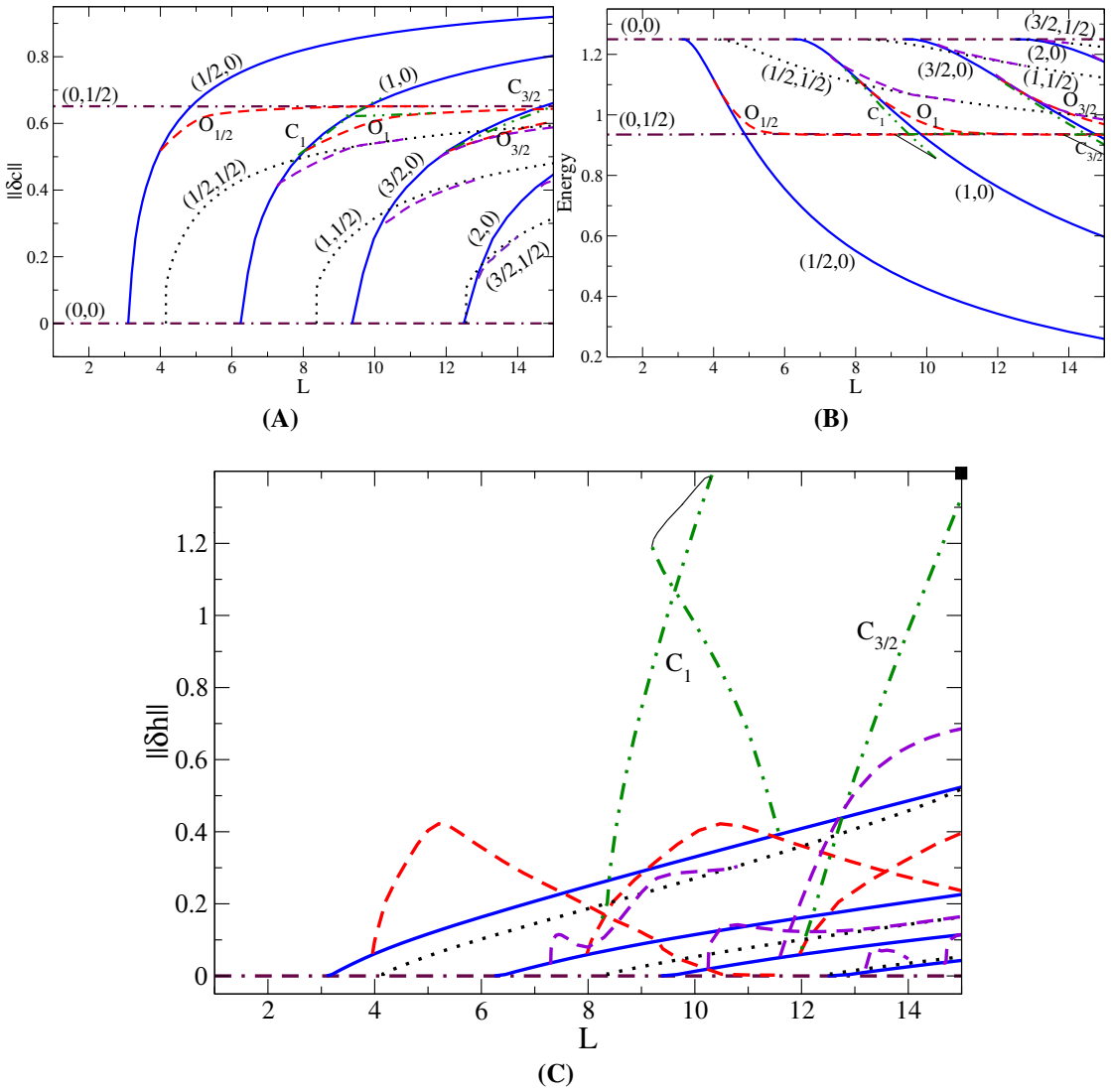

Figure 5.23: The bifurcation diagrams for steady film solutions in dependence of the domain size L for modulated films of thickness $H = 5$ and without energetic bias ($a^+ = 0$). Shown are (A) the norm $||\delta c||$, (B) the energy E, and (C) the norm $||\delta h||$. The dot-dashed horizontal lines correspond to the laterally homogenous $(0, n)$-solutions for $n = 0$ (dash-dash-dot) and $n = 1/2$ (dash-dot); the blue solid lines are laterally structured $(m, 0)$-states for $m = 1/2, 1, 3/2$ and 2; the black dotted lines are checker-board $(m, 1/2)$-states for $m = 1/2, 1$ and $3/2$; the red and purple dashed lines corresponds to various types of oblique solutions. Finally, the green dot-dot-dashed curves (marked C_1 and $C_{3/2}$) represent solutions of large surface modulation that have no counterpart in the case without surface modulation (cf. Fig. 5.6). The fine black solid lines are hypothetical connections that shall serve as a guide to the eye. For details see main text.

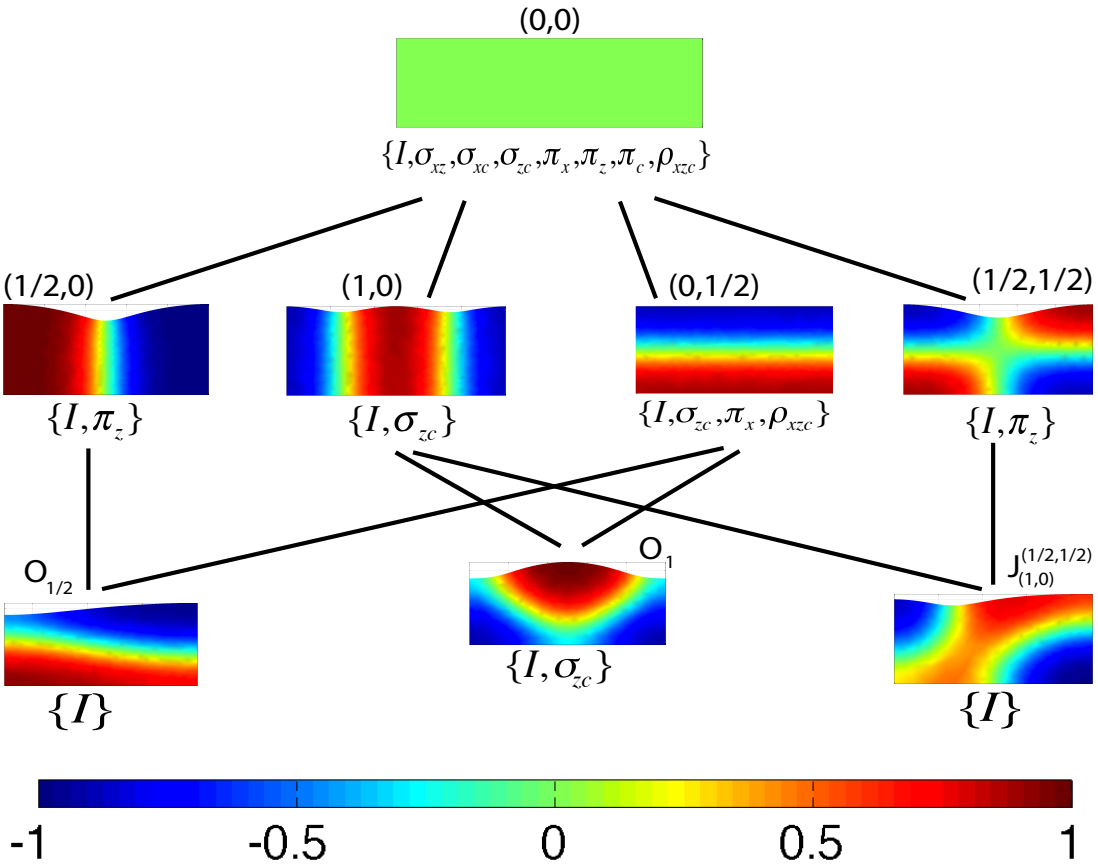

Figure 5.24: For the case of films of thickness $H = 5$ without energetic bias and with height modulations we show (i) typical steady concentration profiles on the various branches in the bifurcation diagram of Fig. 5.23, (ii) the corresponding symmetries (excluding translations, see main text) and (iii) the relations between the branches. The concentration profiles on the second row are on branches (from the left): $(1/2, 0)$, $(1, 0)$, $(0, 1/2)$ and $(1/2, 1/2)$ all for $L = 10$, whereas the ones on the third row are on branches (from the left) $O_{1/2}$ at $L = 7$, O_1 at $L = 10$, $J^{(1/2,1/2)}_{(1,0)}$ that joins $(1, 0)$ and $(1/2, 1/2)$ at $L = 9$. For remarks on symmetries and line styles see caption of Fig. 5.15.

films of unbiased modulated surface is given in Fig. 5.23. A selection of corresponding profiles, their symmetry groups and relations between them are given in Fig. 5.24. Inspecting Fig. 5.23(A) and (B), i.e., the bifurcation diagrams in terms of $||\delta c||$ and E, respectively, one notes that it is rather difficult to discern differences to the case of a flat surface (Fig. 5.6). All branches discussed for Fig. 5.6 are also present in Fig. 5.23 with slightly larger norm $||\delta c||$ and slightly lower energy. Now all these solutions have acquired a surface deflection that for the laterally structured solutions increases monotonically with L, but behaves non-monotonically for the various branches of oblique solutions [Fig. 5.23(C)]. The most important qualitative change is the appearance of solutions with large surface modulation that have no counterpart in the case of flat surfaces (neither without nor with surface deflection). In Fig. 5.23 they are marked by the green dot-dot-dashed lines, that we name C_1 and $C_{3/2}$. In terms of $||\delta c||$ and E they

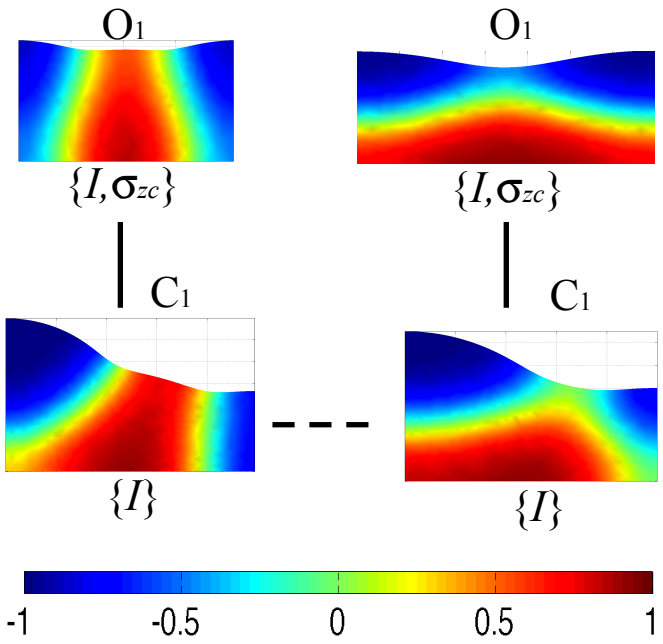

Figure 5.25: Shown are further profiles from the branch O_1 and also from the branch C_1 that bifurcates from O_1 shown in Fig. 5.23. The figure extends Fig. 5.24. Anti-clockwise, the profiles are on O_1 at $L = 8.2$, on C_1^a at $L = 9$ and $L = 9.5$, and back on O_1 at $L = 12$. For remarks on symmetries and line styles see caption of Fig. 5.15.

stay rather close to other already known branches (what makes their numerical detection rather cumbersome). However, they are strikingly different in terms of $||\delta h||$: The surface modulation strongly increases with L. For instance, one part of the C_1 branch emerges at about $L = 8$ from the O_1 branch, then continues till $L = 10$ where its surface modulation is more than three times stronger than that of the other branches. There is another part of the C_1 branch that emerges at about $L = 11.7$ also from the O_1 branch. It continues towards smaller L and also reaches at $L = 9$ a $||\delta h||$ about three times larger than that of the other branches. Both branching points on the O_1 branch are period doubling bifurcations related to the suppression of a coarsening mode of instability, and the two parts of the C_1 branch have the same symmetries.

A schematic is given in Fig. 5.25 where this time we also indicate the translational symmetries. These considerations allow us to deduce that the two parts of the C_1 branch are actually connected via two saddle node bifurcations. The resulting hypothetical branch that we are not able to get with our numerical method is indicated in Fig. 5.23 by a fine black line that may serve as a guide to the eye. We expect similar behaviour for the $C_{3/2}$ branch that bifurcates from the $O_{3/2}$ branch. It is also remarkable that the C_1 branch is locally the one of lowest energy, when comparing to the other branches involved in the transition [i.e., O_1, (0,1/2), (1,0)]. The agreement between the bifurcation points from the laterally homogeneous solutions and the predictions of the dispersion relation (not

shown) is good. However, note that there is some room for interpretation as to where exactly some of the bifurcations are in Fig. 5.23 as some of the branches approach each other rather slowly [e.g., O_1 and $(0, 1/2)$].

Note finally, that here as in the case of a flat surface, the absence of an energetic bias implies that most branches are actually two-fold or even four-fold with the different instances being related by the symmetry $c \to -c$ (see Section 5.3.1). In particular, the 'new' large surface modulation C_1 branch is two-fold. This degeneracy is lifted in the case with energetic bias at the free surface that we consider next.

5.3.4 Height-modulated Films With Energetic Bias

The fourth and final case we investigate, are modulated films with surface bias. Our focus lies on an explanation of the differences to the other cases for the selected film heights $H = 2.5$ and $H = 5.0$. In particular for $H = 5.0$, we restrict our attention to the relatively low energetic bias of $a^+ = 0.1$ because otherwise we are restricted by problems with the convergence of our numerical procedures. This is not the case for the smaller height of $H = 2.5$. There we discuss the case of $a^+ = 0.4$. For much larger energetic bias the surface tension contrast between the two components becomes unphysically large. Even before, at $a^+ = 1/2S$ configurations with three phase contact regions cease to exist.

Even for an imposed flat surface, the liquid-liquid interface is not any more perpendicular to the free surface if an energetic bias is considered. If the free surface is free to move, three curved interfaces meet in the three phase contact region. The angles θ_1 and θ_2 of the diffuse interface between the two fluids and the left and the right part of the free surface can be estimated in the sharp interface limit. They are given above in Eqs. (5.5) and (5.6). For $S = 1$ and $a^+ = 0.1$ one has approximately $\theta_1 = 1.91$ and $\theta_2 = 2.26$, values that well agree with the angles seen in Figs. 5.30 and 5.31, below. At $a^+ = 0.4$, $\theta_1 = 1.04$ and $\theta_2 = 2.76$ in agreement with Fig. 5.27 below.

Films of small thickness ($H = 2.5$) The bifurcation diagram for $H = 2.5$ for height-modulated films with an energetic bias of $a^+ = 0.4$ is given in Fig. 5.26. A selection of corresponding profiles, their symmetry groups and relations between them is given in Fig. 5.27. Dispersion relations for various a^+ can be found in Fig. 5.28. Compared to the other cases with $H = 2.5$, an energetic bias of $a^+ = 0.4$ leads to significant

changes in the film profiles. The horizontal dot-dashed line in Fig. 5.26 corresponds to the weakly stratified state (for a profile see first row of Fig. 5.27) that is unstable w.r.t. lateral perturbations for $L > L_{1/2} \approx 3.7$. This value results from the linear stability analysis: The dispersion relation for $a^+ = 0.4$ in Fig. 5.28 gives $k_c = 0.85$ implying the laterally structured $(1, 0)$ branch bifurcates at about $L_1 = 7.4$. However, a close inspec-

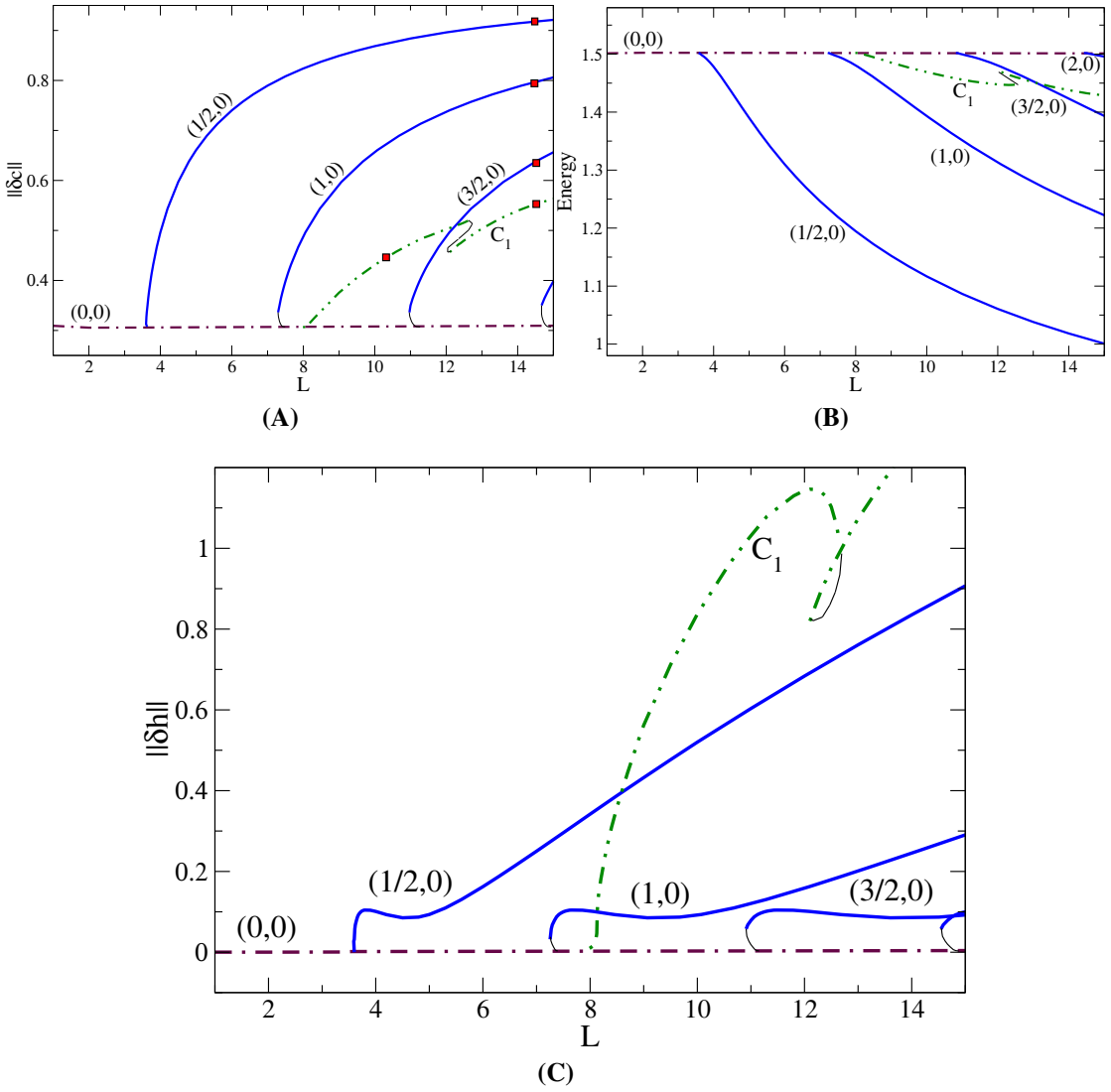

Figure 5.26: The bifurcation diagram for steady modulated films for energetic bias $a^+ = 0.4$ and $H = 2.5$ in dependence of the domain size L. Shown are (A) the norm $||\delta c||$, and (B) the norm $||\delta h||$. The dot-dashed horizontal line corresponds to the $(0, 0)$ branch, the solid lines are the laterally structured $(m, 0)$ branches, and the green dot-dot-dashed lines represent the C_1 branch of solutions with strong surface modulations. The fine black solid lines are hypothetical connections that are discussed in the main text.

tion of the laterally structured branches indicates that they end at an L slightly smaller than the respective L_c with an amplitude larger than zero. This indicates that the primary bifurcations are subcritical and a very short unstable branch is missing from our

bifurcation diagram. Note that the energetic bias shifts all primary bifurcations towards larger L, in good agreement to the dispersion relations (Fig. 5.28, cf. also Fig. 5.21). Remarkably, the surface deflection does not increase monotonically along the $(m, 0)$ branches. From the saddle-node bifurcation, it first increases rapidly, then goes slightly down again, before increasing nearly linearly (Fig. 5.26(B)). Examples for profiles on the laterally structured branches can be found on the second row of Fig. 5.27. Another

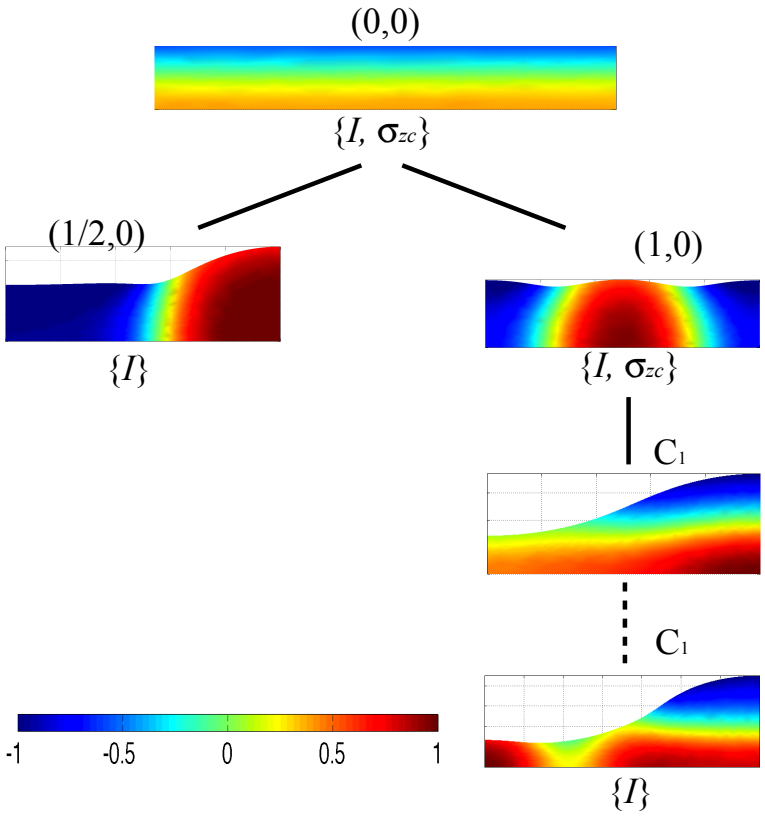

Figure 5.27: For the case of height modulated films of thickness $H = 2.5$ with energetic bias $a^+ = 0.4$ we show (i) typical steady concentration profiles from the $(0, 0)$, $(1/2, 0)$, $(1, 0)$ and C_1 branches in Fig. 5.26 (indicated there by small symbols), and (ii) the corresponding symmetries (excluding translations) and (iii) the relations between the branches. The concentration profiles for the $(1/2, 0)$ and $(1, 0)$ branch are at $L = 14$. For the branch C_1 they are at $L = 10$, and $L = 14$. For remarks on symmetries and line styles see caption of Fig. 5.15.

major difference is the appearance of a branch C_1 of solutions (green dot-dot-dashed lines in Fig. 5.26) with large surface modulation similar to the ones described for modulated films of medium height without bias (see Figs. 5.23 and 5.25). Here, however, they are not related to any oblique O_i branch as there exists none, but our hypothesis is that they are related to the 'oblique' solutions on the subcritical piece of the $(1, 0)$ branch that we could not obtain. Considering the symmetries of the solutions (Fig. 5.27) and the dispersion relation (Fig. 5.28) that only indicates one instability mode it seems

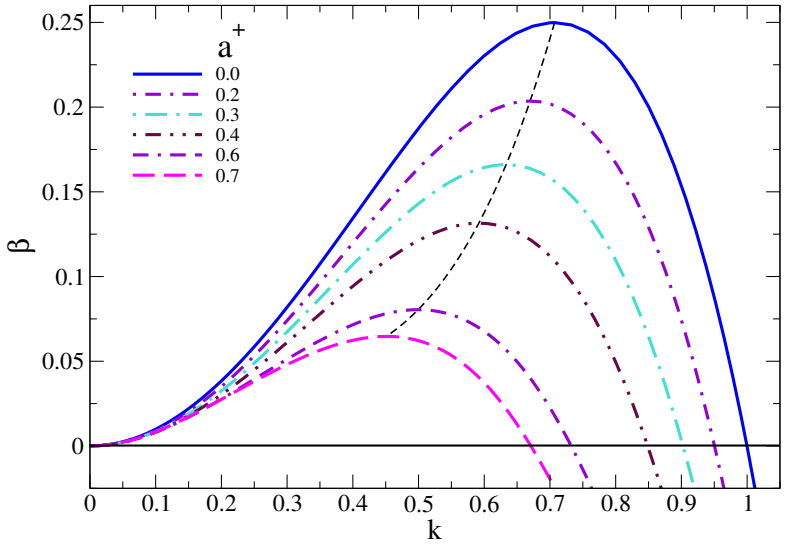

Figure 5.28: Linear stability for thin films ($H = 2.5$) with modulated free surface ($\alpha = 1$). The dispersion relation has taken at different energetic biases at the free surface for the homogeneous branching ($n = 0$) solution as a function of the wave-number k. Different energetic biases are considered as it has been shown in the legends as energetic biases result to positive surface tension, energetic biases result to non-logical surface tension where the behaviour of the dispersion relation becomes strange. The solid black (in colour) curve as a function of the wave-number k represents the local maxima of the growth rate $\beta_{\max}$ whereas the thin dashed light-green curve joining to it starts following the local minimum when the local maxima is no longer exist. The critical wave-number is not exist for higher energetic bias. The thin dashed line is parameterized by a^+ and follow the maxima $(k_{\max}, \beta_{\max})$ of the dispersion relations.

clear that the C_1 branch does not emerge from the 'weakly' modulated $(0,0)$ branch. Most probably it emerges from the laterally structured $(1,0)$ branch in a period doubling bifurcation close to the primary bifurcation. This particular feature is better visible for $H = 3.5$ shown bellow. We expect that the $(1,0)$ branch beyond this period doubling bifurcation is stable w.r.t. to coarsening. This is remarkable as it is an effect that only appears due to the possible modulation of the free surface, i.e., it is due to the coupling of two rather different degrees of freedom. However, at this point the effect remains hypothetical. Reduced models are needed to investigate it further. On the C_1 branch the surface modulation strongly increases with L. It seems to undergo two further saddle-node bifurcations at about $L = 12$ where we introduce a fine black line in Fig. 5.26 that indicates the hypothetic connection of the two parts of the C_1 branch that we have determined.

In Fig. 5.27 relations between the various branches are indicated as solid and dashed straight lines if they are symmetry-breaking pitchfork and not symmetry-breaking saddle-node bifurcations, respectively. As for simplicity we do not include translations in the given scheme, we need to add that in the pitchfork bifurcation between the $(0,0)$ and the $(1,0)$ branch it is actually the translational symmetry T^x_∞ that is broken. Note also that

all parts of the dot-dot-dashed C_1 branches are connected by saddle-node bifurcations implying that all profiles have the same symmetries.

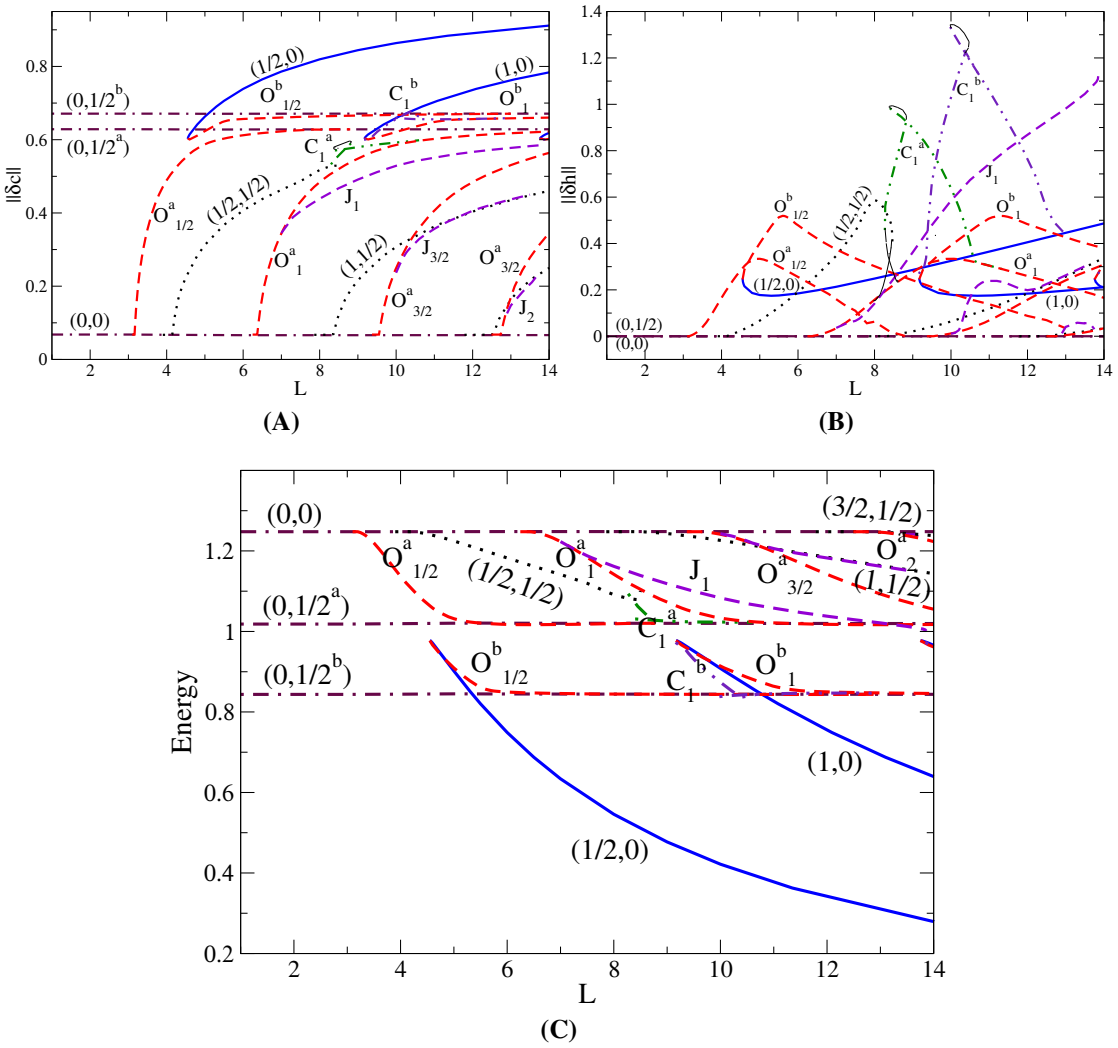

Figure 5.29: Bifurcation diagram for modulated film solutions with energetic bias $a^+ = 0.1$ for $H = 5.0$ as function of the domain size L. Shown are (A) the norm $||\delta c||$, and (B) the norm $||\delta h||$. The dot-dashed horizontal lines correspond to the laterally homogenous $(0, n)$-solutions for $n = 0$ (dash-dash-dot) and $n = 1/2$ (dash-dot); the blue solid lines are laterally structured $(m, 0)$-states for $m = 1/2, 1$; the black dotted lines are checker-board $(m, 1/2)$-states for $m = 1/2, 1$; the dashed lines correspond to various types of oblique solutions. Finally, the green and purple dot-dot-dashed curves (marked C_1^a and C_1^b) represent solutions of large surface modulation that do not exist for flat films (cf. Fig. 5.14). The fine black solid lines are hypothetical connections that are explained in the main text.

Films of medium thickness ($H = 5$) Finally, we increase the film height to $H > \pi$ where layered solutions become possible, a situation analysed for modulated films without bias in Section 5.3.3, and for flat films with bias in Section 5.3.2. We expect

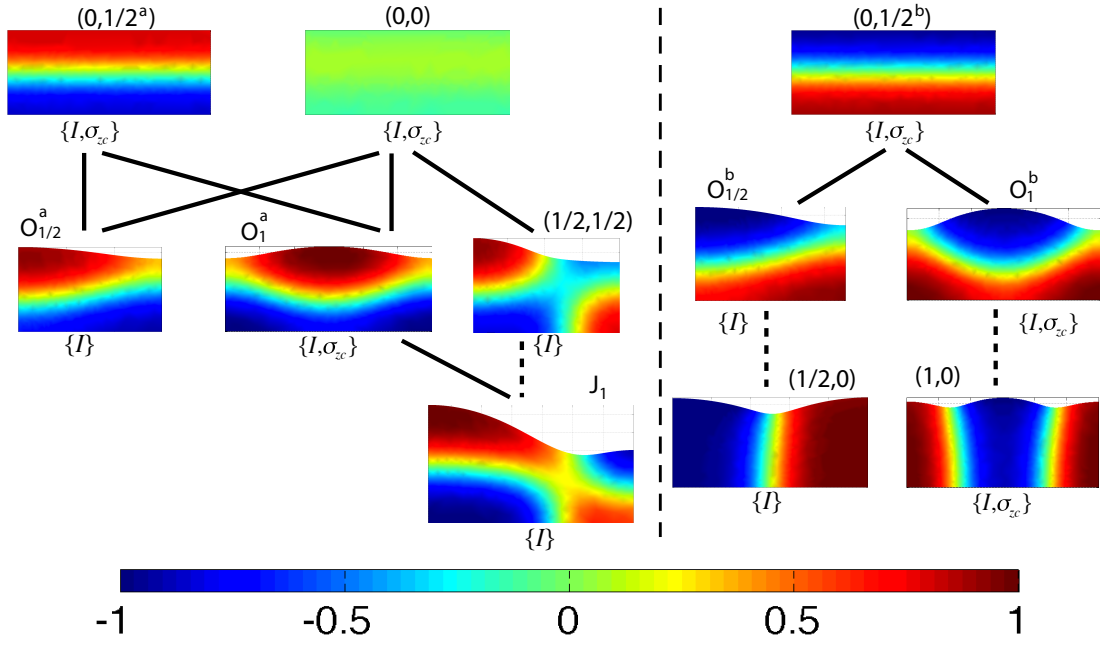

Figure 5.30: For the case of modulated films of thickness $H = 5.0$ with energetic bias $a^+ = 0.1$ we show (i) typical steady concentration profiles on the various branches in Fig. 5.23, (ii) the corresponding symmetries except translations (see main text) and (iii) the relations between the branches. The profiles left [right] of the vertical dashed line belong to the high [low] energy group of solutions. The C_1^i solutions are not included (see Fig. 5.31). The profiles from the $(0,0)$, $(0,1/2^a)$, $(0,1/2^b)$, $(1/2,0)$, and $(1,0)$ branches are for $L = 10$; the $O^a_{1/2}$ and $O^b_{1/2}$ profiles are for $L = 6$ and $L = 7$, respectively; the O^a_1 and O^b_1 profiles are for $L = 12$; the J_1 profile is for $L = 13.5$. For remarks on symmetries and line styles see caption of Fig. 5.15.

this final most 'complex' situation to reflect elements of both these previously studied cases.

The bifurcation diagram for $H = 5.0$ for height-modulated films with a small energetic bias of $a^+ = 0.1$ is given in Fig. 5.29, whereas a selection of corresponding profiles, their symmetry groups and relations between them are given in Figs. 5.30 and 5.31. For dispersion relations for the various stratified solutions we refer the reader to Appendix B.

A first inspection of Fig. 5.29(A), i.e., the bifurcation diagram in terms of $||\delta c||$ shows that much of the basic structure is very similar to Fig. 5.14, i.e., a similar case with a flat free surface. All layered $[(0,0),(0,1/2^a),(0,1/2^b)]$, laterally structured $[(m,0)]$, and oblique $[O^a_m, O^b_m]$ branches behave qualitatively similar. A quantitative comparison is not possible as Fig. 5.29 is for $a^+ = 0.1$ while Fig. 5.14 is for $a^+ = 0.2$. In the case of modulated free surface for $a^+ = 0.2$ we are not able to obtain all parts of all the branches presented in Fig. 5.29 due to numerical convergence problems. However, from the partial results we have, one deduces that in the case with surface modulation,

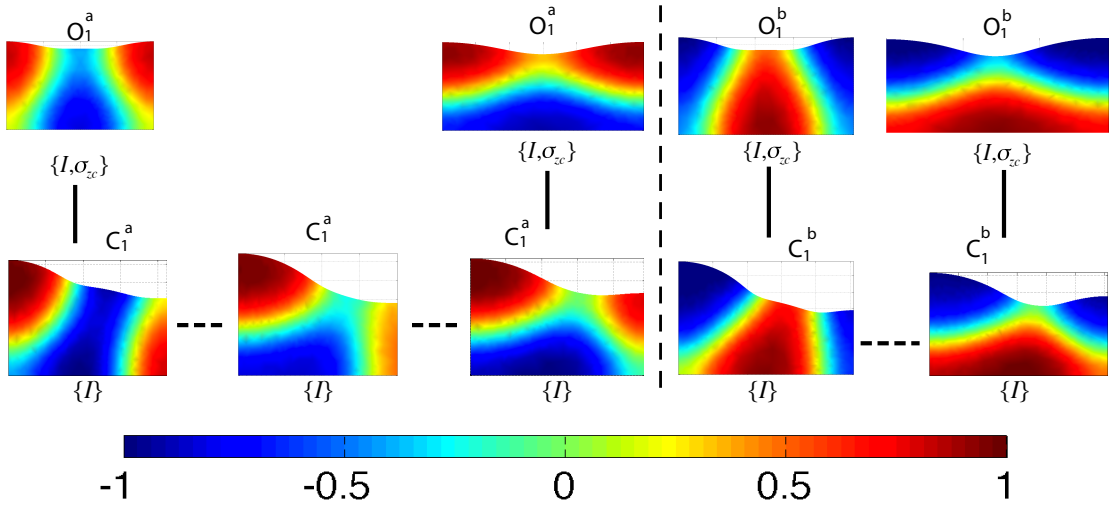

Figure 5.31: Shown are profiles from the large surface modulation branches C_1^a and C_1^b that bifurcate from O_1^a and O_1^b, respectively (cf. Fig. 5.29). Left of the vertical dashed line we show anticlockwise from top left profiles from O_1^a at $L = 8$, C_1^a at $L = 8.4$ (left half of branch), $L = 8.4$ (right half of branch) and 9.7 and from O_1^a at $L = 12$. Right of the vertical line we show anticlockwise from the top left profiles from O_1^b at $L = 9.1$, C_1^b at $L = 9.7$ and 11. and finally O_1^b at $L = 14.5$. The middle profile In the second row on the left hand side is from a point close to the saddle node bifurcation and illustrates the transition between the two neighbouring profiles. For remarks on symmetries and line styles see caption of Fig. 5.15.

secondary bifurcations are shifted to slightly larger L, the norms [energies] of all these branches are slightly higher [lower] than in the case of a flat surface, in accordance to previous observations. All solutions have acquired a surface deflection [Fig. 5.29(B)]. For the laterally structured solutions $(m, 0)$ it increases monotonically after a small decrease near the saddle-node bifurcation where the $(m, 0)$ branches emerge together with the O_m^b branches. However, most other branches behave non-monotonically.

Comparing with the case of a modulated film without bias [Fig. 5.23], one notices that again there are solutions with large surface modulation present that do not exist for flat surfaces. In Fig. 5.29 they are marked by the green and purple dot-dot-dashed lines. There are two sets of them that we name C_1^a (green) and C_1^b (purple). Both result through the breaking of the $c \to -c$ symmetry from the (two-fold) C_1 branch in the case without energetic bias [cf. Fig. 5.23]. As before, they stay rather close to other already known branches in terms of $||\delta c||$ and E. Their surface modulation strongly increases in a small range of L. The C_1^b reaches the largest amplitudes. The various pieces of the C_1^a and C_1^b branches emerge from the O_1^a and O_1^b branches, respectively. All related branching points on the O_1^i branches ($i = a, b$) are period doubling bifurcations related to the suppression of a coarsening mode of instability. The two respective parts of the two C_1^i branches ($i = a, b$) have the same symmetries, as schematically shown in Fig. 5.31. Again we deduce that the pieces of the C_1^i branches are actually connected via two

saddle node bifurcations. The resulting hypothetical branch is indicated in Fig. 5.29 by a fine black line.

Another important qualitative change is related to the checkerboard solutions [see $(1/2, 1/2)$ branch]. Without energetic bias [Fig. 5.23] they continue to large L. However, we know already from the case of flat films that an energetic bias results in a re-connection with some of the J branches (see Section 5.3.2). The effect is visible more clearly here: The $(1/2, 1/2)$ branch emerges at about $L = 4.2$ from the weakly stratified branch. Then its surface deflection increases until $L \approx 8$ where it starts to decrease quickly, it passes a saddle-node and joins the O_1^a branch at slightly lower L. We have not been able to obtain the small subcritical part of the branch numerically and indicate its hypothetical path by a fine black line in Fig. 5.29. Increasing the energetic bias makes the behaviour more pronounced and shifts the subcritical bifurcation of the checkerboard to the oblique branch towards larger L.

Note finally, that in Fig. 5.30 some of the solutions seem to have the same symmetries although they are connected by a symmetry-breaking pitchfork bifurcation. This results from the exclusion of translational symmetries from our schemes. In particular, the transitions from the $(0, 0)$ to the O_1^a branch, and from the $(0, 1/2^b)$ to the O_1^b branch, both break the translational symmetry T_∞^x.

With this we end the presentation of our results for the four selected cases, i.e., flat and modulated films with and without energetic bias at the free surface. The next section concludes, situates our results in the wider context and gives an outlook onto future work.

Medium films with relatively large bias. In the previous examples where films of thickness $H = 5$ with modulated surface have been investigated, the case where a^+ is higher than the saddle node bifurcation a_{sn}^+ has not been mentioned. This is because of a convergence problem encountered for films of thickness $H = 5$. Instead, we introduce films of medium thickness $H = 3.5$ with energetic bias $a^+ = 0.2$ where solutions are well converged. For such film thickness this energetic bias is located beyond the saddle node bifurcation (see the points a_{sn}^+ in Fig. 5.1, and Fig. 5.2 for $H = 3.5$). This enables us to study the behaviour of the medium films behind the saddle node bifurcation. As in the flat film case, the weakly stratified branch (0,0) and the stratified branch $(0,1/2^a)$ merge at the saddle node bifurcation. However, beyond a_{sn}^+ the checkerboard and oblique solutions O_i^a do not exist any more and the only remaining solutions are

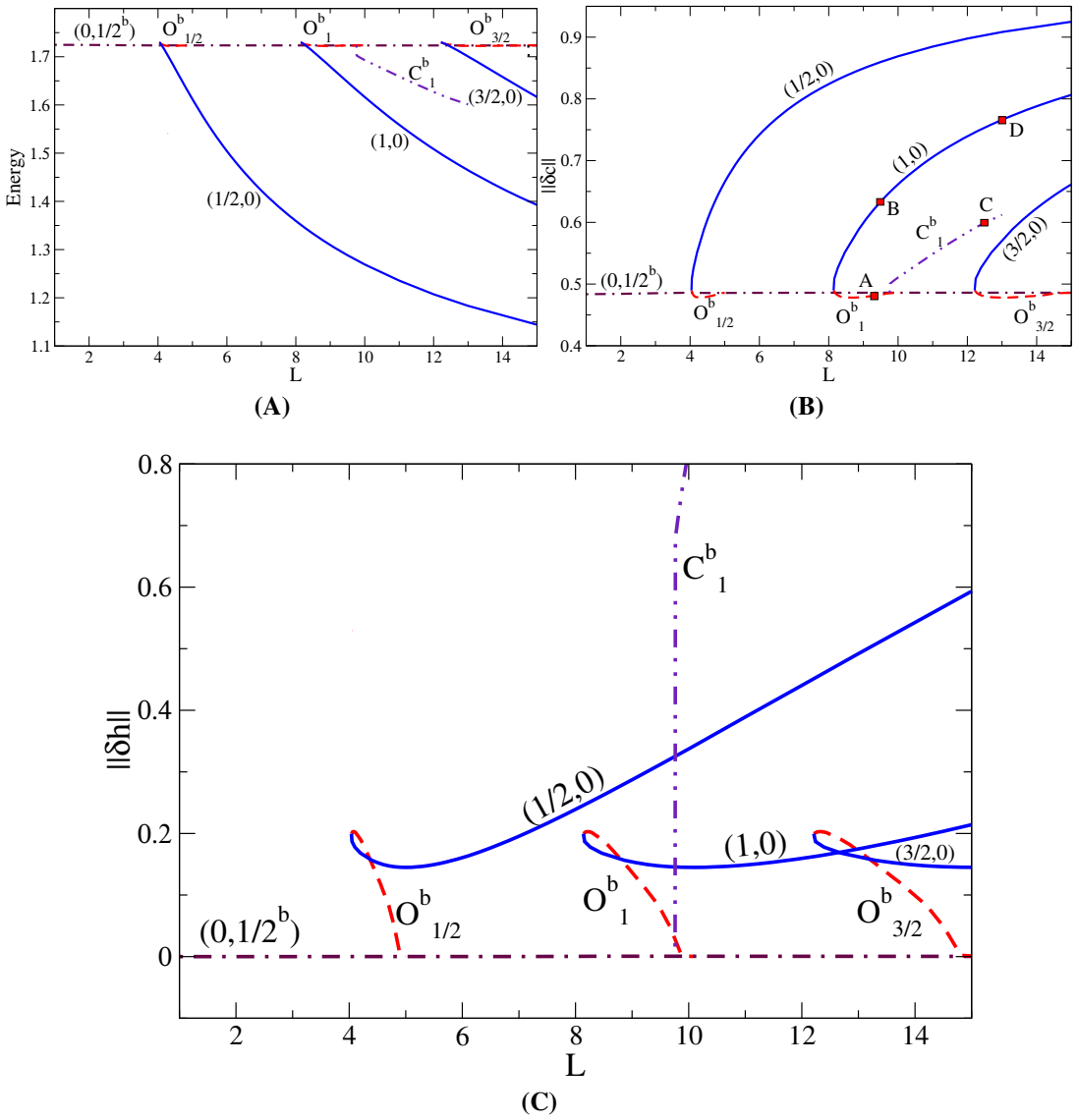

Figure 5.32: Bifurcation diagrams for steady state solutions representing the energy, L_2-norm of the concentration field, and the L_2-norm of the surface deflection as functions of the lateral domain size L, for modulated free surface film of thickness $H = 3.5$, and energetic bias $a^+ = 0.2$.. The (Maroon-dashed-dotted) solution represents the stratified layered solution (0,$1/2^b$). The (Red-dashed) curves represent the oblique $O_i^b, i = 1, 2, 3$, solutions that join to the stratified solution indicated by (0,$1/2^b$). The (Indigo double-dotted dashed) curves represent the very high surface deflection branches. The (Blue-solid) curves represent the lateral layered solutions.

the set of branches that are energetically lower, i.e., the stratified (0,$1/2^b$), O_i^b, and laterally structured branches. The horizontal dotted-dashed branch in Fig. 5.32 represents the (0,$1/2^b$) branch. As in all the previous cases, the L_2-norm of surface modulations is identical to zero. The oblique solutions O_i^b, that bifurcates from (0,$1/2^b$) joins the laterally structured branches $(m_i, 0)$ at a saddle node bifurcation. The branch C_1^b bifurcates from the oblique branch at the point where the reflection symmetry σ_{zc} and the translation T_L^x are broken. The behaviour of the L_2-norm of surface modulation is

quit similar to the corresponding branches for films of thickness $H = 5$. Results of the

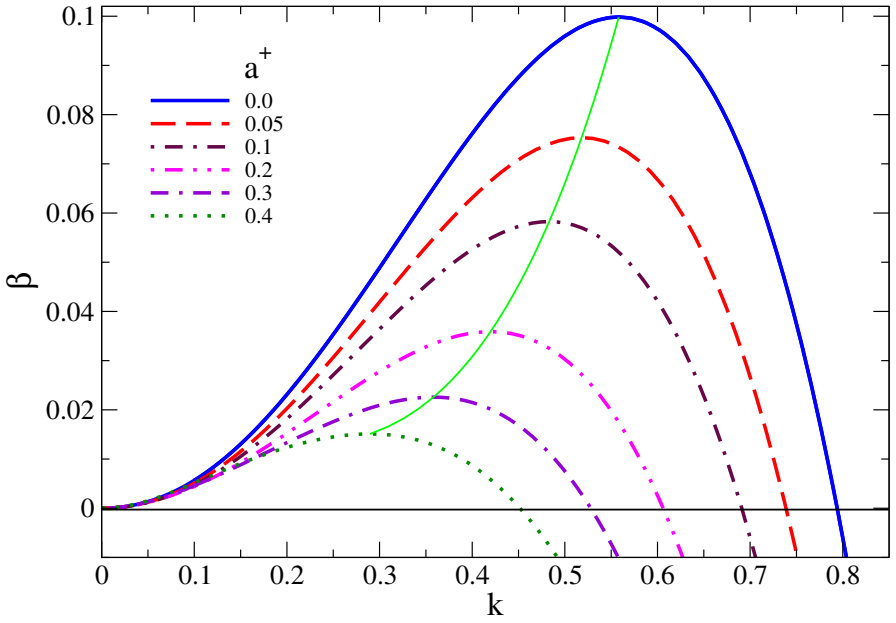

Figure 5.33: Linear stability for films with flexible deformable free surface of medium thickness $H = 3.5$, at different energetic biases as it is shown in the legends. The stratified n=$1/2^b$ branch is considered. The solid curve (green in colour) represents the local maxima of the growth rate as a function of the wavenumber k.

linear stability analysis are depicted in Fig. 5.33. They show the stability for different energetic biases for the branch (0,$1/2^b$). For $a^+ = 0.2$, the value of k_c is about 0.61 which indicates that the bifurcation point of the branch O_1^b from the branch (0, $1/2^b$) is at about $L_c = 10.36$ which means the oblique solutions convergence slowly to the stratified film near the bifurcation point (see Fig. 5.32). For further dispersion relations for this film we refer to Appendix B. Panel (C) of Fig. 5.32 shows complex perturbations at the free surface in the neighbourhood of the saddle nodes where the oblique and the laterally structured branches join. In panel (A) of Fig. 5.35 we show the critical wave number k_c and the k_{max} corresponding to the maximal growth rate β_{max} that is shown in panel (B) for the weakly stratified branches $(0, 0)$ and the stratified branches $(0, 1/2^a)$ and $(0, 1/2^b)$. In Fig. 5.34 we show film profiles at the points marked on the branches in Fig. 5.32(B). The L_2-norm of surface modulation for the branch C_1^b increases rapidly. This branch must ultimately connect to another branch. Unfortunately, the surface modulation is very high and the initial solution is difficult to find. In fact, we do not know how this branch behaves after that point. From our point of view, the translation symmetry which has been broken must be recovered in some way and the branch has to join another branch which has that translation symmetry.

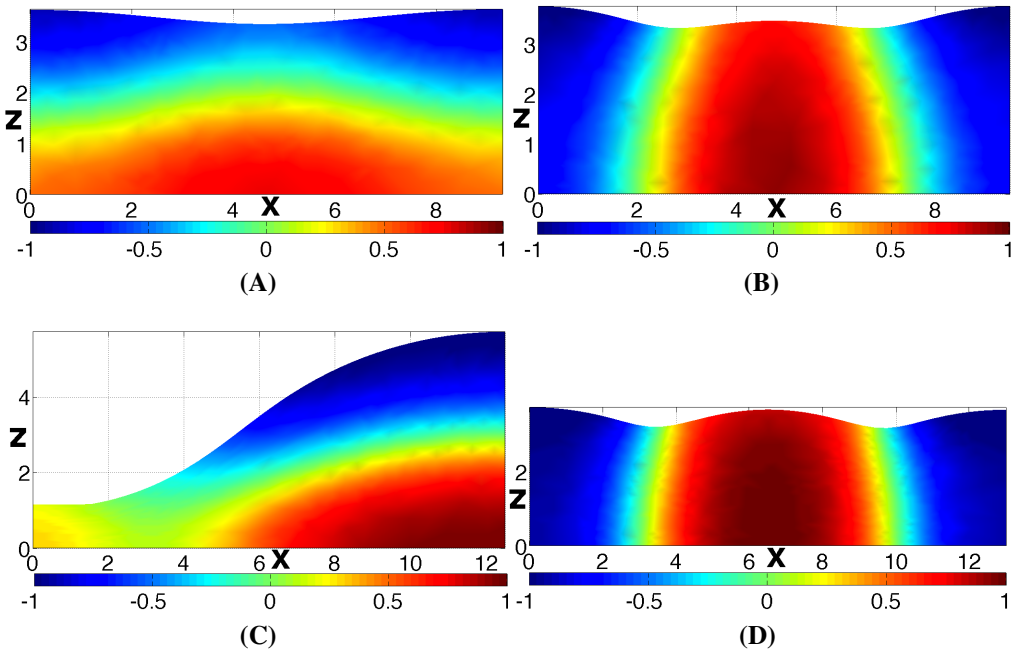

Figure 5.34: Film and concentration profiles for film of medium thickness H=3.5, with energetic bias $a^+ = 0.2$ at the free surface. According to the the small squared marked in the bifurcation diagram for the concentration field Fig. 5.32(B). Panel (A) represents the profile at the point A. Panel (B) represents the profile at the point B on the branch (1,0). Panel (C) represents the profile at the point C on the C_1 branch. Panel (D) represents the profile at the point D on the branch (1,0).

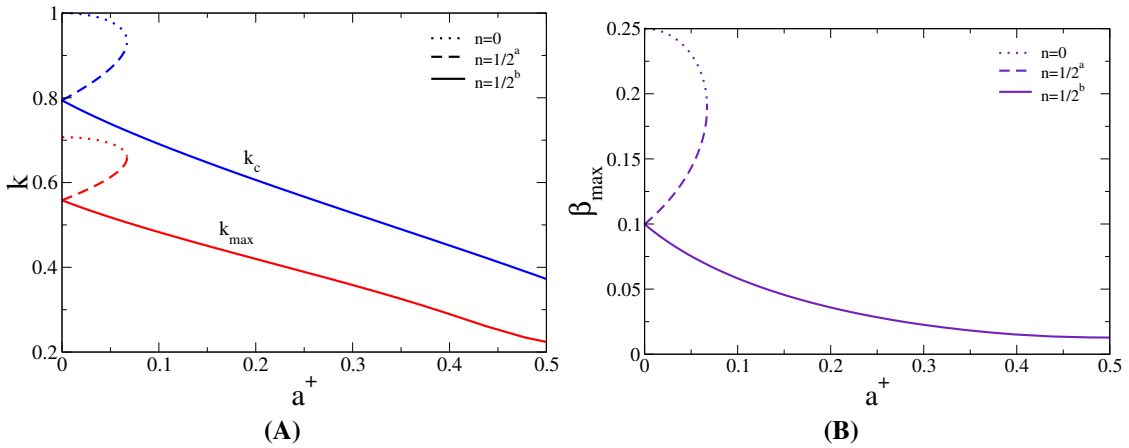

Figure 5.35: Shown in panel (A) are k_c and k_{max}, and panel (B) shows β_{max}. All are for flexible film of mean height $H = 3.5$ and for the branches that shown by the legends, and as functions of the energetic bias a^+.

5.4 Summary

In this chapter, we have investigated in parallel the linear stability of the stratified films, the bifurcation diagrams, and relations between the bifurcations and symmetry groups. First we have introduced results in 1d for three different film thicknesses. More such results have been given by the authors of [87]. We have used these results as a guide line of our study in 2d system. Studying the steady state in two dimensions has involved investigations of the bifurcation diagrams of the energy and the L_2-norm(s) of concentration and surface deformation for the modulated surface case. The symmetry groups and their relation with the bifurcations are also included in the study. Furthermore, stability investigations have been involved using the full time dependent model-H. This has been used to study the linear stability of the system and to determine the bifurcation points of the branches that bifurcate from the (0,0) branches and the stratified branches (0,1/2). Films with flat surface and others with free surface modulations are introduced. In the flat film case, the surface is imposed to be flat by introducing a very high surface tension at the free surface. This has been avoided in the films with height fluctuations. In the flat film case we have been able to introduce relatively high energetic biases. Results for two different film thicknesses have been introduced with their linear stability results for the particular branches (0,0) and (0,1/2), as well as their symmetry groups. Thereafter, attention focused on the case with surface modulations. In this part, the results have included also the bifurcation diagrams for surface modulations $||\delta h||$. The energetic bias for this case has been kept small to avoid convergence difficulties. Another film thickness ($H = 3.5$) has been introduced to study the case where the saddle node bifurcation $a^+_{\rm sn}$ is exceeded ($a^+ > a^+_{\rm sn}$). The results have shown an interesting behaviour for the flat films and films with surface modulations. Further studies of the dispersion relation is included in Appendix B. In the next chapter we introduce our analysis of the bifurcations in the case of off-critical mixtures.

Chapter 6

Non-linear Analysis for Off-critical Mixture

6.1 Introduction

In the previous chapter we have presented results for a critical mixture ($\bar{c} = 0$) considering flat and surface modulated films. In systems studied experimentally, the binary mixture is more likely to consist of an off-critical mixture ($\bar{c} \neq 0$) [96]. In this chapter we introduce results for the case $c \neq 0$ in the form of bifurcation diagrams for L_2-norms of concentration, surface deflection, and the free energy when varying the mean concentration $\bar{c}$ whereas the lateral domain size, mean film thickness, and energetic bias are kept fixed. Neutral and biased free surfaces are considered. As in the critical case the substrate is assumed to be energetically neutral. For the off-critical case we considered only the bifurcations for $\bar{c} \neq 0$. Here however, the energetic bias breaks the symmetry ($c \to -c$) of the bifurcation diagrams. Therefore, we investigate solution for $\bar{c} > 0$ and for $\bar{c} < 0$.

If a branch passes through the concentration $\bar{c} = 0$ of the critical case then we call it by the name introduced in the critical case but we do not give specific names to those branches that do not exist in the critical case. Here we do consider the case of an imposed flat surface and consider only films that are free to modulate their surface ($\alpha = 1$). For the thin film case ($H < \pi$) when there is no vertical layering inside the film, we study films of thickness $H = 3$. However, for the off-critical films of medium thickness we study films of thickness $H = 5$ where one may observe more structuring types.

In the first part of this chapter, we introduce the bifurcation diagrams for neutral films of thickness $H = 3$ and $H = 5$ and in the second part we investigate the bifurcation diagrams for the same film heights for small energetic bias at their free surface. In fact, this part involves a large number of branches and we will restrict our study to the limited number of branches that also exists in the critical case or is closely related.

6.2 Neutral Thin Films of Thickness $H = 3$

We analyse first the solutions for a film of thickness $H < \pi$ with neutral surfaces, where no layered film state exists for $c = 0$ [57]. We choose $H = 3$ as a representative value of this range of parameters. As for the lateral domain size, we choose $L = 10$ to allow for lateral structures of modes $m = 1/2$ and $m = 1$. Therefore, only the following three branches do exist: the homogeneous branch (0,0), and the laterally structured branches $(1/2, 0)$ and $(1, 0)$. Now we proceed to discuss each of these branches. The bifurcation diagrams are given in Fig. 6.1.

In the critical case the branch $(1/2, 0)$ corresponds to a vertically homogeneous state with a composition field with period $2L$ in the lateral direction. The L_2-norm of surface deflection starts with $||\delta h|| \approx 0.32$ at critical composition, increases with mean concentration to reach an absolute maximum at $\bar{c} \approx 0.7$, then it decreases and the branch turns back at a saddle-node at $\bar{c} \approx 0.723$, beyond the spinodal limit at $\bar{c} = 1/\sqrt{3}$ but far below the binodal for infinite systems at $\bar{c} = 1$. One may see the location of this saddle-node as the binodal of the studied finite system. The lower part of the branch bifurcates subcritically from the homogeneous branch (0,0) at about $\bar{c} = 0.548$. This result can be obtained also from the analysis of the linear stability of this film see Eq. (4.63). Initially, we call this branch the weakly laterally structured branch. Notice the closeness of the critical value to the spinodal boundary at $\bar{c} = 1/\sqrt{3}$. Fig. 6.2 illustrates the transformations that the states on the branch $(1/2, 0)$ undergo as we follow the branch from a state with strong surface deflection and lateral composition gradients in the middle of the film at $\bar{c} = 0$ up to a perfectly flat and homogeneous base state as this branch connects with $(0, 0)$. Notice that this transition happens with the point of least height of the film moving always in the same direction (leftwards in the panels), and reaching the lowest value at the saddle node (point c in Fig. 6.1(A)).

The states of this branch change qualitatively when the saddle node at $\bar{c} \approx 0.723$ is passed, beyond this point $||\delta c||$ decreases rapidly as regions of a single phase disappear

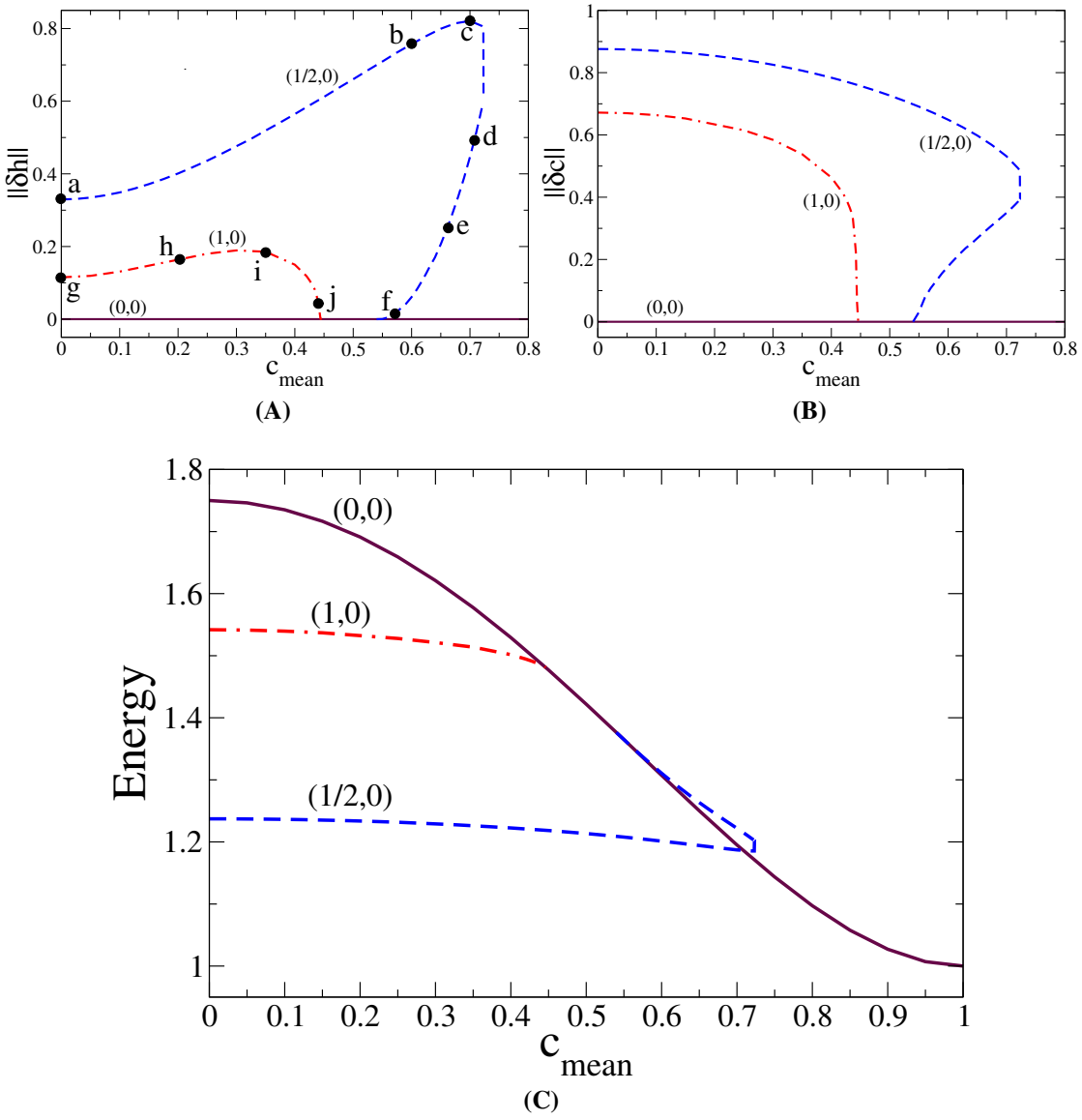

Figure 6.1: Shown are, panel (A) L_2-norm for surface deflection, panel (B) L_2-norm for the concentration field, and panel (C) the energy for the branches $(0,0)$, the brown solid curve; $(1/2,0)$ branch, the blue dashed curve; and (1,0) branch, the red dotted dashed curve; as functions of the mean concentration $\bar{c}$. The lateral domain size is fixed at $L = 10$ and the film thickness fixed at $H = 3$. The film surface is assumed neutral ($a^+ = 0$).

as we follow the branch (more notorious in the disappearance of the dark blue regions of Figs. 6.1(D), (E) and (F)), preparing a continues transition to the homogeneous base state. Overall the norm of the concentration ($||\delta c||$) declines from $||\delta c|| \approx 0.88$ at the critical composition to $||\delta c|| \approx 0.45$ at the saddle node bifurcation, and then as we follow the branch it decreases up to merging to the homogeneous state $(0,0)$ with $||\delta c|| = 0$ at $\bar{c} = 0.548$. This is a qualitatively different behaviour than found for the norm of surface modulations that changes non-monotonically.

As has been discussed in the previous chapter, the branch $(1,0)$ corresponds to vertically homogeneous states with period L along the lateral direction. This state does only exist within the spinodal region. Its L_2-norm reaches a maximum at $||\delta h|| \approx 0.18$, and then decays monotonically, merging with the branch (0,0) at $\bar{c} = 0.449$ in a supercritical pitchfork bifurcation (see section 4.6). A sequence of selected profiles (black dots in Fig. 6.1(A)) for this state is shown in Fig. 6.3. The maximum of the L_2-norm of surface deflection corresponds to local minima of the thickness of the film. As for the concentration norm, at $\bar{c} = 0$ the norm $||\delta c|| \approx 0.67$ is maximal, and then declines monotonically as the mean concentration increases to join the $(0,0)$ branch. The decrease of $||\delta c||$ for the $(1/2,0)$ and $(1,0)$ branches is consistent with the interface widening that occurs as we approach the single phase region of the phase diagram of binary mixtures.

Notice that the local minimum in the thickness of the film corresponds to the position of the three phase contact line. Greater deflections of the free surface are possible for the branch $(1/2,0)$ with only a single contact line than for the branch $(1,0)$ with a depression of the surface at each of the two contact lines. This leads to the higher $||\delta h||$ for the $(1/2,0)$ branch with respect to the $(1,0)$ branch. If we now consider that the largest variations of composition are at the diffuse interfaces a similar reasoning explains why $||\delta c||$ for the $(1/2,0)$ is higher than for the $(1,0)$ branch.

Finally, Fig. 6.4(A) and (B) show the dependence of the L_2-norms as a function of the lateral extension of the film for various values of the mean concentration. For small $\bar{c}$, the primary bifurcation is supercritical and then at some value $\bar{c}^*$ the bifurcation changes its character and becomes subcritical. Here the state with lower $||\delta h||$ and $||\delta c||$ is the one with wider diffuse interface, as discussed above. For higher $\bar{c}$, there is a region between the saddle-node bifurcation at L^* and critical length L_c where two branches exist. Note that L_c increases monotonically with $\bar{c}_c$ and goes to infinity at the spinodal line.

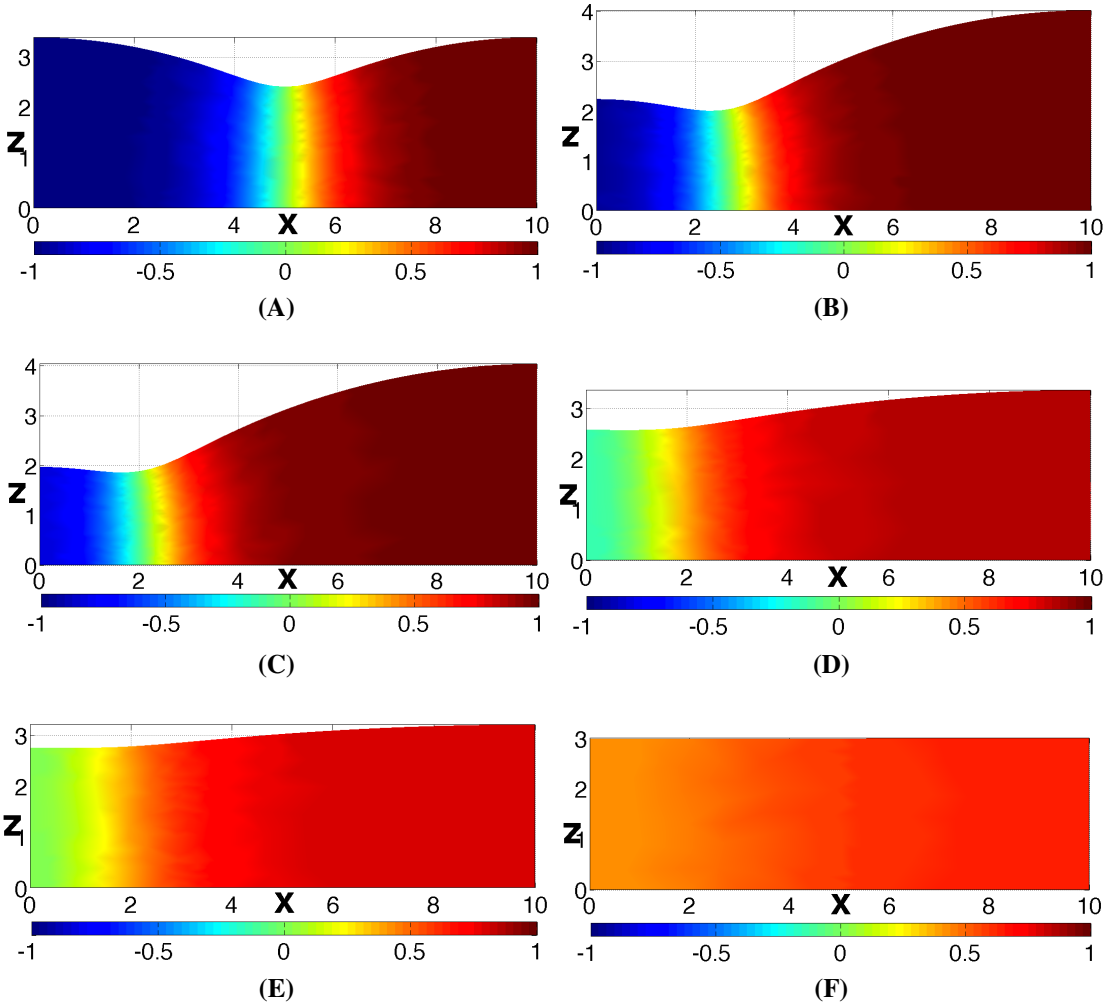

Figure 6.2: Shown are the film and concentration profiles for the branch $(1/2, 0)$ at the corresponding points in Fig. 6.1(A). Panels A,B,C,D,E and F correspond to the labels a,b,c,d,e and f, respectively.

If one only considers systems of lateral domain size $L = 10$, the change from the supercritical to the subcritical transition discussed above is not seen for the film $(1, 0)$. However, it appears for larger lateral domain size (see Fig. 6.5). One may refer to the dispersion relation in Fig. 4.3 to compare the bifurcation points for particular values of the lateral domain size L, film thickness H and the critical mean concentration $\bar{c}_c$.

The branch $(1, 0)$ only exists within the spinodal region and for lateral domain sizes beyond $L = 2\pi$, as shown in Fig. 6.5. It is always supercritical for the range of L explored, and its L_2-norm of concentration field decreases, for fixed L, when approaching the spinodal. The branch joins the homogeneous branch in a pitchfork bifurcation at $\bar{c} = 0.449$. This result is supported by analysing the linear stability of the homogeneous film (see Eq. (4.63)). The L_2-norm of the surface deflection only increases with $\bar{c}$ for

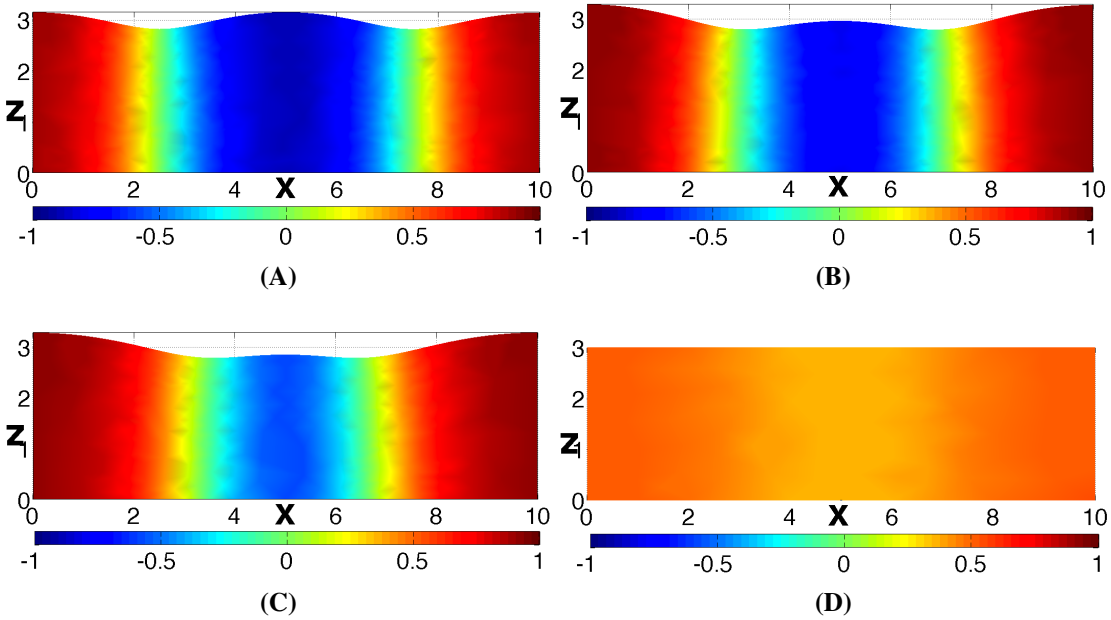

Figure 6.3: Shown are the film and concentration profiles for the branch $(1,0)$ taken at the points in Fig. 6.1(A). Panel (A) corresponds to the label (g), panel (B) corresponds to the label (h), panel (C) corresponds to the label (i) and panel (D) corresponds to the label (j).

lateral domain sizes large enough, where the system has more freedom to deform the interface in the contact region.

The energy per unit of length of the three branches is compared in Fig. 6.1(C). The homogeneous branch $(0,0)$ has neither deflection nor composition variation and the associated L_2-norms are zero for all mean concentrations (Fig. 6.1(A) and (B)). However, this branch has a larger energy than the $(1/2,0)$, $(1,0)$ branches and therefore is energetically unfavourable. This is due to the fact that inside of the binodal line, for a given mean concentration, the homogeneous state has greater free energy than the phase separated states. The smaller energy of the $(1/2,0)$, $(1,0)$ branches shows that the decrease of the total free energy by phase separation is larger than the cost of producing a deformed free surface. The energy per unit length of the branch $(0,0)$ is maximal at $\bar{c}=0$ and decreases monotonically with $\bar{c}$ reaching its minimum at the binodal line (Fig. 6.1(C)). This monotonous decrease accounts for the lower energetic cost to mix two species when the relative amount of one of them diminishes. The main contribution to the difference of energy between $(1/2,0)$ and $(1,0)$ branches comes from their different number of internal diffusive interfaces, and therefore from the energetic cost required to build them.

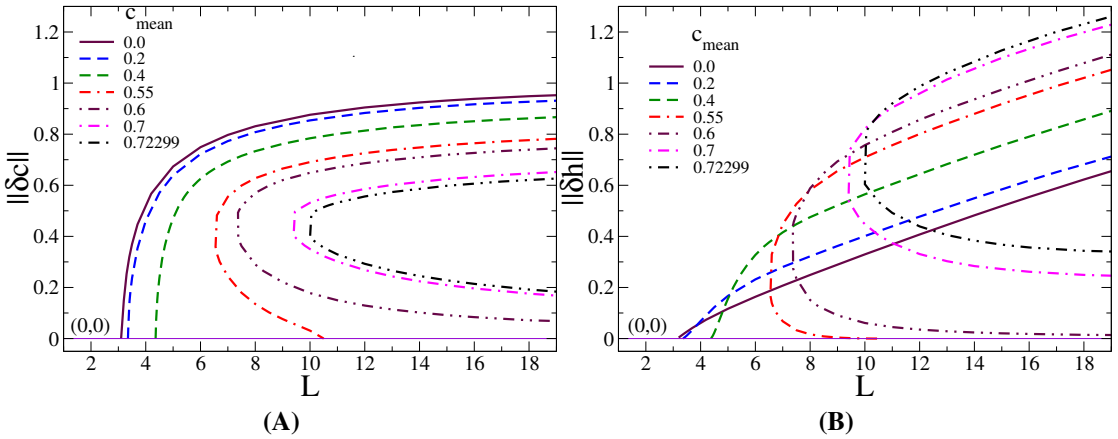

Figure 6.4: For the laterally structured film $(1/2, 0)$ of thickness $H = 3$, shown are panel (A), the L_2-norm of concentration field, and panel (B), the L_2-norm of surface modulations, as functions of lateral domain size L. Different average concentrations are considered (see legends). The film surface is assumed neutral ($a^+ = 0$).

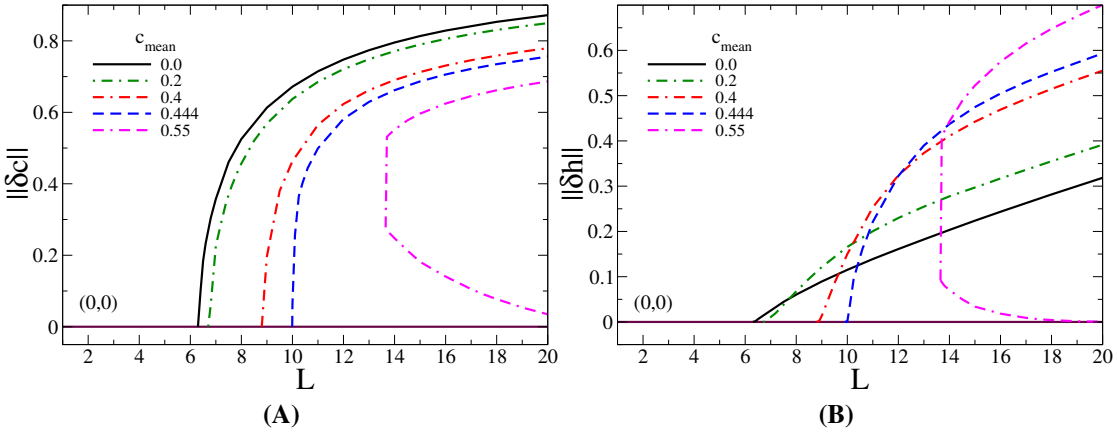

Figure 6.5: For the laterally structured film $(1, 0)$ of thickness $H = 3$, shown are panel (A), the L_2-norm of concentration field, and panel (B), the L_2-norm of surface modulations, as functions of lateral domain size L. Different average concentrations are considered (see the legends). The film surface is assumed neutral ($a^+ = 0$).

6.3 Neutral Thin Films of Thickness $H = 5$

For $H > \pi$, layered solutions fit inside a flat film with critical composition (see Fig. 4.2) and are laterally invariant solutions in addition to the homogeneous film. In particular, for $\pi \leq H = 5 < 2\,\pi$ the possible layered states have mode number $n = 1/2$, which corresponds to configurations with two layers.

6.3.1 Layered Films Solutions

Layered stratified solutions $(0, 1/2)$ are characterised by flat surfaces, i.e., zero $||\delta h||$. This is due to the diffuse interface of the polymers being entirely inside of the bulk of the film. There exists no contact line and therefore no deflection of the free surface.

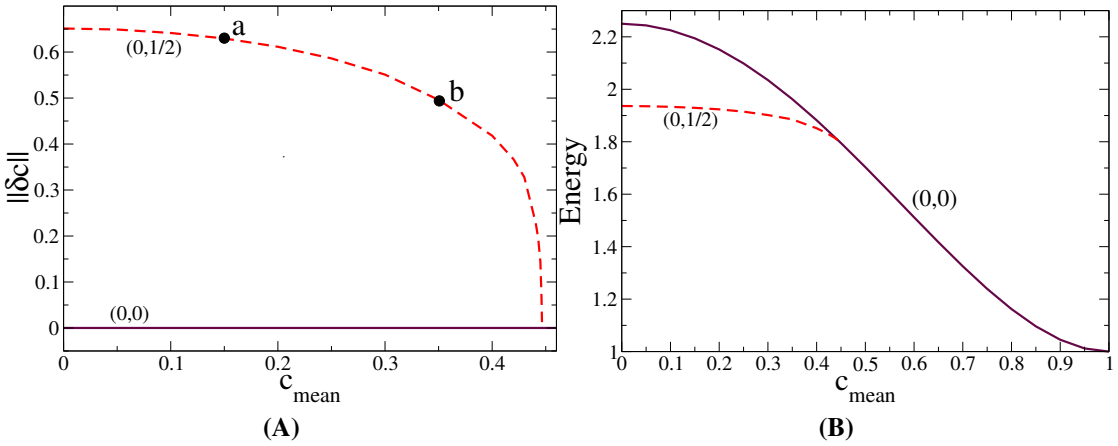

Figure 6.6: Shown are, panel (A) the L_2-norm for the concentration field, and panel (B) the energy, for the branches, $(0, 0)$ which depicted by brown-solid curve and the stratified $(0, 1/2)$ depicted by the red-dashed curve, as functions of the mean concentration $\bar{c}$. The film surface is assumed neutral ($a^+ = 0$). The film thickness is given by $H = 5$, and the lateral domain size is fixed at $L = 10$.

As shown in Fig. 6.6(A), the branch $(0, 1/2)$ exists only within the spinodal region, its concentration L_2-norm is maximal at critical composition, and decreases monotonically with the average composition up to $\bar{c} = 0.449$, where it merges through a pitchfork bifurcation with the homogenous solution. This can be obtained from linear stability analysis for the off-critical case (see Eq. (4.63) by substituting $m = 0, n = 1/2, H = 5, L = 10$). It is interesting to observe that the energy of this branch is lower than that of the homogeneous state (c.f. Fig. 6.6(B)), showing that the energetic cost to produce the horizontal diffuse interface is not as large as the energy gained by separating the two components.

As the average concentration $\bar{c}$ increases, the position of the diffuse interface shifts towards the substrate (as in Fig. 6.7) or towards the free surface, decreasing the maximal vertical gradient in composition once $\bar{c}$ is close enough to the value at the bifurcation, leading in such a way to a continuous transition towards the homogeneous state.

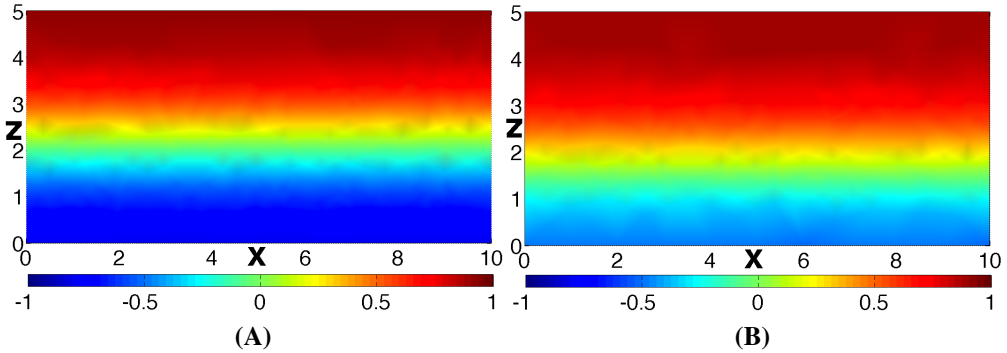

Figure 6.7: Shown are film and concentration profiles at the points depicted in Fig. 6.6(A). Panel (A) is the profile at label (a), and panel (B) is the profile at label (b).

6.3.2 Checkerboard Like Films

We now proceed to study states arising from the combination of laterally structured and vertical modes. For $H = 5$ and $L = 10$ the checkerboard states $(1/2, 1/2)$ and $(1, 1/2)$ fit into a flat film at critical composition (see Section 5.3.1).

The checkerboard branch $(1/2, 1/2)$ In the neutral critical case the checkerboard film $(1/2, 1/2)$ can be seen as a superposition of the laterally structured films (1/2,0) and the vertically stratified film (0,1/2). As the mean concentration increases, the difference in the concentration between the two components increases. Liquid 2 becomes the minority component that for $a^+ > 0$ is preferred at the free surface. Increasing $\bar{c}$ from $\bar{c} = 0$ first results in a decrease in the L_2-norm of the surface modulations until $\bar{c} \approx 0.14$, i.e., between the points (a) and (b) in Fig. 6.8(A) caused by a decreasing contrast between the two phases. Beyond this point the rich area of liquid 1 disappears and the norm of surface modulation declines to be a perfectly flat homogeneous film at the bifurcation point ($\bar{c} = 0.411$). This result can be obtained from analysing the linear stability for the neutral off-critical mixture introduced in section 4.6 by substituting $m = n = 1/2, L = 10$ and $H = 5$ in Eq. (4.63). During this process (see Fig. 6.8(B)), the L_2-norm of the concentration field decrease monotonically up to the homogeneous state.

Energetically, the checkerboard film (1/2,1/2) is lower energetically as compared to the homogeneous state and the checkerboard film $(1, 1/2)$ (see Fig. 6.8(C)). The energy of this film shows a slight increase until the maxima at about $\bar{c} = 0.125$ and then it decreases towards the energy of the homogeneous state. Panels A,B,C,D of Fig. 6.9

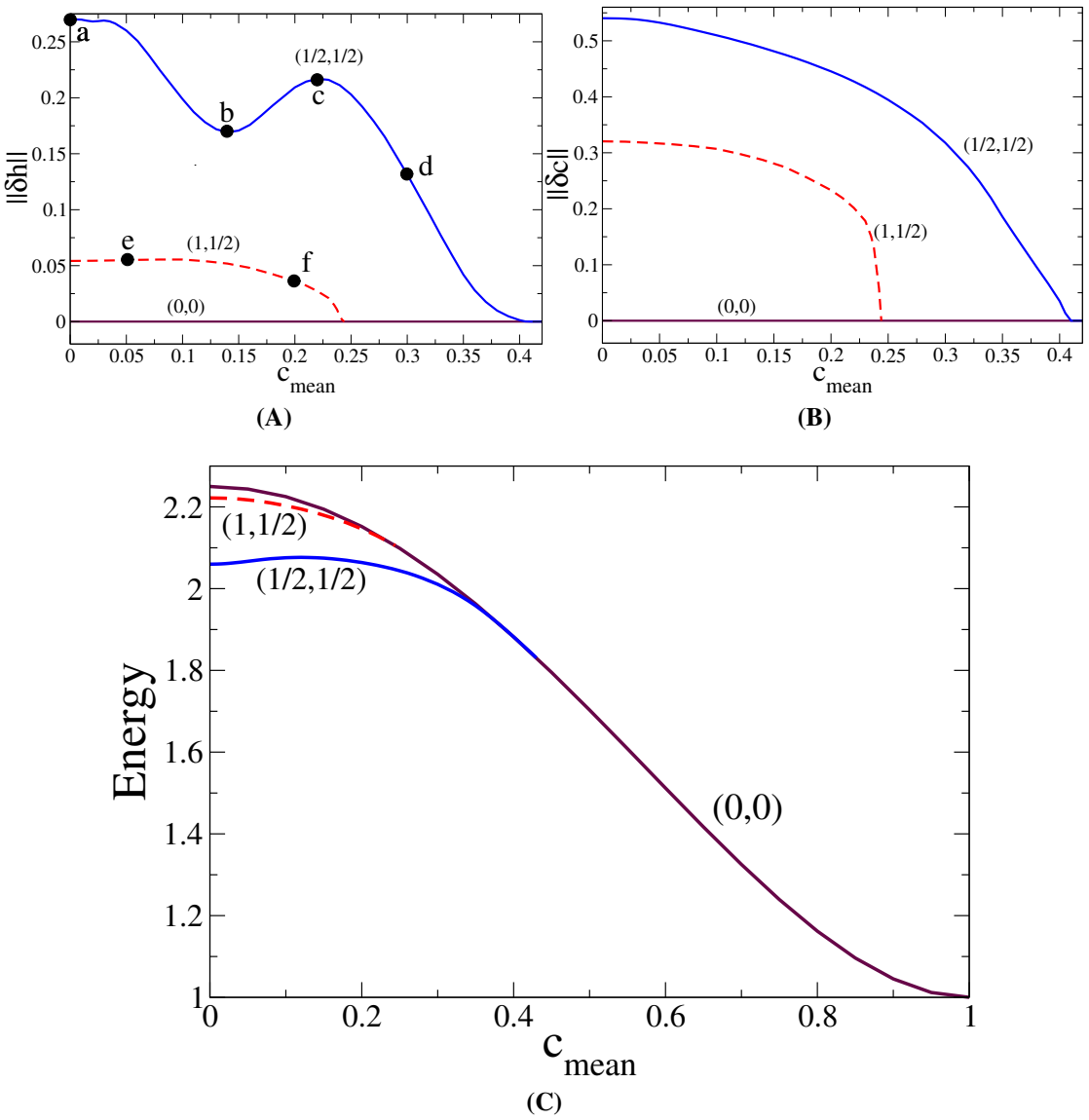

Figure 6.8: Shown are: panels (A), the L_2-norm for surface deflection, panel (B) the L_2-norm for the concentration field, and panel (C) the energy, as a functions of the mean concentration $\bar{c}$. Branch $(0,0)$ corresponds to the brown-solid line, the checkerboard branch $(1/2,1/2)$ corresponds to the blue-solid, and the checkerboard $(1,1/2)$ corresponds to red-dashed line. The film surfaces are assumed neutral ($a^+ = 0$). The lateral domain size is fixed at $L = 10$ and film thickness $H = 5$.

show the concentration profiles at the points indicated by labels a, b, c, d in Fig. 6.8(A), respectively.

The checkerboard branch $(1, 1/2)$ The branch $(1, 1/2)$ can be pictured at critical composition as the superposition of three laterally structures ($m = 1$) and two vertical layers ($n = 1/2$). This branch exists within the spinodal region, with the deflection and composition norms decreasing monotonically with $\bar{c}$ (c.f. Fig. 6.8).

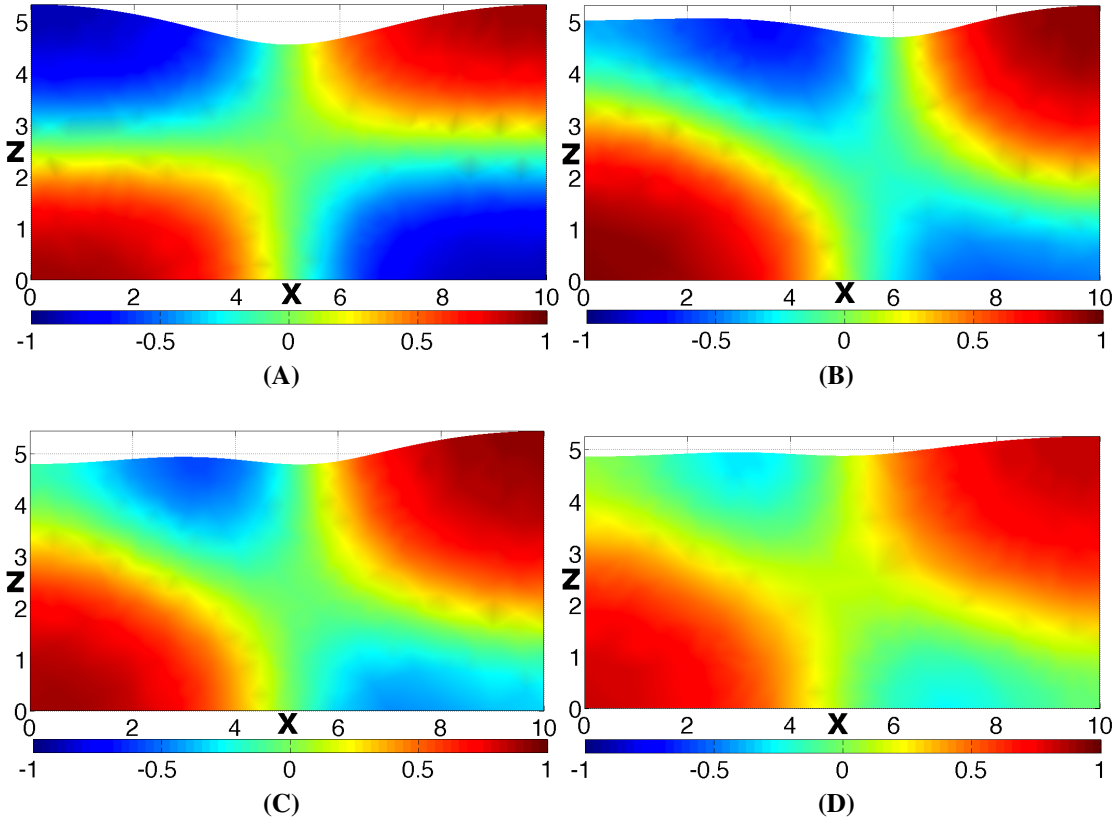

Figure 6.9: Shown are film and concentration profiles of checkerboard branch $(1/2, 1/2)$. Panels (A,B,C,D) are the profiles at the labels (a,b,c,d) shown in Fig. 6.8(A), respectively.

The lateral mode gives rise to two contact lines on the upper surface and the energy per unit of length is larger than that of the $(1/2, 1/2)$ branch, as expected due to the cost of an additional lateral interface. A look at the film profiles along this branch in Fig. 6.10 shows how the transition from the checker-board structure to the homogeneous state at the pitchfork bifurcation at $\bar{c} \approx 0.24$ is driven by the progressive widening of the vertical and horizontal interfaces.

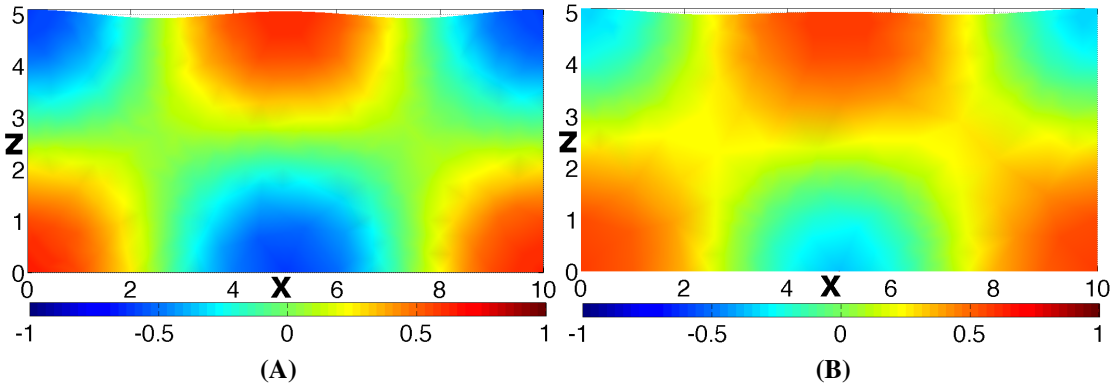

Figure 6.10: Shown are film and concentration profiles of checkerboard branch $(1, 1/2)$. Panel (A) is the profile at label (e), and panel (B) is the profile at the label (f) shown in Fig. 6.8 (A), respectively.

6.3.3 Laterally Structured Films

In contrast to the thin film case, the laterally structured films of medium thickness ($\pi \leq H < 2\pi$), are able to produce structures that consist of droplets either attached to the free surface or to the substrate as well as oblique states that join the laterally structured $(m, 0)$ and the layered films $(0, n)$. In the following paragraphs we investigate the laterally structured and the oblique films for lateral domain size $L = 10$.

Laterally structured solution $(1/2, 0)$ and related sub-branches A film thickness of $H = 5$ allows for more freedom for the internal diffuse interfaces, in particular, far from the critical mixture ($\bar{c} = 0$). At the pitchfork bifurcation of the branch $(1/2, 0)$ two new sub-branches emerge in addition to the one observed in the thin film case. Each of the three branches represents a different transition to the homogenous state as we follow the branch. In Fig. 6.11 we show the bifurcation diagrams for the norms of surface modulations and concentration profiles as well as the total free energy of the system. The points (a - i) introduced in Fig. 6.11(A) correspond to the profiles (A-I) shown in Fig. 6.12, respectively.

At $\bar{c} = 0$ we recover the results discussed in the previous chapter (see profile A in Fig. 6.12). Increasing $\bar{c}$ from the label (a) in Fig. 6.11(A) , as we follow the $(1/2, 0)$ branch we go through the point (b) that corresponds to the profile in panel (B) of Fig. 6.12. Panel (C) of Fig. 6.12 that corresponds to the point (c) in Fig. 6.11(A) shows the transition through a weakly laterally structured film which is as described for films

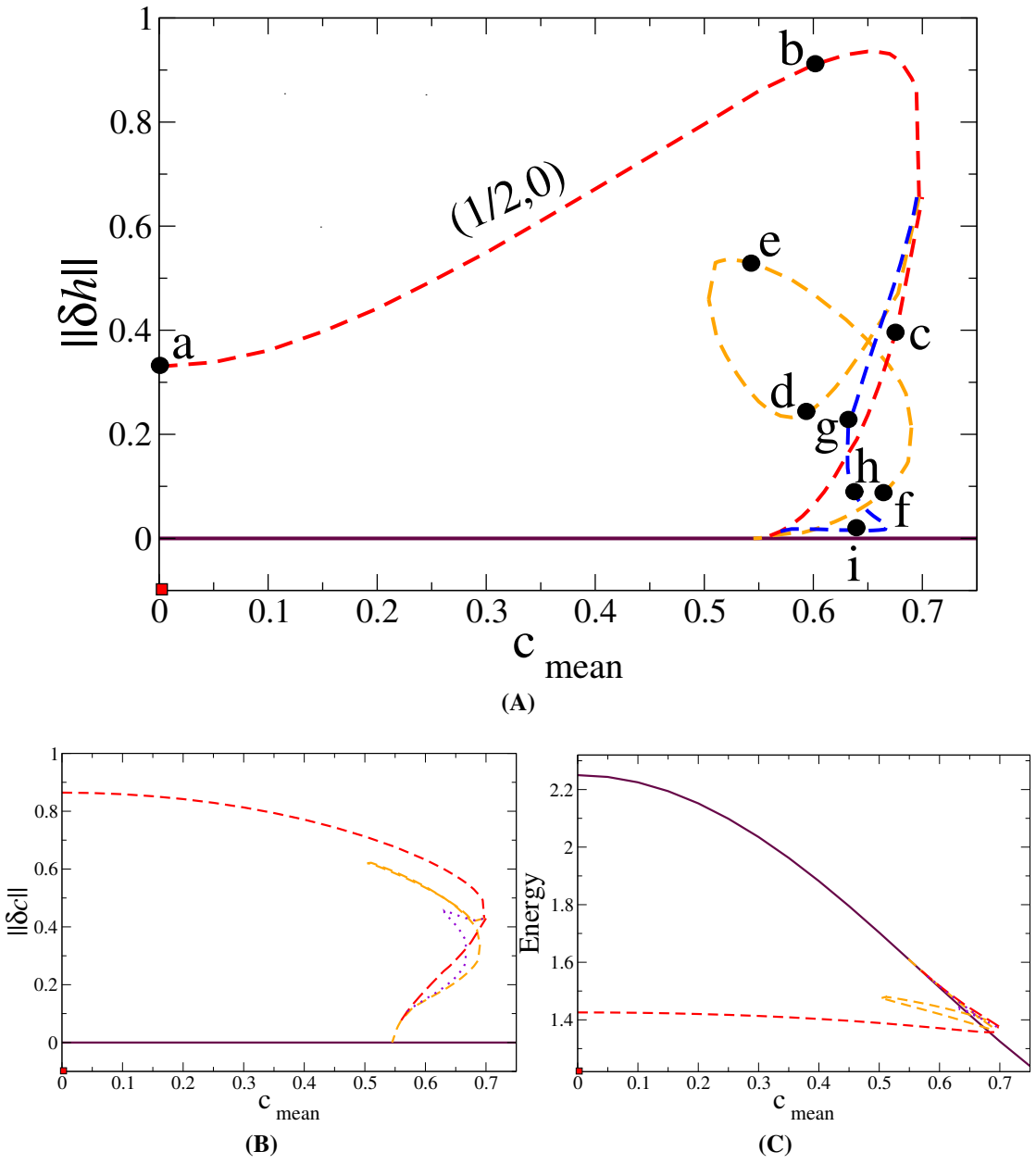

Figure 6.11: Shown are, panel (A) L_2-norm for surface deflection, panel (B) L_2-norm for the concentration field, and panel (C) the energy, as function of the mean concentration $\bar{c}$. Branch $(0,0)$ is shown with a brown-solid line, $(1/2,0)$ with doted–dashed curves. The film thickness is $H = 5$ and the lateral domain size $L = 10$. The film surfaces are neutral ($a^+ = 0$).

of thickness $H = 3$ (see Figs. 6.1 and 6.2). Close to the bifurcation from the homogenous state the weak branches are characterised by an energy which is even higher than the energy of the completely homogeneous film. This indicates that this subcritical part of the $(1/2, 0)$ branch represents threshold solutions that need to be overcome by finite size disturbances to go from a homogeneous film to a laterally structured one.

The panels (D), (E) and (F) of Fig. 6.12 that correspond to labels (d), (e) and (f) in Fig. 6.11(A) display selected profiles corresponding to one of the branches that bifurcates at $\bar{c} \approx 0.723$ from the $(1/2, 0)$ branch. Advancing along this branch, from (b) towards (d) the internal interface is displaced and the contact point moves along the substrate towards the corner leading eventually to a detachment of the diffuse interface from the substrate, and to the creation of a droplet of liquid 2 at the upper surface surrounded by liquid 1. The droplet is situated either in the left or right corner of the film. Notice that advancing further on the branch squeezes the droplet up to its disappearance when the branch merges with the homogeneous state at $\bar{c} = 0.548$. From the profiles (D), (E) and (F) in Fig. 6.12 it can be observed that the inclined internal interfaces are normal to the free surface at the contact point. This is due to Young's equation that relates the contact angles at the three phase contact. The loop structure of the branch is related to a hysteresis between solutions with a contact point on the substrate (as in profile B) and droplets detached from the substrate (as in profile E).

The panels (G), (H) and (I) of Fig. 6.12 that correspond to the points (g), (h) and (i) in Fig. 6.11(A), respectively, exhibit states corresponding to the other branch that emerges at $\bar{c} = 0.723$ from the $(1/2, 0)$ branch. This branch follows an "opposite" evolution compared to the previous one, with the upper contact point shifting towards the left or right border until it detaches from the free surface leading to a drop of liquid 2 attached to the substrate and surrounded by liquid 1. Finally, the drop shrinks and disappears. As an example, the state (I) shows a state close to the smooth transition to the completely homogeneous state.

Laterally structured solution $(1, 0)$ and related oblique films The laterally structured $(1, 0)$ branch is shown as a dot-dashed blue line in Fig. 6.13(A). This branch behaves differently from the one in Fig. 6.1 for $H = 3$ where it shows no saddle node bifurcations and ends supercritically. Advancing through this branch starting from $\bar{c} = 0$ (Profile K in Fig. 6.14), one passes through profiles F, G, H and I (Fig. 6.14). The contact points of the original $(1, 0)$ solution approach each other, until they merge giving

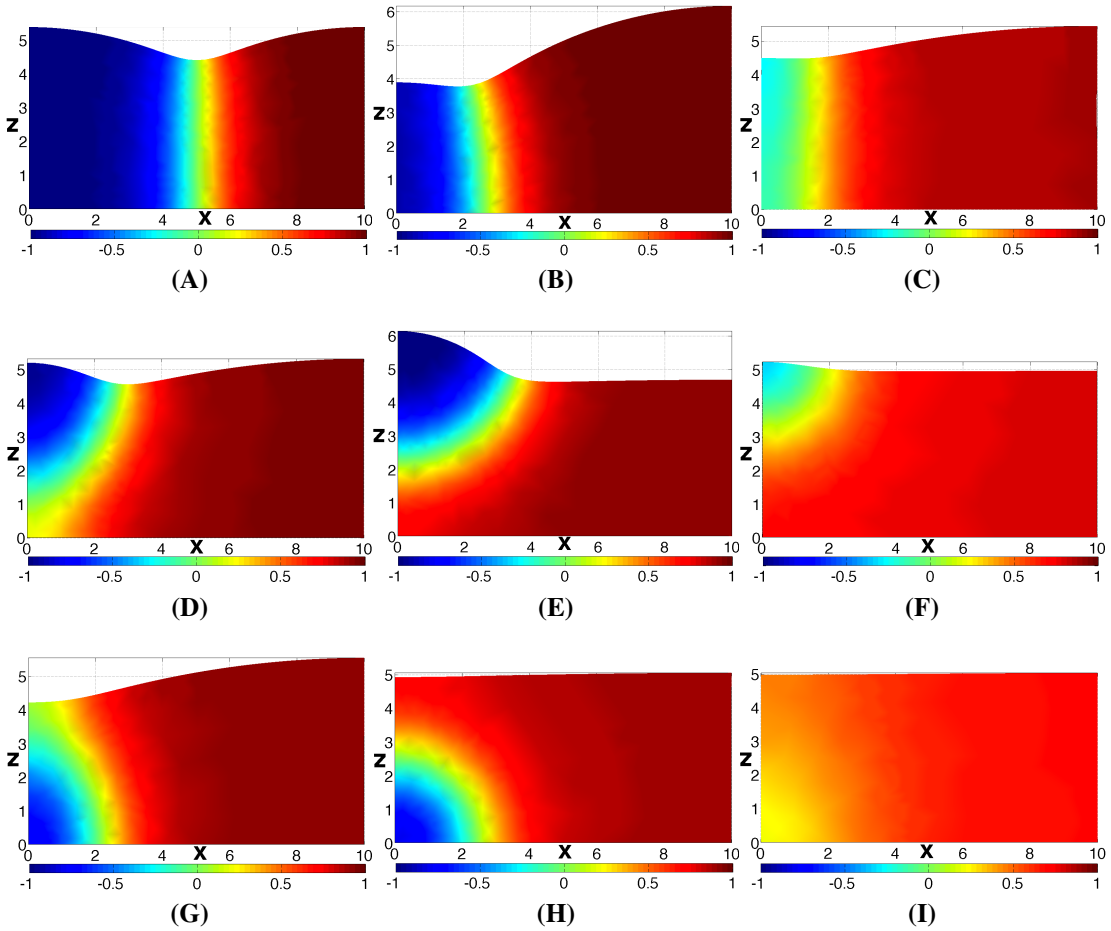

Figure 6.12: Shown are film and concentration profiles for the branch $(1/2, 0)$ and related sub-branches taken at the corresponding labels in Fig. 6.11(A), respectively. Panels (A,I) correspond to labels (a,i), respectively and lie on the same branch. Panels (A,B,C) correspond to labels (a,b,c), respectively and lie on the same branch. Panels (D,E,F) are profiles correspond respectively to labels (d,e,f) that lie on the second branch which also bifurcates from the laterally structured film at the saddle node bifurcation. Panels (G,H,I) are profiles correspond respectively to labels (g,h,i) that lie on the third branch which also bifurcates from the laterally structured film at the saddle node bifurcation.

rise to a droplet at the lower substrate (compare the labels (g) and (h) in Fig. 6.13(A) to the profiles (G) and (H) in Fig. 6.14), respectively. The transition is hysteretic and comes with two saddle-node bifurcations on the $(1, 0)$ branch. This branch ends subcritically on the homogeneous branch after passing through another saddle node bifurcation that is well visible in Fig. 6.13(B) (compare the label (i) in Fig. 6.13(A) to the profile (I) in Fig. 6.14). Note that, there is no weakly laterally structured film similar to the one observed in films of thickness $H = 3$ shown in Fig. 6.3(C), (D). In the critical case without bias, the oblique films O_1^a and O_1^b are related by a $(c \to -c)$ symmetry. Once we move to the off-critical case these two branches become different (see e.g. the red

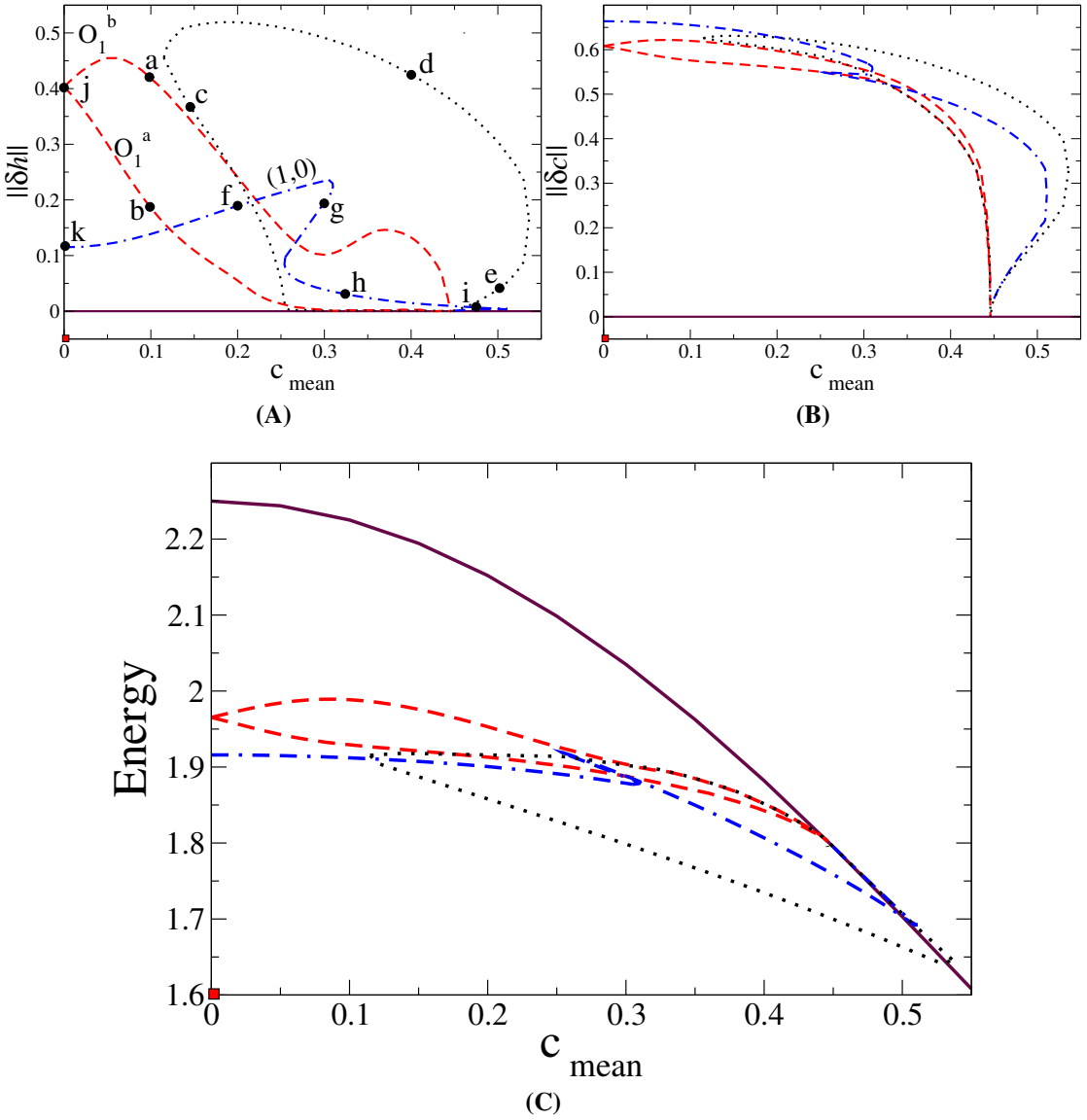

Figure 6.13: Shown are, panel (A) L_2-norm for surface deflection, panel (B) L_2-norm for the concentration field, and panel (C) the energy for the branches. Branch $(0,0)$ is shown with brown-solid line, $(1,0)$ with blue dot-dashed lines. The oblique solutions O_1 depicted by the red dashed curves. The black dotted branch is not existed in the critical case (has not got name), all as functions of the mean concentration $\bar{c}$. The film thickness is given by $H = 5$ and the lateral domain size is fixed at $L = 10$. The film surfaces are neutral ($a^+ = 0$).

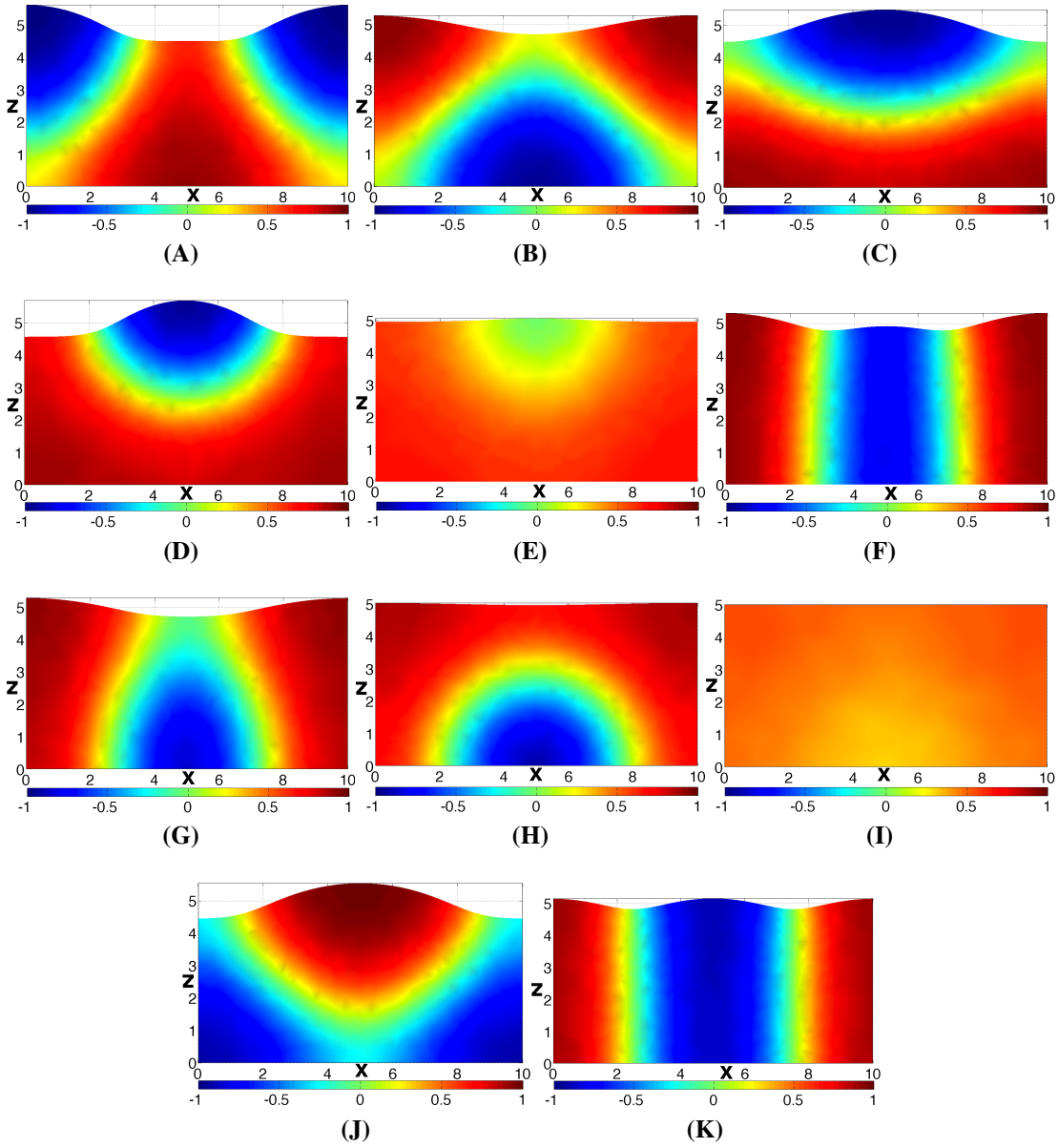

Figure 6.14: Shown are film and concentration profiles for the branch $(1, 0)$ and related branches taken at the corresponding points in Fig. 6.13(A). I.e., panels (A,B,C,D,E,F,G,H,I,J,K) are taken at the corresponding labels a,b,c,d,e,f,g,h,i,j,k), respectively.

dashed lines in Fig. 6.13, and the profiles A, B in Fig. 6.14). As the mean concentration increases the surface deflection for the two branches declines and they follow different paths, but eventually merge to the homogeneous film at the same point ($\bar{c} = 0.449$) (see the red dashed lines in Fig. 6.13). The norm of the surface modulations for the O_1^a film, i.e., fluid 1 on the top (see Fig. 6.14(B)), first declines fast towards the homogeneous state but then approaches it slowly until reaching the bifurcation point at $\bar{c} = 0.449$. The norm of the surface deformations of the oblique film O_1^b (fluid two on top Fig. 6.14(A)) first increases with $\bar{c}$, starting from $\bar{c} = 0$ until it reaches a maximum at $\bar{c} = 0.055$. Then it overall declines, with a small non-monotonous part, towards the homogeneous state until they meet at the bifurcation point at $\bar{c} = 0.449$.

There is a related branch which does not exist in the critical case. It seems to describe a complete loop starting and ending at the same bifurcation at $\bar{c} = 0.449$ point on the homogeneous branch (see the black dotted line in Fig. 6.13). To describe the behaviour of the films on this loop, we start from the bifurcation point $\bar{c} = 0.449$ following the lower part of the branch (clockwise), on the interval [0.26,0.449], where the film is characterised by low surface modulations. Here, liquid 2 (the minority phase) is spread over liquid 1 and this layer vanishes at the bifurcation point. Between the saddle node bifurcation at $\bar{c} \approx 0.12$ and the point $\bar{c} = 0.26$, we observe a rapid decrease in $||\delta h||$. This is caused by the rising of a droplet of liquid 2 that sits at the free surface (see Fig. 6.14(C)). This process ends at the saddle node bifurcation. Now, as the mean concentration increases again on the upper most part of the branch the droplet shrinks with a slight decrease in the norm of the surface modulations (see Fig. 6.14(D)). Eventually, the droplet gradually disappears as the branch passes another saddle-node bifurcation while it comes closer to the homogeneous state. Fig. 6.14(E) shows the film profile at the label (e) in Fig. 6.13(A).

The L_2-norm of the concentration field for the solutions is shown in Fig. 6.13(B), and the L_2-norm of the energy is shown in Fig. 6.13(C). Note that, the subcritical parts of the branches near the bifurcation point from the homogeneous state have a higher energy than the homogeneous film indicating their role as threshold solutions.

6.4 Films with Energetic Bias

Next we study the off-critical case for films with energetic bias at the free surface. As we have seen in the critical case (Chapter 5), switching on the energetic bias divides the

bifurcation diagrams into two groups of branches. A group of higher energy and another one of lower energy. The group of higher energy consists of the weakly stratified branch $(0,0)$, the stratified branch $(0,1/2^a)$, the checkerboard films and connecting branches. In the off-critical case, these branches only exist for $\bar{c} \in [-0.365, 0.4]$ (upper branch in Fig. 6.15(C)). The group of lower energy consists of the stratified branch $(0,1/2^b)$, the laterally structured branches $(1/2,0)$, (1,0) and the connecting branches. The group exists for a larger range of the mean concentration. In the following discussion we introduce those branches in detail for biased films of thickness $H = 5$. The energetic bias is fixed at $a^+ = 0.1$. Here we restrict our study to particular films such as the weakly stratified film (0,0), the stratified films $(0,1/2^{a,b})$, the laterally structured films $(1/2,0)$ and $(1,0)$, the oblique films $O_1^{a,b}$, and the checkerboard branches $(1/2,1/2)$ and $(1,1/2)$. We fix the lateral domain size at $L = 12$. In fact, the lateral domain size $L = 12$ allows for new branches which enrich the picture. Here we will not consider more than the films mentioned above.

6.4.1 Weakly Stratified and Stratified Films

In the critical case we have observed that with energetic bias the homogeneous film can not exist any more. Instead, it becomes a weakly stratified film. Also the two identical branches of stratified solutions that are related by a $(z \to -z)$ symmetry for $a^+ = 0$ separate into two different branches one of them with higher energy than the other one. Following these branches in the off-critical case one finds one branch that consists of the weakly stratified $(0,0)$ and the stratified $(0,1/2^a)$ states joined to each other at a saddle node bifurcation (see solid brown and dot-dashed red lines in Fig. 6.15). This structure spans the range $\bar{c} \in [-0.365, 0.4]$. In contrast, the branch of the stratified $(0,1/2^b)$ state exists in all the considered $\bar{c}$ range (see Fig. 6.15)(C). Note that, all the other branches are joined in some way to these three main branches. Therefore we include them in all the subsequent bifurcation diagrams for the biased case. The profile of the weakly stratified $(0,0)$ branch at label (a) shown in Fig. 6.15(C) is given by profile A in Fig. 6.16 and the profiles of the stratified $(0,1/2^a)$ and $(0,1/2^b)$ at the labels (b) and (c) in Fig. 6.15(C) correspond to panels B and C in Fig. 6.16, respectively.

Close to the saddle node bifurcations, the concentration profiles of the weakly stratified and the stratified films are very similar to each other and and become exactly the same at the saddle node bifurcation.

6.4.2 Laterally Structured Films

The increase of the lateral domain size to $L = 12$ for the film with thickness $H = 5$ does not affect the laterally structured films $(m, 0)$. The films still exist and they behave similarly as for $L = 10$.

Laterally structured solution branch $(1/2, 0)$ and related branches The behaviour of the laterally structured branch $(1/2, 0)$ for the energetically biased films can be different from the neutral case. As the symmetry $(c \to -c)$ of the bifurcation diagrams is broken, the pitchfork bifurcations are not symmetric any more. The separation into the stratified films $(0, 1/2^a)$ and $(0, 1/2^b)$, must affect the laterally structured film in some way. Here we describe the differences by comparing the neutral case to the biased case through Fig. 6.15 and Fig. 6.11. In the neutral case on each side (positive and negative $\bar{c}$) two branches bifurcate from the $(1/2, 0)$ branch at large $\bar{c}$, i.e., three branches in total connect to the homogeneous state. In the biased case one of these three branches (the weakly laterally structured) disappears completely. However, also of the other two only one is kept on each side ($\bar{c} > 0$ and $\bar{c} < 0$). This remaining branch joins the stratified branch $(0, 1/2^b)$ in a subcritical bifurcation. For the stratified branch with positive $\bar{c}$ we observe that liquid 2 forms a minority layer at the free surface (see profile C in Fig. 6.16). This is only consistent with a branch $(1/2, 0)$ that shows a droplet of liquid 2 on top of liquid 1. At the pitchfork bifurcation the droplet on top spreads completely over liquid 1.

For negative $\bar{c}$ the stratified branch $(0, 1/2^b)$ consists of a thick layer of liquid 2 on top of a thin layer of liquid 1 attached to the substrate. Here the transition becomes consistent for a film with a droplet of liquid 1 attached to substrate which finally (near the bifurcation point) will spread along the substrate and becomes the minority layer. Note that, the droplet only appears close to the saddle-node bifurcations at large $|\bar{c}|$. However, in the middle part the branch shows "normal" laterally structured states. Some hysteresis between the two solution types results in the saddle-node bifurcation on the $(1/2, 0)$ branch. Looking at Fig. 6.15, the overall comparison shows that the modulations in the bifurcation diagrams are larger for positive $\bar{c}$ than that for negative $\bar{c}$. For instance, the energies and the L_2-norms of the surface modulations for most branches are higher at $\bar{c} > 0$ than at $\bar{c} < 0$.

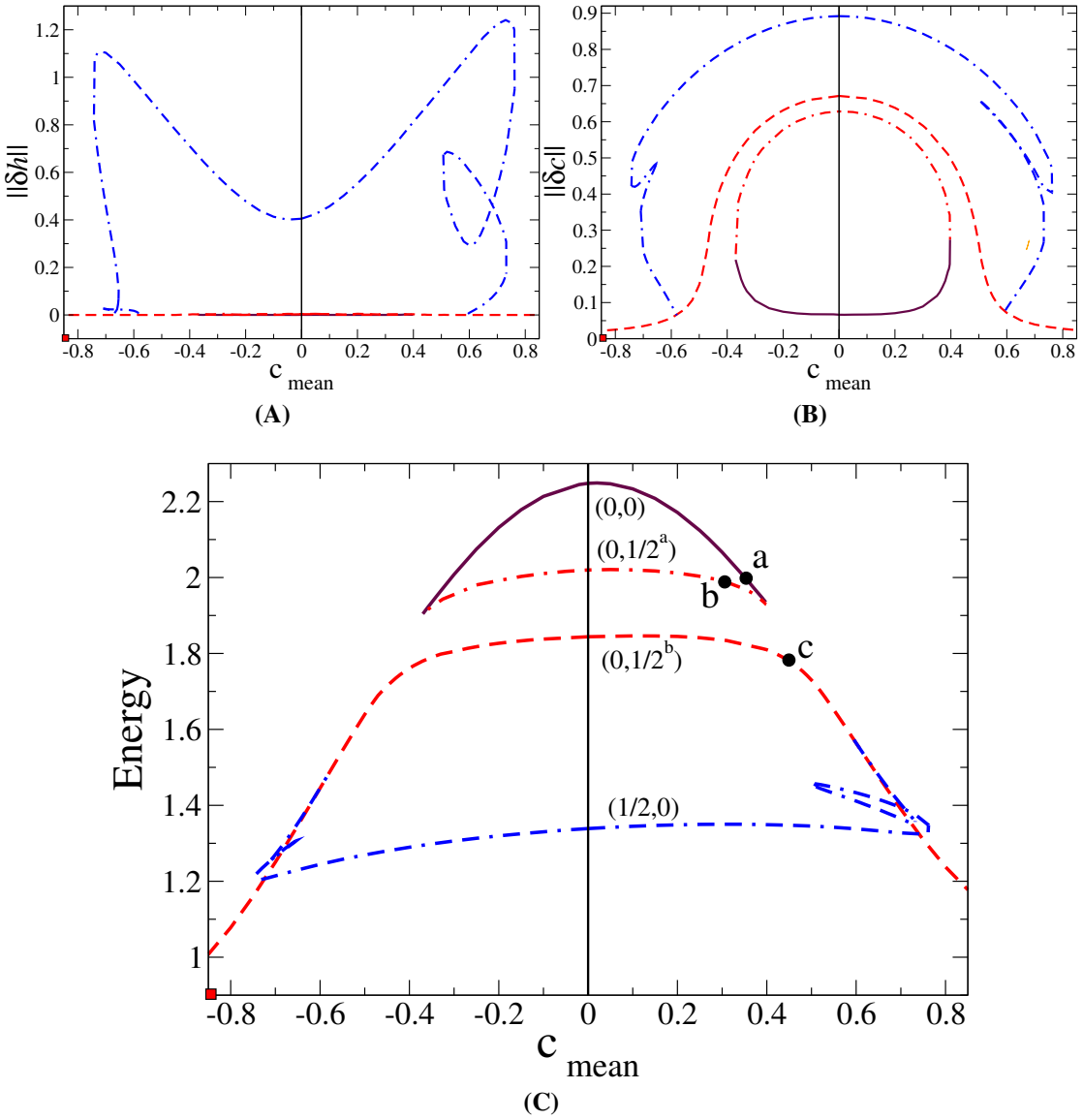

Figure 6.15: Shown are: Panel (A) L_2-norm for surface deflection, panel (B) L_2-norm for the concentration field, panel (C) the energy, as functions of the mean concentration $\bar{c}$. The weakly stratified branch $(0,0)$ is depicted by brown solid curve. The red dot-dashed curve represents the stratified branch $(0,1/2^a)$. The dashed red curve represents the stratified branch $(0,1/2^b)$. The blue dot-dashed curve corresponding to the laterally structured branch $(1/2,0)$. The energetic bias is given by $a^+ = 0.1$. The film with surface modulations and of thickness $H = 5$ where the lateral domain size is fixed at $L = 12$.

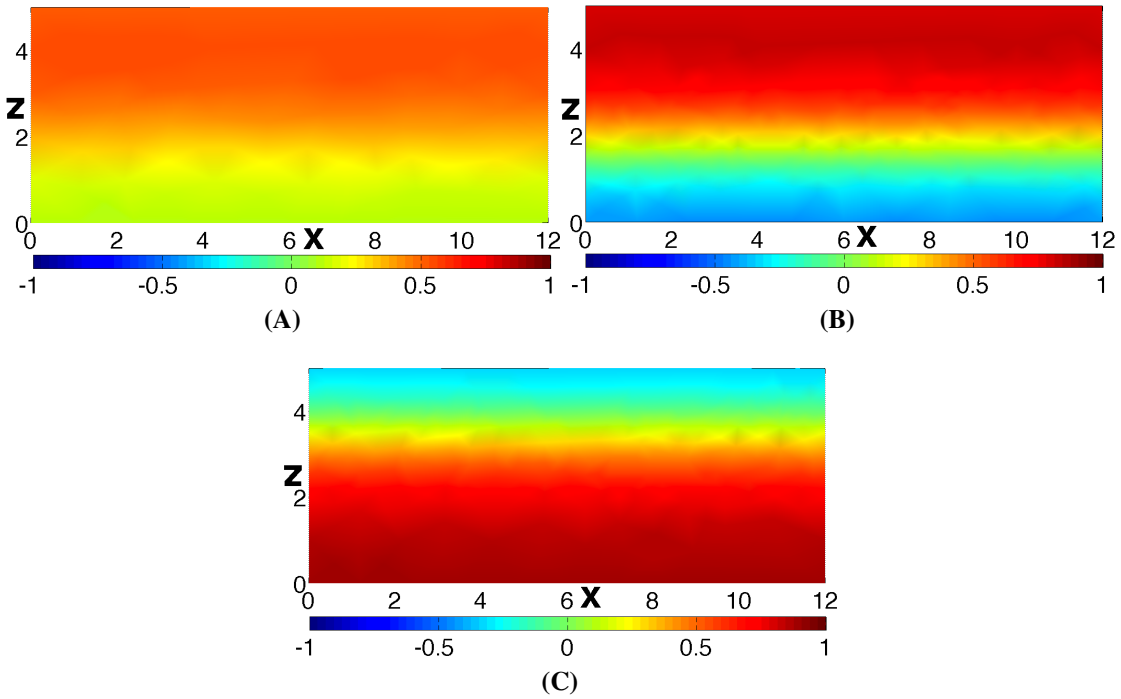

Figure 6.16: Shown are the film and concentration profiles of the weakly stratified $(0,0)$ at the $\bar{c} = 0.38$, and the stratified branches $(0,1/2^{a,b})$ at $\bar{c} = 3.5$ and $\bar{c} = 4.5$, respectively. Profiles A,B,C correspond to the labels a,b,c in Fig. 6.15(C).

Laterally structured solution $(1,0)$ and related branches The bifurcation diagrams of the branch $(1,0)$ and related branches are shown in Fig. 6.17. We have included the weakly stratified and the stratified $(0,1/2^a)$ and $(0,1/2^b)$ branches as they represent the main branches in the bifurcation diagrams. The (1,0) branch becomes rather complex and involves several saddle-node bifurcations. If we follow the branch $(1,0)$ starting from $\bar{c} = 0$ for increasing $\bar{c}$ the film first behaves similarly to the neutral case. I.e., liquid 2 is squeezed inbetween two regions of liquid 1. When the two contact regions approach a hysteretic transition occurs to a central droplet that tends to detach from the substrate (see profile H in Fig. 6.18). Beyond the second saddle node bifurcation the droplet floats to the free surface producing a relatively large mound of liquid 2. Liquid 2 is strongly preferred at the free surface which causes the largest deformation at the free surface (see label (i) in Fig. 6.17(A) that corresponds to profile I in Fig. 6.18). Following the branch further the droplet shrinks monotonically (see for instance profile J in Fig. 6.18) before it spreads completely along the free surface producing a thin layer on top of liquid 1 as we reach the pitchfork bifurcation from the stratified $(0,1/2^b)$ branch at $\bar{c} \approx 0.547$.

As we follow the laterally structured film $(1,0)$ starting from $\bar{c} = 0$ and decreasing in $\bar{c}$ (in negative $\bar{c}$), liquid 1 is squeezed inbetween two regions of liquid 2. The two

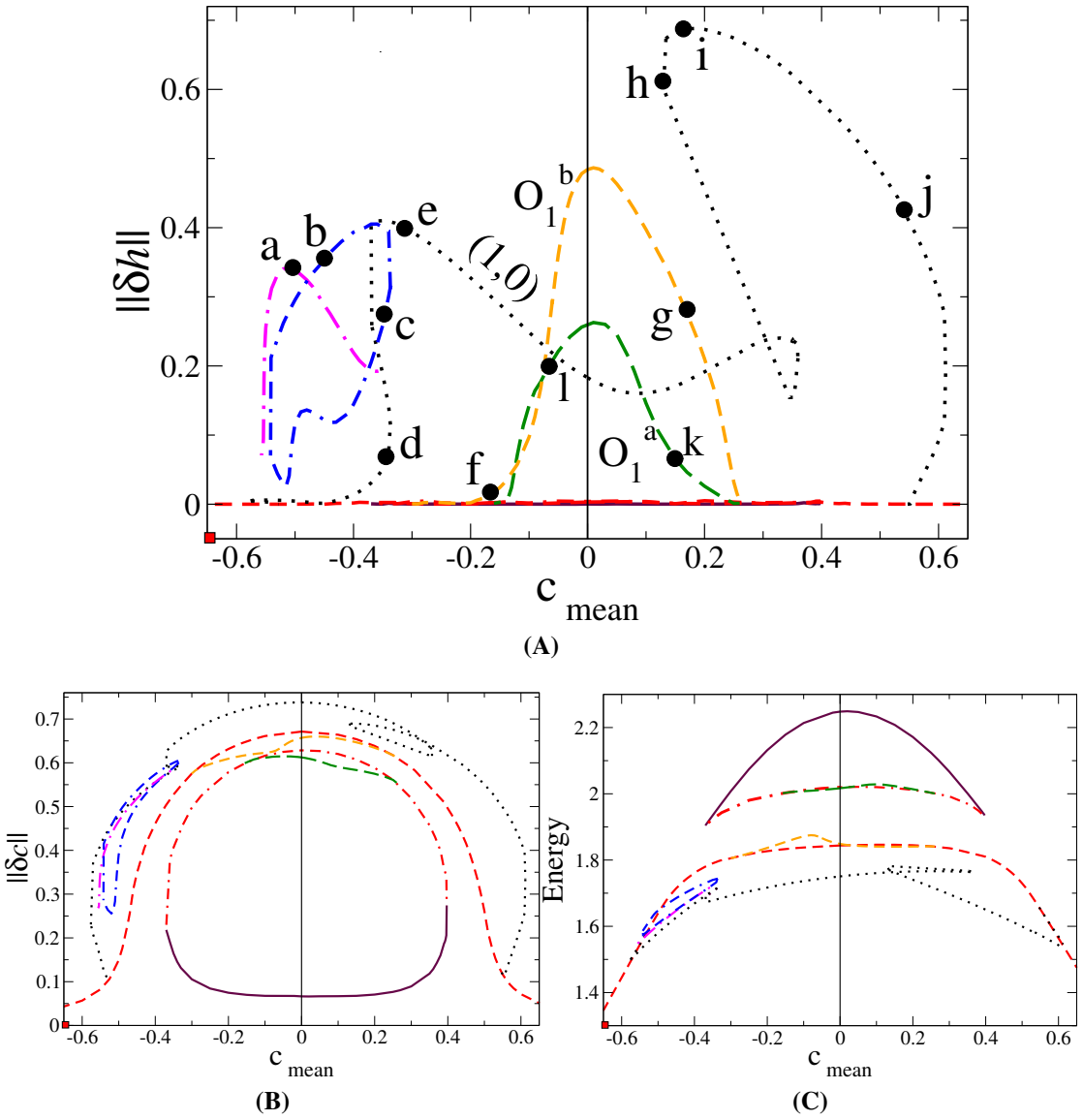

Figure 6.17: Shown are: Panel (A) L_2-norm for surface deflection, panel (B) L_2-norm for the concentration field, panel (C) the energy, as functions of the mean concentration $\bar{c}$. The weakly stratified branch $(0,0)$ is depicted by brown solid curve. The red dot-dashed curve represents the stratified branch $(0,1/2^a)$. The dashed red curve represents the stratified branch $(0,1/2^b)$. The black doted curve corresponds to the laterally structured branch $(1,0)$. The green dashed and orange dashed correspond to the oblique branches O_1^a and O_1^b, respectively. The curves which are not crossing $\bar{c}=0$ are not named and can be recognised from the profiles. The energetic bias is $a^+ = 0.1$. The film with surface modulations and of thickness $H = 5$ where the lateral domain size is fixed at $L = 12$.

regions of liquid 2 are strongly attracted to the free surface producing large mounds around liquid 1 (see Fig. 6.18(E)) which corresponds to label (e) in Fig. 6.17(A). Once the first saddle node bifurcation is passed liquid 1 disconnected from the surface and sinks inside liquid 2 producing a droplet attached to the substrate. The small distance to the free surface causes a small depression (see profile D in Fig. 6.18 that corresponds to label (d) in Fig. 6.17(A)). This droplet is not completely detached from the free surface until we reach the next saddle node bifurcation. Beyond this point, the droplet of liquid 1 is completely inside liquid 2 and the norm of the surface modulations declines dramatically. As we follow the branch further the droplet of liquid 1 spreads completely producing a thin layer of liquid 1 along the substrate preparing to join the stratified branch $(0, 1/2^b)$ at the pitchfork bifurcation at $\bar{c} \approx -0.53$. On the left hand side of the panels of Fig. 6.17, we show a loop as a blue dashed curve. In fact it is not clear where this branch bifurcates from and where it ends. It might actually be a closed loop. We show this branch in this figure as we suspect it is in some way related to the branch $(1, 0)$. On this branch a droplet of the minority phase (liquid 1) is attached to the free surface of a film of liquid 2. The concentration profiles at the labels (c) and (b) in Fig. 6.17 correspond to panels C and B in Fig. 6.18, respectively. Also the dash-dotted branch (magenta) seems to bifurcate from the branch $(1, 0)$. A film profile on this branch is shown in panel A in Fig. 6.18 that correspond to label (a) in Fig. 6.17.

The long-dashed green and short-dashed orange branches in Fig. 6.17 correspond to the oblique films O_1^a and O_1^b (see Fig. 5.29 and the corresponding profiles in Fig. 5.30), respectively. In the critical case the symmetry ($c \to -c$) of the oblique solutions is broken by the energetic bias as is as well the symmetry ($\bar{c} \to -\bar{c}$) of the bifurcation diagram. As a result the two branches have different behaviour. We describe first the oblique branch O_1^b and then return to the branch O_1^a. Following the branch O_1^b with increasing $\bar{c}$ starting from $\bar{c} = 0$ the interface between the two components gradually straightens and simultaneously the concentration of liquid 2 is reduced (see profile G in Fig. 6.18 that corresponds to label (g) in Fig. 6.17(A)). Finally, at the bifurcation point the interface between the two components becomes horizontal and liquid 1 is completely covered by a thin layer of liquid 2 when the branch joins the branch $(0, 1/2^b)$ of stratified films at $\bar{c} = 0.26$.

Following the branch when $\bar{c}$ is decreased (towards negative $\bar{c}$), the concentration of liquid 1 reduces and also the interface between the two components gradually straightens (see profile F in Fig. 6.18 that corresponds to label (f) in Fig. 6.17). At $\bar{c} = -0.3$

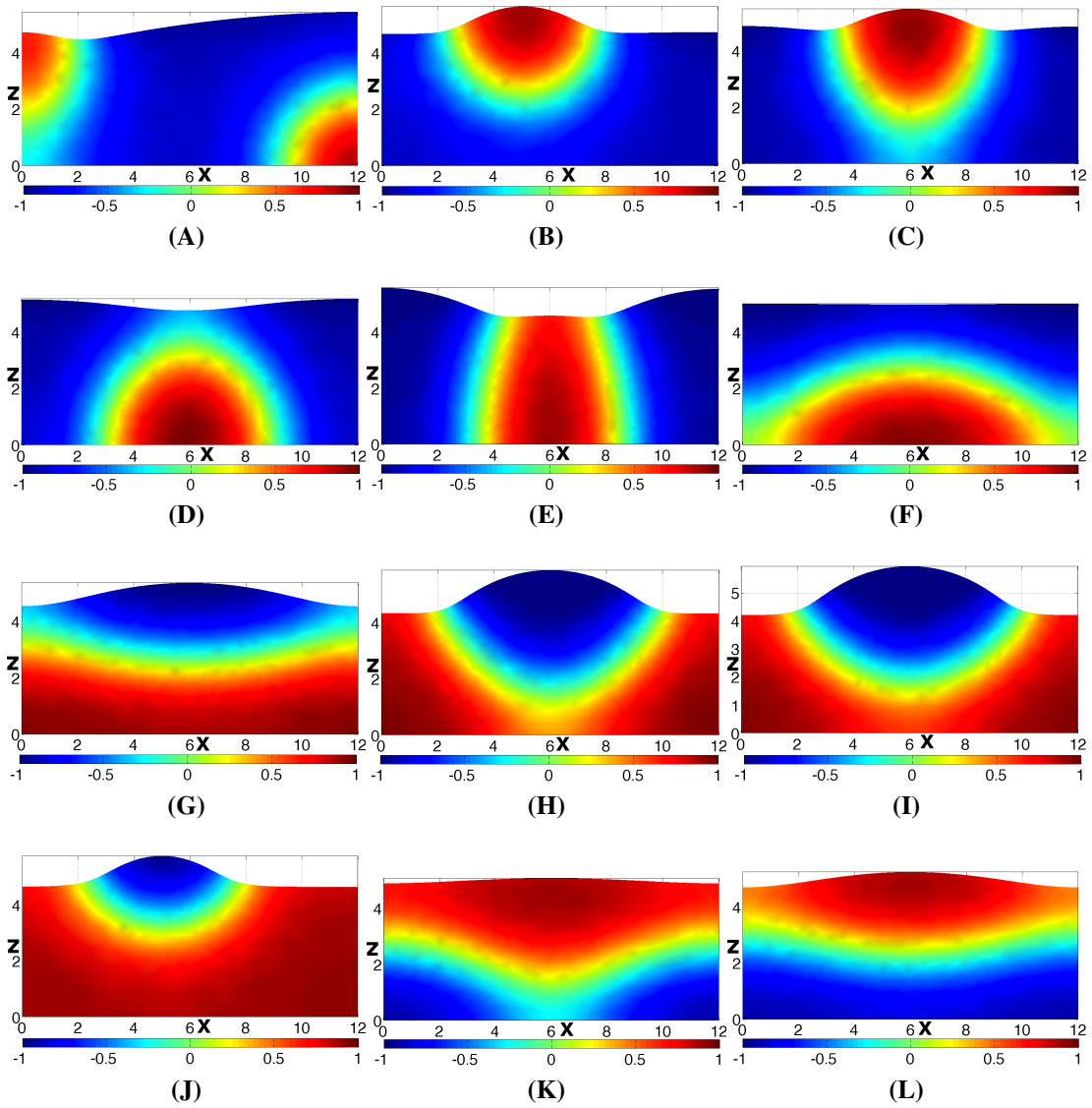

Figure 6.18: Shown are film and concentration profiles for the branch $(1, 0)$ and related branches taken at the corresponding points in Fig. 6.17(A). Panels (A,B,C,D,E,F,G,H,I,J) are taken at the corresponding labels (a,b,c,d,e,f,g,h,i,j), respectively.

the branch reaches the bifurcation where it joins to the stratified film $(0, 1/2^b)$. The behaviour along the branch O_1^a is quite similar to that at the branch O_1^b but with less surface modulations. The difference is that the branch O_1^a ends at the stratified film $(0, 1/2^a)$ at the bifurcation points $\bar{c} = 0.26$ and $\bar{c} = -0.16$. Note that, the thickness of the stratified layers of the minority and majority liquids at the bifurcation points depends on the position of the bifurcation point of the branch ($\bar{c}_c$ of the stratified branch).

6.4.3 Checkerboard Films

As well as the other films, the individual checkerboard solutions break the $(c \to -c)$ symmetry because of the energetic bias. However, the branch is still two-fold as the two instances are still related by the $(x \to -x)$ reflection symmetry. The checkerboard films are in the high energy set of branches (see Fig. 6.19). The more internal interfaces the checkerboard structure has the higher is the energy and the lower is the surface modulation. Note that, the norm of surface modulations for the film $(1/2, 1/2)$ is three times higher than that for the film $(1, 1/2)$. All the checkerboard branches bifurcate form the weakly stratified film. The large changes in the surface modulations of the checkerboard films normally occur when the contact regions between the two phases and the domain boundary passes through the corners of the rectangular domain.

The checkerboard $(1/2, 1/2)$ branch The profile of the checkerboard film $(1/2, 1/2)$ in the critical case can be seen in Fig. 5.30. With energetic bias the maximal surface modulation is not found at $\bar{c} = 0$ but at a slightly higher $\bar{c} \approx 0.05$ (compare to the neutral case given in Fig. 6.8). As we follow the branch starting from $\bar{c} = 0$ increasing the mean concentration we observe first a decrease and then a small non-monotonous perturbation in $||\delta h||$ before it rapidly approaches zero and joins the weakly stratified branch. Here the minority phase (liquid 2) collects at the bottom (attached to the substrate) when it joins the weakly stratified branch (see profile A in Fig. 6.20). Following the branch starting at $\bar{c} = 0$ decreasing towards negative $\bar{c}$ the film joins the weakly stratified branch after a very steep descent that we have only in part obtained numerically. The minority phase (liquid 1) forms a layer on top of the majority phase (liquid 2). As we can not follow the branch numerically, we completed the missing branches hypothetically by a thin solid black curve (see Fig. 6.19) Profiles of this branch at the labels (a) and (b) in Fig. 6.19 are given by panels (A) and (B) of Fig. 6.20. The branch $(1/2, 1/2)$ emerges in pitchfork bifurcations from the weakly stratified branch.

The checkerboard $(1, 1/2)$ branch The checkerboard branch $(1, 1/2)$ exists in a smaller $\bar{c}$ range than the branch $(1/2, 1/2)$. The highest surface modulation occurs at $\bar{c} \approx -0.12$, in contrast to the branch $(1/2, 1/2)$ where it occurs at $\bar{c} > 0$. The checkerboard branch $(1, 1/2)$ ends on the weakly stratified one in pitchfork bifurcations. The

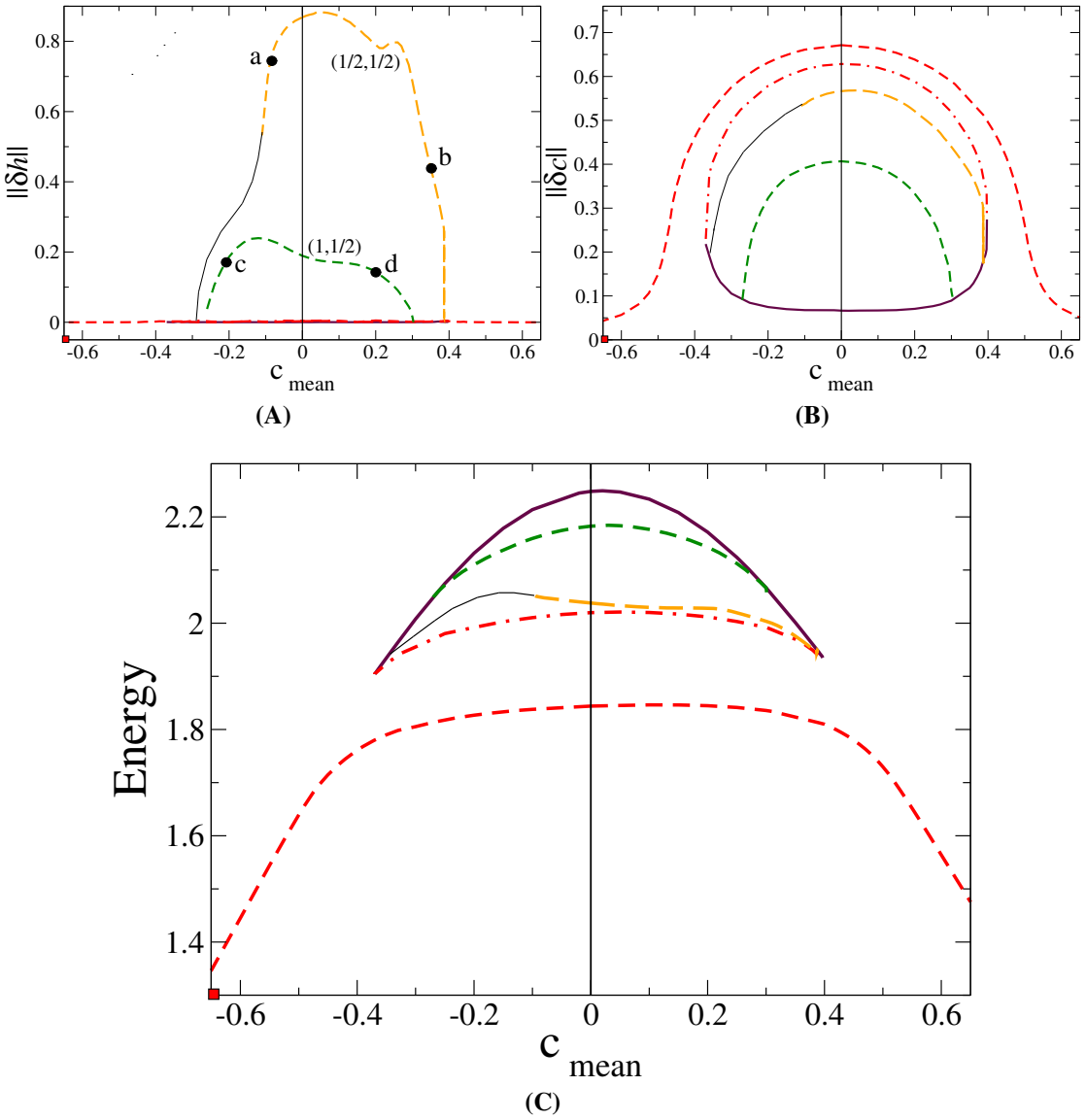

Figure 6.19: Shown are: Panel (A) L_2-norm for surface deflection, panel (B) L_2-norm for the concentration field, panel (C) the energy, as functions of the mean concentration $\bar{c}$. The weakly stratified branch $(0, 0)$ is depicted by brown solid curve. The red dot-dashed curve represents the stratified branch $(0, 1/2^a)$. The dashed red curve represents the stratified branch $(0, 1/2^b)$. The orange dashed and green dashed correspond to the checkerboard branches $(1/2, 1/2)$ and $(1, 1/2)$, respectively. The energetic bias is given by $a^+ = 0.1$ and $a^- = b^{\pm} = 0$. The film with surface modulations and of thickness $H = 5$ where the lateral domain size is fixed at $L = 12$.

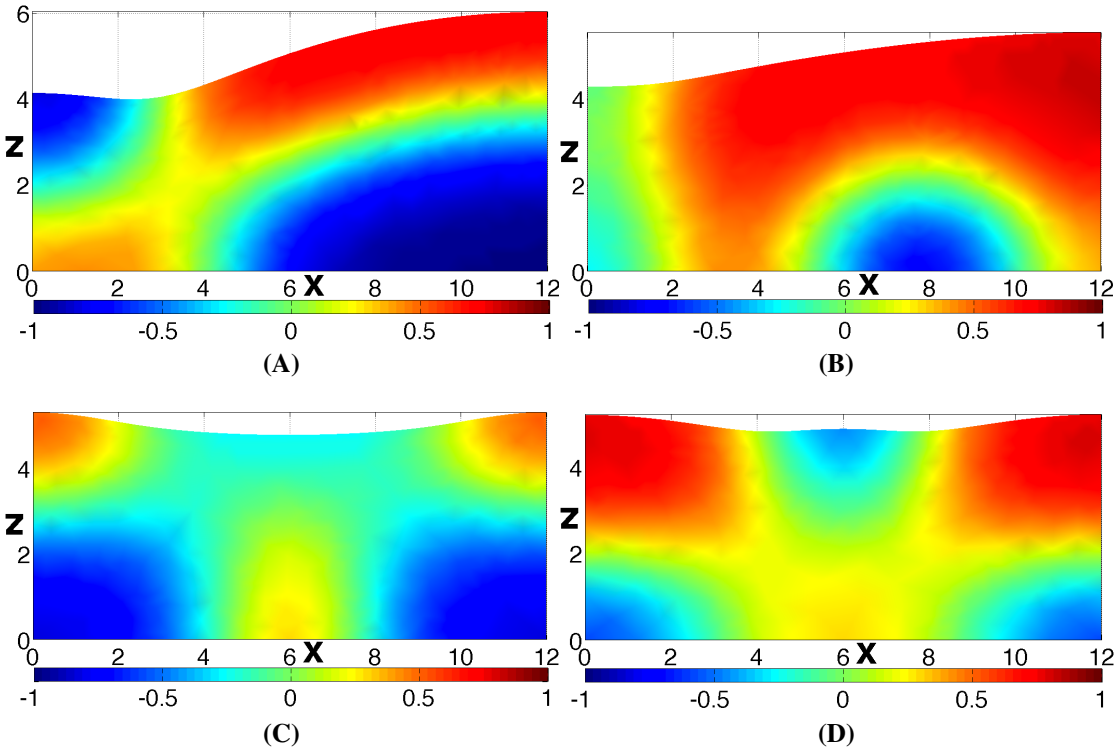

Figure 6.20: Shown are Panel (A) the film and concentration profile at $\bar{c} = -0.08$, panel (B) the film and concentration profile at $\bar{c} = 0.35$ for the checkerboard film $(1/2, 1/2)$ denoted by the labels (a) and (b) in Fig. 6.19. Panels (C) and (D) show the film and concentration profiles for the checkerboard film $(1, 1/2)$ at $\bar{c} = -0.2$ and $\bar{c} = 0.2$, respectively

.

concentration profiles at labels (c), (d) shown in Fig. 6.19 correspond to panels C and D of Fig. 6.20

6.5 Summary

Films in the off-critical case with modulated free surface ($\alpha = 1$) have been studied fixing the lateral domain size and film thickness at particular values. First we have investigated films of thickness $H = 3$ without energetic bias for lateral domain size $L = 10$. We have analysed the difference in the film behaviour of the branches $(1/2, 0)$ and $(1, 0)$ by looking at the bifurcation diagrams varying the lateral domain size for several values of the mean concentration $\bar{c}$. We observed changes in the bifurcations for the laterally structured film $(1/2, 0)$ from subcritical to supercritical. The branch $(1, 0)$ behaves differently as for the chosen domain size it does not reach the point where the character of the bifurcation changes. Then, attention has been focused on neutral films of thickness $H = 5$ where the picture becomes rather crowded as many more branches exist. Therefore we have studied the branches in separate figures. For this type of

film we have first introduced the stratified films, checkerboard films and the laterally structured films $(1/2, 0)$ and $(1, 0)$. Finally, we have introduced the oblique films and the laterally structured film $(1, 0)$. Next, we have investigated films with energetic bias $a^+ = 0.1$ and for this case we have considered films of lateral domain size $L = 12$ and film thickness $H = 5$. As the symmetry ($\bar{c} \to -\bar{c}$) of the bifurcation diagram is broken, we have investigated the branch structure for $\bar{c} > 0$ and $\bar{c} < 0$. Here we have also separated the bifurcation diagrams of the various branches to be studied individually. The study included the laterally structured films $(1/2, 0)$ and $(1, 0)$ with their related oblique branches and also the checkerboard films $(1/2, 1/2)$ and $(1, 1/2)$. To clarify the behaviour of the films along the bifurcation diagrams we have supplemented the study of the bifurcation diagrams by concentration profiles at selected points. In fact, in the off-critical case there exist more branches that should be investigated in a future work.

Chapter 7

Conclusion and Outlook

We have studied films of binary mixtures of immiscible liquids. In particular our interest has focused on determining film thickness and concentration profiles for a two-dimensional system in the two-phase region. The film is situated on a solid energetically neutral substrate that is assumed to be perfectly smooth and horizontal, i.e., no lateral driving forces occur. The upper surface of the film is open to the atmosphere i.e., it is a free surface that may become modulated due to effective forces. The modulation of the free surface and the concentration field are coupled through a pair of the non-linear evolution equations using model-H. The model couples the transport equations of the concentration, the convective Cahn-Hilliard equation, and of momentum, the Navier-Stokes equations, to describe phase separation of a binary liquid mixture or a liquid-gas mixture. In this model, the mixture components are characterised by their concentration gradient. In the past, model-H has mainly been employed to study fluid dynamics in the bulk and simplified by assuming an isothermal setting.

To obtain solutions of the mathematical model we have employed a number of mathematical methods. For the steady states, the finite element method has been used to discretise the domain into a finite number of elements. We have used triangular elements with linear edges. The shape functions are fixed for all the unknown values (Isoparametric coordinates) and written in the natural coordinate system. The free energy functional has been rewritten using a finite element discretisation. An initial solution is built using a coarse meshing which has been used as an indicative solution. Then in subsequent calculations the coarse mesh is refined, especially at the interfaces and the modulated free surface.

The calculations of the layered base states and of their linear stability are performed using numerical continuation techniques (AUTO) [25]. The problem takes the form a system of ordinary differential equations, together with the boundary conditions at the substrate and at the free surface in addition to one integral condition (mass conservation) discretised in space. The equations for the steady state and for the real linear perturbations can be rewritten as a ten-dimensional dynamical system. The resulting algebraic system of equations is solved using an iterative method, starting from known solutions using a combination of Newton and Chord iterative methods. The technique allowed us to follow known solutions when a given set of control parameters is changed.

In the main body of work we have extensively studied non-linear steady state solutions and their bifurcations as a function of several control parameters, such as film thickness, energetic bias at the free surface (corresponding to a linear Marangoni effect), lateral domain size, and the mean concentration of the mixture. We have introduced two types of film surfaces: (i) Flat films where we imposed a strong surface tension at the free surface to keep the surface flat and (ii) films with deformable free surface. We have grouped our results in two parts: in chapter 5 we have discussed critical films i.e., assuming the mean concentration is zero while in chapter 6 attention has been given to off-critical films i.e., when the average mean concentration in the system differs from zero. For the critical films, we have recalculated the one-dimensional results for the bifurcation diagrams for the concentration field and the energy, whilst varying the energetic bias for particular film thicknesses [87]. We have used the 1d results to guide our parameter selection in the 2-dimensional case, in particular, for the energetic bias at the free surface. In the 2d case we investigated neutral flat films and also flat films with energetic bias considering two different film thicknesses, $H = 2.5$ and $H = 5$. For thin films ($H = 2.5 < \pi$) only films that are the laterally stratified or homogeneous films can exist which is consistent with the study in Ref. [44] (see Fig 1.2 (vi)). However, for films of medium thickness ($\pi < H = 5 < 2\pi$) the phase separation can results in other types of film structuring such as stratified layers, checkerboard structuring and oblique solutions. Some of the oblique solutions are also observed experimentally (see Fig 1.2 (iii)-(vi)). Our results showed also a coarsening solution which coarsens from a higher period to lower period. For the case of a film with a modulated surface, we have found more solutions than in the case of flat films. These additional solutions are characterised by their rapid changes in surface modulations. After studying the neutral case, we turned our attention to films with an energetic bias at their free surface. In fact, the stratified solutions play an important role in our results. When the mixture is at the critical total concentration and the free surface is neutral, the two stratified film

solution branches (liquid 1 above liquid 2 and vice versa) are related by symmetry and so lie on the same branch in the bifurcation diagram. This makes the bifurcation diagrams simpler than the ones in the biased surface case where this symmetry is broken. The observations in the biased case show that the stratified solution branches separate, as confirmed by the study of the one-dimensional case. As a consequence of the separation of the stratified film solution branches, the entire bifurcation diagram splits into two groups of branches containing respective laterally stratified films, oblique films and also checkerboard films. We call one group of branches the energetically low group and the other one the energetically high group (see for instance in Fig. 5.14(A)). For the energetically biased films, increasing the energetic bias as the continuation parameter leads to a convergence of the branches $(0,0)$ and the stratified $(0,1/2^a)$ until they join at a saddle node bifurcation $a_{\rm sn}^+$. When the energetic bias exceeds $a_{\rm sn}^+$, these solutions disappear and only one stratified solution remains which we denote $(0,1/2^b)$. For flat films of thickness $H=5$ we have shown results for energetic bias less than $a_{\rm sn}^+$ and also results beyond the point $a_{\rm sn}^+$. However, for the films with modulated surface we have faced some convergence difficulties at high energetic bias. Therefore, we have chosen to present results for thinner films ($H=3.5$) beyond the saddle node bifurcation and without convergence problems.

The linear stability analysis of homogeneous and vertically stratified steady critical films with respect to harmonic disturbances in the lateral direction has been performed. The eigenvalue problem for infinitesimal perturbations of the base state solution has been considered. The evolution of the corresponding normal modes determines the growth rate of the disturbances as a function of the lateral wave number k. The linear stability analysis of the system has been carried out in the general case and the long-wave limit of the general dispersion relation is derived. The stability of the system is investigated in the absence of flow, and in the presence of the Marangoni effect, and the influence of Korteweg stresses on the stability has also been introduced. In particular the system of equations is linearised in the small amplitude of the perturbations ϵ, the pressure is eliminated and the linearised model-H is written as an eigenvalue problem. The linearised boundary conditions are also determined. The base states $c_0(z)$ and solutions $c_1(z), w_1(z), \beta$ of the eigenvalue problem are all obtained employing the numerical continuation algorithms of AUTO [25]. The results show that almost all of our stratified solutions are linearly unstable above a critical domain size. We have also been able to determine the critical wave number k_c which is used to specify the bifurcation points for the branches that bifurcate from the homogeneous and vertically stratified

branches. These support the results gained using the bifurcation diagrams (see the tables introduced in Appendix B). In fact, the comparison is valid only for low energetic bias ($a^+ < 0.5$), and for the case of higher energetic bias the results of the two approaches show differences which we believe is due to the fact that our model reaches its limit of applicability, where the surface tension becomes negative (an unphysical phenomenon of course).

The symmetries of the solutions and boundary conditions for the critical films have been investigated. We have observed that the symmetries of the cuboid (box-shaped object) contains all of our solutions. The three dimensions of the box map to the lateral coordinate x, the vertical coordinate z and the average concentration c of our system. The results show differences in the symmetry groups for the flat films and films of surface modulations, resulting from breaking the symmetry of the boundary conditions at the free surface. Although the translation symmetries can also be considered for our solutions and boundary conditions, these are only discussed here briefly and we intend to focus on this aspect further in future studies.

Off-critical films of a binary mixture have been introduced in chapter 6, where we consider only films with modulated free surfaces and restrict our study to determining the bifurcation diagrams for the energy and the L_2-norms of the concentration and surface modulations as functions of the mean concentration c. First, we have studied the neutral films where we fixed the lateral domain size at $L = 10$. Here we have considered two film thicknesses, thin ($H = 3$) and medium ($H = 5$). As in the critical case, for thin films the only solutions that exist are the homogeneous and the laterally stratified solutions $(1/2, 0)$ and $(1, 0)$. As the stratified structuring is not allowed for such film thickness, no other profile configurations can exist and following the solution branches we find modulations in the concentration and the free surface as well as the energy before they terminate at the homogeneous solution branches which they join at the saddle node bifurcation. However, for neutral films of thickness $H = 5$ the laterally structured solution branches terminate at the homogeneous one, through several branches that show various different profile configurations, which bifurcate at saddle node bifurcations.

In the experimental results from Ref. [30] for the off-critical films of a binary mixture that are shown in Fig. 1.4, mounds are produced by droplets and holes of one liquid inside the other are clearly observed. Our results show similar mounds and holes for average concentrations far from the critical state, we find new branches of solutions that

do not exist in the critical case. Many of these new branches bifurcate at saddle node bifurcations from the branches that are present in the critical case.

In the work presented in this thesis, we have discovered that liquid films of binary mixture of immiscible liquids can undergo phase separation to form very many different structures. The phase separation can be influenced by many factors, such as the film thickness, the lateral domain size, the mean concentration of the mixture, the energetic bias at the free surface of the film, that corresponds to the Marangoni effect. Depending on these factors the film profiles can take different structures such as a completely homogeneous film, laterally stratified, horizontally stratified, checkerboard structuring, oblique structuring, coarsening solutions and many other structures. The difference in the concentrations of the mixtures plays an important role in producing droplets of the minority species rich phase, producing mounds or holes inside the majority species rich phase. The structures formed in the off-critical film are more complicated than in the critical case. We also noted that most of the bifurcations for the off-critical compositions far from the critical composition, are saddle node bifurcations.

Appendix A

Symmetry Group

A.1 Symmetries of Cuboid

A symmetry operation may be visualised geometrically by its invariant geometric element, usually called symmetry element. The symmetry element may be a point, line, or plane depending on the symmetry operation. It may correspond to the centre of inversion (point), the rotation axis (line), or the reflection (mirror) plane. Only the identity operation I and the translations T do not define such a symmetry element. The symmetry element of a symmetry operation is uniquely defined, however, more than one symmetry operation may belong to a symmetry element. In fact there exists a confusion concerning the terms "symmetry element" and "symmetry operation". It is caused by the fact that symmetry operations are the group elements of the symmetry groups. Symmetry operations can be combined resulting in other symmetry operations and forming a symmetry group. Symmetry elements can not be combined such that the combination results in a uniquely determined other symmetry element. As a consequence, symmetry elements do not form groups, and group theory can not be applied to them. Nevertheless, the description of symmetry by symmetry elements is very useful, as will be seen in the following discussion.

Here we give an example that illustrates the way how to extract the symmetry groups of our solutions in the critical case. Consider the planes xz, xc, zc that are perpendicular to the axises c, z, x, respectively. We assume the origin in the centre of the cuboid (see Fig. A.1). Let the symbol I indicate the identity element of the symmetry group (no action) and the symbols σ_{xz}, σ_{xc} and σ_{zc} indicate the reflections at the planes xz, xc and

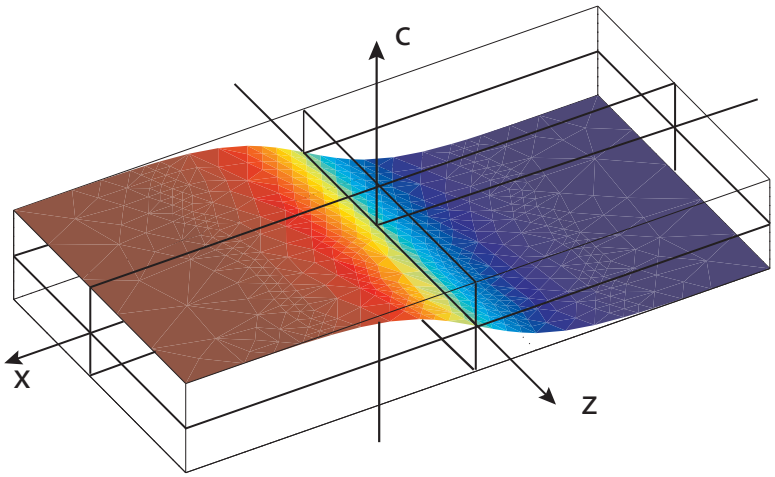

Figure A.1: Shown is the the profile of the branch (1/2,0). The figure shows how the symmetries of the profile have been extracted.

zc, respectively, the symbols π_x, π_z, π_c indicate the rotation about x, z and c axes by the angle π radian, respectively, and ρ_{xzc} indicates the inversion through the origin. Then the solution profile shown in Fig. A.1 which represents the solution branch $(1/2, 0)$ for a film with a flat free surface can be used as an example to illustrate how the symmetries of our solutions are extracted. If we reflect this solution profile at the plane xc we obtain exactly the same solution (surface) which indicates that this solution is invariant under the operation σ_{xc}. Another operation is the rotation of the solution profile about the z axis which yields the same solution, i.e., it is invariant under the operation π_z. The solution is also invariant under inversion through the origin in addition to identity operation. Note that, the resulting set $\{I, \sigma_{xc}, \pi_z, \rho_{xzc}\}$ is a group. Therefore, the solution $(1/2, 0)$ for flat film is invariant under the symmetry group $\{I, \sigma_{xc}, \pi_z, \rho_{xzc}\}$. That is a subgroup of the symmetry group of the cuboid (given in Table A.1) Note that, the

Table A.1: Group table for cuboid that in our case is spanned by two spatial dimensions (x, z) and concentration c.

	I	σ_{xz}	σ_{xc}	σ_{zc}	π_x	π_z	π_c	ρ_{xzc}
I	I	σ_{xz}	σ_{xc}	σ_{zc}	π_x	π_z	π_c	ρ_{xzc}
σ_{xz}	σ_{xz}	I	π_x	π_z	σ_{xc}	σ_{zc}	ρ_{xzc}	π_c
σ_{xc}	σ_{xc}	π_x	I	π_c	σ_{xz}	ρ_{xzc}	σ_{zc}	π_z
σ_{zc}	σ_{zc}	π_z	π_c	I	ρ_{xzc}	σ_{xz}	σ_{xc}	π_x
π_x	π_x	σ_{xc}	σ_{xz}	ρ_{xzc}	I	π_c	π_z	σ_{zc}
π_z	π_z	σ_{zc}	ρ_{xzc}	σ_{xz}	π_c	I	π_x	σ_{xc}
π_c	π_c	ρ_{xzc}	σ_{zc}	σ_{xc}	π_z	π_x	I	σ_{xz}
ρ_{xzc}	ρ_{xzc}	π_c	π_z	π_x	σ_{zc}	σ_{xc}	σ_{xz}	I

symmetry groups of all the other solutions for different films are extracted in the same way as we have compared all the symmetries of the cuboid with our solutions.

A.2 Translation Symmetries

If we consider the translations of solutions within an extended (periodically closed) domain of size $4L$, where L is our computational domain then the maximal symmetry group consists of the translations $L, 2L, 3L, 4L = 0$ denoted by $T^x_L, T^x_{2L}, T^x_{3L}, T^x_{4L} = I$ (see Fig. A.2), respectively. All the translation symmetries of our solution are contained in this symmetry group. The group table is given as Table A.2. The only proper subgroup is the group $\{I, T^x_{2L}\}$ and the group table is given in Table A.3. Note that, the translation symmetry can be applied on all the results shown in Chapter 5 and every solution has either the full symmetry group $\{T^x_L, T^x_{2L}, T^x_{3L}, I\}$ or the proper symmetry subgroup $\{I, T^x_{2L}\}$.

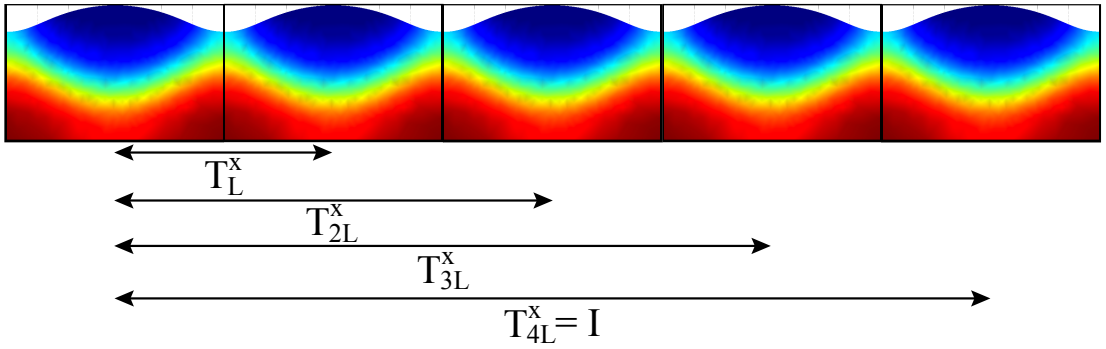

Figure A.2: Sample shows a $n = 1$ profile translated by L, $2L$, $3L$ and $4L = I$. This profile is invariant under all the translations.

Table A.2: Translation symmetry group table.

	I	T^x_{3L}	T^x_{2L}	T^x_L
I	I	T^x_{3L}	T^x_{2L}	T^x_L
T^x_{3L}	T^x_{3L}	T^x_{2L}	T^x_L	I
T^x_{2L}	T^x_{2L}	T^x_L	I	T^x_{3L}
T^x_L	T^x_L	I	T^x_{3L}	T^x_{2L}

Table A.3: The table for the only proper translation symmetries subgroup. The element T^x_{2L} corresponds to translation by $2L$ and $T^x_{4L} = I$.

	I	T^x_{2L}
I	I	T^x_{2L}
T^x_{2L}	T^x_{2L}	I

The only proper subgroups of this group are the identity and the group presented by the following group table. We do not consider here the complete group containing beside

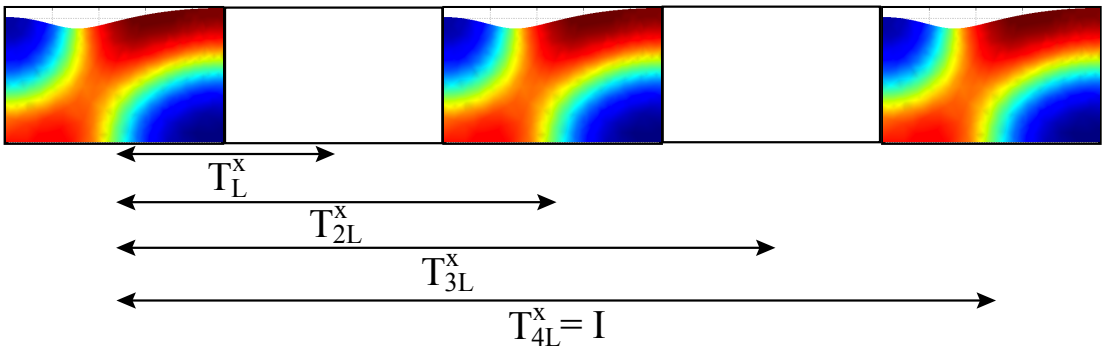

Figure A.3: Sample shows a $n = 1/2$ profile translated by $2L$ and $4L = I$. This profile is invariant under these translations.

others all the elements of table A.1 and A.2 as the present consideration are sufficient to order all the solution branches we have found numerically.

Appendix B

Additional Linear Stability Results

Additional linear stability results have been calculated for flat films and films with modulated free surface in the critical case. Below we complete the picture for cases for which the bifurcation diagrams are not shown in Chapter 5. We present the dispersion relations and also tables that show the critical lateral domain size of the system and the corresponding critical wavenumber for various films depending on the film thickness and the energetic bias. This allows for a quantitative comparison of the different employed methods.

B.1 Linear Stability for Films of Thickness $H = 3.5$

We studied films of thickness $H = 3.5$ in Chapter 5, without showing the linear stability analysis for layered film. This is done here for both flat films and films with modulated free surface for the homogeneous (weakly stratified) and stratified films. Here we show only the dispersion relations that have not been introduced in chapter 5.

B.1.1 Flat Films

In this section we show the dispersion relation for flat films of thickness $H = 3.5$. The dispersion relation for the branches (0,0) and $(0,1/2^a)$ are introduced in Figs. B.1(A) and (B) respectively, whereas the dispersion relation for the branch $(0,1/2^b)$ is introduced in Fig. B.2 considering different energetic biases. We consider the neutral film and films with energetic biases $a^+ = 0.05$ and with energetic bias $a^+_{\text{sn}} \sim 0.0677$.

As the film is of medium thickness, the branches (0,0) and (0,$1/2^a$) annihilate at the saddle node bifurcation at $a^+_{\rm sn} \sim 0.0677$ Beyond that point there remains only the solution branch (0,$1/2^b$) (see also Figs. 5.1 and 5.2 in the main text). As we consider films with an imposes flat surface, we can go further towards higher energetic bias. Here the dispersion relations are given for $a^+ = 0.05, 0.1, 0.2, 0.3, 0.4, 0.6$ and 1.

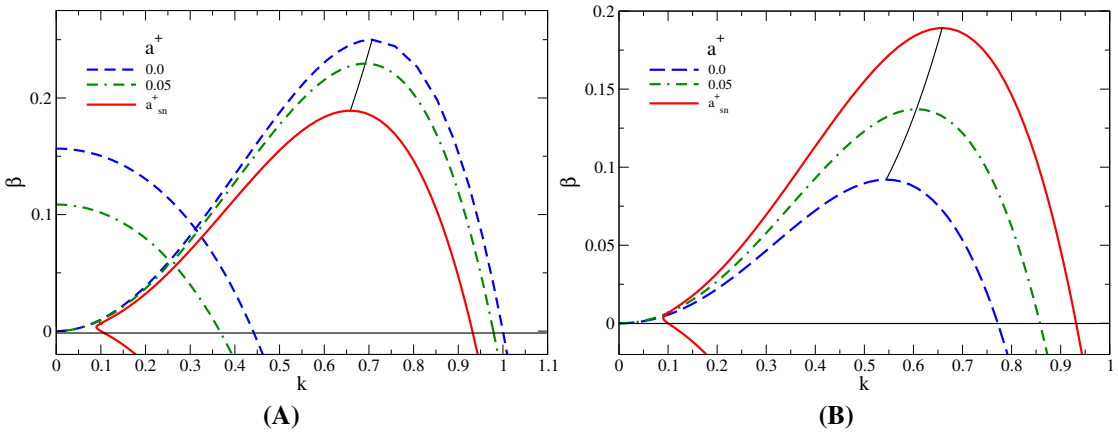

Figure B.1: Shown are the dispersion relations for flat films of thickness ($H = 3.5$). Panel (A) are dispersion relations for the branch (0,0). Panel (B) are dispersion relations for the branch (0,$1/2^a$). The dispersion relations are for the neutral case, at the energetic bias $a^+ = 0.05$ and at the saddle node bifurcation $a^+_{\rm sn} = 0.0677$ as shown in the legends.

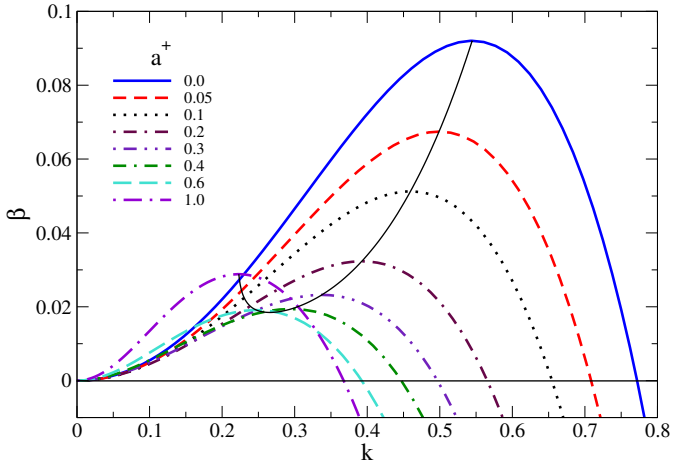

Figure B.2: Linear stability for flat film of thickness $H = 3.5$ for different energetic biases at the free surface for (0,$1/2^b$) branch. The curves represent different energetic biases as given in the legend. The thin solid curve follows the local maxima of the growth rate β_{max}.

In panel (A) of Fig. B.3 we show the critical wave number k_c and the wavenumber of the fastest mode k_{max}, i.e., the value of k that corresponds to β_{max}. In panel (B) we show the maximal growth rates of various branches as functions of the energetic bias.

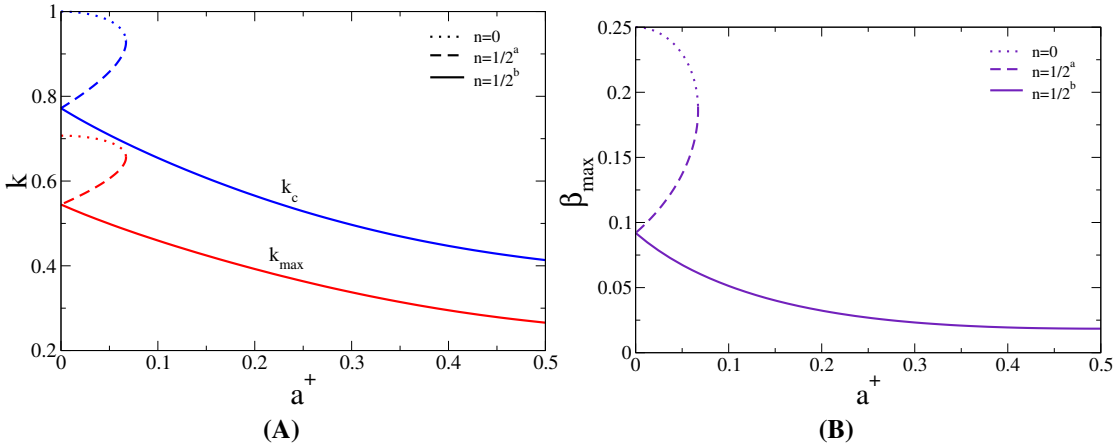

Figure B.3: Panel (A) shows the critical wavenumber k_c and fastest growing wavenumber k_{max}. Panel (B) shows local maxima of the growth rate β_{max} for flat film of thickness $H = 3.5$ as functions of the energetic bias at the free surface a^+. The individual lines correspond to the various branches as indicated by the legends.

B.1.2 Films with Surface Modulations

The dispersion relations for films of thickness $H = 3$ with surface modulations given in Fig. B.4. We show the dispersion relation for the homogeneous branch $(0, 0)$ and for the branch $(0, 1/2^a)$ in Fig. B.4(A) and (B), respectively. The black thin line follows β_{max} for different energetic biases.

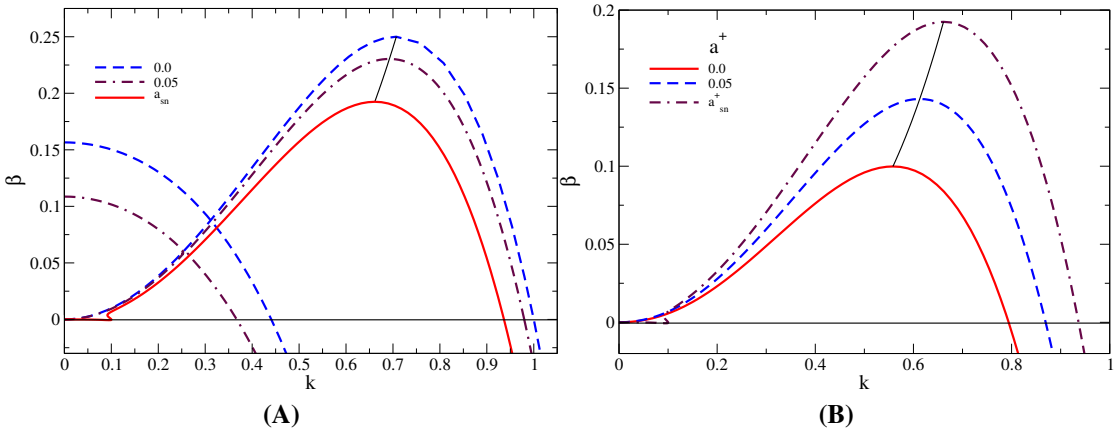

Figure B.4: Shown are the dispersion relations for surface modulated films of thickness $H = 3.5$ for the neutral film, film with energetic bias $a^+ = 0.05$ and at the saddle node bifurcation a^+_{sn} as shown in legends. Panel (A) depicts the dispersion relation for the branch (0,0). Panel (B) depicts the dispersion relation for the branch $(0,1/2^a)$.

B.2 Linear Stability for Films of Thickness $H = 5$

Here we introduce the linear stability for films with surface modulations of thickness $H = 5$. Compared to the case of flat films, there are some differences in the dispersion relation particularly for higher energetic bias. These differences appear as a shift in the points of critical lateral domain size L_c towards larger values. For modulated surface films we consider $\alpha = 1$ in Eq.3.49. This implies that the surface tension reaches values where it lose the physical meaning (negative surface tension) at smaller a^+ than that for flat films particularly for the branch $(0, 1/2^b)$. Thin curves shown in Figs. B.5 and B.6

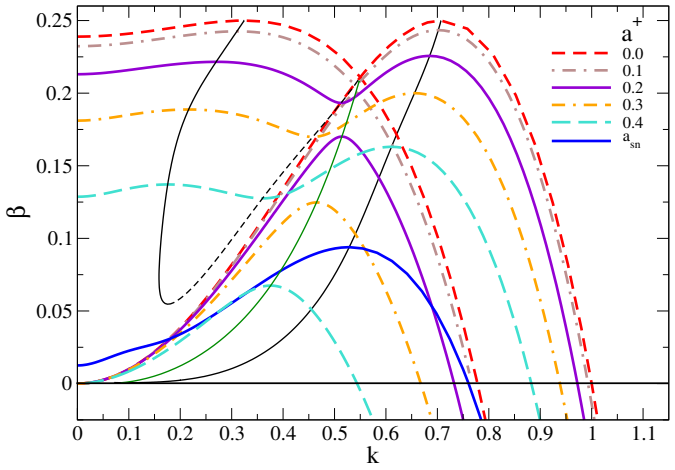

Figure B.5: The linear stability of the $(0, 0)$ branch for surface modulated film of thickness $H = 5.0$. Shown are the cases without ($a^+ = 0$) and with ($a^+ > 0$) energetic bias at the free surface for a^+ as given in the legend. Given are two sets of dispersion curves: for the lateral instability mode (larger $k_{\max}$ at $a^+ = 0$), and for the checker-board instability mode (smaller $k_{\max}$ at $a^+ = 0$). The thin dotted and dashed lines are parameterized by a^+ and follow the maxima ($k_{\max}, \beta_{\max}$) and minima of the dispersion relations.

are following the local maximal growth rate β_{max} (or local minimum growth rate). They show also some differences to the flat film case. Note that, the dispersion relation for the branch $(0, 1/2^b)$ shown in Fig. B.6 behaves in a different way particularly for relatively high energetic bias. In Fig. B.7(A) we show the critical wavenumber k_c and k_{max} that corresponds to β_{max} and in Fig. B.7(B) we show the β_{max} as a function of the energetic bias a^+.

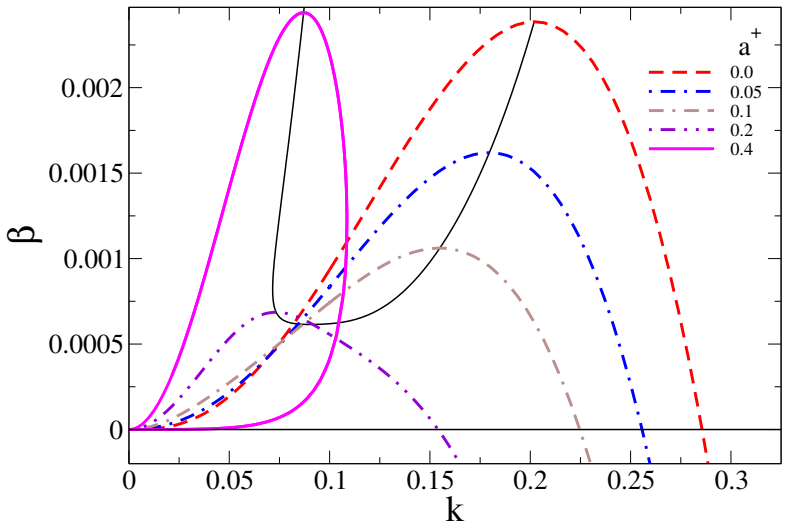

Figure B.6: Linear stability for films of thickness $H = 5$ with modulated free surface. The dispersion relation of the branch $(0,1/2^b)$ is considered for different energetic biases as depicted in the legends. The thin solid curve represents the local maxima of the growth rate (β_{max}) in terms of the energetic bias a^+.

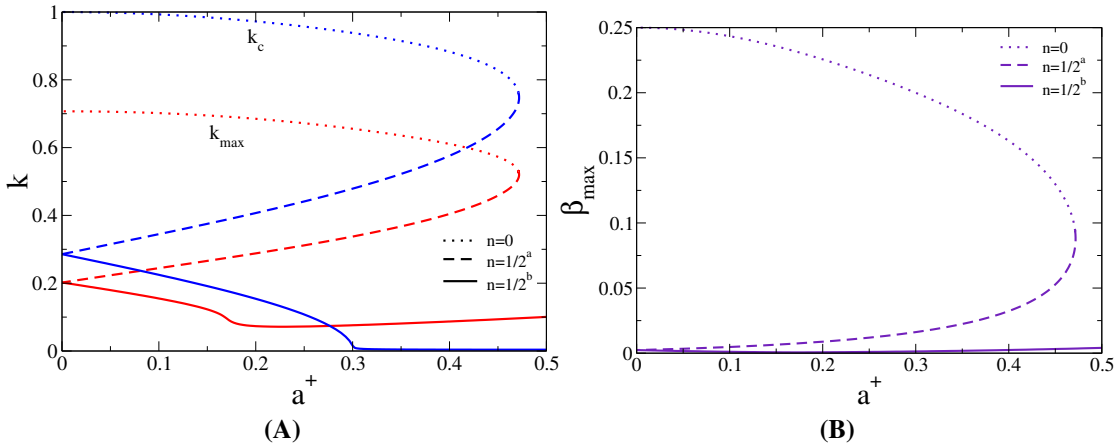

Figure B.7: Shown in panel (A) are the critical wavenumber k_c and the fastest growing wave number k_{max} as functions of the energetic bias a^+. Panel (B) shows local maxima of the growth rate β_{max} in terms of the energetic bias a^+ for film with modulated free surface of thickness $H = 5$.

B.3 Tables of the critical domain size and the corresponding critical wave number

Here we introduce tables that collect our results for the critical domain size L_c and the corresponding critical wave number k_c as obtained from the linear stability analysis

Table B.1: The critical wavenumber k_c and the related system size L_c where one expects a steady state bifurcation for (0,0) branch at different energetic biases and for different film thicknesses. The symbols k_c^L and L_c^L indicate the critical wavenumber and the corresponding lateral domain size for the laterally stratified branches, respectively. The symbols k_c^{Ch} and L_c^{Ch} indicate to the critical wavenumber and the corresponding lateral domain size for the checkerboard branches, respectively.

Mean Height	Energetic Bias	Flat Film				Height-Modulated Film			
H	a^+	k_c^L		L_c^L		k_c^L		L_c^L	
2.5	0.0	1.000		2π		1.000		2π	
	0.1	0.985		6.379		0.988		6.360	
	0.2	0.945		6.649		0.958		6.559	
	0.3	0.893		7.036		0.903		6.958	
	0.4	0.835		7.525		0.850		7.392	
		k_c^L	k_c^{Ch}	L_c^L	L_c^{Ch}	k_c^L	k_c^{Ch}	L_c^L	L_c^{Ch}
3.5	0.0	1.000	0.443	2π	14.183	1.000	0.443	2π	14.183
	0.05	0.979	0.369	6.418	17.028	0.980	0.370	6.411	16.990
	$\sim a_{\text{sn}}^+$	0.932	0.107	6.742	58.721	0.937	~ 0.099	6.706	~ 63.467
5	0.0	1.0000	0.7788	2π	8.0678	1.0000	0.7774	2π	8.0823
	0.1	0.9950	0.7685	6.3148	8.1759	0.9944	0.7682	6.3186	8.1791
	0.2	0.9729	0.7317	6.4582	8.5871	0.9720	0.7336	6.4642	8.5649
	0.3	0.9391	0.6656	6.6906	9.4399	0.9394	0.6674	6.6885	9.4144
	0.4	0.8847	0.5479	7.1021	11.4678	0.8830	0.5448	7.1157	11.5330
	$\sim a_{\text{sn}}^+$	0.7597		8.2706		0.7618		8.2478	

Table B.2: The critical wavenumber k_c and the related domain size L_c for the stratified branch (0,$1/2^a$) with different film heights H and energetic bias a^+, calculated from the linear stability results

Mean Height	Energetic Bias	L.S for Flat Film		L.S for Height-Modulated Film	
H	a^+	k_c	L_c	k_c	L_c
3.5	0.0	0.7727	8.1315	0.7948	7.9054
	0.05	0.8585	7.3188	0.8708	7.2154
	$\sim a_{\text{sn}}^+$	0.9333	6.7322	0.9370	6.7056
5	0.0	0.1235	50.8760	—	—
	0.1	—	—	—	—
	0.2	—	—	—	—
	0.3	0.3780, 0.1200	16.6222, 52.3599	—	—
	0.4	0.5360	11.7224	—	—
	$\sim a_{\text{sn}}^+$	0.7618	8.2478	—	—

(Chapter 5) for flat films and films with surface modulations at different mean thicknesses and for various energetic biases at their free surface.

Table B.3: The critical wavenumber k_c and the related domain size L_c for the stratified branch (0,$1/2^b$) with different film heights H and energetic bias a^+, calculated from the linear stability results

Mean Height H	Energetic Bias a^+	L.S for Flat Film		L.S for Height-Modulated Film	
		k_c	L_c	k_c	L_c
3.5	0.0	0.7731	8.1273	0.7954	7.8994
	0.05	0.7094	8.8570	0.7402	8.4885
	0.1	.06555	9.5853	0.6922	9.0771
	0.2	0.5652	11.1167	0.6068	10.3546
	0.3	0.4967	12.6499	0.5287	11.8842
	0.4	0.4476	14.0375	0.4537	13.8488
5	0.0	0.1235	50.8760	0.2866	21.9232
	0.1	0.1749	35.9244	0.2555	24.5917
	0.2	0.1939	32.4043	0.2244	27.9999
	0.3	0.2074	30.2950	0.1555	40.4063
	0.4	0.2185	28.7560	—	—

Bibliography

[1] D.J. Acheson. Elementary fluid dynamics. Oxford University Press, USA, 1990.

[2] H. Ade, AP Smith, S. Qu, S. Ge, J. Sokolov, M. Rafailovich, et al. Phase segregation in polymer thin films: Elucidations by x-ray and scanning force microscopy. EPL (Europhysics Letters), 45:526, 1999.

[3] H. W. Alt and I. Pawlow. A mathematical model of dynamics of non-isothermal phase separation. Physica D, 59:389–416, 1992.

[4] D. M. Anderson, G. B. McFadden, and A. A. Wheeler. Diffuse-interface methods in fluid mechanics. Ann. Rev. Fluid Mech., 30:139–165, 1998.

[5] L. K. Antanovskii. A phase field model of capillarity. Phys. Fluids, 7:747–753, 1995.

[6] L. K. Antanovskii. Microscale theory of surface tension. Phys. Rev. E, 54:6285–6290, 1996.

[7] M. Assenheimer, B. Khaykovich, and V. Steinberg. Phase separation of a critical binary mixture subjected to a temperature gradient. Physica A, 208:373–393, 1994.

[8] G. K. Batchelor. An introduction to fluid dynamics. Cambridge Univ. Pr., 2000.

[9] K. J. Bathe. Finite Element Procedures. Prentice-Hall, Inc., 5th edition, 1996.

[10] N. Bessonov, J. A. Pojman, and V. Volpert. Modelling of diffuse interfaces with temperature gradients. J. Eng. Math., 49:321–338, 2004.

[11] K. Binder. Spinodal decomposition in confined geometry. J. Non-Equilib. Thermodyn., 23:1–44, 1998.

[12] D. Bonn, J. Eggers, J. Indekeu, J. Meunier, and E. Rolley. Wetting and spreading. Rev. Mod. Phys., 81:739–805, 2009.

[13] R. Borcia and M. Bestehorn. Phase-field model for Marangoni convection in liquid-gas systems with a deformable interface. Phys. Rev. E, 67:066307, 2003.

[14] R. Borcia and M. Bestehorn. Phase-field simulations for evaporation with convection in liquid-vapor systems. Eur. Phys. J. B, 44:101–108, 2005.

[15] A.J. Bray. Theory of phase-ordering kinetics. Adv. Phys., 51:481–587, 2002.

[16] J. W. Cahn and J. E. Hilliard. Free energy of a nonuniform system. 1. Interfacual free energy. J. Chem. Phys., 28:258–267, 1958.

[17] A. M. Cazabat, F. Heslot, S. M. Troian, and P. Carles. Fingering instability of thin spreading films driven by temperature gradients. Nature, 346:824–826, 1990.

[18] R. Chhabra. Bubbles, drops, and particles in non-Newtonian fluids. CRC Press, Boca Raton, Fla, 1993.

[19] G. Coulon, B. Collin, D. Ausserre, D. Chatenay, and TP Russell. Islands and holes on the free surface of thin diblock copolymer films. i. characteristics of formation and growth. J. Physique, 51:2801–2811, 1990.

[20] R. V. Craster and O. K. Matar. Dynamics and stability of thin liquid films. Rev. Mod. Phys., 81:1131–1198, 2009.

[21] J. Crawford, M. Golubitsky, M. Gomes, E. Knobloch, and I. Stewart. Boundary conditions as symmetry constraints. Singularity Theory and its Applications, pages 63–79, 1991.

[22] J. D. Crawford and E. Knobloch. Symmetry and symmetry-breaking bifurcations in fluid dynamics. Ann. Rev. Fluid Mech., 23:341–387, 1991.

[23] P. G. de Gennes. Wetting: Statics and dynamics. Rev. Mod. Phys., 57:827–863, 1985.

[24] C. M. Dekeyser, S. Biltresse, J. Marchand-Brynaert, P. G. Rouxhet, and C. C. Dupont-Gillain. Submicrometer-scale heterogeneous surfaces by PS-PMMA demixing. Polymer, 45:2211–2219, 2004.

[25] E. J. Doedel, R. C. Paffenroth, A. R. Champneys, T. F. Fairgrieve, Y. A. Kuznetsov, B. E. Oldeman, B. Sandstede, and X. Wang. AUTO 2000: CONTINUATION AND BIFURCATION SOFTWARE, 2002.

[26] P. G. Drazin and N. Riley. The Navier-Stokes equations: a classification of flows and exact solutions. Cambridge Univ Pr, 2006.

[27] E. B. Dussan V and S. H. Davis. On the motion of a fluid-fluid interface along a solid surface. Journal of Fluid Mech., 65:71–95, 1974.

[28] K. R. Elder, T. M. Rogers, and R. C. Desai. Early stages of spinodal decomposition for the cahn-hilliard-cook model of phase separation. Phys. Rev. B, 38:4725, 1988.

[29] M. H. Eres, L. W. Schwartz, and R. V. Roy. Fingering phenomena for driven coating films. Phys. Fluids, 12:1278–1295, 2000.

[30] B. D. Ermi, A. Karim, and J. F. Douglas. Formation and dissolution of phase-separated structures in ultrathin blend films. Journal of Polymer Science Part B: Polymer Physics, 36:191–200, 1998.

[31] T. E. Faber. Fluid dynamics for physicists. Cambridge Univ Pr, 1995.

[32] H. P. Fischer, P. Maass, and W. Dieterich. Novel surface modes in spinodal decomposition. Phys. Rev. Lett., 79:893–896, 1997.

[33] H. P. Fischer, P. Maass, and W. Dieterich. Diverging time and length scales of spinodal decomposition modes in thin films. Europhys. Lett., 42:49–54, 1998.

[34] C. Foiaş. Navier-Stokes equations and turbulence, volume 83. Cambridge Univ Pr, 2001.

[35] J. B. Franzini, E. J. Finnemore, and R. L. Daugherty. Fluid mechanics with engineering applications. McGraw-Hill, 1997.

[36] L. Frastia, U. Thiele, and L. M. Pismen. Determination of the thickness and composition profiles for a film of binary mixture on a solid substrate. Math. Model. Nat. Phenom., 6:62–86, 2011.

[37] N. Fraysse and G. M. Homsy. An experimental study of rivulet instabilities in centrifugal spin coating of viscous newtonian and non-newtonian fluids. Phys. fluids, 6:1491, 1994.

[38] M. Geoghegan and G. Krausch. Wetting at polymer surfaces and interfaces. Prog. Polym. Sci., 28(2):261–302, 2003.

[39] A. A. Golovin, S. H. Davis, and A. A. Nepomnyashchy. A convective Cahn-Hilliard model for the formation of facets and corners in crystal growth. Physica D, 122:202–230, 1998.

[40] A. A. Golovin, A. A. Nepomnyashchy, S. H. Davis, and M. A. Zaks. Convective Cahn-Hilliard models: From coarsening to roughening. Phys. Rev. Lett., 86:1550–1553, 2001.

[41] L. V. Govor, J. Parisi, G. H. Bauer, and G. Reiter. Instability and droplet formation in evaporating thin films of a binary solution. Phys. Rev. E, 71:051603, 2005.

[42] S. J. Han. Domain structures on PS-PMMA mixture films. J. Korean Phys. Soc., 54:749–753, 2009.

[43] J. Heier, J. Groenewold, S. Huber, F. Nesch, and R. Hany. Nanoscale structuring of semiconducting molecular blend films in the presence of mobile counterions. Langmuir, 24:7316–7322, 2008.

[44] S. Y. Heriot and R. A. L. Jones. An interfacial instability in a transient wetting layer leads to lateral phase separation in thin spin-cast polymer-blend films. Nat. Mater., 4:782–786, 2005.

[45] P. C. Hohenberg and B. I. Halperin. Theory of dynamic critical phenomena. Rev. Mod. Phys., 49:435–479, 1977.

[46] R. B. Hoyle. Pattern formation: an introduction to methods. Cambridge Univ Pr, 2006.

[47] J. Iannelli. Characteristics Finite Element Methods in Computational Fluid Dynamics. Springer-Verlag Berlin Heidelberg, 2006.

[48] K. D. Jandt, J. Heier, F. S. Bates, and E. J. Kramer. Transient surface roughening of thin films of phase separating polymer mixtures. Langmuir, 12:3716–3720, 1996.

[49] D. Jasnow and J. Viñals. Coarse-grained description of thermo-capillary flow. Phys. Fluids, 8:660–669, 1996.

[50] R. Kenzler, F. Eurich, P. Maass, B. Rinn, J. Schropp, E. Bohl, and W. Dieterich. Phase separation in confined geometries: Solving the Cahn-Hilliard equation with generic boundary conditions. Comp. Phys. Comm., 133:139–157, 2001.

[51] T. Kerle, J. Klein, and R. Yerushalmi-Rozen. Accelerated rupture at the liquid/liquid interface. Langmuir, 18:10146–10154, 2002.

[52] C. J. Lawrence. The mechanics of spin coating of polymer films. Phys. Fluids, 31:2786, 1988.

[53] L. Leger and J. F. Joanny. Liquid spreading. Rep. Prog. Phys., 55:431, 1992.

[54] I. Leshev and G. Peev. Film flow on a horizontal rotating disk. Chem. Eng. Process., 42:925–929, 2003.

[55] J. Lowengrub and L. Truskinovsky. Quasi-incompressible Cahn-Hilliard fluids and topological transitions. Proc. R. Soc. London Ser. A-Math. Phys. Eng. Sci., 454:2617–2654, 1998.

[56] Z. Ma. Group theory for physicists. World Scientific Pub Co Inc, 2007.

[57] S. Madruga and U. Thiele. Decomposition driven interface evolution for layers of binary mixtures: II. Influence of convective transport on linear stability. Phys. Fluids, 21:062104, 2009.

[58] L. Mahadevan, M. Adda-Bedia, and Y. Pomeau. Four-phase merging in sessile compound drops. J. Fluid Mech., 451:411–420, 2002.

[59] P. Müller-Buschbaum, E. Bauer, S. Pfister, S. V. Roth, M. Burghammer, C. Riekel, C. David, and U. Thiele. Creation of multi-scale stripe-like patterns in thin polymer blend films. Europhys. Lett., 73:35–41, 2006.

[60] P. Müller-Buschbaum, J. S. Gutmann, and M. Stamm. Control of surface morphology by the interplay between phase separation and dewetting. J. Macromol. Sci.–Phys., 38:577–592, 1999.

[61] A. Münch, C. P. Please, and B. Wagner. Spin coating of an evaporating polymer solution. Phys. Fluids, 23:102101, 2011.

[62] T. Nambu, Y. Yamauchi, T. Kushiro, and S. Sakurai. Micro-convection, dissipative structure and pattern formation in polymer blend solutions under temperature gradients. Faraday Discuss., 128:285–298, 2005.

[63] L. O. Naraigh and J. L. Thiffeault. Bubbles and filaments: Stirring a cahn-hilliard fluid. Phys.Rev. E, 75:016216, 2007.

[64] A. Novick-Cohen. The nonlinear Cahn - Hilliard equation: Transition from spinodal decomposition to nucleation behavior. J. Stat. Phys., 38:707–723, 1985.

[65] R. M. Olson and S. J. Wright. Essentials of engineering fluid mechanics. Harper & Row New York, 1980.

[66] A. Ōnuki. Phase transition dynamics. Cambridge Univ Pr, 2002.

[67] A. Oron, S. H. Davis, and S. G. Bankoff. Long-scale evolution of thin liquid films. Rev. Mod. Phys., 69:931–980, 1997.

[68] R. Paul, U. Karabiyik, M.C. Swift, and et al. Phase separation in poly(tert-butyl acrylate)/polyhedral oligomeric silsesquioxane (poss) thin film blends. Langmuir, 24:5079–5090, 2008.

[69] L. M. Pismen and Y. Pomeau. Disjoining potential and spreading of thin liquid layers in the diffuse interface model coupled to hydrodynamics. Phys. Rev. E, 62:2480–2492, 2000.

[70] S. B. Pope. Turbulent flows. Cambridge Univ Pr, 2000.

[71] D. Prieling and H. Steiner. Analysis of mass transfer in thin liquid films on spinning disks using the integral method. PAMM, 11:583–584, 2011.

[72] S. Puri and K. Binder. Power laws and crossovers in off-critical surface-directed spinodal decomposition. Phys. Rev. Lett., 86:1797–1800, 2001.

[73] S. Puri and K. Binder. Surface-directed phase separation with off-critical composition: Analytical and numerical results. Phys. Rev. E, 66:061602, 2002.

[74] S. Puri, K. Binder, and H. L. Frisch. Surface effects on spinodal decomposition in binary mixtures: The case with long-ranged surface fields. Phys. Rev. E, 56:6991, 1997.

[75] J. Raczkowska, J. Rysz, A. Budkowski, J. Lekki, M. Lekka, A. Bernasik, K. Kowalski, and P. Czuba. Surface patterns in solvent-cast polymer blend films analyzed with an integral-geometry approach. Macromolecules, 36:2419–2427, 2003.

[76] P. C. Ray and B. S. Dandapat. Flow of thin liquid film on a rotating disk in the presence of a transverse magnetic field. Q. J. Mechanics. Appl. Math., 47:297–304, 1994.

[77] G. Reiter. Dewetting of thin polymer films. Phys. Rev. Lett., 68:75–78, 1992.

[78] O. Reynolds. On the dynamical theory of incompressible viscous fluids and the determination of the criterion. Proceedings of the Royal Society of London, 56:40–45, 1894.

[79] D. H. Sattinger. Bifurcation and symmetry breaking in applied mathematics. J. Amer. Math. Soc., 3, 1980.

[80] W. R. Schowalter. Mechanics of non-Newtonian fluids. Pergamon press New York, 1978.

[81] L. W. Schwartz and R. V. Roy. Theoretical and numerical results for spin coating of viscous liquids. Phys. Fluids, 16:569–584, 2004.

[82] A. Sharma, R. Khanna, and G. Reiter. A thin film analog of the corneal mucus layer of the tear film: An enigmatic long range non-classical dlvo interaction in the breakup of thin polymer films. Colloid Surf. B-Biointerfaces, 14:223–235, 1999.

[83] A. Sharma and G. Reiter. Instability of thin polymer films on coated substrates: Rupture, dewetting and drop formation. J. Colloid Interface Sci., 178:383–399, 1996.

[84] M. Souche and N. Clarke. Phase equilibria in polymer blend thin films: A hamiltonian approach. J. Chem. Phys., 131:244903, 2009.

[85] R. H. Stogner, G. F. Carey, and B. T. Murray. Approximation of Cahn–Hilliard diffuse interface models using parallel adaptive mesh refinement and coarsening with c^1 elements. Int. J. Numer. Meth. Engng., 76:636–661, 2008.

[86] T. Suo and D. Yan. Phase behaviors of polymer solution confined between two concentric cylinders. Polymer, 52:1686–1691, 2011.

[87] U. Thiele, S. Madruga, and L. Frastia. Decomposition driven interface evolution for layers of binary mixtures: I. Model derivation and stratified base states. Phys. Fluids, 19:122106, 2007.

[88] C. Ton-That, A. G Shard, and R. H Bradley. Surface feature size of spin cast PS/PMMA blends. Polymer, 43:4973–4977, 2002.

[89] G. A. Truskey, F. Yuan, and D. F. Katz. Transport phenomena in biological systems. Pearson/Prentice Hall, 2004.

[90] C. Tufano, G. W. M. Peters, and H. E. H. Meijer. Confined flow of polymer blends. Langmuir, 24:4494–4505, 2009.

[91] J. D. Van der Waals. The thermodynamic theory of capillarity under the hypothesis of a continuous variation of density. J. Stat. Phys., 20:200–244, 1979.

[92] N. Vladimirova, A. Malagoli, and R. Mauri. Diffusion-driven phase separation of deeply quenched mixtures. Phys. Rev. E, 58:7691–7699, 1998.

[93] N. Vladimirova, A. Malagoli, and R. Mauri. Diffusiophoresis of two-dimensional liquid droplets in a phase-separating system. Phys. Rev. E, 60:2037, 1999.

[94] N. Vladimirova, A. Malagoli, and R. Mauri. Two-dimensional model of phase segregation in liquid binary mixtures. Phys. Rev. E, 60:6968–6977, 1999.

[95] S. Walheim, M. Böltau, J. Mlynek, G. Krausch, and U. Steiner. Structure formation via polymer demixing in spin-cast films. Macromolecules, 30:4995–5003, 1997.

[96] H. Wang and R. J. Composto. Thin film polymer blends undergoing phase separation and wetting: Identification of early, intermediate, and late stages. J. Chem. Phys., 113:10386–10397, 2000.

[97] G. Wen, Z. Sun, T. Shi, J. Yang, W. Jiang, L. An, and B. Li. Thermodynamics of PMMA/SAN blends: Application of the sanchez-lacombe lattice fluid theory. Macromolecules, 34:6291–6296, 2001.

[98] S. K. Wilson, R. Hunt, and B. R. Duffy. The rate of spreading in spin coating. J. Fluid Mech., 413:65–88, 2000.

[99] L. T. Yan and X. M. Xie. Wetting-layer formation mechanisms of surface-directed phase separation under different quench depths with off-critical compositions in polymer binary mixture. J. Chem. Phys., 126:064908, 2007.

[100] J. Z. Zhu, L. Q. Chen, J. Shen, and V. Tikare. Coarsening kinetics from a variable-mobility Cahn-Hilliard equation: Application of a semi-implicit Fourier spectral method. Phys. Rev. E, 60:3564–3572, 1999.

[101] O. C. Zienkiewicz and R. L. Taylor. The Finite Element Method, volume 1,2,3. Butterworth-Heinemann, 5th edition, 2000.